From Knowledge to Wisdom

JEPE

ISSN 1934-8975 (Print)
ISSN 1934-8983 (Online)

Journal of Energy and Power Engineering

Volume 8, Number 3, March 2014

David Publishing Company
www.davidpublishing.com

Journal of Energy and Power Engineering

Volume 8, Number 3, March 2014 (Serial Number 76)

DAVID PUBLISHING

David Publishing Company
www.davidpublishing.com

Publication Information:
Journal of Energy and Power Engineering is published monthly in hard copy (ISSN 1934-8975) and online (ISSN 1934-8983) by David Publishing Company located at 240 Nagle Avenue #15C, New York, NY 10034, USA.

Aims and Scope:
Journal of Energy and Power Engineering, a monthly professional academic journal, covers all sorts of researches on Thermal Science, Fluid Mechanics, Energy and Environment, Power System and Automation, Power Electronic, High Voltage and Pulse Power, Sustainable Energy as well as other energy issues.

Manuscripts and correspondence are invited for publication. You can submit your papers via Web Submission, or E-mail to energy@davidpublishing.com or info@davidpublishing.com. Submission guidelines and Web Submission system are available at http://www.davidpublishing.org, www.davidpublishing.com.

Editorial Office:
240 Nagle Avenue #15C, New York, NY 10034, USA
Tel: 1-323-984-7526, 001-323-410-1082
Fax: 1-323-984-7374
E-mail: energy@davidpublishing.com; info@davidpublishing.com

Abstracted / Indexed in:
Database of EBSCO, Massachusetts, USA
Database of Cambridge Science Abstracts (CSA), USA
Chinese Database of CEPS, American Federal Computer Library Center (OCLC), USA
Ulrich's Periodicals Directory
Summon Serials Solutions
Chinese Scientific Journals Database, VIP Corporation, Chongqing, China
Chemical Abstracts Service (CAS)
ProQuest
CNKI
Google Scholar

Subscription Information:
Price:
Print $800 (per year)
Online $600 (per year)
Print and Online $880 (per year)

David Publishing Company
Tel: 1-323-984-7526, 001-323-410-1082; Fax: 1-323-984-7374
E-mail: order@davidpublishing.com
Digital Cooperative Company: www.bookan.com.cn

David Publishing Company
www.davidpublishing.com

Journal of Energy and Power Engineering

Volume 8, Number 3, March 2014 (Serial Number 76)

Contents

Power and Electronic System

Journal of Energy and Power Engineering 8 (2014) 399-413

Effects of Latitude and Design Variables on Performance and Cost of a Solar Heating System with Seasonal Storage

Gianfranco Rizzo and Cecilia Pisanti

Department of Industrial Engineering, University of Salerno, Fisciano (SA) 84084, Italy

Received: July 24, 2013 / Accepted: October 09, 2013 / Published: March 31, 2014.

Abstract: A thermo-economic model for the simulation and optimization of a CSHPSS (central solar heating plant with seasonal storage) is presented. The model, written in Matlab, allows to analyze the effects of different design and operating variables on plant performance and cost. Daily and seasonal variations of solar irradiation at different latitudes are considered, and an original approximate model for thermal stratification is included. Since a limited computational time is required, the simulation model can be effectively integrated with a non-linear constrained optimization procedure so as to determine the optimal choice of design variables for different locations and operating conditions. The comparison between a two-variable and four-variable optimization for five different locations at various latitudes has been presented, showing a significant decrease in pay-back time with latitude. Finally a sensitivity analysis on the most important design and operating variables has been performed and presented. It emerges that the optimal insulator thickness always decreases with latitude. The optimal tilt angle is slightly lower than latitude only when the plant is designed to cover the whole thermal load, while higher tilt values are selected in case of partial load covering.

Key words: Solar thermal plant, seasonal storage, model, optimization.

Nomenclature

A	Solar collector area (m^2)
AM	Air mass (/)
A_{st}	Water storage area (m^2)
D	Day index (1-365) (/)
E	Equality constraint
E_d	Thermal energy demand (kWh)
E_{SUN}	Solar energy (kWh)
F	Objective function
f_{SUN}	Solar radiation reduction factor (/)
G	Inequality constraint
H	Hour (1-24) (/)
I_0	Solar constant = 1366 (W/m^2)
Irr	Irradiance (W/m^2)
k_1, k_2	Parameters in the stratification model
L	Insulation thickness (m)
LB	Lower bound
P_{loss}	Reservoir thermal losses (W)
P_{SUN}	Solar power (W/m^2)
SUN_f	Solar fraction (/)
T^*	Variable in collector efficiency model
t_{amb}	Ambient temperature (°C)
t_{bottom}	Bottom temperature in the water reservoir (°C)
t_g	Ground temperature (°C)
t_m	Solar collector mean temperature (°C)
t_{max}	Maximum allowed temperature in the water reservoir (°C)
t_{mean}	Mean temperature in the water reservoir (°C)
t_{top}	Top temperature in the water reservoir (°C)
U_1, U_2	Parameters of the collector efficiency model
UP	Upper bound
V	Reservoir volume (m^3)
x	Decision variables
z	Zenith angle (rad)

Greek Symbols

η	Solar collector efficiency (/)
η_0	Parameter in the collector efficiency model
Δt	Difference between top and bottom temperature in the water reservoir
β	Tilt angle (rad)

Corresponding author: Gianfranco Rizzo, professor, research fields: conventional and renewable energy plants, hybrid solar vehicles, internal combustion engines modeling and control. E-mail: grizzo@unisa.it.

δ	Declination (rad)
θ	Incidence angle (rad)
λ	Thermal conductivity (W/mK)
φ	Latitude (rad)
Ψ	Azimuth (rad)
ω	Hour angle (rad)

1. Introduction

The perspective depletion of fossil fuels and the serious concerns about climate changes due to CO_2 emission in the atmosphere are strongly stimulating the recourse to renewable energy sources and to energy savings [1]. European community [2] and governments are committed to achieving significant improvements in terms of renewable share of final energy (Fig. 1).

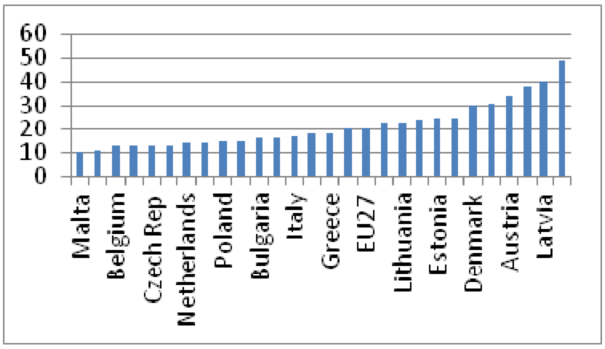

Fig. 1 EU renewable shares, targets for 2020.

Thermal uses represent a relevant fraction of the energy consumption. Solar thermal power is largely used in many countries, particularly in China, to cover this energy demand (Fig. 2). At the end of 2010, a thermal installed power of 185 GW for solar collectors for hot water/space heating was already in existence, and other 30 GW were installed during 2010 [1]. Solar plants can provide part of the thermal power needed for space heating, but they have an intrinsic drawback, since most of the solar power is available during summer, when the demand for thermal power is at its minimum level. In this case, most of the thermal power produced during summer would be wasted.

The usage of solar-cooling may partly overcome this problem, since the exceeding thermal power could be used for refrigeration and air-conditioning through absorption cooling plants. This solution, anyway, is limited by the relatively high cost and low efficiency of such plants. Moreover, there are many cases in which air-conditioning is not needed: significant examples are represented by schools, normally closed during summer.

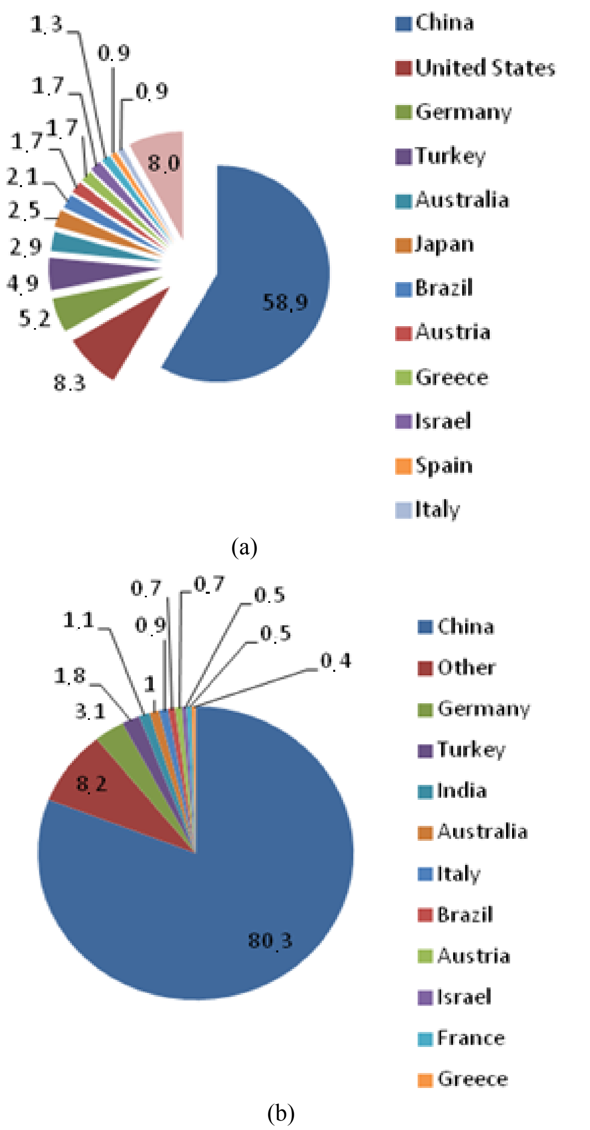

Fig. 2 Solar heating, top countries, 2009: (a) percent existing [3] and (b) added capacity [1].

However, combined with seasonal heat storage, solar energy can make a major contribution to heating. When solar energy is coupled with seasonal energy storage, the system is known as a CSHPSS (central solar heating plant with a seasonal storage): the main idea of these plants is to store energy during summer and to retrieve it during the winter. The essential components of a CSHPSS system include an array of solar collectors, a storage system, and the distribution network for the load (Fig. 3): it must be underlined that in CSHPSS the capacity of

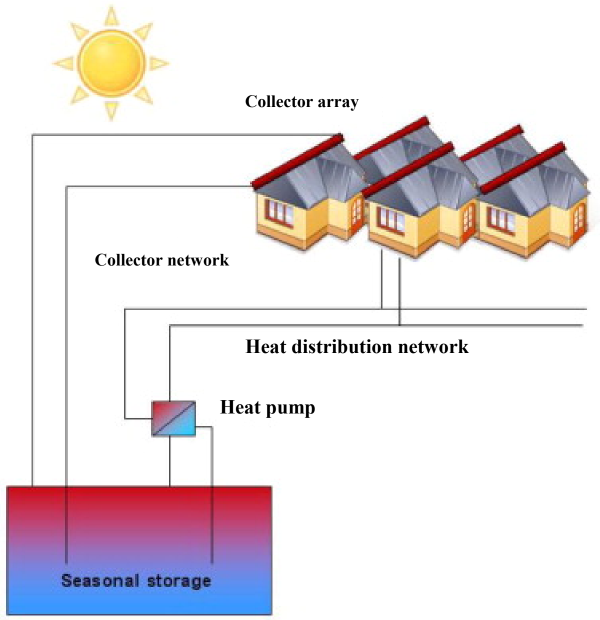

Fig. 3 General representation of a CSHPSS.

the seasonal storage must be large enough to retain most of the summer energy collected and at the same time undergo low energy losses.

In the next sections, after a brief review of the systems for seasonal heat storage and the possible modeling approaches, a model for simulation and optimization of a thermal solar plant with seasonal water storage is presented [4]. The thermo-economic model includes the description of thermal stratification in the reservoir by means of an original correlation, validated over literature data. The resulting code is therefore characterized by limited computational time, being so suitable for optimal design analysis. In fact, while most studies focus on the analysis of storage volume and solar panel area as the major design variables, there is a lack in the available literature on optimal design analysis of such plants, and on the effects of other design and operating variables, such as tilt angle, latitude and insulation thickness. The following sections show a sensitivity analysis based on several variables on five European cities placed at different latitudes. Such analysis has been carried out after comparing the data resulting from optimization with two and four variables with the aim of testing their influence on plant performance and costs.

2. Literature Review: Seasonal Heat Storage Systems

In the last decades, several pilot projects on CSHPSS plants have been developed, mainly in central and northern Europe. Attention was particularly given to the costs involved in heat storage, since economic feasibility is the most critical factor for this technology.

A technical assessment of the different technologies for solar thermal energy storage is presented in Ref. [5]. Both sensible heat and latent heat storage technologies, with phase change materials, can be adopted [4, 5]. Storage systems are usually classified as “water storage”, “earth storage”, “ground diffusive storage” and “aquifer storage” [6-9]:

- Water storage use tanks constructed from concrete, steel or fiberglass. The tank is located underground to benefit from the insulating and structural properties of the surrounding ground, and to minimize the above-ground space requirements. Insulation is applied to any above-ground surface of the tank [8, 10];
- Earth storage (or pit) systems are essentially large artificially-dug holes usually filled with water and gravel. They have low cost and ease of construction;
- In ground diffusive storage (or Borehole Systems), heat is stored directly in the ground. Heat exchangers are installed in boreholes drilled in ground that is suitable for heat storage [5, 11, 12]. Studies have also been carried out on use of ground source heat pumps [11];
- In aquifer storage systems, a naturally-occurring water-saturated media (usually sand) is used as the storage medium. The system is not as diffused as the previous three types.

For space heating applications, usually low temperature (less than 100 °C) sensible heat storage is used. Water is the most suitable thermal storage liquid in such temperature range, due to its high thermal capacity, large availability and low cost.

Since the 90s, several pilot and demonstration CSHPSS plants have been built in Germany, within a governmental R&D program. The monitoring of such

plants has proved to be well matched with the simulation performed during the design phase. Moreover, no major problems during their construction and operation occurred. In 2003, the cost for solar heating with such systems were, at maximum, twice as high as the conventional heat cost [7]. An accurate study on construction techniques and costs of water seasonal storage, based on three pilot projects in Germany, has been published in 1977 [13]: a unit cost of about 90 €/m^3, including cost for insulation, were estimated for large volume storage (10.000 m^3), while the long term goal was set to about 50 €/m^3.

Studies on the techniques to prevent oxygen penetration in the storage were performed and the use of steam cushion and of nitrogen atmosphere was discussed [13].

The thermal performance and economic feasibility of two types of central solar heating systems with seasonal storage in Turkey have been investigated by Ucar and Inalli [14, 15]. The effects of different ground types were studied with a finite element analysis; pay-back time ranging from 19 years to 34 years has been found.

A study on a CSHPSS under construction in Cheju island (Korea) is also available [10]: the plant has been simulated using TRNSYS to predict thermal performance and economic outcomes for two different types of solar collectors (flat plate and vacuum tube), and the return of investment was ranging from 18 to 30.

In most cases, TRNSYS simulation model has been used for simulation [16] in order to perform a parametric analysis of the main design variables (storage volume and solar panels area). Although an TRNOPT (optional optimization tool) was available [16], little or no studies in literature on CSHPSS performed via optimization analysis can be found. A study on the optimization of a near-zero energy solar home via Genetic Algorithms has been presented [17], but seasonal storage was not investigated. In order to limit the computational time required by the optimization analysis, a simplified (one-zone) modeling approach was used [18]. In case of a seasonal storage, a multi-year simulation is needed in order to reach steady operation. Following recent studies of the authors [4], a simplified model of a thermal solar plant with seasonal storage, also considering thermal stratification, is presented in next section. Thermal stratification plays an important role in the thermal plant management. Stratification has been studied both experimentally and numerically [19, 20].

Usually, rather complex models are used to describe thermal stratification [16]. Although these models are adequate to perform detailed design analysis of the water storage system, they are not suitable to be integrated in optimization studies, normally requiring hundreds or thousands of iterations.

3. Model of Thermal Solar Plant with Seasonal Storage

A simplified analytical model of solar irradiation has been adopted, able to describe seasonal and daily variations of irradiance, and the effects of latitude, also considering real sky conditions.

Two different types of solar collectors have been considered: flat pate and vacuum tube. Their efficiency curves are shown in Fig. 4.

A parabolic efficiency curve has been implemented in the model:

$$\eta = \eta_0 + U_1 T^* + U_2 T^{*2} \tag{1}$$

Where,

$$T^* = \frac{t_m - t_{amb}}{Irr} \tag{2}$$

The parameters for the two collectors are presented in Table 1. It can be observed that the quadratic terms are zero (flat plate) or almost negligible (vacuum tube).

In order to precisely estimate solar collector performance, an analytical model for the hourly ambient temperature has been developed, considering sinusoidal variations between daily minimum (at midnight) and maximum temperatures (at midday). Daily minimum and maximum temperatures are estimated by linear interpolation from monthly average values, available on-line for many locations [18]. The

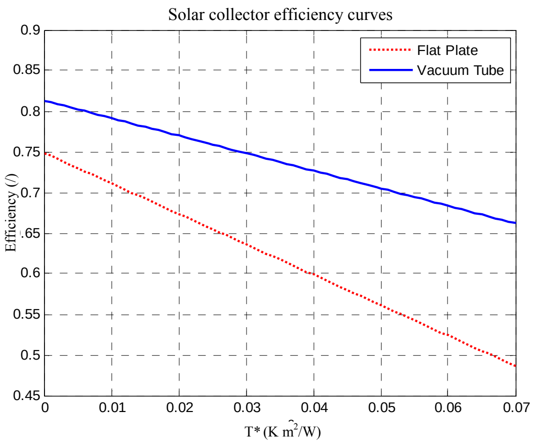

Fig. 4 Solar collector efficiency curves.

Table 1 Parameters for collector efficiency models.

Collector type	η_0	U_1	U_2
Flat plate	0.7486	-3.7465	0
Vacuum Tube	0.8131	-2.16	-0.001

equations of the solar collector simplified performance model are reported in the Appendix.

Thermal losses are estimated by the following equation:

$$P_{loss} = \frac{\lambda}{L} A_{st}\left(t_{mean} - t_g\right) \quad (3)$$

as a function of insulation thickness L, thermal conductivity λ, storage area A_{st}, mean storage temperature t_{mean} and ground temperature t_g. This latter is computed as the yearly average value of ambient temperatures, for each location [18].

About stratifications effect in this paper, a simple model based on the synthesis of physical data describing the most relevant aspects of thermal stratification (grey-box approach) has been applied. The model has been developed starting from a detailed study on thermal stratification in water thermal storage of different aspect ratio in static mode, published by Khalifa et al. [19]. The results have confirmed that thermal stratification is maximized at higher aspect ratio (i.e., AR = 2), while it is less pronounced at lower aspect ratio (AR = 0.5). AR is in this case defined as ratio between height and diameter.

The results obtained with AR = 1 are shown in Fig. 5. This figure shows stratification effects in four subsequent times (a, b, c, d). For each time frame, the difference ΔT between maximum temperature t_{top} and minimum temperature t_{bottom}, and the mean temperature t_{mean} (computed as the mean value between t_{top} and t_{bottom}) have been computed and plotted in Fig. 6. It can be observed that the relationship between these variables is remarkably linear.

The linear model expressing the difference between top and bottom temperature as a function of mean temperature (presented in Fig. 6) has been then integrated by further relations. These relations express the condition that thermal stratification tends to zero when water mean temperature approaches external temperature t_{min}, or in case it approaches the maximum allowed water temperature t_{max}. The resulting model, synthesized in the following Eqs. (4)-(7), is shown in Fig. 7.

$$t_{top} = t_{mean} + \Delta t/2 \quad (4)$$

$$t_{bottom} = t_{mean} - \Delta t/2 \quad (5)$$

$$\Delta t = \min\left[(k_1 + k_2 t_{mean}) \\ 2(t_{max} - t_{mean}) \\ 2(t_{mean} - t_{min})\right] \quad (6)$$

$$\Delta t \geq 0 \quad (7)$$

The parameters of the linear model k_1 and k_2 in Eq. (6) have been identified by linear regression techniques: their values are respectively -7.7039 and 0.3329.

The model has been validated over the measured data available for a water reservoir of a CSHPSS in Germany [21]. The mean temperature has been computed as the mean of top and bottom measured temperature (red and blue lines). Then, the estimated top and bottom temperatures (red and blue dotted lines) have been computed by means of the model Eqs. (4)-(7). It can be observed that the matching between measured and computed data is quite satisfactory, suggesting that most of thermal stratification occurring in a typical water reservoir for CSHPSS can be explained considering static effects. Some significant deviations occur in first starting phase, where transient effects may be more relevant. Although these remarks cannot be generally valid, such a model can be used to make an approximate estimate of thermal stratification

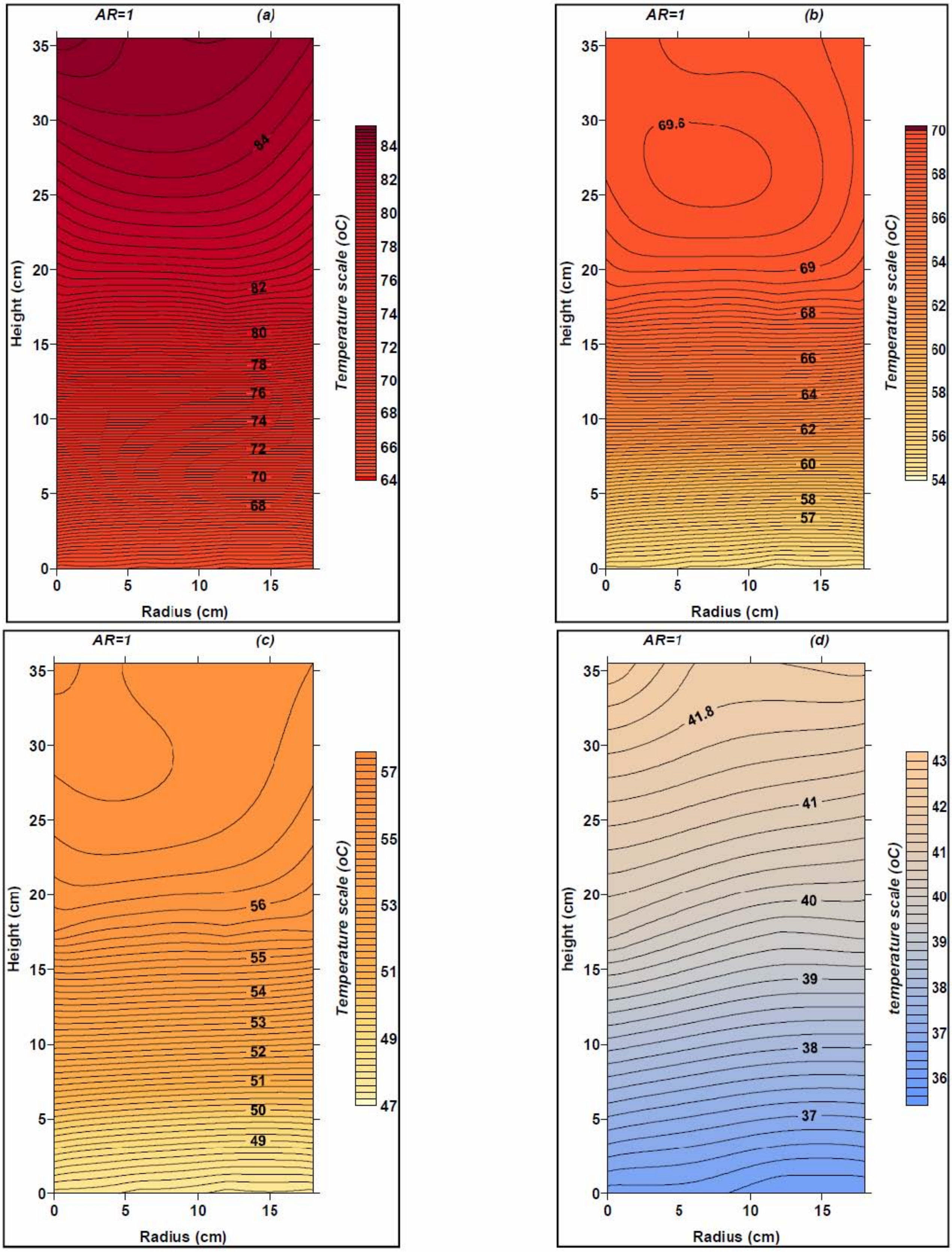

Fig. 5 Thermal stratification in static conditions in a water storage (aspect ratio = 1) from Ref. [19].

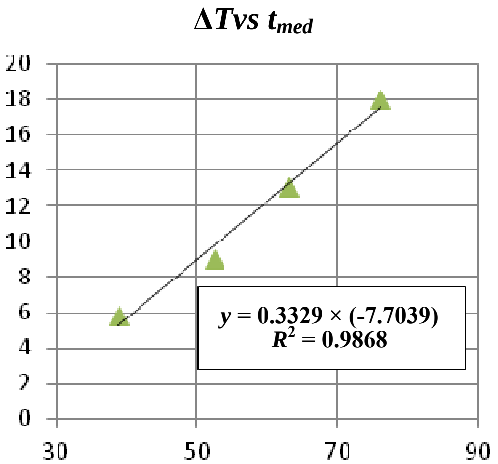

Fig. 6 Difference between top and bottom temperature vs. mean temperature in a water storage [19].

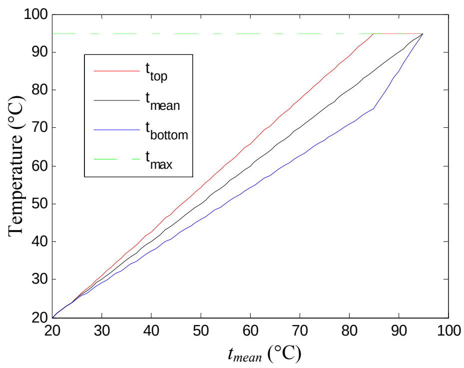

Fig. 7 Thermal stratification model.

in water if a more detailed model is unavailable or cannot be used because of an excessive computational time (i.e., for optimization studies).

The model is numerically integrated from given initial conditions for a certain number of years, until convergence is reached, in terms of difference between initial and final value of the water storage temperature. The thermal and economic performance is then evaluated with reference to the last year. A variable step 4th order Runge-Kutta method, implemented in the "ode45" routine of Matlab [22], has been used. Preliminary numerical studies were performed in order to set proper values of maximum allowable integration step and of termination criteria, in order to find the best compromise between numerical precision, stability and computational time. This aspect is particularly relevant, since the model has to be integrated within an optimization procedure, where hundreds of iterations may occur. Computational time is about 50 s for a year simulation (CPU Intel® Core™ i3, 4 GB RAM, 3.07 GHz).

4. Simulation of a CSHPSS

In order to investigate the effects of design variables in a CSHPSS, both simulation and optimization analyses have been performed.

4.1 Parametric Analysis

A first parametric analysis has been performed to assess the effects of storage volume V and solar panel area A, indicated as the most influential variables in literature [10]. V and A were therefore varied in a large range of values, while other values were fixed: all the values are reported in Table 2. Two sets of simulations have been performed both for a plant with VT (vacuum tube) collectors and with FP (flat plate) collectors. This first set of results has been conducted considering latitude and insulation data of Naples [4].

Total insulation cost is computed considering unit cost, insulation thickness and area.

The graphs presented in Fig. 8 show the storage temperature versus time (in hours) for three different cases, characterized by the same storage volume (1,000 m^3) and increasing solar panel area (100-200-300 m^2). The black, red and blue lines represent respectively the mean, top and bottom water temperature, estimated by the stratification model. Temperature trajectories of both starting year and steady solution are represented in the graphs.

The following figures from Figs. 9-11 report the solar fraction SUN_f, defined as the fraction of the thermal energy demand E_d covered by solar energy E_{SUN}, versus storage volume and panel area for all the computed cases:

$$SUN_f = \frac{E_d}{E_{SUN}} \tag{8}$$

The contour plots of payback (Fig. 9), mean solar collector efficiency (Fig. 10) and storage thermal losses Fig. 11) are also shown. The solutions at the left

Table 2 Data for simulation analysis.

Components	Values
Collector type	Flat plate
Tilt angle	40°
Insulator thickness (m)	0.23
Thermal conductivity (W/mK)	0.04
City	Naples
Tank volume (m^3)	25-1,000
Collector area (m^2)	25-1,000
Temperature radiators input (°C)	35
Temperature radiators output (°C)	30
Thermal load (MWh/year)	91.5
Insulation cost (€/m^3)	48
Panel cost flat plate (€/m^3)	300
Panel cost vacuum tube(€/m^3)	450

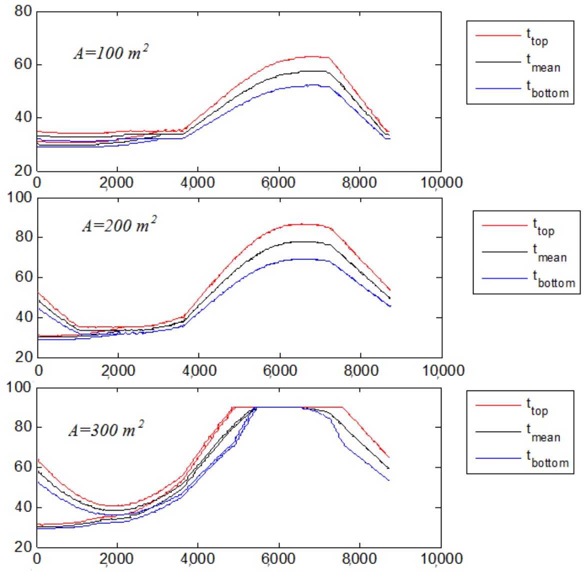

Fig. 8 Simulation analysis. Reservoir temperature (°C) vs. time (h). Solar surface (A) = 100-300 m^2. Reservoir volume (V) = 1,000 m^3. Collector type: flat plate. Location: Naples.

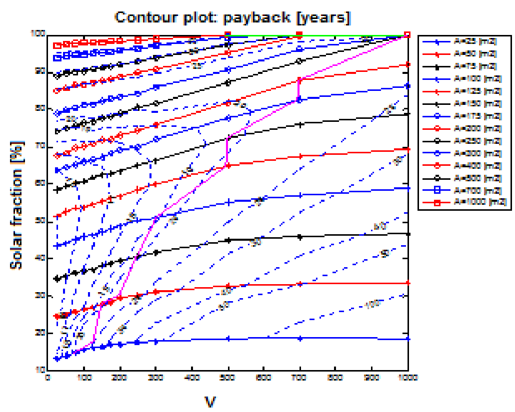

Fig. 9 Solar fraction vs. reservoir volume (m^3), for different solar panel area. Dotted lines: pay-back time (years). Collector type: flat plate. Location: Naples.

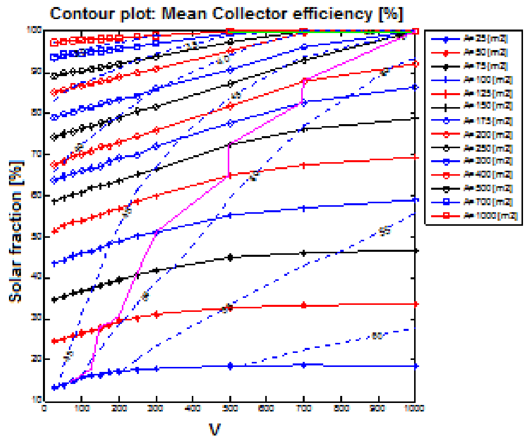

Fig. 10 Solar fraction vs. reservoir volume (m^3), for different solar panel area. Dotted lines: solar collector efficiency (%). Collector type: flat plate. Location: Naples.

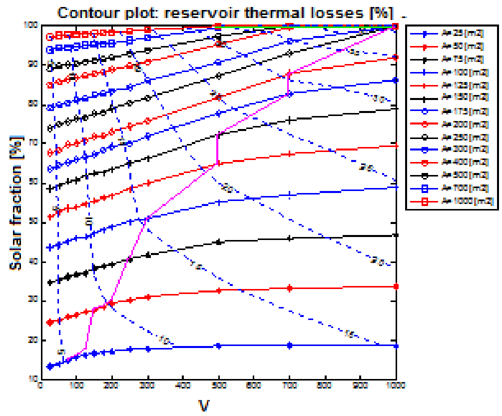

Fig. 11 Solar fraction vs. reservoir volume (m^3), for different solar panel area. Dotted lines: reservoir thermal losses (%). Collector type: flat plate. Location: Naples.

of the purple line are characterized by heat dissipation during summer, indicating that storage volume is undersized with regard to solar panel area. This case occurs for the lower graph of Fig. 9 (300 m^2): In fact, during summer part of solar heat must be dissipated, to avoid that the storage temperature exceeds the maximum allowed temperature (90 °C). It can be observed that temperature stratification is not reported during such phase, since it is assumed that heat from solar panel is added until the entire storage reaches its maximum allowable temperature, to maximize heat storage. Solar fraction is 100%, in this case (Fig. 10). In the second case (A = 200 m^2) maximum temperature reaches about 80 °C and no dissipation occurs, while solar fraction comes up to about 92%. In the third case

(A = 100 m^2) the storage is oversized and therefore underutilized: Maximum temperature is about 60 °C, and solar fraction stops at about 59%. The best payback is reached in the second case (A = 200 m^2) (Fig. 9), while the third case (A = 100 m^2) is characterized by higher average solar collector efficiency (Fig. 10) and lower storage losses (Fig. 11), due to lower storage temperatures.

The study of the results (Figs. 9-11) shows that the effect of solar collectors area over solar fraction is non-linear: an increase in solar area from 100 m^2 to 200 m^2 produces a significant improvement in solar fraction (from approximately 43% to 68% at the minimum storage volume), while passing from 300 m^2 to 400 m^2 results in a much lower improvement (from approximately 78% to 85%). Also the effect of storage volume is non-linear: the slope of the constant solar area curves is positive and almost constant until the saturation conditions (purple lines) are reached, tending to assume an asymptotic behavior afterwards. The observed effects of storage volume and panel area over solar fraction and the pay-back time values, ranging from 15 years up, are consistent with other studies available in literature [11, 14, 15].

5. Optimization Approach

Non-linear effects occur for most of the variables affecting plant performance. In this case, the best set of design variables can not be determined solely by analyzing each variable independently of other variables, since they are interdependent. Therefore, the adoption of a non-linear optimization approach is required [23]. The plant model has been then integrated with a nonlinear constrained optimization algorithm, in order to determine the optimal combination of design and operating variables corresponding to the best values of the performance indices. The mathematical problem is formulated in the following way:

$$\min_x f(x) \tag{9}$$

$$G(x) \leq 0 \tag{10}$$

$$E(x) = 0 \tag{11}$$

$$LB \leq x \leq UB \tag{12}$$

The objective function $f(x)$ is represented by the simple pay-back time, defined as the ratio between the plant cost C_{Plant} and the yearly savings S.

The plant cost is computed by adding up the cost of (1) solar panels; (2) water reservoir; (3) thermal insulator. Yearly savings are computed as the difference from fuel cost with the conventional thermal plant and the fuel cost for auxiliary with solar plant (This latter being zero in case that solar fraction is 100%), in correspondence of the last computed year (i.e., at steady conditions).

The equality constraint Eq. (11) may express the condition that the solar fraction must be equal to a given value (i.e., 100%), while inequality constraints Eq. (10) may express the condition that no dissipation occurs, and therefore storage temperature is always below the maximum allowed value.

All the design variables are assumed to be positive, i.e., LB = 0 in Eq. (12). A classical 2nd order Quasi-Newton approach is used [23], as implemented in the routine "fmincon" of the optimization toolbox of Matlab [22].

Preliminary tests have been performed, to verify the functionality of the procedure. The graphs in Fig. 12 show the values of design variables (storage volume and panel area) and of the objective function (pay-back time) versus the iterations, for two different cases (flat plate and vacuum tube). For this computation, lower values for storage cost (40 €/m^3) and for insulation cost (40 €/m^3) were assumed with respect to the values reported in Table 2.

It can be observed that, starting from arbitrary initial values (A = 600 m^2, V = 600 m^3), optimal solutions are found in both cases in approximately 60 iterations. Very similar optimum pay-back time was obtained (about 17.9 years). The optimal storage volume V is also quite similar in the two cases (about 1,130 m^3). In case of vacuum tube, however, lower surface is suggested for solar panels, as expected (Table 3).

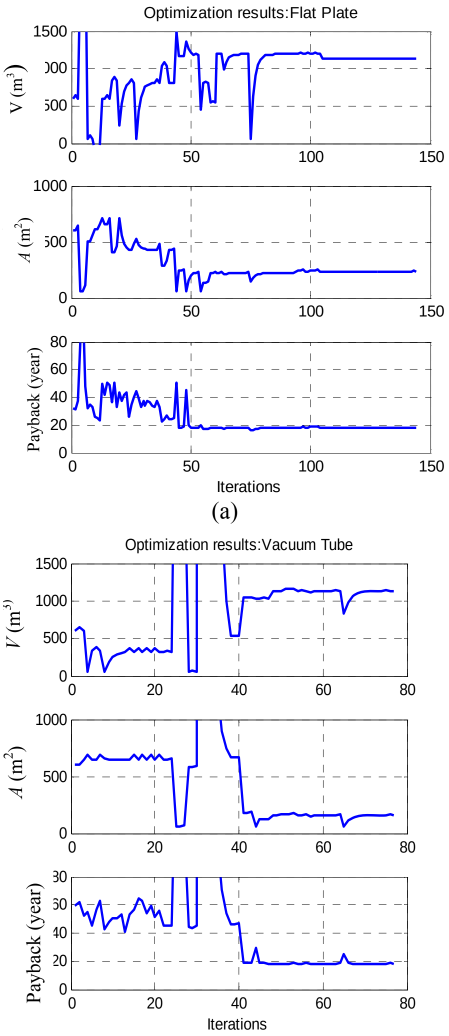

(a) (b)

Fig. 12 Optimization results: design variables and objective function vs. iterations.

Table 3 Optimization results: optimal values of design variables and objective function.

Solar collector type	V (m^3)	A (m^2)	Pay-back time (year)
Flat plate	1,125	239	17.8
Vacuum tube	1,136	161	17.9

※Optimized values for five different cities.

Computational time for each test is less than two hours on a PC, and therefore compatible with the use of model for design purposes.

The optimization analysis has been done for five different cities: Messina, Naples, Turin, Munich and Hamburg. For each city payback value has been minimized considering two (area and volume) or four Variables (area, volume, insulator thickness and tilt angle).

Payback values for both cases are shown in Fig. 13: until latitude 45° the two curves almost overlap, while at higher latitudes the two curves tend to diverge. Pay-back values resulting from four-variable optimization (curve with circles) show to be always lower compared to those obtained optimizing only volume and area (upper curve), as expected. In both cases payback grows significantly with latitude, with an almost linear trend: at lower latitudes (Messina), payback time is less than one half compared to higher latitudes (Hamburg). The above results are apparently mismatched with the fact that these plants are mostly studied and developed in central Europe, while little attention is paid to them in southern Europe.

The comparison of the optimal values for the optimized variables in the two cases (Tables 4 and 5) shows that quite different solutions may be proposed for reservoir volume and panel area (i.e., Hamburg). Moreover, the optimal tilt angle proposed does not seem to be correlated to latitude, while there is a systematic and significant increase of insulator thickness with latitude (Table 5). However, the interpretation of such outcomings should take into account that tilt angle and insulator thickness have much lower influence on plant payback compared to the other decision variables (volume and area), and that therefore their optimal values might be affected by a significant spread.

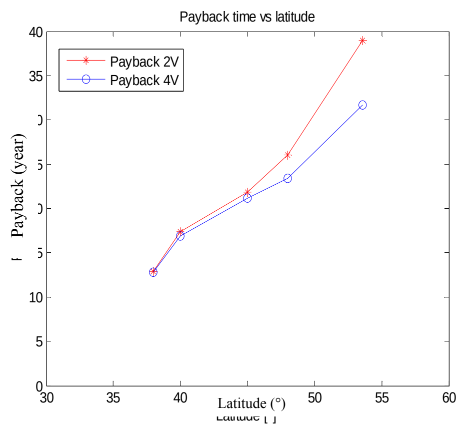

Fig. 13 Optimized values of payback at different latitudes with 2 or 4 variables.

Table 4 Optimized values with an optimization in 2 variables, the collector is a flat plate, insulator thickness 0.25 m, storage cost 40 €/m^2.

City	Messina	Naples	Turin	Munich	Hamburg
Latitude (°)	38	40	45	48	53.6
V (m^3)	805	1,033	1,006	1,095	2,487
A (m^2)	180	241	350	433	531
V/A (m)	4.47	4.29	2.88	2.53	4.68
Payback	12.86	17.36	21.84	26.06	38.99
Wasted heat	0	0	0	0	0
Plant cost (k€)	88.46	119.53	151.04	179.99	269.81
Solar energy ($\frac{kWh}{m^2 day}$)	6.5	5.41	4.91	4.22	3.5
Heat losses (%)	32.89	40.63	46.58	47.11	61.88

Table 5 Optimized values with an optimization in 4 variables, the collector is a flat plate.

City	Messina	Naples	Turin	Munich	Hamburg
Latitude (°)	38	40	45	48	53.6
V (m^3)	782	972	1,210	1,043	1,154
A (m^2)	165	244	253	290	414
V/A (m)	4.74	3.98	4.79	3.60	2.79
Payback	12.76	16.84	21.12	23.39	31.68
Wasted heat	0	0	0	0	0
Plant cost (k€)	88.77	116.73	147.35	159.99	220.48
Thick (m)	0.26	0.26	0.30	0.47	1.33
Tilt (deg)	37.2	36.9	34.5	41.4	37.5
Heat losses (%)	31.5	38.73	43.09	21.91	9.29

6. Sensitivity Analysis

Most studies in literature on CSHPSS plant [7, 10, 11, 14, 24, 25] focus on the effects of solar panel area and reservoir volume, that are of course the most important design variables in such plants. Anyway, a significant effect may be played by other design variables, such as insulator thickness and tilt angle, and also by other exogenous variables, as fuel and energy cost. A sensitivity analysis on the most important design and operating variables has been performed through the simulation model and presented hereafter.

The study has been performed for the five European cities listed in the previous paragraph, to assess the influence of latitude on payback time. The results shown in the following graphs refer to plants with a flat plate collector.

Two different cases have been analyzed, considering different values of collector area and tank volume, for the five locations:

(1) Case A: fixed values, A = 300 m², V = 300 m³; solar fraction less than 100%;

(2) Case B: optimized values with 2 variables; solar fraction is 100% in such case.

In order to highlight the effects of latitude, the results for Hamburg (the highest latitude) and Messina (the lowest latitude) have been compared hereafter.

In the next paragraphs, the effects of insulator thickness and tilt angle are presented, while the effects of latitude are summarized at the end of the chapter.

6.1 Effect of Insulator Thickness

The payback time for a plant in Hamburg attains quite large values (about 40 years for Case A, and 27 years for Case B, optimized), as shown in Figs. 14 and 15, where the lowest values are marked by red circles. It can be also observed that the best insulator thickness differs significantly in the two cases (0.3 m in Case A and 0.7 m in Case B, where the reservoir volume is much greater).

The payback values of a plant in Messina are much lower than in previous case (about 17 years in Case A and 13 years in Case B). Moreover, payback values are much less sensitive to insulator thickness (Figs. 16 and 17), with the minimum value in both cases of about 0.2 m.

In Case B, it can be noticed that a linear trend follows the minimum value.

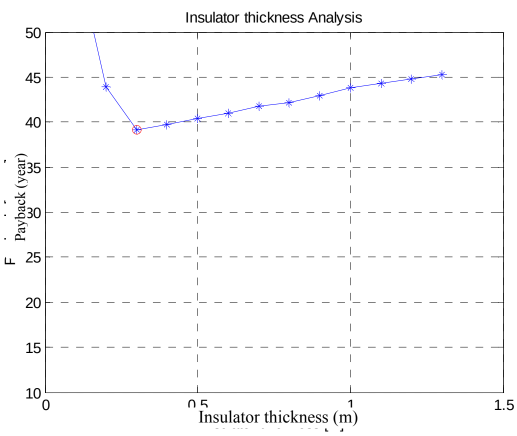

Fig. 14 Payback time for Hamburg with Case A values.

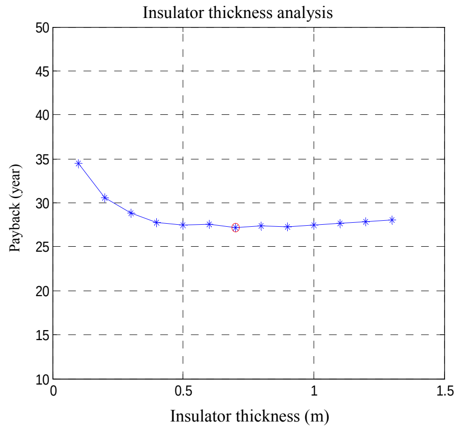

Fig. 15 Payback time for Hamburg with Case B values.

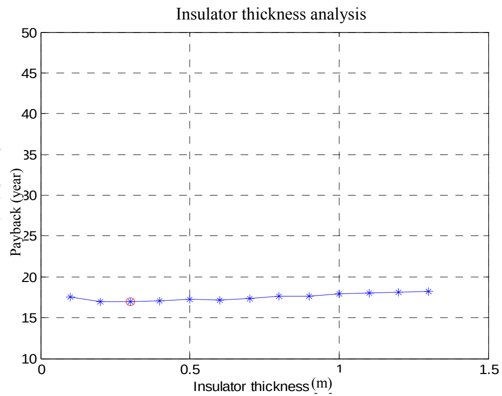

Fig. 16 Payback time for Messina with Case A values.

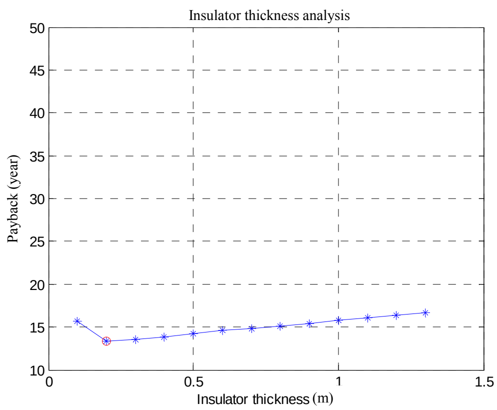

Fig. 17 Payback time for Messina with Case B values.

6.2 Effect of Tilt Angle

Payback time values in Hamburg for Case A are almost constant in a large range of tilt angles (30°-60°) (Fig. 18), while for Case B (Fig. 19) the trend of the payback is almost regular, as a second order curve, and the minimum value is reached at a tilt angle value lightly lesser than Hamburg latitude angle.

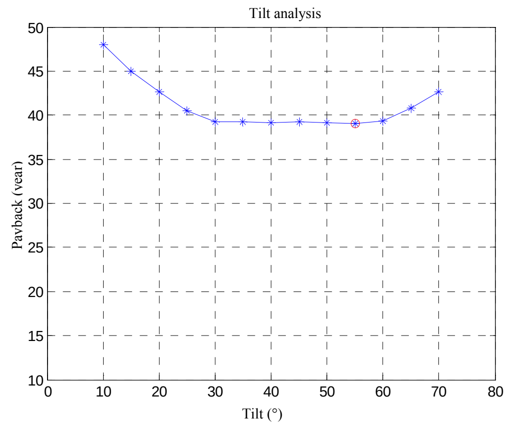

Fig. 18 Payback time for Hamburg with Case A values.

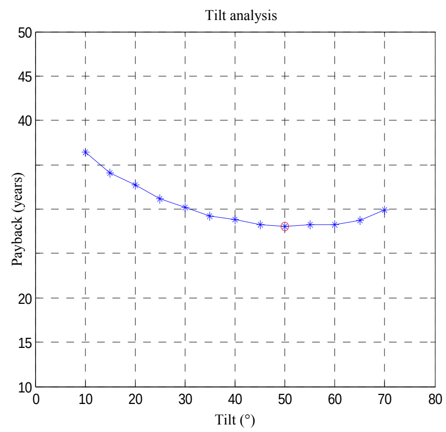

Fig. 19 Payback time for Hamburg with Case B values.

A similar result has been obtained also for the other cities: the minimum value of payback time is reached at a tilt angle slightly lesser than the latitude of the place. The comparison of the results obtained at lowest latitudes (Messina), for Cases A and B (Figs. 20 and 21) looks quite interesting. While in the optimal Case B, the best tilt angle is near the latitude, for case A the best payback is found at much higher values (60°). This result can be explained considering that in Case A, the reservoir volume is undersized, and does not allow to store all the solar energy collected during summer. Therefore, it is more convenient to adopt higher tilt angles, in order to maximize the solar radiation during winter time.

7. Conclusions

The economic feasibility of thermal solar plants with seasonal water storage has been recently improved, due

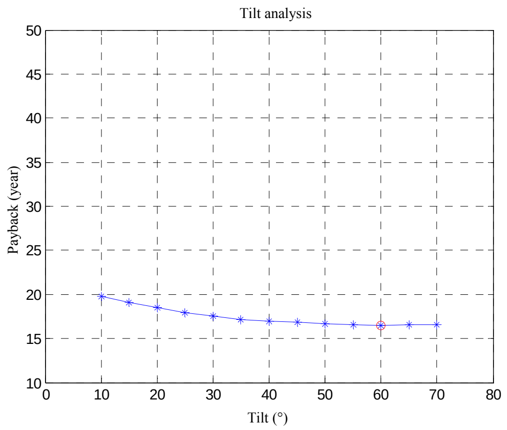

Fig. 20 Payback time for Messina with Case A values.

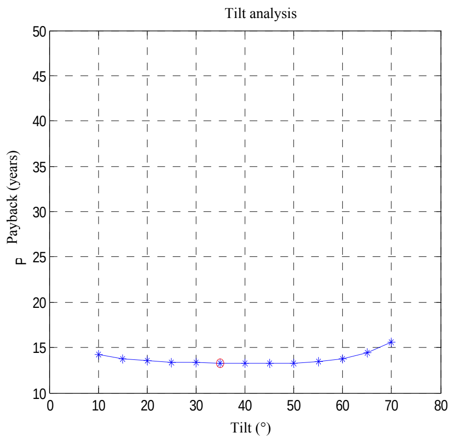

Fig. 21 Payback time for Messina with Case B values.

to the parallel increase of fuel cost, decrease of solar collectors cost and the adoption of incentives in some countries including Italy [26]. In spite of all this, systematic studies on optimal design of such plants are still missing in literature. A thermo-economic model suitable both for simulation and optimization analysis has been presented, including an original approximate description of thermal stratification. An extensive parametric analysis on the effects of storage volume and panel area over solar fraction, pay-back time, average collector efficiency and thermal losses has been presented and discussed.

An optimization analysis has been performed, with two and four decision variables, and the results have been commented. The results show that the benefits of a complete (i.e., four variables) optimization tend to increase at higher latitudes.

The parametric analysis has confirmed that panel area and reservoir volume are the most influential variables, as expected. It has also been observed that the optimal tilt angle is slightly lower than latitude, when the plant is designed to cover the whole thermal load, while higher tilt values may be convenient in case of partial load covering (lower solar fraction). Optimal insulator thickness always decreases with latitude, as expected.

Finally, the results have shown that the economic feasibility of such plants improves significantly at low latitudes. Such a conclusion clashes with the fact that these solutions are not so commonly adopted in countries at lower latitude, such as Italy, with respect to countries like Germany and Sweden, where these plants have been mostly studied.

Acknowledgments

The contributions given to this study by Claudia Poto, Vito Della Corte and Claudia Tramontano for their dissertations in Mechanical Engineering at the University of Salerno are gratefully acknowledged.

References

[1] Renewables 2010 Global Status Home Page, http://www.ren21.net.

[2] Renewable energy, target for 2020, European Commission Web site, http://ec.europa.eu/energy/renewables/targets_en.htm.

[3] W. Weiss, F. Mauthner, Solar heat worldwide, markets and contribution to the energy supply 2009, IEA Solar Heating & Cooling Programme, May 2011.

[4] G. Rizzo, A model for simulation and optimal design of a solar heating system with seasonal storage, in: Proc. of ECOS 2012 Conference, Perugia, Italy, June 26-29, 2012.

[5] H.E.S. Fath, Technical assessment of thermal energy storage technologies, Renewable Energy 14 (1-4) (1998) 35-40.

[6] A. Sharma, V.V. Tyagi, C.R. Chen, D. Buddhi, Review on thermal energy storage with phase change materials and applications, Renewable and Sustainable Energy Reviews 13 (2009) 318-345.

[7] T. Schmidt, D. Mangold, H. Muller-Steinhagen, Central solar heating plants with seasonal storage in Germany, Solar Energy 76 (2004) 165-174.

[8] R. Fuller, L. Aye, Seasonal storage for solar thermal systems in Australia?, in: Proceedings of the 45th Conference of the Australian and New Zealand Solar Energy Society, Maroubra, Oct. 2-6, 2007.

[9] V. Lottner, M.E. Schulz, E. Hahne, Solar-assisted district heating plants: Status of the German rogramme solarthermie-2000, Solar Energy 69 (6) 449-459.

[10] M. Chung, J.U. Park, H.K. Yoon, Simulation of a central solar heating system with seasonal storage in Korea, Solar Energy (64) (4-6) (1998) 163-178.

[11] K. Lim, S. Lee, C. Lee, An experimental study on the thermal performance of ground heat exchanger, Experimental Thermal and Fluid Science 31 (2007) 985-990.

[12] B. Sannera, C. Karytsasb, D. Mendrinosb, L. Rybachc, Current status of ground source heat pumps and underground thermal energy storage in Europe, Geothermics 32 (2003) 579-588.

[13] R. Kubler, N. Fisch, E. Hahne, High temperature water pit storage projects for the seasonal storage of solar energy, Solar Energy 61 (2) (1997) 97-105.

[14] A. Ucar, M. Inalli, Thermal and economical analysis of a central solar heating system with underground seasonal storage in Turkey, Renewable Energy 30 (2005) 1005-1019.

[15] A. Ucar, M. Inalli, Thermal and economic comparisons of solar heating systems with seasonal storage used in building heating, Renewable Energy 33 (2008) 2532-2539.

[16] TRNSYS Home Page, http://www.trnsys.com/>.

[17] R. Charron, A. Athienitis, The use of genetic algorithms for a net-zero energy solar home design optimization tool, in: PLEA2006—The 23rd Conference on Passive and Low Energy Architecture, Geneva, Switzerland, Sept. 6-8, 2006.

[18] Database of Weather Data Home Page, http://www.weatherbase.com.

[19] A.N. Khalifa, A.T. Mustafa, F.A. Khammas, Experimental study of temperature stratification in a thermal storage tank in the static mode for different aspect ratios, ARPN Journal of Engineering and Applied Sciences 6 (2) (2011) 53-60.

[20] C. Cruickshank, S. Harrison, Analysis of a modular thermal storage for solar heating systems, in: Canadian Solar Buildings Conference, Montreal, Aug. 20-24, 2004.

[21] T. Schimidt, J. Nussbicker, S. Raab, Monitoring results from German central solar heating plants with seasonal storage, in: ISES 2005 Solar World Congress, Orlando Florida, USA, Aug. 6-12, 2005.

[22] Matlab technical documentation Home Page, http://www.mathworks.it/help/techdoc/index.html.

[23] P.E. Gill, W. Murray, M.H. Wright, Practical Optimization, Academic Press, London, 1981.

[24] H. Kerskes, Seasonal thermal storage, in: 25th International Conference on Efficiency, Cost, Optimization and Simulation of Energy Conversion Systems and Processes, Perugia, Italy, June 26-29, 2012.

[25] Active Solar Preheat Systems, Department of Defense, USA, Unified Facilities Criteria [Online], http://buildingcriteria2.tpub.com/ufc_3_440_01/index.htm.

[26] Incentives on Thermal Solar plants in Italy (Conto energia termico) [Online], http://www.gse.it/it/Conto%20Termico/Pages/default.aspx.

[27] R. Foster, M. Ghassemi, A. Cota, Solar Energy: Renewable Energy and the Environment, Energy and Environment series, in: A. Ghassemi (Ed.), CRC Press Taylor & Francis Group, New York, 2009.

[28] Renewable Resource Data Centre Home Page, http://www.nrel.gov/rredc (accessed Mar. 31, 2014).

Appendix A

The following equations describe the solar power absorbed by a solar collector with tilt angle β and azimuth ψ, in a location of latitude φ; to compute these values next equations have been presented and also shown in Ref. [27]. The model predicts the direct solar irradiance with sunny sky *Irr*. The reduction factor f_{SUN} is introduced in 0 to predict irradiance under real sky conditions. This factor has been identified for different locations (Fig. 1A), starting from average real monthly solar data [28].

$$\delta = 0.4093\, sin\left(2\pi \frac{284 + d}{365}\right) \tag{1A}$$

$$\omega = 2\pi\,(12 - h)/24 \tag{2A}$$

$$z = a\cos(\sin\delta \sin\varphi + \cos\delta \cos\varphi \cos\omega) \tag{3A}$$

$$AM = min\left[1/sin\left(\frac{\pi}{2} - z\right), 38\right] \tag{4A}$$

$$Irr = 1.1 \cdot I_0 \cdot 0.7^{AM^{0.678}} \tag{5A}$$

$$\psi_{SUN} = a\cos\left(\frac{\sin\delta\cos\varphi - \cos\omega\cos\delta\sin\varphi}{\cos\left(\frac{\pi}{2} - z\right)}\right) \tag{6A}$$

$$\theta = a\cos\left(\cos\left(\frac{\pi}{2} - z\right) \cdot \cos(\psi - \psi_{SUN}) \cdot \sin\beta\right) \tag{7A}$$

$$P_{SUN} = Irr \cdot f_{SUN} \cdot \cos\theta \tag{8A}$$

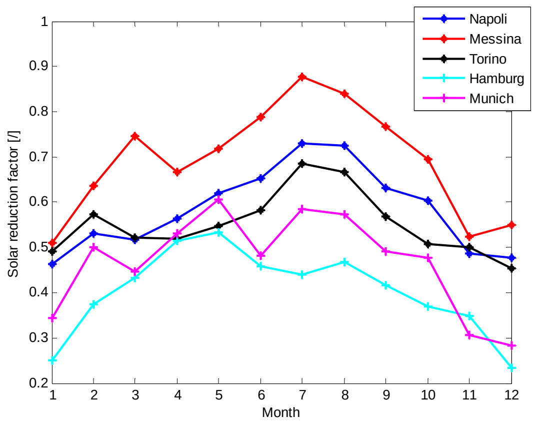

Fig. 1A Solar reduction factor for different locations.

Journal of Energy and Power Engineering 8 (2014) 414-422

Energy-Saving Design for Hydraulic Tube Bender

Jyh-Chyang Renn, Chin-Yi Cheng and Meng-HanLin

Department of Mechanical Engineering, National Yunlin University of Science and Technology, Douliou 64002, Taiwan

Received: July 24, 2013 / Accepted: September 02, 2013 / Published: March 31, 2014.

Abstract: Generally speaking, hydraulic control systems can be divided into two different driving concepts. The first one is the well-known hydraulic valve-controlled system and the second one is the pump-controlled system. The former possesses the feature of fast dynamic response. However, the poor energy-saving performance is its major fault. On the contrary, the hydraulic pump-controlled system has the significant advantage of energy-saving which meets the current demand in modern machine design. In this paper, the simulation analysis using MatLab/SimuLink and DSHplus software for a newly developed energy-saving hydraulic tube bender is conducted. Instead of the conventional fixed displacement hydraulic pump, the new hydraulic tube bender utilizes an internal gear pump with AC servomotor as its driving power source. In the new energy-saving hydraulic circuit, the use of conventional pressure relief valve and unloading valve are no longer necessary since the demanded flow-rate and pressure output can be precisely obtained by continuously changing the speed of the AC servomotor. In addition, two closed-loop control schemes using fuzzy sliding-mode controller are adopted and compared. To compare the energy-saving control systems, such as load-sensing control system, constant supply pressure control scheme and conventional hydraulic control scheme. Furthermore, the simulation results also show that the newly developed hydraulic tube bender can save up to 43% of energy consumption in a working cycle as compared to the conventional hydraulic tube bender.

Key words: Hydraulic energy-saving, pump-controlled system, fluid power, tube bender.

Nomenclature

Designation	Denotation	Unit
A	Piston average area	(m^2)
A_a	Piston actuating area (chamber A)	(m^2)
A_b	Piston actuating area (chamber B)	(m^2)
B	Flow constant	($m^2/min\cdot\sqrt{bar}$)
b	Newton's friction coefficient	(N s/m)
C_d	Flow coefficient	(-)
d_v	Spool diameter	(mm)
E_{oil}	Oil bulk modulus	(bar)
F_L	Disturbance load	(N)
M	Mass of load	(kg)
N	Reference rotational speed input	(rpm)
p_{Ls}	Load-sensing pressure	(bar)
p_s	Supply pressure	(bar)
Q_a	Volumetric flow-rate going into the chamber A	(L/min)
Q_b	Volumetric flow-rate coming out of the chamber B	(L/min)
Q_s	Supply flow-rate	(L/min)
Δp_{set}	Reference pressure drop Input	(bar)
P_{sset}	Reference supply pressure Input	(bar)
P_{pump}	Power consumption of pump	(kW)
T	Time constant of AC servomotor	(s)
u	Actuating signal	(V)
Vp	Pump displacement	(cc)
V_a	Volume of chamber A	(m^3)
V_b	Volume of chamber B	(m^3)
V_{pipe}	Volume of connecting pipe	(m^3)
X_v	Spool displacement	(mm)
Y	Displacement of cylinder piston	(m)
$\dot{Y}$	Velocity of cylinder piston	(m/s)
$\ddot{Y}$	Acceleration of cylinder piston	(m/s^2)
ρ	Oil density	(kg/m^3)

Corresponding author: Chin-Yi Cheng, Ph.D. candidate, research fields: automation control, pneumatic and hydraulic system control. E-mail: g9511706@yuntech.edu.tw.

1. Introduction

Nowadays, hydraulic systems still play a very important role in modern industry due to the large output force, high power/weight ratio and excellent stiffness. Research in the field of hydraulic control system has been published. The publications concentrated on the parallel control of the motion

control and energy-saving control on a hydraulic valve controlled system. Rotational speed control and load-sensing control on a hydraulic valve controlled motor system were integrated using PID control (Proportional-Integral-Derivative controller) [1]. In this paper, a conventional hydraulic tube bender shown in Fig. 1 is chosen for the study of implementing the hydraulic energy-saving design. Fig. 2 shows a typical working cycle of the chosen hydraulic tube bender [2]. It is observed that eight sequential steps are required to complete the 90 degrees bending of a straight tube. They are: (A) advancing the main pushing unit; (B) clamping the tube; (C) advancing the bending unit together with auxiliary pushing unit and bending the tube (90 degrees); (D) retracting the main pushing unit, (E) releasing the clamping of tube; (F) retracting the auxiliary pushing unit; (G) removal of tube and (H) retracting the bending unit. Fig. 3 shows eight sequential schemes to demonstrate these eight steps. In the hydraulic circuit of a conventional tube bender, a fixed-displacement vane pump is generally utilized as shown in Fig. 4. In addition, a pilot-operated pressure balanced relief valve together with a two-way solenoid operated valve is used as well to construct the unloading circuit. However, the hydraulic supply pressure of the conventional tube bender has to be set at the maximal demanded pressure of 120 bar to ensure the proper function of all eight steps. Thus, from Fig. 2, it is clear that huge energy lost in the working cycle is inevitable since only the step C requires the maximal supply pressure of 120 bar. For the rest seven steps, however, the actually demanded supply pressure is much lower than the maximal pressure of 120 bar [2, 3]. On the other hand, recent performance improvements in the AC servomotor provide a promising alternative to design the energy-saving hydraulic circuit [4-7]. In details, the demanded flow-rate and pressure output of the hydraulic pumping unit can be precisely obtained by continuously changing the speed of the AC servomotor. In this paper, therefore, the implementation of energy-saving design is mainly based on the AC servomotor-controlled scheme. In the

Fig. 1 A hydraulic tube bender [5].

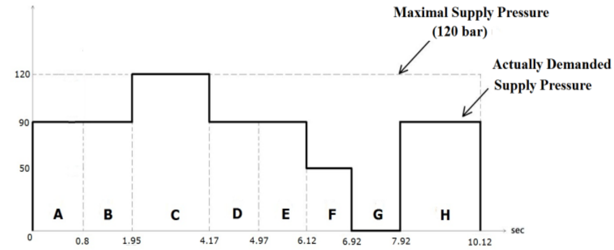

Fig. 2 Demanded pressure in a working cycle.

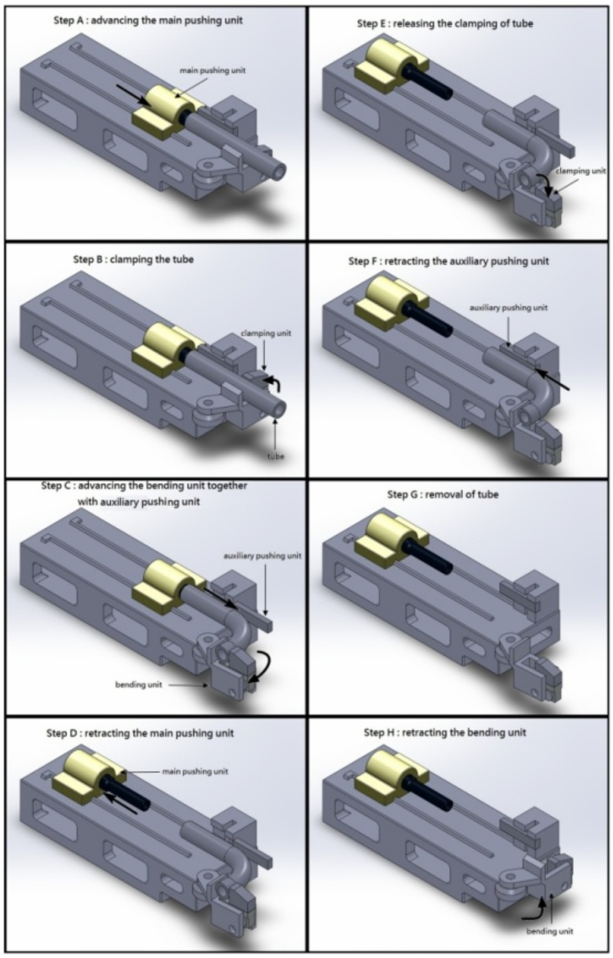

Fig. 3 Eight sequential schemes to demonstrate the eight steps of tube bending.

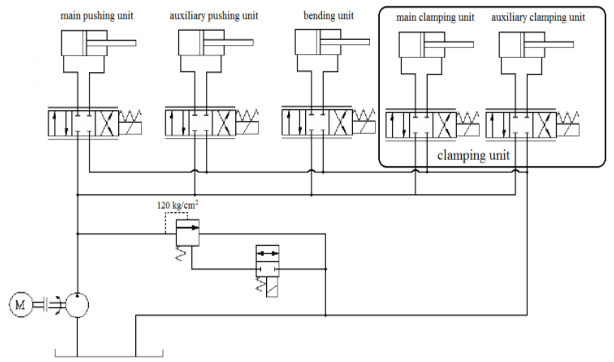

Fig. 4 Schematic circuit diagram of a conventional hydraulic tube bender.

following, the proposed energy-saving control scheme is firstly outlined.

2. Energy-Saving Control Scheme

In this paper, two closed-loop control schemes using fuzzy sliding-mode controller are adopted and compared. The first one is load-sensing control strategy and the other one is constant pressure control scheme [4]. Fig. 5 shows the block diagram of the load-sensing control. A fixed pressure drop, Δp_{set}, across the control solenoid valve serves as the reference input. The load pressure, p_{Ls}, is measured by a pressure sensor and fedback to the closed-loop control system to ensure that the supply pressure, p_s, can be real-time adjusted according to the variable load pressure. Consequently, the actual pressure drop, $\Delta p = p_s - p_{Ls}$, can be maintained as a constant by the closed-loop control. On the other hand, Fig. 6 shows the block diagram of constant pressure control. In this configuration, the reference supply pressure input, P_{sset}, is varied according to the different demanded pressure levels at various steps as shown in Fig. 2. Thus, the reference supply pressure input is actually not a constant and has to be changed at different steps. Besides, it is worth mentioning that the fuzzy sliding-mode scheme is chosen as the closed-loop controller because it provides a dither-like chattering signal. Such a signal is proven to be effective to overcome the nonlinear friction disturbances [1].

The combination of fuzzy-logic-controller with sliding mode controller results in the fuzzy sliding-mode

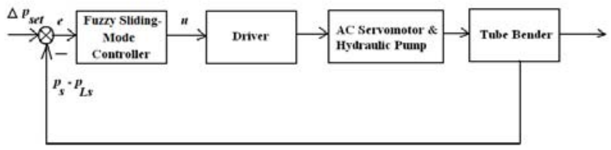

Fig. 5 Load-sensing control block diagram.

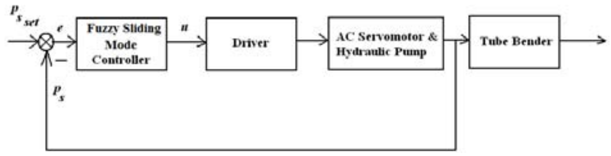

Fig. 6 Constant pressure control block diagram.

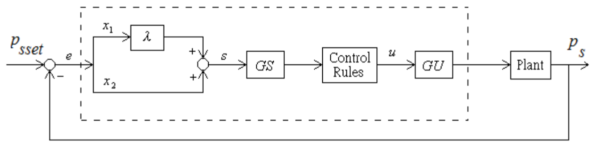

Fig. 7 Scheme of the proposed fuzzy sliding-mode control.

controller. As an example, the constant pressure control scheme combining the fuzzy sliding-mode controller is illustrated as follows. Fig. 7 shows the schematic block diagram of the fuzzy sliding-mode controller. The error signal, $e(k)$, and the error signal change, $\Delta e(k)$, are denoted by x_1 and x_2 respectively, that is:

$$x_1 = e(k) = p_{sset} - p_s \tag{1}$$

$$x_2 = \Delta e(k) = e(k) - e(k\text{-}1) \tag{2}$$

where, p_{sset}: reference supply pressure input, p_s : actual supply pressure.

Unlike the conventional controller, there are four procedures involved in the implementation of a fuzzy sliding-mode controller, fuzzification of the input, fuzzy inference based on the knowledge, the defuzzification of the rule-based control signal and the determination of the scaling factors.

2.1 Fuzzification

The proposed fuzzy sliding-mode controller requires only one input signal, s, which is exactly the combination of the parameters x_1 and x_2.

$$s = \lambda x_1 + x_2 \tag{3}$$

The usual triangular fuzzy membership functions for the input signal, s, and for the output signal, u, are utilized. The input signal also represents the switching surface of the sliding mode controller.

2.2 Inference

The inference process consists of nine typical rules driven by the linguistic values of the input signal, s. There are:

If s is very large-positive, then u is very large-positive;

If s is large-positive, then u is large-positive;

If s is medium-positive, then u is medium-positive;

If s is small-positive, then u is small-positive;

If s is zero, then u is zero;

If s is small-negative, then u is small-negative;

If s is medium-negative, then u is medium-negative;

If s is large-negative, then u is large-negative;

If s is very large-negative, then u is very large-negative.

2.3 Defuzzification

The defuzzification is to transform control signal into exact control output. In the defuzzification, the method of center of gravity is used.

$$u = \frac{\sum_{i=1}^{n} W_i B_i}{\sum_{i=1}^{n} W_i} \tag{4}$$

where,

u: output of the fuzzy sliding-mode controller;

W_i: the degree of firing of the i_{th} rule;

B_i: the centroid of the consequent fuzzy subset of the i_{th} rule.

2.4 Determination of Scaling Factors, GS and GU

Before the input signal, s, is fed into the fuzzy-sliding mode controller, it has to be multiplied by the scaling factor, *GS*, so that the product is normalized in the interval [-1, 1]. Similarly, the output signal of the fuzzy-sliding mode controller, u, is multiplied by the scaling factor, *GU*, to meet the actual operating voltage range, -10 V to 10 V, of the AC servomotor. It is also worth mentioning that the values of the factors, *GS* and *GU*, affect the system response greatly.

3. Modeling, Simulation Results and Discussion

In this paper, two commercial software packages, the MatLab/SimuLink and DSHplus, are chosen as simulation tools to analyze the energy-saving performance. Firstly, the modeling procedure by MatLab/SimuLink will be outlined.

The dynamics of the utilized AC servomotor can be simplified as a first-order function. In addition, a simplified model for a typical single-acting hydraulic cylinder is shown in Fig. 8. The volumetric flow-rate output of the hydraulic pump is given by Merritt [3].

$$Q_s = Vp \times (1 - e^{-t/T})N \tag{5}$$

where, Vp: displacement of pump; T: time constant of AC servomotor; N: reference rotational speed input.

In practice, the time constant, T, can be derived from the data sheet of the AC servomotor and is estimated to be 50 ms [8].

From continuity equation, the dynamic model for the supply pressure can be simplified as:

$$\frac{dP_s}{dt} = \frac{E_{oil}}{V_{pipe}}(Q_s - Q_a) \tag{6}$$

where, Q_a denotes the volumetric flow-rate going into the chamber A of cylinder and can be described by:

$$Q_a = BX_v\sqrt{(P_s - P_a)} \tag{7}$$

Similarly, the volumetric flow-rate coming out of the chamber B of cylinder can be obtained as:

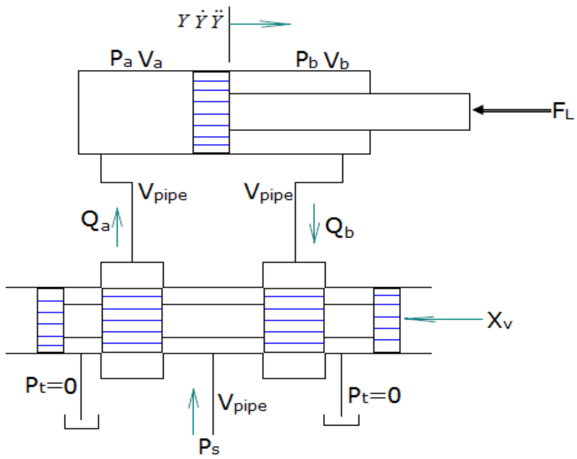

Fig. 8 A simplified model for a single-acting hydraulic cylinder [2].

$$Q_b = BX_v\sqrt{P_b} \quad (8)$$

where, X_v : spool displacement; B: flow constant.

Since the switching directional control valve is utilized in the circuit design, the spool displacement, X_v, is set to be the maximal stroke +3 or -3 mm.

The flow constant, B, in Eq. (8) can further be expressed as:

$$B = C_d\pi d_v\sqrt{2/\rho} \quad (9)$$

where,

C_d: flow coefficient;

d_v: diameter of the valve spool;

ρ: density of the hydraulic oil.

If the internal and external leakages of the cylinder are both negligible, the simplified dynamic pressure equations for both chambers of the cylinder are:

$$\frac{dP_a}{dt} = \frac{E_{oil}}{V_a+V_{pipe}}(Q_a - A\dot{Y}) \quad (10)$$

$$\frac{dP_b}{dt} = \frac{E_{oil}}{V_b+V_{pipe}}(-Q_b + A\dot{Y}) \quad (11)$$

where,

E_{oil}: bulk modulus of oil;

V_a: volume of chamber A;

V_b: volume of chamber B;

V_{pipe}: volume of connecting pipe;

A: average area of piston;

$\dot{Y}$: velocity of the piston.

Finally, the equation of motion is given:

$$M\ddot{Y} + b\dot{Y} = A_aP_a - A_bP_b - F_L \quad (12)$$

where,

M: mass of load;

$\ddot{Y}$: acceleration of piston;

b: Newton's friction coefficient;

A_a: actuating area of piston in chamber A;

A_b: actuating area of piston in chamber B;

F_L: disturbance load.

Thus, the MatLab/SimuLink model for the single-acting hydraulic cylinder is shown in Fig. 9. Since there are totally five hydraulic cylinders in the conventional tube bender, the whole hydraulic circuit model containing five single-acting hydraulic cylinders built by MatLab/SimuLink is shown in Fig. 10. On the

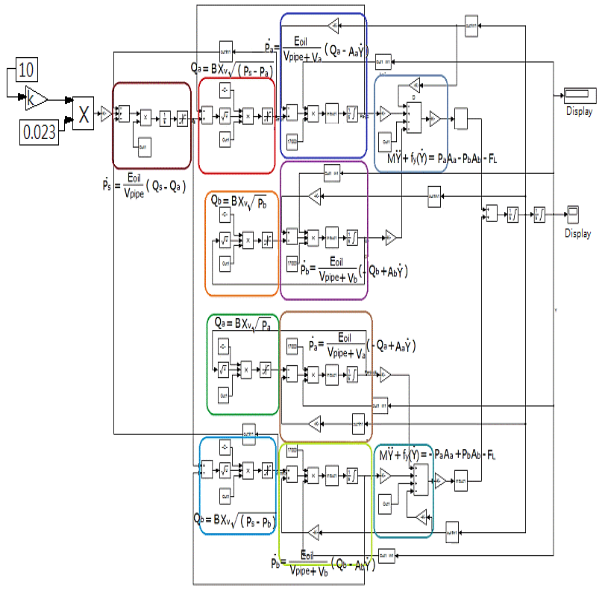

Fig. 9 MatLab/SimuLink model for the single-acting hydraulic cylinder.

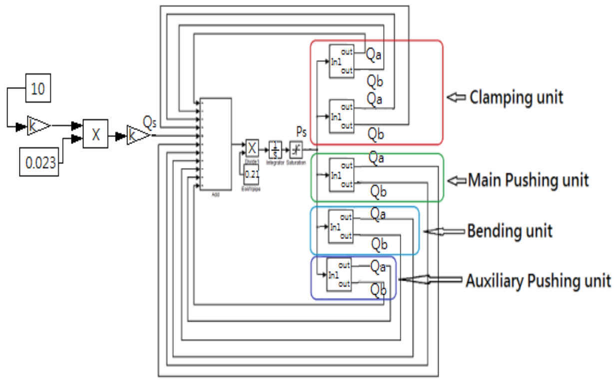

Fig. 10 MatLab/SimuLink model for the conventional hydraulic tube bender.

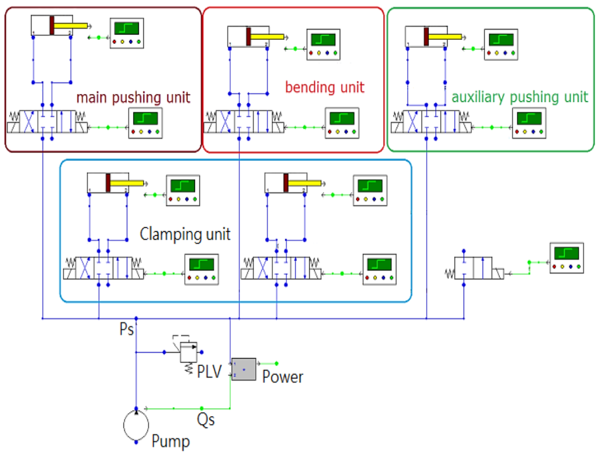

Fig. 11 Hydraulic circuit model built by DSHplus for conventional tube bender.

other hand, to double check the validity of the above mentioned modeling and simulation, the hydraulic circuit model for the same conventional tube bender by using the second commercial software package DSHplus is established and shown in Fig. 11. Fig. 12 shows the simulation displacements of the main pushing cylinder by two different software packages respectively. Similarly, two calculated actuating pressure curves of the main pushing cylinder are also depicted in Fig. 13. Obviously, from Figs. 12 and 13, the calculated cylinder displacements as well as actuating pressure curves derived from MatLab/SimuLink and DSHplus respectively are almost identical. It can therefore be verified that the modeling procedure and simulation results by MatLab/SimuLink are reliable and can be used for further energy-saving analysis.

It is worth mentioning that the block diagram shown in Fig. 11 is actually an open loop control scheme. It is necessary to incorporate the proposed fuzzy sliding-mode controller into the control structure and form a closed-loop control block diagram. In addition, two proposed control schemes, the constant pressure control and load-sensing control, have also to be implemented. Thus, based on the simplified block diagrams shown in Figs. 5 and 6, two comprehensive closed-loop control block diagrams can be obtained as shown in Figs. 14 and 15, respectively. In the following, the control performances of these two closed-looped control schemes will be discussed and compared.

After adequate simulations, all important data and information of the whole tube bender system, like the pressure and flow-rate etc., can be obtained. The power consumption of the pumping unit can easily be calculated by the following Eq. (13).

$$P_{pump} = \frac{p_s \times Q_s}{600} \qquad (13)$$

where,

P_{pum} : power consumption of the pump;

p_s: supply pressure;

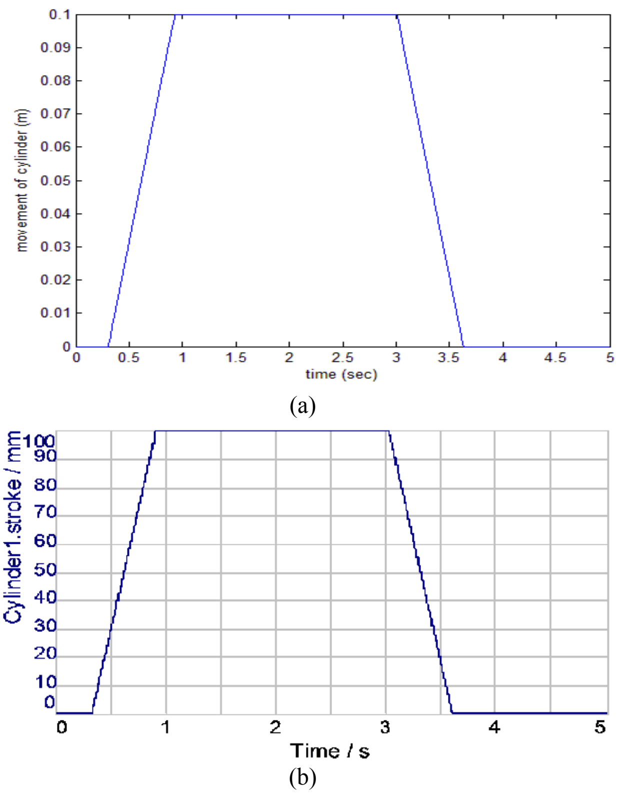

Fig. 12 Simulation cylinder displacements of the main pushing unit by two different software packages (open loop). (a) MatLab/SimuLink results; (b) DSHplus results.

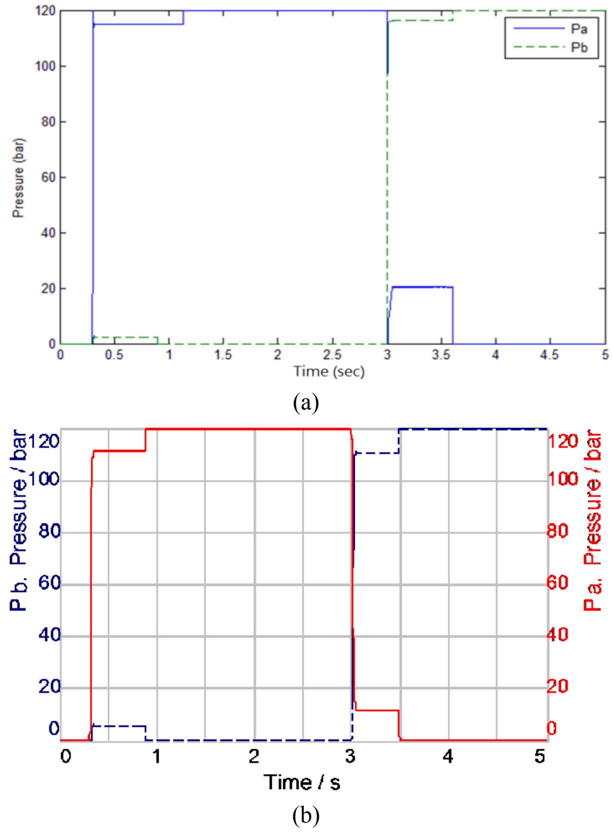

Fig. 13 Simulation actuating pressure curves of the main pushing unit by two different software packages (open loop). (a) MatLab/SimuLink results; (b) DSHplus results.

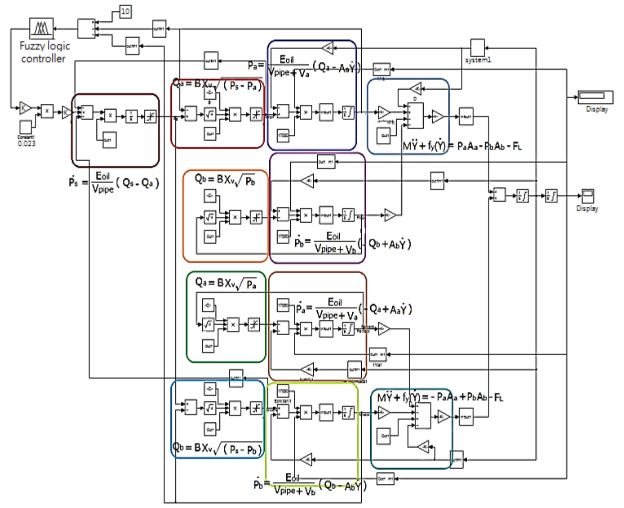

Fig. 14 Closed-loop load-sensing control block diagram for the main pushing cylinder.

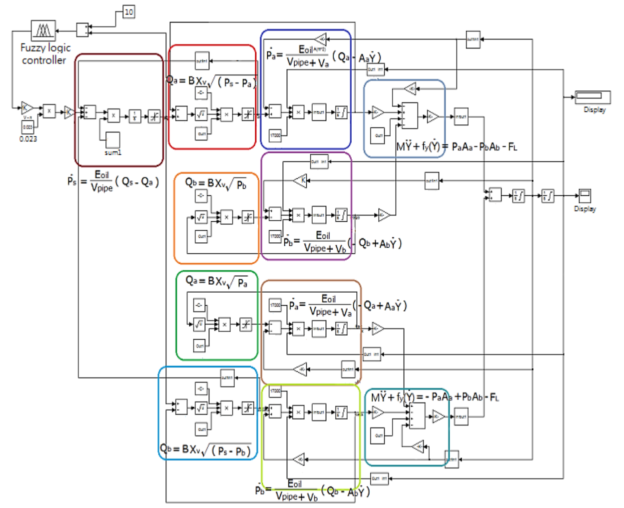

Fig. 15 Closed-loop constant pressure control block diagram for the main pushing cylinder.

Q_s: supply flow-rate.

As an illustrated example, the simulation results of supplied actuating pressure and volumetric flow-rate by load-sensing control for the main pushing cylinder are shown in Fig. 16, where the pressure drop, Δp_{set}, is set to be 3 bar. It is noticeable that both the pressure and flow-rate curves for the advance and retraction of the main pushing cylinder are depicted. In addition, Fig. 17 shows the similar simulation results by constant pressure control scheme, where the reference supply pressure input, P_{sset}, is set to be 90 bar according to the demanded pressure level at step A shown in Fig. 2. Comparing Figs. 16 and 17, it is actually not easy to tell the differences of the pressure and volumetric flow-rate signals during the advance and retraction phases of the main pushing cylinder. However, if Eq. (13) and appropriate numerical calculations are applied to evaluate the power consumption, the difference of driving power between two utilized closed-loop control strategies for the main pushing cylinder in one working cycle is more obvious as shown in Fig. 18.

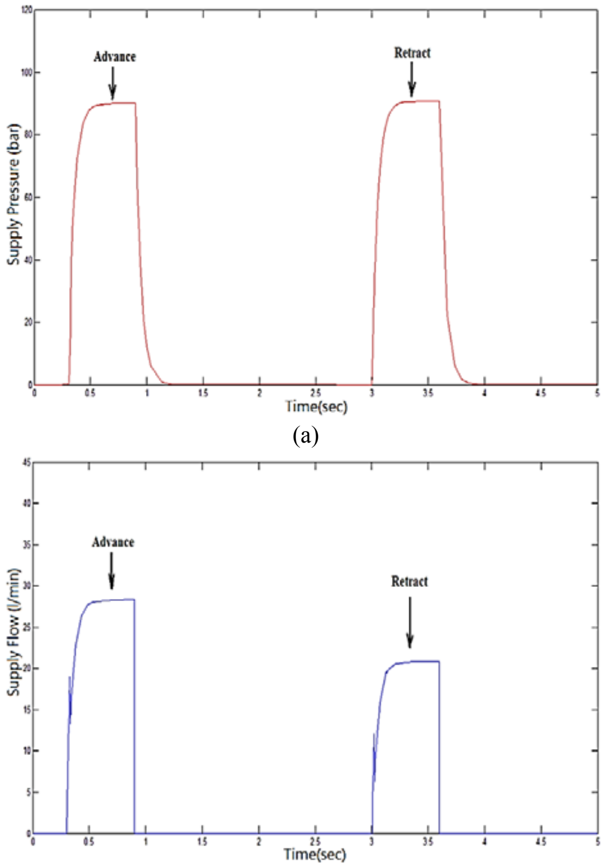

Fig. 16 Simulation results of (a) supplied actuating pressure and (b) volumetric flow-rate by load-sensing control for the main pushing cylinder.

It is worth mentioning that the energy-saving analysis using DSHplus is not executed in this paper because the proposed fuzzy sliding-mode controller is not available in the current library of the commercial software package DSHplus.

Table 1 shows the comparisons of overall energy consumption of pumping unit between the conventional and newly designed energy-saving hydraulic tube bender. It is observed that the energy-saving performance

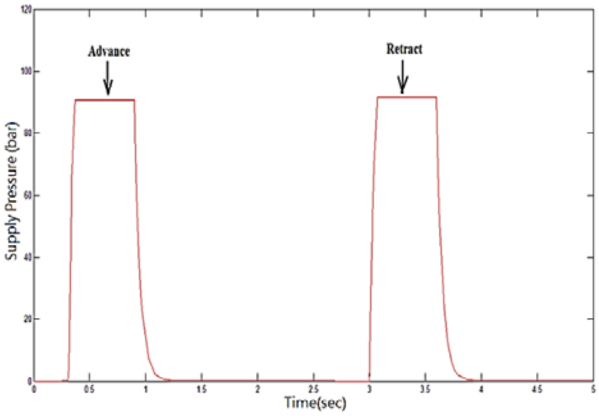

(a)

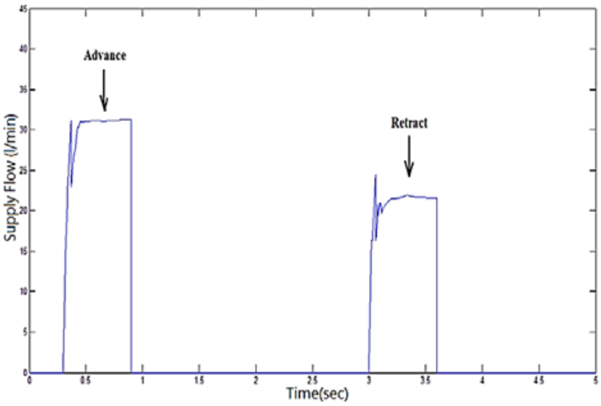

(b)

Fig. 17 Simulation results of (a) supplied actuating pressure and (b) volumetric flow-rate by constant pressure control for the main pushing cylinder.

of constant pressure control scheme is somewhat better than that of load-sensing control scheme. Furthermore, the simulation results also show that the newly designed hydraulic tube bender can save up to 43% of

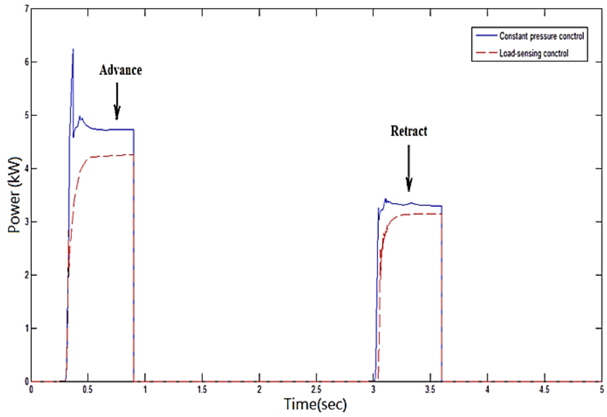

Fig. 18 Simulation results of power consumption between two utilized closed-loop control strategies for the main pushing cylinder.

energy consumption in a working cycle as compared to the conventional hydraulic tube bender. These results prove the validity of the proposed energy-saving hydraulic circuit design as well as the effectiveness of proposed closed-loop control schemes.

4. Conclusions

In this paper, a new energy-saving hydraulic tube bender is successfully designed based on the simulation analysis using MatLab/SimuLink and DSHplus. The introduction of the additional commercial software package DSHplus is merely to verify the validity of proposed modeling procedure and simulation results. In addition, three conclusions may also be drawn from this research.

Table 1 Comparisons of energy consumption between conventional and new energy-saving hydraulic tube bender.

Item	Conventional			Load-sensing control			Const. pressure control		
Step	*Ps* (bar)	*Qs* (l/min)	P_{pump} (KW)	*Ps* (bar)	*Qs* (l/min)	P_{pump} (KW)	*Ps* (bar)	*Qs* (l/min)	P_{pump} (KW)
A	120	41.4	8.28	88.75	29.88	4.42	89.6	32.58	4.86
B	120	41.4	8.28	89.68	32.32	4.96	89.6	32.43	4.84
C	120	41.4	8.28	119.04	38.04	7.55	119.54	38.37	7.64
D	120	41.4	8.28	89.96	22.06	3.31	89.71	23.93	3.58
E	120	41.4	8.28	88.95	24.67	3.66	89.92	23.58	3.53
F	120	41.4	8.28	49.53	15.18	1.25	49.82	14.38	1.19
G	0	41.4	0	0	0	0	0	0	0
H	120	41.4	8.28	89.94	27.51	4.12	89.65	28.79	4.3
Total energy(kJ)									
	75.51			42.92			43.75		
Energy-saving percentage									
	0%			43.16%			42.06%		

(1) The simulation results derived from MatLab/SimuLink and DSHplus respectively are nearly identical. It can therefore be verified that the modeling procedure and simulation results by MatLab/SimuLink are reliable and can be used for further energy-saving analysis.

(2) Simulation results show that the newly designed hydraulic tube bender can save up to 43% of energy consumption in a working cycle as compared to the conventional hydraulic tube bender. This result not only shows the potential of energy-saving design but also encourages the future real implementation of the new tube bender.

(3) The energy-saving performance of constant pressure control scheme is somewhat better than that of load-sensing control scheme. Besides, the former utilized only one pressure sensor while the latter requires two pressure sensors to calculate the actual pressure drop. Therefore, the better choice would be undoubtedly the constant pressure control scheme which will be suggested to be implemented in the future real layout of the new hydraulic tube bender.

Acknowledgments

The financial support of the National Science Council under grant number NSC-101-2622-E-224-014-CC3 is greatly appreciated. In addition, the industrial project supported by SOCO Machinery Co., LTD. is also acknowledged.

References

[1] B. Zhahe, Energy-saving circuits of hydraulic systems with variable supply pressure and its regulation, Ph.D. Thesis, RWTH Aachen, Germany, 1993. (in German)

[2] J.C. Renn, Position control of a pneumatic servo-cylinder using fuzzy-sliding surface controller, Int. J. of Fluid Power 3 (3) (2002) 19-25.

[3] H.E. Merritt, Hydraulic Control Systems, John Wileys and Sons, Cincinnati, Ohio, USA, 1967.

[4] H. Murrenhoff, Systematic approach to the control of hydrostatic drives, Proc. of the Institution of Mechanical Engineers, Part I: Journal of Systems & Control Engineering 213 (I5) (1999) 333-347.

[5] M.H. Chiang, Y.W. Chien, D.D. Yu, Implementation of integrated control of path control and energy-saving control for hydraulic servo systems, J. CSME 24 (2) (2003) 50-58.

[6] S. Ota, K. Sugimura, K. Suzuki, Energy saving of oil hydraulic pump unit by idling stop with accumulator, in: Proceedings of the 8th JFPS International Symposium on Fluid Power, Okinawa, Japan, Oct. 25-28, 2011.

[7] Hydraulic Tube Bender, SOCO Co. Ltd Web site, http://www.soco.com.tw.

[8] HES Series AC Servomotor, Catalogue of Delta Electronics, DELTA Web site, 2012, http://www.delta.com.tw.

Journal of Energy and Power Engineering 8 (2014) 423-430

Reducing the Gas Pressure Drop in Suction Mufflers of Hermetic Reciprocating Compressors

Jônatas Ferreira Lacerda[1], José Luiz Gasche[2], João Fabio Parise de Lara[2] and Danilo Martins Arantes[2]

1. Research and Development Department, Tecumseh do Brasil Ltda, São Carlos-SP 13570-820, Brazil

2. Department of Mechanical Engineering, Unesp-Univ Estadual Paulista, Ilha Solteira-SP 15385-000, Brazil

Received: October 11, 2013 / Accepted: November 14, 2013 / Published: March 31, 2014.

Abstract: The suction muffler of hermetic reciprocating compressors is installed in order to attenuate the noise generated by the gas pulsation of the flow through the suction valve. However, the installation of the suction muffler affects the operation of the compressor owing to gas pressure drop, which causes volumetric and energetic efficiency loss due to the gas specific volume augmentation. Therefore, there is a compromise between sound attenuation and pressure drop increase, which has to be taken into account by compressor designers. In this work, it presents a numerical solution to the flow through a suction muffler in order to analyze the pressure field and point out the main contributions to the overall pressure drop of the flow. A commercial CFD (computational fluid dynamics) code was used to perform the numerical simulations and the results were validated by using experimental data. After analyzing the pressure field, the geometry of the muffler was modified intending to decrease the flow pressure drop. The geometric modification produced a 28% reduction on the overall pressure drop, without influencing the sound attenuation.

Key words: Refrigeration, hermetic, reciprocating, compressor, muffler.

1. Introduction

Current reciprocating compressors have their suction lines provided with an acoustic damping system, named suction mufflers or acoustic filters, which have the main function of attenuating the noise generated by the gas pulsation of the flow through the suction valve. Suction mufflers usually consist of a set of cavities and tubes which are maintained in fluid communication in relation to each other. The noise generated due to gas pulsation in the suction valve is confined in these cavities, attenuating the sound.

However, the installation of the muffler produces an undesired effect, the augmentation of the pressure drop of the flow in the suction line, which increases the gas specific volume. The ultimate consequence is the reduction of the mass flow rate of the refrigerant pumped by the compressor, causing volumetric and[1] energetic efficiency loss [1-3]. Therefore, the compressor designer must provide an efficient acoustic damping system which gives the lowest pressure drop in the suction line at the same time.

CFD (computational fluid dynamics) techniques have been used as evaluation tools for predicting pressure drop and superheating in suction lines of reciprocating compressors in order to enhance efficiency, increasing the development speed and reducing the number of experimental tests required. Pérez-Segarra et al. [4] and Deschamps et al. [5] have developed an unsteady one-dimensional model for the whole compressor using a finite volume technique. Choi et al. [6] have carried out a steady state three-dimensional analysis of the flow in the suction muffler and verified numerically and experimentally the decrease of cooling capacity due to the increase of both suction gas temperature and pressure drop. Optimization studies using DOE (design of experiment) and CFD have been performed by Kim et al. [7] and

Corresponding author: José Luiz Gasche, associate professor, research fields: refrigeration systems, computational fluid dynamics. E-mail: gasche@dem.feis.unesp.br.

Gosavi et al. [8] using the pressure drop minimization in the suction muffler as the design parameter. Nagy et al. [9] also have used DOE and CFD to investigate both pressure drop and thermal insulation effects on suction mufflers over compressor performance in transient conditions. For the geometric modifications proposed, the authors have concluded that the relevant change of the COP (coefficient of performance) was caused by a change of temperature. Lang et al. [10] have accomplished a coupling procedure among 0-d, 1-d, and 3-d transient models, for simulating the compression process of a reciprocating compressor. The 3-d simulation was applied only for the gas inside the muffler, while the rest of the domain was modeled in 0-d and 1-d way. The authors have concluded that the proposed methodology can be used to make forecast of pressure drop, temperature gain, COP and cooling capacities of compressors with different muffler designs, but they have not proposed any new geometry for reducing the overall pressure drop.

In this work, it presents a numerical study of the flow through a suction muffler, focusing on the overall pressure drop. An experimental apparatus was built in order to give the overall pressure drop of the flow through the suction muffler, which is used as validating parameter for the numerical modeling. A commercial CFD code is used to perform a steady, isothermal and three dimensional simulation of the flow. The main objective is to investigate the pressure field in order to identify the main contributions to the overall pressure drop. After analyzing the pressure field, a new geometry is proposed, which gives a lower pressure drop without interfering on the acoustic damping efficiency.

2. Experimental Procedure

The experimental apparatus is schematically presented in Fig. 1. The experimental apparatus consists of a tube connecting the compressed air line to a Coriolis mass flow meter (mass flow rate ranging from 0.05 to 1 kg/min and uncertainty of ±0.20% Full Scale Output), and from this to the cavity named Environment A, which was made from a compressor housing. The suction muffler inlet is installed inside the Environment A and its outlet is in direct contact with the ambient environment, called Environment B. A differential pressure transducer (0-140 kPa, with total error band of ±0.25% FSO: full scale output) is installed in the housing surface to measure the pressure difference between both environments, taking care of avoiding any leakage. A data acquisition system is used to treat all signals and register the data. The experimental results are presented in Section 4.

3. Numerical Procedure

A commercial code based on element-based finite volume method to solve the continuity and Navier-Stokes equations is used to solve the incompressible, isothermal, and steady state, and three dimensions flow through the muffler. The pressure and velocity variables are stored at the nodes and the algebraic equations system is solved as a single system by a multigrid coupled solver. The high resolution interpolation scheme [11] was used to interpolate the advection terms and the SST (shear stress transport) model [12] was used as turbulence model. Parallel computation was performed using the domain decomposition method.

The geometry of the suction muffler is shown in Fig. 2a. The geometry was imported from a CAD (computer aided design) software and cleaned-up to remove small radius and other features that unnecessarily make the mesh generation more inefficient. Tetrahedral elements with inflated region at the wall were used, as shown in Fig. 2b. A mesh parametric study was accomplished by varying the size of the elements, numbers of layers, growth rate and inflation thickness in order to verify their influence on the computational time, convergence level, and dimensionless wall distance y^+, given by:

$$y^+ = u_\tau y / \nu \tag{1}$$

where y is the distance between element nodes and wall,

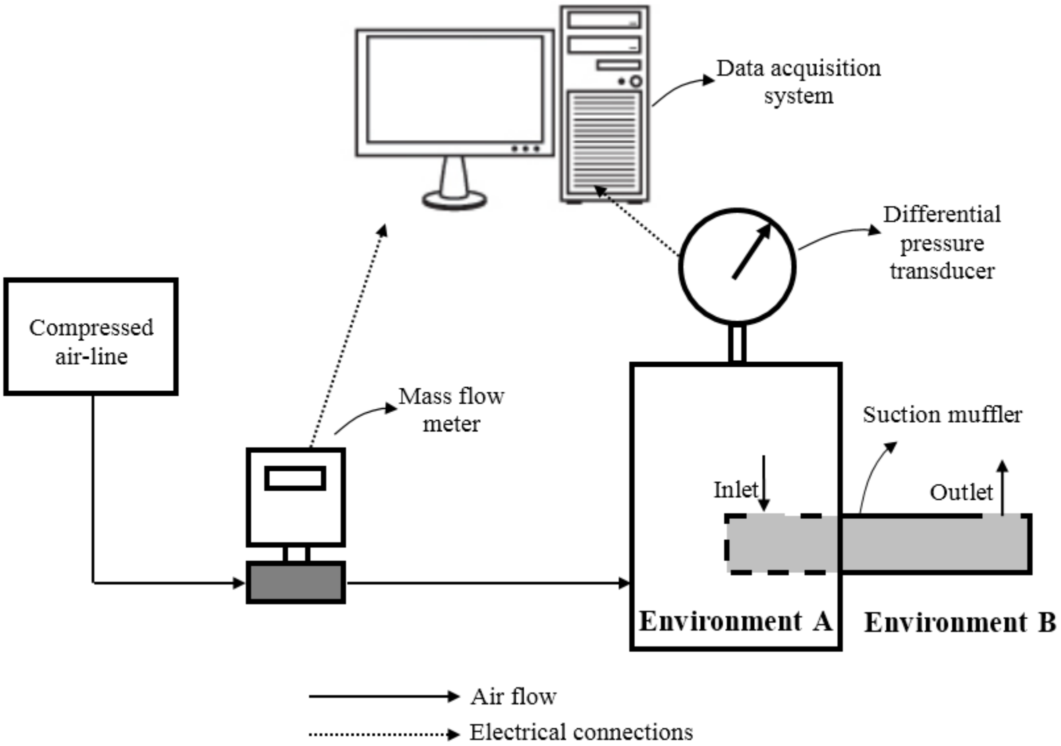

Fig. 1 Schematic of the experimental apparatus.

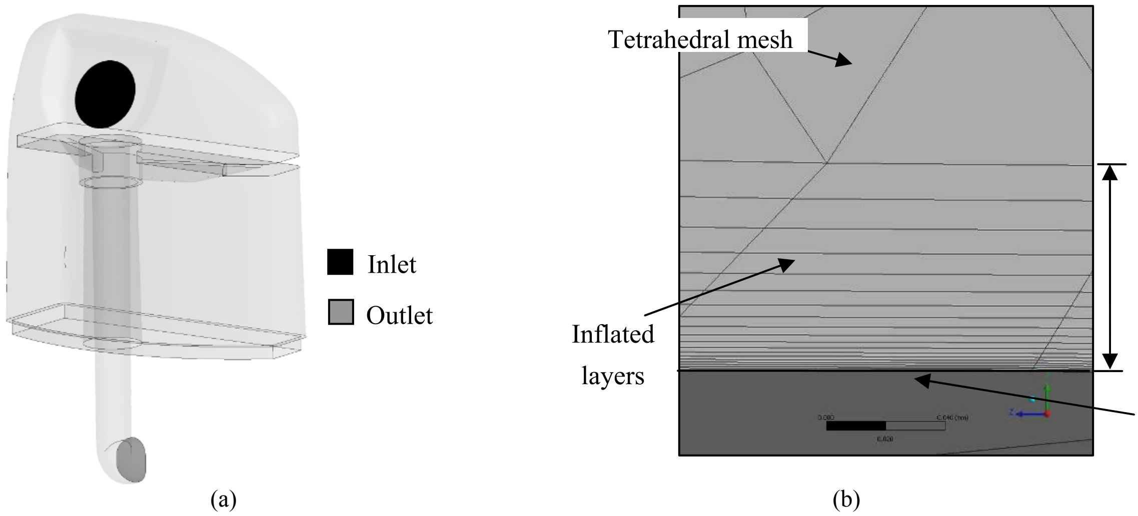

Fig. 2 (a) Geometry of the suction muffler and (b) mesh detail close to the wall.

ν is the local kinematic viscosity and $u_\tau = (\tau_w/\rho)^{1/2}$ is the friction velocity, where τ_w is the wall shear stress. This dimensionless distance defines the mesh resolution close to the wall and must be kept below 2.0 when the Shear Stress Transport turbulence model is used. Such model does not use the law of the wall to interpolate the velocity profile close to wall. Otherwise, the governing equations are solved for all control volumes, requiring higher mesh resolution close to wall due to high gradients in these regions.

The mesh configuration that showed the best compromise between computational time, convergence level, and lower y^+ presented element size equal to 2.0 mm, number of inflated layers equal to 10, growth rate equal to 1.2 and inflation thickness equal to 0.1 mm, as shown in Fig. 3.

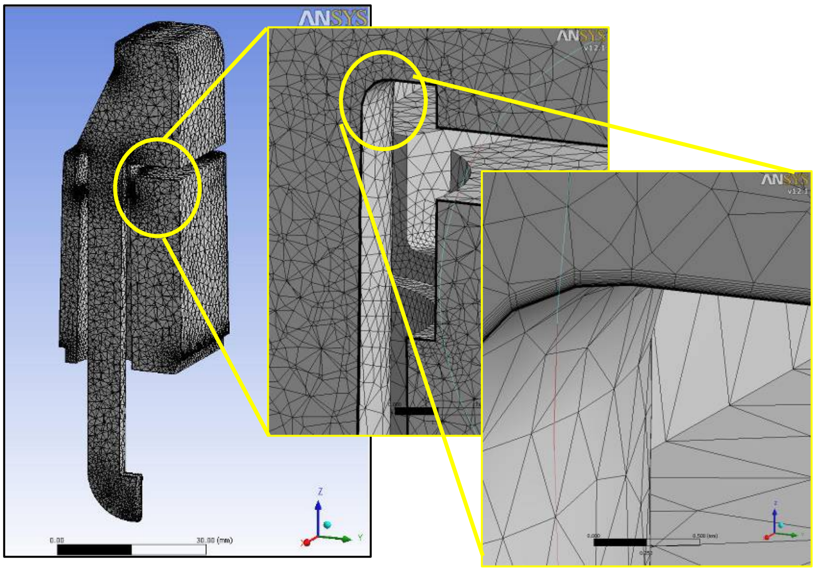

Fig. 3 Final mesh configuration.

All the simulations were performed considering constant inlet air mass flow rate (from 1.0 to 3.0 g/s) in atmosphere conditions (1 atm and 25 °C) with 5% turbulence intensity, and opening outlet with zero relative pressure as boundary conditions. Maximum residuals lower than 10-4 were used as convergence criteria.

4. Results and Discussions

Fig. 4 shows the comparison between numerical and experimental results of the overall pressure drop for several mass flow rates. Each point on the figure is an average value from 25 measurements, with 4.4% maximum 3σ deviation. The numerical results show good agreement with experimental data, showing maximum difference around 6.0%, which can be attributed in part to geometric imperfections present in the real suction muffler that could not be represented in the numerical model. The total RMS uncertainty is about 8.0%, when the uncertainty of the pressure transducer is combined with the 3 σ deviation. From these results, one can say that the numerical model is numerically validated and can be used in order to analyze the flow for overall pressure drop improvement purposes, having in mind the total uncertainty of 8%.

One of the advantages of the numerical analysis for this problem is that, once validated, it is possible to identify with higher accuracy the regions of the geometry responsible for the major losses in the overall pressure drop. Figs. 5 and 6 show the pressure field in the suction muffler flow for mass flow rates equal to 1.0 and 3.0 g/s, respectively. In these figures, three main regions can be pointed out as the main contributors to the overall pressure drop, which are the entrance of the inner tube, the inner tube, and the outlet 90° curve (outlet bend).

Fig. 7 depicts the contribution of the three regions for the same cases. For the highest mass flow rate, one can observe that the entrance region and the inner tube contribute both with 24% for the overall pressure drop, while the outlet bend contributes with 47% for the overall pressure drop. For the lowest mass flow rate the behavior is similar. Therefore, the first geometric change can be made in the outlet bend.

Four test cases were analyzed considering the outlet bend radius: no bend radius, bend radius r = 1.0, r = 2.0, and r = 3.0 mm (Fig. 8). As can be seen in Fig. 9, the pressure drop is drastically reduced when the bend radius is increased, achieving about 28% of reduction for r = 3.0 mm, when compared with no bend radius. It is important to highlight that hermetic reciprocating

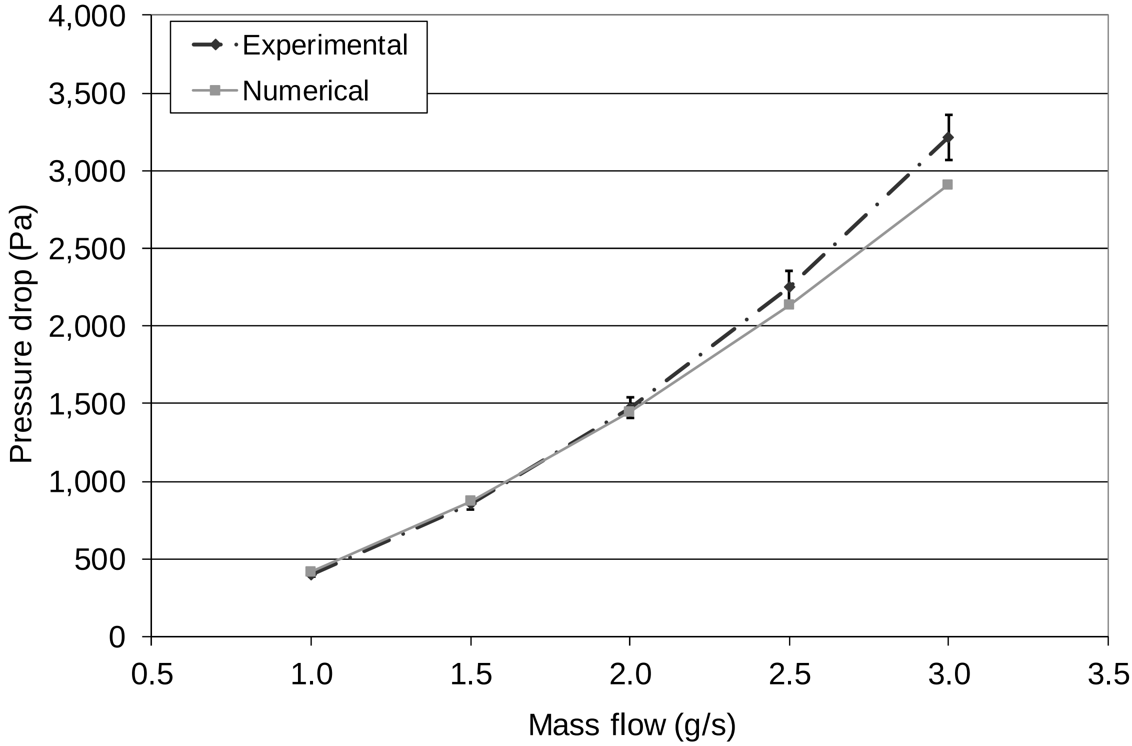

Fig. 4 Experimental and numerical results for the overall pressure drop of the flow through the suction muffler.

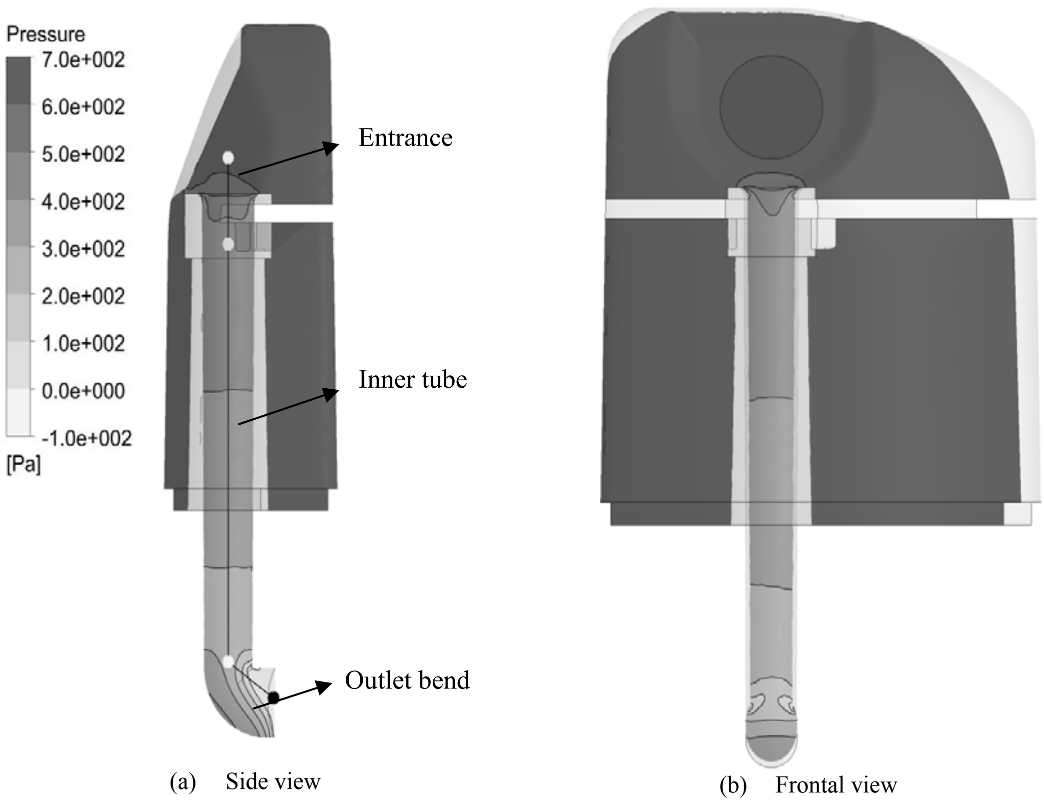

Fig. 5 Pressure field in the muffler for mass flow rate equal to 1.0 g/s.

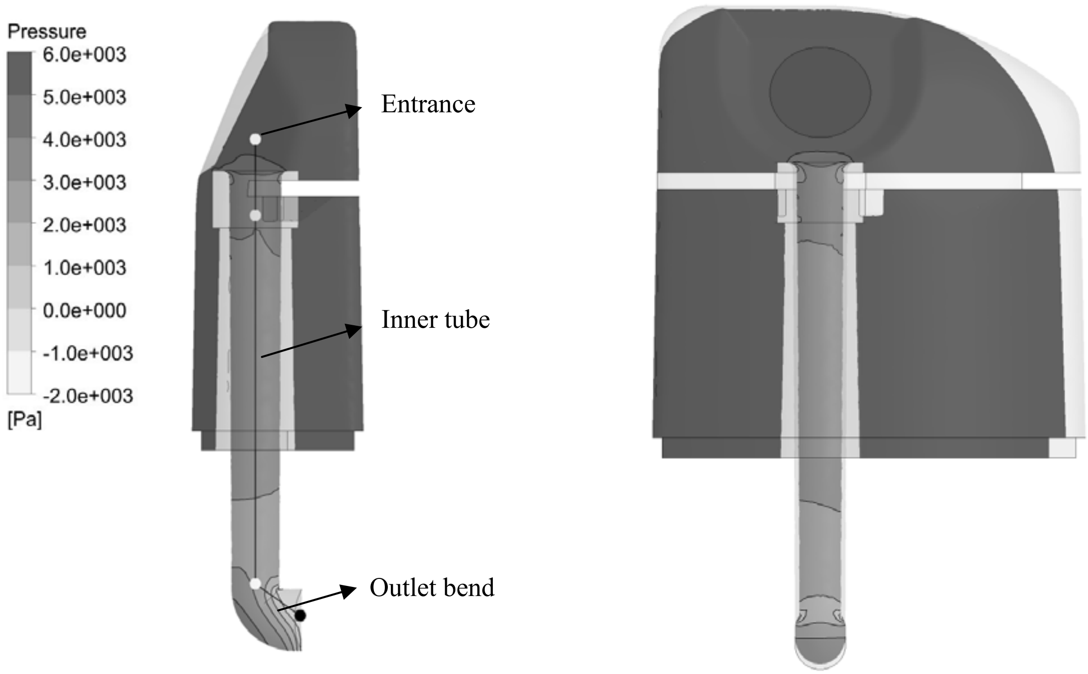

(a) Side view (b) Frontal view

Fig. 6 Pressure field in the muffler for mass flow rate equal to 3.0 g/s.

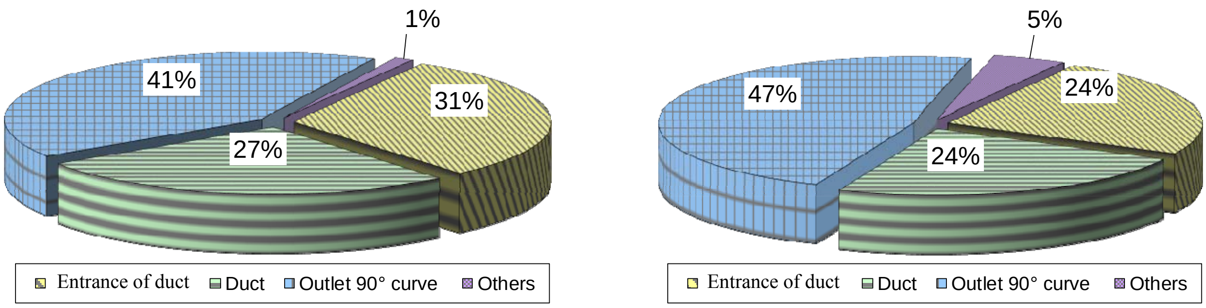

(a) Mass flow rate equal to 1.0 g/s. (b) Mass flow rate equal to 3.0 g/s.

Fig. 7 Partial contributions for the overall pressure drop.

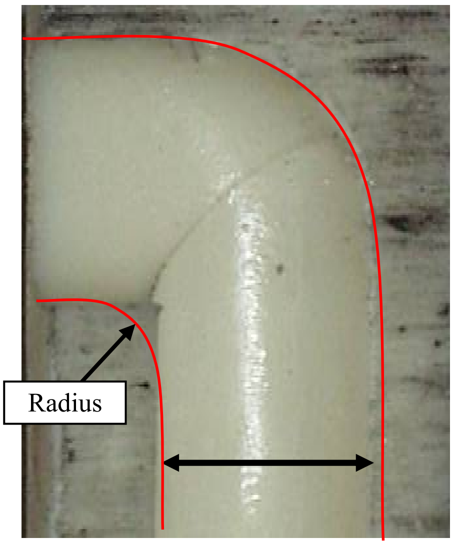

Fig. 8 Outlet bend radius.

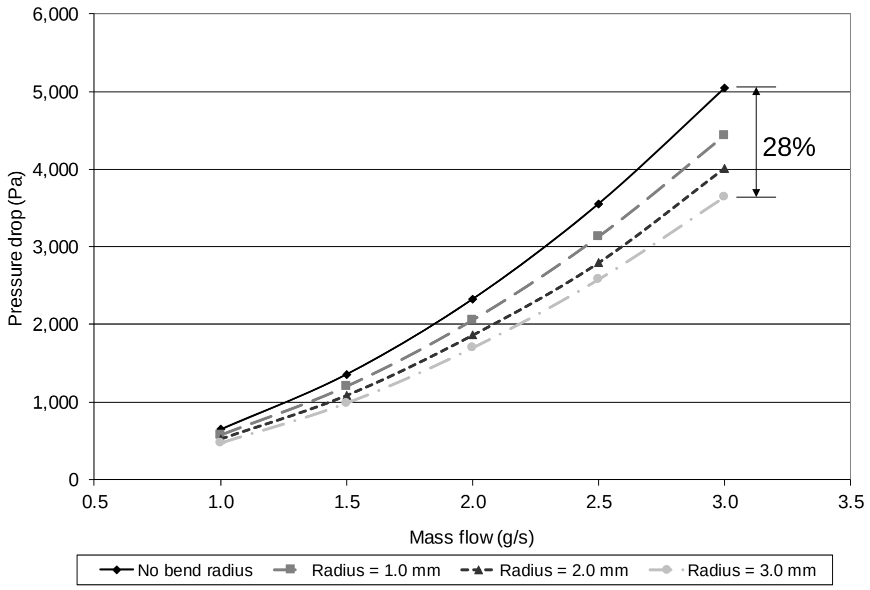

Fig. 9 Comparison of the overall pressure drop for several bend radius.

compressors operate with refrigerant gas instead of air and in pulsating transient condition instead of steady state. Fagotti and Possamai [13] advise that evaluation of the pressure losses in suction mufflers must be carried out considering the flow as transient due to the great interaction with the suction valve, and showed great difference of the pressure drop between results obtained with a steady state versus a transient analysis for the same boundary conditions. Transient analysis of suction mufflers is not the main subject of the present work, leading to provisory conclusions. Further investigations considering the transient regime of the flow through suction mufflers will be carried out in the future.

4. Conclusions

In the present work, an experimentally validated numerical procedure was established to evaluate the overall pressure drop of the flow in the suction muffler of hermetic reciprocating compressors. The results showed that three main regions contribute to the overall pressure drop: the entrance, the inner tube, and the outlet bend. Based on the results, four test cases were numerically studied considering the radius of the outlet bend as the parameter for analysis. The numerical analysis shows that there is an overall pressure drop reduction of 28% for bend radius equal to 3.0 mm, when compared with bend radius equal to zero (no bend radius).

Acknowledgments

The authors acknowledge to Tecumseh do Brasil for the financial Support in this work.

References

[1] J.J. Jacobs, Analytic and experimental techniques for evaluating compressor performance losses, in: International Compressor Engineering Conference, West Lafayette, USA, July 12-15, 1976.

[2] W.W. von Nimitz, Pulsation and vibration control requirements in the design of reciprocating compressor and pump installations, in: International Compressor Engineering Conference, West Lafayette, USA, July 11-13, 1984.

[3] J.E. Schreiner, C.J. Deschamps, J.R. Barbosa, A systematic approach to analyze volumetric inefficiencies in refrigeration compressors, in: Proc. of 20th International Congress of Mechanical Engineering, Gramado, Brazil, Nov. 15-20, 2009.

[4] C.D. Pérez-Segarra, F. Escanes, A. Oliva, Numerical study of the termal and fluid-dynamic behaviour of reciprocating compressors, in: International Compressor Engineering Conference, West Lafayette, USA, Nov. 1994.

[5] C.J. Deschamps, F.C. Possamai, E.L.L. Pereira, Numerical simulation of pulsating flow in suction mufflers, in: International Compressor Engineering Conference, West Lafayette, USA, June, 2002.

[6] J.K. Choi, J.M. Joo, S.K. Oh, S.W. Park, Smart suction muffler for a reciprocating compressor, in: International Compressor Engineering Conference, West Lafayette, USA, Aug. 30, 2000.

[7] B.H. Kim, S.T, Lee, S.W. Park, Design of the suction muffler of a reciprocating compressor using DOE (theoretical and experimental approach), in: International Compressor Engineering Conference, West Lafayette, USA, July 12-15, 2004.

[8] S.S. Gosavi, V.M. Juge, M.M. Nadgouda, Optimization of suction muffler using Taguchi's DOE method, in: International Compressor Engineering Conference, West Lafayette, USA, July, 2006.

[9] D. Nagy, W. Lang, R.A. Almbauer, Evaluation of different suction muffler parameters using DOE, in: Proc. of 7th International Conference on Compressors and Coolants at Papiernička, Cast Papiernicka, Slovak Republic, Sept. 7-9, 2009.

[10] W. Lang, R. Almbauer, A. Burgstaller, D. Nagy, Coupling of 0-, 1- and 3-d tool for the simulation of the suction line of a hermetic reciprocating compressor, in: International Compressor Engineering Conference, Purdue university, Aug. 14-17, 2008.

[11] T.J. Bart., D.C. Jesperson, The Design and application of upwind schemes on unstructured meshes, in: Proc. of 27th Aerospace Sciences Metting at Reno, Nevada, USA, 1989.

[12] F.R. Menter, Two-equation eddy-viscosity turbulence models for engineering applications, AIAA Journal 32 (8) (1994) 1598-1605.

[13] F. Fagotti, F.C. Possamai, Using computational fluid dynamics as a compressor design tool, in: Proc. International Compressor Engineering Conference at Purdue, in: Proc. of 27th Aerospace Sciences Meeting, Nevada, USA, May 23, 2000.

Journal of Energy and Power Engineering 8 (2014) 431-447

Carbon Dioxide Mineralisation and Integration with Flue Gas Desulphurisation Applied to a Modern Coal-Fired Power Plant

Ron Zevenhoven[1], Johan Fagerlund[1], Thomas Björklöf[1], Magdalena Mäkelä[2] and Olav Eklund[2]

1. Department of Chemical Engineering, Åbo Akademi University, Åbo, Turku 20500, Finland

2. Department of Geology & Mineralogy, Åbo Akademi University, Åbo, Turku 20500, Finland

Received: August 27, 2013 / Accepted: October 09, 2013 / Published: March 31, 2014.

Abstract: For Finland, carbon dioxide mineralisation was identified as the only option for CCS (carbon capture and storage) application. Unfortunately it has not been embraced by the power sector. One interesting source-sink combination, however, is formed by magnesium silicate resources at Vammala, located ~85 km east of the 565 MWe coal-fired Meri-Pori Power Plant on the country's southwest coast. This paper assesses mineral sequestration of Meri-Pori power plant CO_2, using Vammala mineral resources and the mineralisation process under development at Åbo Akademi University. That process implies $Mg(OH)_2$ production from magnesium silicate-based rock, followed by gas/solid carbonation of the $Mg(OH)_2$ in a pressurised fluidised bed. Reported are results on experimental work, i.e., $Mg(OH)_2$ production, with rock from locations close to Meri-Pori. Results suggest a total CO_2 fixation capacity ~50 Mt CO_2 for the Vammala site, although production of $Mg(OH)_2$ from rock from the site is challenging. Finally, as mineralisation could be directly applied to flue gases without CO_2 pre-capture, we report from experimental work on carbonation of $Mg(OH)_2$ with CO_2 and CO_2-SO_2-O_2 gas mixtures. Results show that SO_2 readily reacts with $Mg(OH)_2$, providing an opportunity to simultaneously capture SO_2 and CO_2, which could make separate flue gas desulphurisation redundant.

Key words: CO_2 mineral sequestration, large-scale application, coal-fired power plant, desulphurisation.

Nomenclature

AS Ammonium Sulphate
Ex Exergy, J or W
H Enthalpy, J/mol
m Mass, kg
P Power, J or W
Q Heat, J or W
t Time, year
T Temperature, °C or K
X Degree of conversion, -
y Year
Y% Vol CO_2 in flue gas
Δ Difference
Subscripts and superscripts
C Carbonation
E Extraction (of Mg)
$Mg(OH)_{2carb}$ Mg $(OH)_2$ carbonation
$Mg(OH)_{2prod}$ Mg $(OH)_2$ production site rock deposit site

Corresponding author: Ron Zevenhoven, professor, research fields: energy technology, engineering thermodynamics and CCS (carbon capture and storage). E-mail: rzevenho@abo.fi.

1. Introduction

Between 2008 and 2010, the companies Fortum and TVO (Teollisuuden Voima Oyj) explored the possibility of retrofitting the Meri-Pori coal combustion power plant with CO_2 capture technology. Due to a lack of geological storage options within Finland, the CO_2 was to be shipped to the Danish North Sea, by ship, for injection into saline aquifers. The project was, however, discontinued in October 2010 [1-5]. The Meri-Pori power plant (1994) is a 565 MWe coal fired power plant with a thermal efficiency of 43%, producing 2.5 Mt/y CO_2, or 820 kg CO_2/MWh. The plan was to capture and store 1.2 Mt/y of this. For the capture, both oxy-fuel combustion and amino acid salt

technology (Siemens) were considered, the latter being deemed more convenient (easier to retrofit). The CO_2 would have been transported, as a cooled liquid (-50 ºC, ~7 bar), with two or three tanker ships over a distance of 1,000 km to the closest storage site.

The biggest obstacle on Meri-Pori's path to CCS (carbon capture and storage), or better said CCGS (carbon capture and geological storage) was considered to be the energy demand of the capture process. Post-combustion capture required 2-4 GJ/tCO_2 during pilot scale tests, with 90% capture efficiency. Apart from the capture, other cost factors considered are:

- compression and cooling of the CO_2;
- shipping;
- intermediate storage facilities;
- injection into underground storage (including pressurisation to 120 bar).

This would lower the efficiency of the power plant by 10-13 percentage units. In terms of cost (and by deduction, energy), the capture was estimated to account for the largest part, with 50%-80% of the total costs related to CCGS. Transporting the CO_2 was estimated to account for 5%-35% of the total costs, and storage for 5%-25%.

The project was, however, discontinued. This paper explores another possibility for sequestering the CO_2 emitted by the Meri-Pori power plant, namely CO_2 mineralisation, using mineral resources located not too far from the power plant. There are several motivations for this:

- It is known for quite some time (and repeatedly confirmed) that underground storage capacity is not available in Finland [6, 7];
- The Baltic sea region and especially Latvia and the so-called Dalders structure under the Baltic Sea show good potential [8, 9]. Yet there seems be consistent consensus against CCS in Latvia [10] although in Poland (a country with a lot of coal-derived CO_2 emissions) a negative approach to CCS [11] seems to turn for the better [12];
- Finland has vast resources of magnesium silicate-based mineral resources; assessments by the Geological Survey of Finland typically mention 2-3 Gt CO_2 storage capacity in minerals of the Outokumpu-Kainuu region of central Finland alone [13-15];
- Underground storage capacity in west-Russia may seem attractive but export of CO_2 to outside the European Economic Area is prohibited under the EU directive on CCS (which in fact addresses only CCGS) [16];
- Implementation of the above-mentioned EU directive on CCS (i.e., CCGS) in Finnish legislation is ongoing and may result in CO_2 underground storage being forbidden within Finland's borders [17, 18];
- A five-year (2011-2015) research program on CCS is commencing in Finland coordinated by Finlands Cleen Oy CCSP [19] (The work reported here is outside that program, however);
- Finland (at the moment primarily Åbo Akademi University, ÅA) has an extensive track record on CO_2 mineral sequestration R & D, with process routes that use either both magnesium silicate-containing rock [20, 21] or steelmaking slags moving from lab-scale to demonstration scale [22].

Below, the feasibility of CO_2 mineralisation applied to CO_2 produced at the Meri-Pori power plant using four types of minerals and the staged process route that is under development at ÅA is assessed. Moreover, the combined removal and trapping of SO_2 and CO_2 from the flue gas is investigated in an experimental study at the end of this paper. CO_2 pre-capture would be omitted from the CCS chain.

2. Considering the Mineralisation Option

Given that Finland does not possess underground storage sites, CCGS will always entail large transport distances and export of the CO_2. The location of the Meri-Pori plant is indicated in Fig. 1.

Onshore pipeline transport of CO_2 is significantly cheaper than shipping, for distances up to 1,500 km [23]. Of course, the distance between the flue gas/CO_2 production source and the mineral deposit limits the

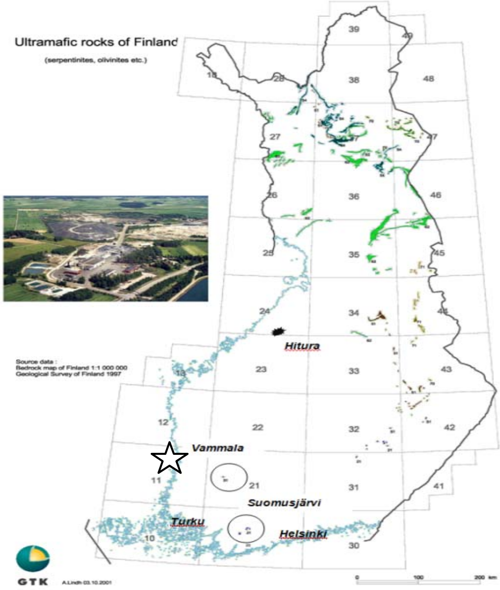

Fig. 1 The location of the Meri-Pori power plant as indicated and ultramafic rock in Finland. Also shown a photo of the nickel mine at Hitura and its location, and ultramafic rock findings in southern Finland at Vammala and Suomusjärvi (circled).

possibilities of transporting complete flue gas flows, not to mention large quantities of minerals. As noted by Brent et al. [24, 25], the preferable way to apply CCS to power plant—generated flue gas would be to have the power plant at a mineral deposit and transport the coal (or other fuel for that matter) to that site.

With proven Mg-rich serpentine ($Mg_3Si_2O_5(OH)_4$) deposits as close as ~85 km from Meri-Pori, in Vammala, and olivine-type material located at Meri-Pori itself, not only could transport costs be minimised, but the whole capture process could potentially be omitted if the carbonation can be applied to the flue gas directly. This then allows for removing the expensive and complicated (especially for gases that contain oxygen) capture step from the CCS chain.

According to BASF (Badische Anilin- und Soda-Fabrik, Germany) [26], there is no market for CO_2 solvents for CCS application to gases that contain oxygen. Chilled ammonia processes are an important alternative for alkanol amine type sorbents for CO_2; the resulting ammonia (bi-) carbonate can be made to react with activated magnesium, for example, in an aqueous solution [27, 28].

If CO_2 pre-capture is removed from the CCS chain the resulting CS (carbon storage) process may be cost-competitive with methods that involve underground storage of CO_2, as there is no need for post-storage CO_2 monitoring. This is particularly urgent since the costs for the capture step alone typically exceed what economically viable CCS may cost. This makes "conventional" CCS economically unattractive irrespective of public acceptance and other non-technical problems. Also the current low "cost" of CO_2 emissions under the European ETS (Emissions Trading Scheme) presents an obstacle for CCS.

Compared to pumping CO_2 into saline aquifers, current mineralisation technology comes with an energy penalty, but without separate capture and long transport distances the energy use should at least be comparable to the capture step of CCGS, of the order of 2-5 GJ/ton CO_2 (mainly heat).

In recent years, research into CO_2 mineralisation has taken a leap forward as demonstrated by the rate at which new process routes are suggested, patented and in several promising cases developed to large-scale application [29]. Many of these processes do not require pure CO_2, but can run with flue gases directly, such as the process routes suggested by Nottingham university [27], Hunwick [28] and also the ÅA route, to be described below in more details.

3. Mineralisation of CO_2

3.1 General

Carbon dioxide mineralisation is the general term describing the sequestration of CO_2 by reacting it with Mg- or Ca-containing compounds, to produce stable carbonates. Magnesium in particular is abundant in the earth's crust, as silicates such as serpentinite and olivine. Calcium also has a potential to store significant amounts of CO_2, although calcium silicates are not as abundant as magnesium silicates. In general, the exothermic reaction between magnesium or calcium silicates and CO_2 can be described by Eq. (1).

Both the process developed by Hunwick [28] and a

similar one by Wang and Maroto-Valer [27] utilise ammonia to capture CO_2. Hunwick claims to react ammonium bicarbonate directly with serpentinite, whereas Maroto-Valer extracts magnesium from mineral with ammonium bisulfate, before carbonating the $MgSO_4$ with ammonium bicarbonate. The latter reports over 90% conversion of Mg to (hydro) carbonates (primarily $Mg_5(CO_3)_4(OH)_2$).

$$(Mg, Ca)_xSi_yO_{x+2y+z}H_{2z}\,(s) + xCO_2\,(g) \leftrightarrow x(Mg, Ca)CO_3(s) + ySiO_2(s) + zH_2O\,(l/g) \quad (1)$$

These reactions occur in nature over geological timescales (hundreds of thousands of years). Research has focused on improving the reaction rates by treating the mineral rock by thermal, mechanical or chemical means [23, 29-31]. Due to the exceptionally large scale of CCS processes, all additives must be recovered, and the energy input is minimised. Strong acids, such as HCl and H_2SO_4 are able to dissolve the rock rapidly, but are difficult to recover. Hence, most promising processes incorporate a combination of weaker acids or ammonium salts and thermal and/or mechanical treatment to produce more reactive magnesium containing species.

A process under development at ÅA—see Fig. 2 for an overview of the process route—uses recoverable AS (ammonium sulphate) salt to extract Mg from grinded serpentinite rock, under elevated temperatures. The extraction has been shown conversions of up to 80% of Mg into reactive $Mg(OH)_2$ or $MgSO_4$, depending on the desired intermediate [32, 33].

$Mg(OH)_2$ reacts directly with CO_2 under elevated temperature and pressure, whereas $MgSO_4$ can be reacted with aqueous ammonium (bi-) carbonate, in both cases producing magnesium carbonates. Here, the route that involves $Mg(OH)_2$ carbonation in a pressurised fluidised bed, aiming at obtaining the reaction heat from the carbonation step at a useful temperature level is considered.

3.2 The ÅA Process Route

3.2.1 Mg $(OH)_2$ Production

In the first process step, S (serpentinite) rock is thermally treated with AS (ammonium sulphate) at 400-500 °C and atmospheric pressure for 10-60 min. A significant amount of the magnesium, Mg, in the rock is thus converted to sulphate, $MgSO_4$, which is highly soluble in water. Unfortunately, $MgSO_4$ cannot be directly converted with CO_2 to $MgCO_3$, but in an aqueous solution it can be converted to $Mg(OH)_2$. After cooling, the solid from the reaction with AS is slurried in water, leaving behind unreacted mineral and insoluble reaction products, e.g., silica. The pH of the filtrate solution is raised to 8-9, precipitating iron and calcium (from the mineral, see Table 1) as FeOOH and $Ca(OH)_2$, respectively, while increasing the pH further to 10-11 precipitates $Mg(OH)_2$.

For the Finnish Hitura nickel mine overburden mineral, the preferable conditions for extraction of Mg (and Fe) to $MgSO_4$ (and $FeSO_4$) are temperatures 400-440 °C, for 30-60 min at S/AS = 0.5-0.7 kg/kg, resulting typically in 60%-66% extraction of Mg. Lower temperatures and longer reaction times give a higher (relative) extraction of iron. Ammonia vapour, NH_3, released during the thermal step is collected and used to give the necessary pH increases for precipitation. It is thereafter recovered for regeneration of the AS salt downstream, using heat from another process step. Nonetheless, the recovery of solid ammonium sulphate from the aqueous form incurs a not insubstantial energy penalty. More detail is given by Nduagu et al. [32, 34-35].

3.2.2 $Mg(OH)_2$ Carbonation

The $Mg(OH)_2$ produced as described above is converted into $MgCO_3$ in a PFB (pressurised fluidised bed) reactor at pressures > 20 bar and temperatures 450-550 °C. (Some more details on the set-up are given in Section 7.2). Results on conversion levels obtained under varying conditions (temperature, pressure, water content of the gas, time, fluidisation velocity) are reported elsewhere [20, 36, 37] for both a synthetic, commercial $Mg(OH)_2$ material and $Mg(OH)_2$ produced from Finnish or Lithuanian serpentinites. (A few tests were made under supercritical CO_2 conditions, pressure >

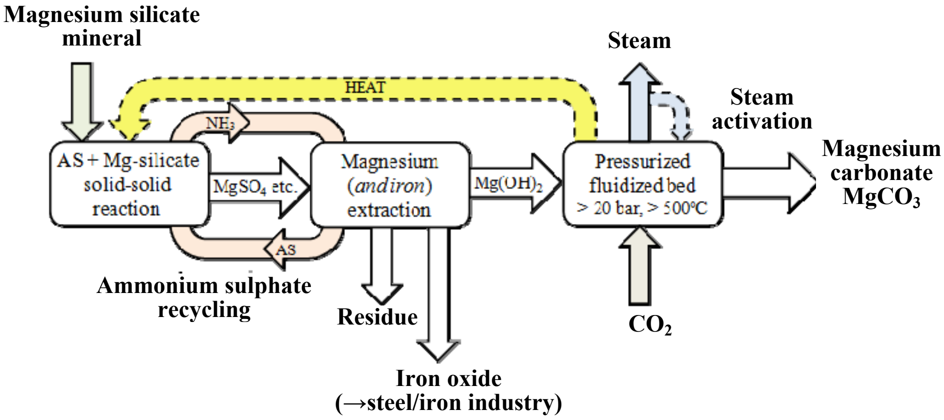

Fig. 2 A schematic illustration of the mineral carbonation process under development at ÅA.

Table 1 CO_2 mineralisation options for operation.

CO_2 capture	Transport of	Mineralisation on	Location
Yes	CO_2	CO_2	At mineral mine
Yes	Rock	CO_2	CO_2-producing site
No	Rock	CO_2-containing gas	CO_2-producing site
No	CO_2-containing gas	CO_2-containing gas	At mineral mine

74 bar, which showed significantly lower conversion levels and rates, suggesting that little benefit should be expected from operating at such pressure levels.) It was found that the $Mg(OH)_2$ materials produced from the serpentinites are much more reactive (as a result of a ~ 10× larger specific surface of ~45 m^2/g vs. ~5 m^2/g), giving conversion levels of 50% within 15 min for ~300 µm particles.

The product gas from the carbonator is a hot, pressurised mixture of CO_2 and H_2O, the solids obtained will be partly recycled for further carbonation conversion. Unfortunately, although the carbonation reaction is rapid, it levels off at carbonation levels up to 65% (the best result obtained so far) [37], which appears to be the result of calcination of $Mg(OH)_2$ to less reactive MgO. However, it is noted that in order for $Mg(OH)_2$ to carbonate, dehydroxylation (i.e., calcination) has to occur [37, 38]. Apparently, carbonation at some point becomes slower than dehydroxylation, resulting in a partially calcined and carbonated product. Thus, below it is assumed that with ~2/3 of the $Mg(OH)_2$ produced also being carbonated the necessary amount of it is 150% of the stoichiometric amount.

3.2.3 Process Energy Input Requirements

Since CCS is one of the solutions to what is in fact an energy problem, routes that lead to the production of large amounts of CO_2 while producing the power and heat for the CCS process are obviously not viable. The Meri-Pori plant produces 820 g CO_2/kWh electricity, thus CCS with an electricity consumption of 1/0.82 = 1.22 kWh = 4.39 MJ/kg CO_2 would have a zero net output of both electricity and CO_2. The use of electricity in CCS processes should be avoided although some power consumption will follow from gas compression and crushing/grinding of solid material. Fortunately, part of the energy input of a CCS processes would be in the form of heat and at ~3% thermal efficiency the Meri-Pori plant produces similar amounts of electricity and (waste) heat.

CCS routes based on CO_2 mineralisation appear to be more dependent on heat as energy input than the "conventional" route that involves underground storage of CO_2, while as done in the ÅA route the heat output from the carbonation reaction can be benefitted from. (Therefore the higher temperature of the carbonation step in the ÅA route, ~500 °C, compared to the earlier suggested process route from the ARC

(Albany Research Center), currently NETL (National Energy Technology Laboratory) Albany, in the US, results in a better LCA (life cycle assessment) performance of the ÅA route compared to the ARC route [39]. The ARC route is based on one-step carbonation in pressurised aqueous solutions at ~150 bar, ~185 °C [40, 41]). At the same time, CO_2 mineralisation routes that involve electrochemical steps (electrolysis, fuel cells) are very unlikely to have a net CO_2 fixation effect [42].

As presented earlier [21] a quick assessment of energy input requirements for the ÅA route can be made based on the reaction heat Q_E or ΔH_E needed for Mg extraction from rock and the heat Q_C or ΔH_C released by $Mg(OH)_2$ carbonation. With Mg extraction conversion $X_E = X_{Mg(OH)2prod}$ and $Mg(OH)_2$ carbonation conversion $X_C = X_{Mg(OH)2carb}$ the net heat input requirements are equal to Eq. (2):

$$\mathrm{Q\ (MJ/kg\ \ CO_2)} = \frac{\Delta H_E}{X_E} - X_C \cdot \Delta H_C \qquad (2)$$

with ΔH_E = 234.6 kJ/mol Mg extracted (value for 480 °C) and ΔH_C = -59.5 kJ/mol Mg carbonated (value for 550 °C) as in Ref. [21]. For serpentinite (rock mainly composed of serpentine) found at Hitura composed of ~84%-wt serpentine, ~3%-wt iron oxides as FeO and ~3%-wt calcium silicates the heat input requirements are given in Table 2 for X_E and X_C ranging from 25% to 100% [21]. Besides this, crushing/grinding of rock contributes to only a few % of the energy input requirements, while process integration and optimisation will result in significant improvements to the energy efficiency [21].

Table 2 Process energy (heat) input requirements (MJ/kg CO_2) according to Eq. (2).

$Mg(OH)_2$ carbonation efficiency						
Mg extraction efficiency	25%	50%	75%	90%	95%	100%
25%	21.33	20.65	20.32	20.11	20.05	19.98
50%	10.66	9.99	9.65	9.45	9.38	9.31
75%	7.11	6.43	6.10	5.89	5.83	5.76
90%	5.92	5.25	4.91	4.71	4.64	4.57
95%	5.61	4.94	4.60	4.40	4.33	4.26
100%	5.33	4.66	4.32	4.12	4.05	3.98

Of course, incomplete Mg extraction would not have a heat penalty (an endothermic reaction that does not occur will not give an energy penalty) and thus only the bottom row of Table 2 would apply. At the same time, if Mg extraction conversion X_E << 100% then crushing and grinding of what is then mainly inert material will give excessive costs and the material must still be heated to > 400 °C. Also, temperatures > 400 °C give increased thermal decomposition of the AS salt, with an energy penalty. Therefore for a case with X_E = 0.75 and X_C = 0.75 the heat input requirements for a Hitura serpentinite-type material (see below) are 4.32 < Q < 6.10 MJ/kg CO_2, and presumably closer to the higher value Note that this is heat of ~ T = 450 °C = 723 K: for surroundings temperature T = 15 °C = 288 K this corresponds to exergy equal to $\mathrm{Ex}(Q) = (1\text{-}T/T°)\cdot Q$ = 2.6-3.7 MJ/kg. Using the exergy of heat allows for comparing it in calculations with power input requirement P, for which the exergy Ex (P) = P.

3.2.4 CO_2 Mineralisation Applied Directly on Power Plant Flue Gas

The capture of CO_2 from flue gases that contain oxygen and other problematic species is more complicated than CO_2 (and H_2S) stripping from natural gas, and is hard to accomplish against an energy penalty lower than 3-4 MJ/kg CO_2 captured [43]. This is one main reason why CO_2 mineralisation R&D increasingly focuses on avoiding CO_2 separation and would operate on the CO_2-containing gas directly. Energy input requirements for CSM (carbon storage by mineralisation) would be of the same order as those for only the capture step of "conventional" CCS. (An LCA study on this approach for CO_2 mineralisation applied to natural gas–fired electricity production in Singapore, using the ÅA route with serpentinite rock purchased from Australia, and considering both CO_2 capture and operating with the flue gas directly was recently reported [44]). In that case, a gas with Y%-vol CO_2 must be compressed to a total pressure of ~20/(Y/100) bar, which is integrated with expansion of a carbonation product gas mixture (in which CO_2 is replaced by H_2O) at the same 20/(Y/100) bar, at ~500 °C,

to atmospheric pressure.

Moreover, the mineralisation of CO_2 from a flue gas may be combined with sulphur capture: $Mg(OH)_2$ may also react with SO_2 (and SO_3) present in the flue gas which would then allow for removing the FGD (Flue Gas Desulphurization) unit from a power plant that uses a sulphur-containing fuel. This is addressed in Sections 7 and 8.

3.3 Utilising Waste Heat

All existing mineralisation processes require significant amounts of energy (usually as heat) in order to achieve sufficient reaction kinetics and/or favourable thermodynamic circumstances. Especially those processes where large amounts of low quality heat are required could benefit from access to sources of waste heat. Such sources may be low quality steam or flue gas from the very power plant the CO_2 would be extracted from.

In the relative vicinity of Meri-Pori (at ~60 km to the south), the Olkiluoto nuclear power plant is located, which produces large amounts of waste heat. Presently this waste heat is rejected into the sea as 29,500 kg/s of cooling water used to condense low quality steam at a temperature of around 200 °C, from each of the two reactors already in operation. The heat carried off with the cooling water amounts to approximately 1,600 MW per reactor. A fraction of that waste heat would be enough to carbonate all the CO_2 emissions from the Meri-Pori power plant [45]. Unit 3 is under construction, for operation in 2015 or 2016 to generate 2,700 MW waste heat besides 1,600 MW electricity.

The ÅA mineralisation process requires heat at above 400 °C. But even with a heat source of a lower than required temperature, significant savings could be achieved using a heat pump. This, of course, would require that the mineralisation could be performed close to the heat source.

4. Mineral Resources and Characterization

4.1 The Rock Resources Considered Suitable

Finland has large amounts of serpentine available. The suitability of any given mining site as a source of mineral for carbonation depends on the magnesium (and calcium) contents of the rock. In addition, the distance from the power plant and total amount of rock, as well as possible nearby sources of waste heat are of importance.

Many mines in relative proximity to Meri-Pori are in operation or have previously been in operation producing large amounts of serpentinite as mine tailings and overburden. Table 3 gives a shortlist of sites with their respective rock compositions.

The Suomusjärvi and Vammala rock and, for comparison with a "better" material, the Hitura nickel mine mining tailings are central for this work—see the locations of these in Fig. 1. The other southern-Finland rock types (Hyvinkää, Lammi and Kaipola) will not be further addressed here [46]. For the work reported here the materials and chemical compositions as given in Table 4 are used.

Table 3 Composition (as oxides) of the Finnish rock considered for mineralization.

Location	MgO %-wt	CaO %-wt	Fe_2O_3 %-wt*	SiO_2 %-wt	Al_2O_3 %-wt	Other %-wt
Suomusjärvi	16.2	8.6	11.4	47.6	10	6.2
Hyvinkää/Mäntsälä**	9.8	11.4	13.2	45.9	13.6	6.1
Lammi/Asikkala**	4.9	6.8	8.0	58.0	15.6	6.7
Kaipola/Kuhmoinen**	7.2	7.5	7.7	55.2	14.9	7.5
Vammala	14.5	5.6	12.5	49.5	8.8	9.1
Hitura	38.1	0.5	14.8	32.6	0.4	13.6

* Calculated, presumably a mixture of FeO and Fe_2O_3, partly (?) Fe_3O_4.
** Not a mining site.

Table 4 Composition (as oxides) of the Finnish rocks for mineralisation as tested.

Working names	MgO %-wt	CaO %-wt	Fe_2O_3 %-wt*	SiO_2 %-wt	Al_2O_3 %-wt	Other %-wt
Hitura#	36.2	0.5	14.4	24.8	<0.1	24.1
Vammala-1¤	19.2	9.0	15.4	45.0	3.5	7.9
Vammala-2¤	28.0	1.4	18.4	39.3	1.3	11.6
Satakunta§ olivine	5.5	8.7	15.3	46.9	16.1	7.5
Suomusjärvi-1¤	13.5	7.8	10.9	50.2	10.8	6.8
Suomusjärvi-2¤	20.9	8.3	11.9	44.3	7.0	7.6

Ref. [34], § Ref [35], ¤ Ref. [46].
* Calculated, presumably a mixture of FeO and Fe_2O_3, partly Fe_3O_4.

4.2 Hitura Mine Rock

The Hitura mine is an operational nickel mine in the province of Oulu, around 350 km (in north-east direction) from Meri-Pori. Rocks from Hitura, tested at ÅA, have been shown to contain ~83% serpentine mineral, which constitutes a MgO content of ~36%. The continuous transport cost by pipeline, for pure CO_2, would amount to less than 5 €/tCO_2. However, should the transported gas be the total (dried) flue gas, the costs can be expected to rise by a factor of three to five, depending on the CO_2 content [23].

The Hitura ultramafic complex consists mainly of serpentinite, with a volume of an estimated 1,300 × 300 × 1,000 m, i.e., 0.39 km^3 = 390 × 10^6 m^3 [47]. With an assumed density ~ 3,000 kg/m^3 it corresponds to ~1,170 Mt material. Given the rock composition with ~ 36%-wt MgO (Table 4), this amount of rock has a theoretical capacity to sequester more than 400 Mt CO_2.

4.3 Vammala (Stormi-Vammala) Nickel Mine Rock

The Stormi ultramafic complex in the Vammala nickel belt is a 1,500 × 600 × 300 m large volume, with an upper layer of 70 m of serpentinite [48]. This gives a volume of 0.063 km^3 = 63 × 10^6 m^3 with an assumed density ~3,000 kg/m^3 this corresponds to ~200 Mt material. Given the rock composition with 20~25%-wt MgO (Table 4), theoretically around 44-55 Mt of CO_2 could be sequestered with the upper layer minerals.

On one hand, the MgO content in the Vammala upper layer serpentinites necessitates the processing of larger amounts of rock (4 ton/ton CO_2 compared to ~3 ton/ton CO_2 for Hitura material), but Vammala, on the other hand, is significantly closer to Meri-Pori compared to Hitura. At a distance of only 75-85 km both pipeline transport costs and capital costs could be kept at a minimum.

The Vammala mine is no longer being mined for nickel, but still produces gold. However, nickel deposits are generally found in ultramafic rock formations, whereas gold tends to be present in quartz formations. There is nonetheless the possibility that the overburden from mining contains serpentinite material. Another option is to reconsider nickel mining in the light of new uses for the mine tailings, or to mine for serpentine without specific regard for nickel altogether. Belvedere Resources, the company operating in Hitura, apparently have been exploring the possibility to start mining nickel in Vammala again. The rocks collected and analysed are from a rock mass nearby, not at, the Stormi mine [46].

4.4 Pori Olivine Deposits Rock

Only a few kilometres south-east of Pori, in the region around Nakkila and Harjavalta, olivine deposits can be found [49]. Historically nickel has been mined in Harjavalta, but presently the only mining activity in the region is copper mining [50]. The chemical composition of olivine favours its use as a source of magnesium due to stoichiometrically higher ratio of Mg to rock, compared to serpentine. Nduagu et al. [34] argued that due to low surface area and porosity, as well as being harder than serpentine, olivine is not well suited for extracting magnesium, according to the method described in Section 3.2.1.

4.5 Suomusjärvi Olivine Deposits Rock

Two samples for testing were taken from the region around Suomusjärvi, located roughly half-way between Turku and Helsinki—see Fig. 1. This is at the south end of the Vammala nickel belt [51]. One sample (Suomusjärvi-1) is a side-material from the Salittu quarry where macadam is mined for roadmaking. The other sample (Suomusjärvi-2) is an olivine-hornblendite actually from Nummi-Pusula (~20 km east of Suomusjärvi), containing ~50% olivine $(Mg,Fe)_2SiO_4$ [46]. Data on amounts of material are not yet available.

5. Production of $Mg(OH)_2$ from the Rocks Considered Suitable

Table 4 summarises the results of $Mg(OH)_2$ production from the materials listed in Table 3, using the procedure described in Section 3.2.1. For most tests,

2 g rock + 3 g ammonium sulphate powder were mixed, with rock particle size 75-125 µm and using an Al sample cup.

The amount of rock, m_{rock}, needed to sequester a unit mass of CO_2 can be calculated from the MgO content of the rock (%MgO) and the extraction of the magnesium from it, producing $Mg(OH)_2$, $X_{Mg(OH)2prod}$ (%) Eq. (3):

$$\frac{m_{rock}}{m_{CO2}}(kg/kg) = \frac{40.3}{44}\cdot\frac{1}{\%MgO/100}\cdot\frac{1}{X_{Mg(OH)2\,prod}(\%)/100} = 0.916\cdot\frac{1}{\%MgO/100}\cdot\frac{1}{X_{Mg(OH)2\,prod}(\%)/100} \quad (3)$$

The values 40.3 and 44 are molar masses (kg/kmol) of MgO and CO_2, respectively. This assumes complete carbonation of $Mg(OH)_2$ to $MgCO_3$; as the best experimental result obtained for that so far is 65% ≈ 2/3, also the requirement of 1½× the amount calculated with Eq. (3) is given in the results presented below.

The number of years it would take to consume the suitable rock material m_{site} at a certain location can be calculated for the sites mentioned above. For a CO_2 sequestration rate of 1.2 Mt/year (as was the plan with the Fortum/TVO project) Eq. (4):

$$t\,(year) = \frac{m_{site}}{m_{rock}/year} = \frac{m_{site}}{\frac{m_{rock}}{m_{CO2}}\cdot m_{CO2}/year} = \frac{m_{site}}{\frac{m_{rock}}{m_{CO2}}\cdot 1.2\ \mathrm{Mt\ CO_2}/year} \quad (4)$$

where, m_{rock}/m_{CO2} (kg(kg) is given by Eq. (3).

6. Feasibility of the Considered Deposits for Meri-Pori CO_2

6.1 Hitura Mine Rock

As noted in Section 4.2, the rock available at Hitura has a theoretical capacity to sequester more than 400 Mt CO_2. Fig. 3 shows the amount of rock needed to carbonate 1 *t* CO_2 as a function of Mg extraction, for full and partial (65%) carbonation extent. With $Mg(OH)_2$ production levels of the order of 80% obtained so far for the rock processing according to Nduagu et al. [32, 34-35], the process would require

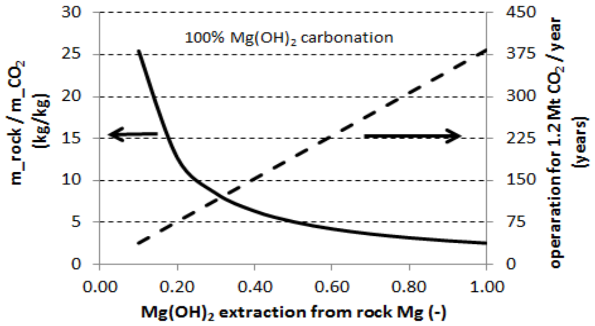

(a)

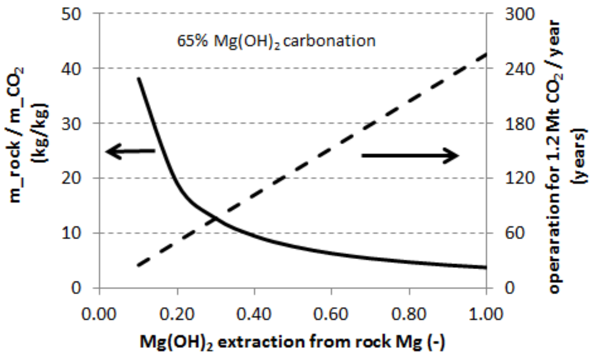

(b)

Fig. 3 Rock consumption rate and availability at Hitura depending on extraction of Mg from the rock, for full (a) or partial (b) carbonation of the $Mg(OH)_2$ produced.

~4½ t rock/ton CO_2 and could sequester 1.2 Mt CO_2/*y* during a period of ~200 years with 65% $Mg(OH)_2$ carbonation.

According to Romão et al. [21]—see also Table 1—the heat requirements would then be ~6 GJ/t CO_2 which can be reduced by heat integration. It would be reduced to ~4 GJ/t CO_2 if extraction and carbonation levels > 90% can be realised.

The distance of around 350 km from Meri-Pori to the Hitura site would add a few €/t (on-shore pipeline) transport costs to this CCS option, making a site like Stormi-Vammala more attractive.

6.2 Vammala (Stormi-Vammala) Nickel Mine Rock

As presented in Section 4.3, the rock available at Stormi-Vammala has a theoretical capacity to sequester ~ 50 Mt CO_2. Fig. 4 shows the amount of rock needed to carbonate 1 t CO_2 as a function of Mg extraction, for full and partial (65%) carbonation extent. With $Mg(OH)_2$ production levels of ~25% obtained for the rock processing [46] the process would require ~12

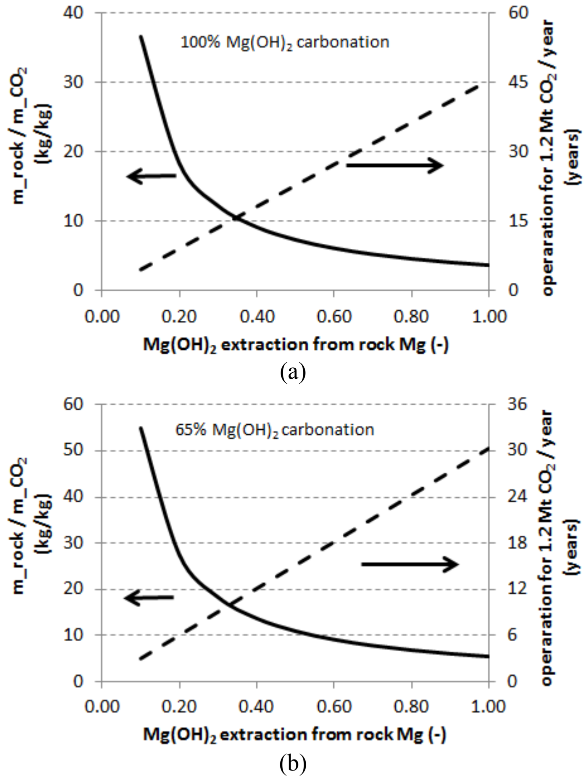

Fig. 4 Rock consumption rate and availability at Stormi-Vammala depending on extraction of Mg from the rock, for full (a) or partial (b) carbonation of the $Mg(OH)_2$ produced.

ton rock/ton CO_2 and could fix 1.2 Mt/y during a period of < 10 years only, with 65% $Mg(OH)_2$ carbonation.

The heat requirements would be in the range of 4.5-20 GJ/t CO_2 depending on whether non-reactive material behaves as inert or not. These values can be reduced somewhat by heat integration but the most urgent need for improvement is the extraction of Mg and producing more $Mg(OH)_2$ from the rock material. With the current result the contribution of crushing and grinding the rock material will change from a few % to a significant energy penalty.

6.3 Pori Olivine Deposits Rock

A small number of experiments were carried out with olivine from Åheim in Norway, which confirmed (with < 10% of present Mg extracted) the hypothesis that the method developed by Nduagu [32], Fagerlund et al. [34] and Salonen et al. [35] is not well applicable to olivines. Tests on the Satakunta olivine diabase gave no good result: Mg extraction was a disappointing 15% of the material's Mg content which is already quite low at only 5.5%. Work at ÅA is ongoing to further analyse the application of the $Mg(OH)_2$ production method on minerals like olivine and enstatite, besides serpentine.

6.4 Suomusjärvi Olivine Deposits Rock

The experimental results showed that $Mg(OH)_2$ could be produced only from the rock material Suomusjärvi-2, (Nummi-Pusula), at an extraction of ~ 14% of the ~21%-wt of MgO in the material. This implies that ~3 t $Mg(OH)_2$ can be produced from ~100 t of rock, which is ~10-15 × the amount of rock needed compared to a Hitura-type serpentinite and crushing/grinding energy needs become a significant cost factor. As noted above, more work is needed on extending the capabilities of the Nduagu et al. [32, 34-35] route to $Mg(OH)_2$ production from "low quality" (< 20%-wt MgO) type of rock.

7. Combined SO_2 Capture and CO_2 Mineralisation: Scope

7.1 Background

Very few studies have been conducted using $Mg(OH)_2$ for SO_x and/or CO_2 capture, mainly due to its limited operational temperature range [52, 53], but there are some studies that consider the use of MgO based sorbents [54, 55]. Still, a similar material that has been much more studied is calcium oxide [52-53, 56-58]. Although calcium-based species are not abundant enough for large scale CO_2 sequestration at levels that mitigate global warming and climate change [59], it is being widely studied for the use of separating CO_2 from flue gases by means of thermal cycling (see e.g. a review by Stanmore and Gilot [60]. The idea is to carbonate CaO in one FB (fluidised bed) reactor and then decompose the formed $CaCO_3$ in another FB releasing a pure stream of CO_2, while simultaneously recovering the CaO for re-use in the first reactor. In contrary to these studies, carbonation of $Mg(OH)_2$ for CO_2 sequestration purposes does not require the

recycling of the reactant, and the product from the carbonation unit is ready for use or final disposal. This is beneficial as the continuous carbonation-calcination cycling has been shown to reduce (often quickly) the performance of the used material (CaO, in most cases) [60].

In the case of simultaneous sulphation and carbonation experiments with $Ca(OH)_2$ or CaO, sulphate formation has been found to dominate in an SO_2 (1 ppm) and CO_2 (6 ppm) containing gas [57]. While the conditions were different from those studied here, it was also noted that SO_2 readily reacts with Ca species at dry conditions, while some humidity was needed to form carbonate. On the other hand, Stanmore and Gilot [60] argued that carbonation is initially much faster than sulphation and only in the longer run does sulphation become the principal reaction. It should be noted that the conditions did not incorporate elevated pressures.

Despite the fact that SO_2 readily reacts with Ca-based sorbents, the conversion levels of 30%-50% [53, 61] leave room for improvement. The reason for the low conversion levels has been attributed to the closing of pores at the surface of the reacting particles due to the larger molar volume of calcium sulphate than that of either calcium oxide or carbonate [60].

To date, most of the experiments using the ÅA mineral carbonation process have only involved pure (pressurized) CO_2. However, in order for the process to become a realistic alternative, it is apparent that it needs to work with diluted CO_2 streams as well, such as industrial flue gases. Here, we present the results from a number of experiments using CO_2 containing a small amount of sulphur dioxide and oxygen, both of which are common components in typical industrial flue gases.

If successful, simultaneous carbonation and sulphation may motivate the removal of FGD equipment from sulphur-containing fossil fuel-fired power plants.

7.2 Materials and Methods

The materials used for the gas-solid carbonation experiments consists of two different types of $Mg(OH)_2$, one commercially obtained (Dead Sea Periclase Ltd.) and one derived from Finnish serpentinite according the ÅA process described briefly above. From here on, these will be referred to as D-$Mg(OH)_2$ and S-$Mg(OH)_2$, respectively.

D-$Mg(OH)_2$ has already been studied extensively [37] and is here used as a reference in this paper. However, the difference between S-Mg $(OH)_2$ and D-$Mg(OH)_2$ is apparent from surface analysis and typically S-$Mg(OH)_2$ has a much higher specific surface area (~50 vs. ~5 m^2/g) and porosity (0.24 cm^3/g vs. 0.024 cm^3/g) than D-$Mg(OH)_2$. For this reason, S-$Mg(OH)_2$ offers a much greater potential in form of reactivity and reaction extent than D-$Mg(OH)_2$.

The gaseous sources for the carbonation experiments were a high purity (99.999% vol) CO_2 bottle and a pre-mixed CO_2-O_2-SO_2 bottle with 90, 8 and 2%-vol of the components, respectively. For some experiments steam was added to the gas stream. The amount of SO_2 in the gas-mixture was varied between 0 and 20,000 ppmv.

A more thorough description of the methods used to carbonate $Mg(OH)_2$ can be found elsewhere [36, 37], but a short summary is also given here.

The experimental setup for gas/solid carbonation at ÅA, see Fig. 5, consists of a small (height ~0.5 m, inner diameter ~1.5 cm) PFB (pressurised fluidised bed) that is operated by preheating the incoming fluidisation gas and by maintaining the reactor at the target conditions during each experiment. The PFB is operated as a bubbling fluidised bed and run in batch mode (max. temp. ~600 °C, max pressure ~100 bar). After each experiment the particles are blown out and collected by a cyclone for easy removal.

The appropriate fluid velocity is regulated/maintained by two flow controllers that allow for the mixing of two gas streams. In addition a HPLC-pump is used for adding water to the system prior to the preheater when steam is required in the reaction gas. In contrary to previous studies, where a simple method of reacting the carbonated product with

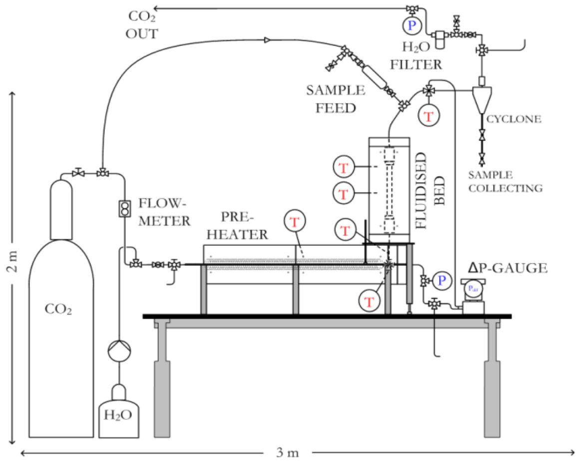

Fig. 5 Schematic diagram of the PFB setup at ÅA [36, 37].

hydrochloric acid could be used for determining the carbonate content [61], the now both carbonated and sulphated $Mg(OH)_2$ samples were analysed for elemental carbon and sulphur using an ELTRA elemental analyser.

7.3 Thermodynamics

We have recently concluded that the reaction between $Mg(OH)_2$ and CO_2 is likely taking place in accordance to the following overall equations [37, 38]:

$$Mg(OH)_2 \leftrightarrow MgO{\cdot}H_2O^* \leftrightarrow MgO + H_2O(g) \qquad (5)$$

$$MgO{\cdot}H_2O^* + CO_2(g) \leftrightarrow MgCO_3 + H_2O(g) \qquad (6)$$

To highlight the role of H_2O, the assumed intermediate product of $Mg(OH)_2$ dehydroxylation is $MgO{\cdot}H_2O^*$, which corresponds to magnesium capable of forming carbonate. In the absence of water the reaction between MgO and CO_2 is slow and likewise if the temperature for $Mg(OH)_2$ dehydroxylation is not exceeded very little carbonation will take place [62]. Adding sulphur dioxide to the reaction gas will compete with the formation of magnesium carbonate, but to what extent is highly dependent on the SO_2 concentration. In any case, a SO_2 concentration at < 0.5%-vol is much lower than that of CO_2 in a typical flue gas. Similar conclusions have also been established for calcium-based species [63].

Hartman and Svoboda [54] suggested alternative reaction mechanisms between magnesium species and SO_2. However, in the reaction conditions investigated here, the formation of $MgSO_3$ is found thermodynamically infeasible (see also Fig. 6), but in the presence of oxygen the following reaction has been suggested [54, 57]:

$$MgO + SO_2(g) + ½O_2(g) \leftrightarrow MgSO_4 \qquad (7)$$

Increasing the concentration of oxygen further, increases the amount of sulphur trioxide in the gas and thus the reaction between MgO and SO_3 also needs to be considered [54]:

$$MgO + SO_3(g) \leftrightarrow MgSO_4 \qquad (8)$$

In addition to the reactions above, the possibility of $MgCO_3$ reacting with SO_2 (or SO_3) to form $MgSO_4$ cannot be ignored. The conversion of $MgCO_3$ to $MgSO_4$ is given by the equation below:

$$MgCO_3 + SO_2(g) + ½O_2(g) \leftrightarrow MgSO_4 + CO_2(g) \qquad (9)$$

From thermodynamic equilibrium calculations (HSC Chemistry 5.11 software) it can be concluded that both Eqs. (8) and (9) are thermodynamically favoured under the experimental conditions investigated here. It appears that $MgSO_4$ is stable up to 640 °C for SO_2 and SO_3 concentrations above 0.1 ppmv. Furthermore, as long as the CO_2/SO_2 ratio is below 10^{10}, sulphation of $MgCO_3$ is also feasible as can be shown in Fig. 6. In other words, even if the concentration of SO_2 is only 0.1 ppbv in CO_2, sulphate is stable. In order to perform the equilibrium calculations, the amount of oxygen in the gas was arbitrarily chosen to be 3.5%-vol.

8. Combined SO_2 Capture and CO_2 Mineralisation: Results

8.1 Test Results with D-$Mg(OH)_2$

In accordance with results from experiments with calcium-based species [56, 57] and the thermodynamic calculations shown in Fig. 6, the reactivity of $Mg(OH)_2$ towards SO_2 (and SO_3) is significant as shown in Fig. 7.

Typically, the concentration of SO_2 in a flue gas is much lower than 20,000 ppmv, hence the most interesting result in Fig. 7 are the ones showing the influence of SO_2 concentrations below 5,000 ppm (0.5%-vol).

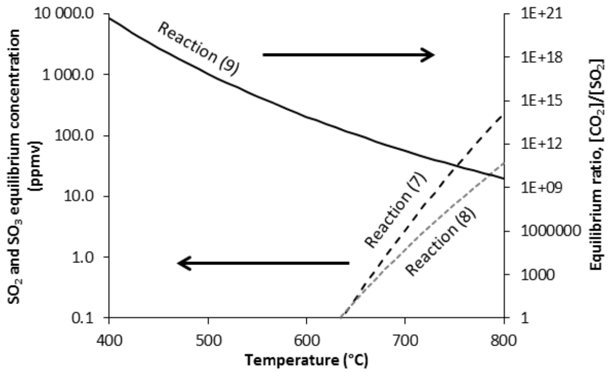

Fig. 6 Equilibrium concentrations of SO_2 (Eq. (7)) and SO_3 (Eq. (8)), together with the equilibrium ratio, CO_2/SO_2 (Eq. (9)) as a function of temperature based on Gibbs energy minimisation calculations (HSC Chemistry 5.11). O_2 (arbitrarily chosen) in the gas phase: 3.5% vol.

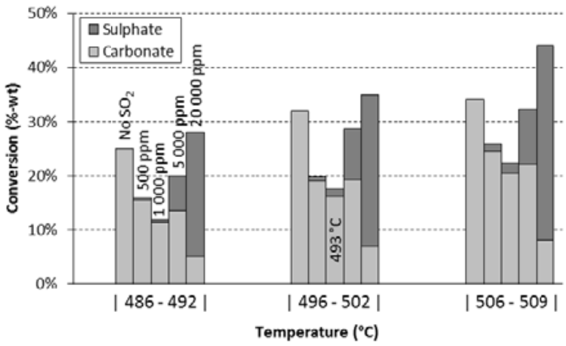

Fig. 7 The influence of SO_2 concentration (0-20,000 ppmv) on the reactivity of D-$Mg(OH)_2$ (125-212 μm) under a total pressure of 25 bar. The experiment time was 15 minutes. p_{O2} = 4·p_{SO2} in dry CO_2.

Interestingly the influence of SO_2 is much stronger than that of CO_2, although it was present in much lower concentrations (90%-vol CO_2 vs. 2%-vol SO_2). However, SO_2 is a much stronger acid than CO_2 and likely has a stronger affinity for the basic surface of the $Mg(OH)_2$ particles. Carbonation is inhibited considerably in the presence of even small amounts (500 ppmv) of SO_2.

The small increase in carbonate formation between experiments performed under 1,000 and 5,000 ppmv SO_2 is interesting, but could be the result of slightly differing temperature conditions inside the fluidised bed.

All experiments shown in Fig. 7 were performed for 15 min. The initial conversion of D-$Mg(OH)_2$ is comparatively fast and can be shown in Fig. 8 from a

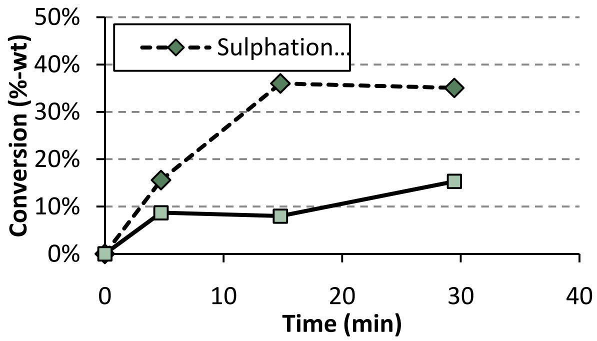

Fig. 8 Reactivity of D-$Mg(OH)_2$ at 510 °C, 25 bar. SO_2 concentration 20,000 ppmv (= 2%-vol).

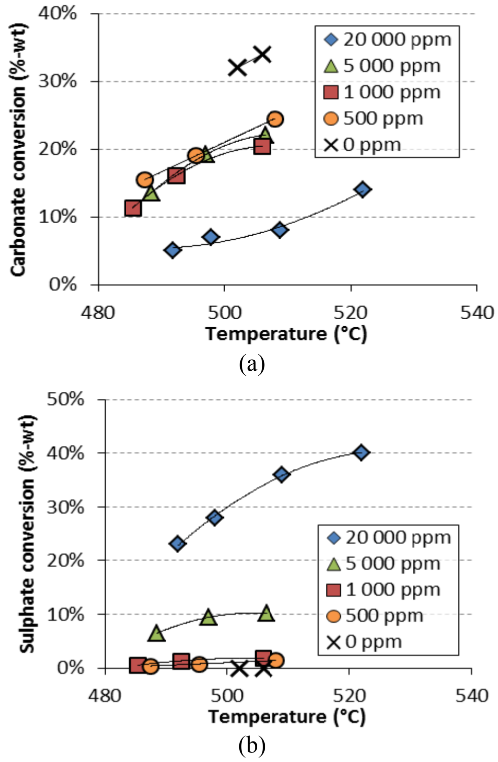

Fig. 9 Carbonate (a) and sulphate (b) conversion using D-$Mg(OH)_2$ as a function of temperature at 25 bar and pO_2 = 4·pSO_2 in dry CO_2.

set of experiments performed under similar conditions (510 °C, 25 bar), but for different durations. However, it should be noted that 2%-vol SO_2 in the gas-phase is atypically high compared to industrial standards.

Although the influence of temperature can be seen from Fig. 7, it is easier to compare its effect on both carbonation and sulphation from Fig. 9.

Increasing the temperature beyond 520 °C at 25 bar, results in the decomposition of $MgCO_3$, which is why this is the maximum temperature in the graphs in Fig. 9.

It is likely that a further increase in temperature would result in a slightly higher sulphation degree after which pore closure is expected. The porosity of the used D-$Mg(OH)_2$ material is relatively low (0.024 cm^3/g) and it has been noted to limit the overall conversion attainable during carbonation experiments [37].

Gaseous sulphur contents between 500 and 5,000 ppmv resulted in similar carbonation but varying sulphation extents. Clearly the formation of sulphates is primarily driven by Eqs. (7) and (8), while the transformation of carbonate to sulphate, Eq. (9), is less pronounced. A similar conclusion was reached by Wang et al. [64], who studied the simultaneous sulphation and carbonation of CaO in a CO_2 rich gas (oxy-fuel combustion) in the presence and absence of steam at 600-800 °C.

8.2 Test Results with Serpentinite-Derived Mg(OH)₂

In order to investigate the effect of pore closure also S-$Mg(OH)_2$ material was used for the experiments. The results from only three such experiments, shown in Fig. 10, indicated that both carbonation and sulphation increased, likely due to the increased particle surface area. However, more experiments are required.

In addition, two experiments with steam in the gas-phase were performed, but both experiments (1%-vol, 2%-vol steam) resulted in lower overall conversion of the material. Thus it seems that, dehydroxylation is a necessary precursor to both carbonation and sulphation. This is a topic for future work, while scale-up tests are ongoing on producing larger batches of S-$Mg(OH)_2$ from various types of rock.

9. Conclusions

A study was made on the application of CO_2 mineral carbonation for the sequestration of CO_2 from the Meri-Pori power plant in Finland, after a plan for "convential" CCS, or rather CCE (carbon capture and export), to a presumably off-shore geological storage

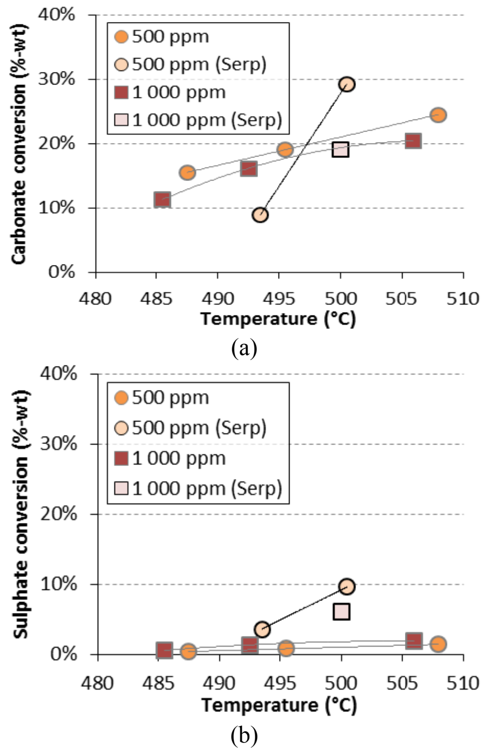

Fig. 10 Carbonate- (a) and sulphate (b) conversion using serpentinite-derived $Mg(OH)_2$ as a function of temperature at 25 bar and p_{O2} = 4·p_{SO2} in dry CO_2. For reference purposes, the results using D-$Mg(OH)_2$ at similar conditions (500 and 1,000 ppmv SO_2) have also been included.

site was cancelled. Serpentinite rock at Hitura, a nickel mine at about ~350 km from Meri-Pori would be useful, with good and well-defined process chemistry and energy efficiency, and is available in much more than sufficient amounts. Serpentinite rock available at a shorter distance of about 70-80 km at Vammala appears to be available in a reasonably sufficient amount but the production of Mg $(OH)_2$ for subsequent carbonation must be improved before it can be considered. Production of Mg $(OH)_2$ from rock from the site is challenging as a result of varying magnesium silicate mineral types (serpentine, amphibole, pyroxene). Yet more improvement and R&D work is needed on olivine-containing dunites (> 90% olivine), peridotites (60%-100% olivine) and olivine diabase-type rock: The latter is available in the immediate surroundings of the Meri-Pori power plant but the $Mg(OH)_2$ production method is not (so far) able to extract more than a few % of the materials Mg

content, which is also much lower than for the serpentinites considered. Also the possibility to co-capture SO_2 and CO_2 was evaluated. It was found that the reactivity of $Mg(OH)_2$ towards SO_2 in the presence of CO_2 at pressurised conditions is significant even under low SO_2 partial pressures. As a consequence, the possibility to replace a conventional flue gas desulphurisation unit with a combined CO_2 and SO_2 scrubber could be considered. However, in order to be more conclusive, additional experiments are required.

Acknowledgments

This work was supported by KH Renlund's Foundation funding 2010 for project "Large scale CO_2 mineralisation in Finland: Broadening the mineral resources horizon". Vilija Vaijegaite and Agne Babarskaite, visiting from Kaunas University of Technology, Lithuania, are acknowledged for the experimental work on the Vammala and Suomusjärvi rocks. Experience Nduagu (currently post-doc at the University of Calgary, Canada) and Inês Romão of ÅA are acknowledged for comments and feedback. The authors would also like to acknowledge Nordkalk Ab Oy, Parainen, and in particular Thomas Nyberg for the analysis of carbonated/sulphated samples.

References

[1] Fortum and Polish PGE cooperate on CCS technology, Carbon Capture and Storage Journal [Online], Apr.17, 2009, http://www.carboncapturejournal.com/.

[2] Siemens, Fortum and TVO cooperate on Finnish project, Carbon Capture and Storage Journal [Online], Oct. 23, 2009, http://www.carboncapturejournal.com/.

[3] Fortum, TVO and Maersk join for Finnish project. Carbon Capture and Storage Journal [Online], Oct. 23, 2009, http://www.carboncapturejournal.com/.

[4] Fortum scraps CCS project in Finland, Carbon Capture and Storage Journal [Online], Nov. 2010, http://www.carboncapturejournal.com/.

[5] M. Iso-Trykkäri, Meri-Pori CCS project [Online], Presented at the ClimBus seminar on CCS, Espoo, Finland, Nov. 11, 2010, http://www.vtt.fi/files/projects/ccsfinland/seminaari2010/12-iso-tryykari.pdf.

[6] T. Koljonen, H. Siikavirta, R. Zevenhoven, I. Savolainen, CO_2 capture, storage and reuse potential in Finland, Energy 29 (2004) 1521-1527.

[7] S. Teir, J. Hetland, E. Lindeberg, A. Torvanger, K. Buhr, T. Koljonen, et al., Potential for CCS (carbon capture and storage) in the Nordic region, VTT Research notes 2556 [Online], 2010, p. 223. http://www.vtt.fi/inf/pdf/tiedotteet/ 2010/T2556.pdf.

[8] A. Shogenova, K. Shogenov, Economical, geological and geophysical modeling of Estonian-Latvian transboundary CO_2 storage, in: CO_2 Capture and Storage in the Baltic Region, Espoo, Finland, May 23, 2013.

[9] R. Vernon, N. O'Neil, R. Pasquali, M. Nieminen, Screening of Prospective Sites for Geological Storage of CO_2 in the Southern Baltic Sea, VTT Technology report [Online], 2013, http://www.vtt.fi/inf/pdf/technology/2013/T101.pdf.

[10] D. Blumberga, J. Gušča, Latvia, Technical University of Riga, Personal communication June 2011, Sept. 2012, May 2013.

[11] M. Liska, Silesian University of Technogoly, Personal Communication, Poland, June 2012.

[12] A. Wojcicki, Storage potential in Poland, in: CO_2 Capture and Storage in the Baltic Region, Espoo, Finland, May 23, 2013.

[13] S. Aatos, P. Sorjonen-Ward, A. Kontinen, T. Kuivasaari, Outlooks for Utilisation of Serpentine and Serpentinite, Geological Survey of Finland (GSF), Report, Kuopio, Finland, 2006.

[14] S. Teir, S. Aatos, A.. Kontinen, R. Zevenhoven, O.P. Isomäki, Silicate mineral carbonation as a possible sequestration method of carbon dioxide in Finland (Silikaattimineraalien karbonoiminen hiilidioksidin loppusijoitus-menetelmänä Suomen oloissa), Materia 63 (1) (2006) 40-46. (in Finnish)

[15] S. Aatos, L. Kujanpää, S. Teir, CO_2 Capture and Geological Storage Applications in Finland, Geological Survey of Finland, 2011, pp. 187-193.

[16] Directive 2009/31/EC on the Geological Storage of Carbon Dioxide, the European Parliament and the Council [Online], http://eur-lex.europa.eu/LexUriServ/LexUriServ.do?uri=OJ:L:2009:140:0114:0135:EN:PDF (accessed Apr. 23, 2009).

[17] E. Ekdahl, H. Idman, Statement on the applicability of directive 2009/31/EC in Finland for Finnish Ministry of the Environment, K/468/42/2010, Mar. 14, 2011.

[18] Proposal for implementation of legislation on CCS, Finnish Ministry of the Environment [Online], http://www.ym.fi/fi-FI/Ajankohtaista/Tiedotteet/Tiedotteet_2012/Hallitus_esittaa_lakia_hiilidioksidin_ta%281065%29 (accessed Apr. 24, 2012).

[19] Finlands Cleen Oy Carbon Capture and Storage Program Home Page, http://www.cleen.fi/en/program_overviews/ccsp_carbon_capture_and_storage_program.

[20] J. Fagerlund, E. Nduagu, I. Romão. R. Zevenhoven, CO_2 fixation using magnesium silicate minerals, Part 1: Process description and performance, Energy 41 (2012) 184-191.

[21] I. Romão, E. Nduagu, J. Fagerlund, L.M. Gando-Ferreira, R. Zevenhoven, CO_2 fixation using magnesium silicate minerals, Energy 41 (2012) 203-211.

[22] H.P. Mattila, I. Grigaliūnaitė, A. Said, S. Filppula, C.J. Fogelholm, R. Zevenhoven, Process efficiency and optimization of PCC (precipitated calcium carbonate) production from steel converter slag, in: Proc. of ECOS 2012, Perugia, Italy, June 26-29, 2012.

[23] B. Metz, O. Davidson, H. de Coninck, M. Loos, L. Meyer, IPCC Special Report on Carbon Dioxide Capture and Storage Working Group III of the IPCC [Online], Cambridge Univ. Press, 2005, http://ipcc.ch/publications_and_data/publications_and_data_reports.shtml.

[24] G.F. Brent, From Eco-efficiency to industrial symbiosis: Life-cycle approaches for the coal and related industries in the context of climate change, Ph.D. Thesis, University of Sydney/Chemical and Biomolecular Engineering, Sydney, Australia, 2011.

[25] G.F. Brent, D.J. Allen, B.R. Eichler, J.G. Petrie, J.P. Mann, B.S. Haynes, Mineral carbonation as the core of an industrial symbiosis for energy-intensive minerals conversion, J. Industr. Ecol. 16 (2011) 94-104.

[26] T. Katz, CO_2 capture processes—applications and options, in: 11th Int. Conf. on Carbon Dioxide Utilisation (ICCDU-XI), Dijon, France, June 27-30, 2011.

[27] X. Wang, M. Maroto-Valer, Dissolution of Serpentine using recyclable ammonium salts for CO_2 mineral carbonation, FUEL 90 (3) (2011) 1229-1237.

[28] R.J. Hunwick, A new integrated approach to mineralisation-based CCS, Modern Power Systems 29 (11) (2009) 25-28.

[29] R. Zevenhoven, J. Fagerlund, J.K. Songok, CO_2 mineral sequestration—developments towards large-scale application, Greenhouse Gases: Science and Technology 1 (2011) 48-57.

[30] J. Sipilä, S. Teir, R. Zevenhoven, Carbon Dioxide Sequestration by Mineral Carbonation—Literature Review Update 2005-2007, Åbo Akademi Univ., Heat Engineering Lab. report VT 2008-1 [Online], Turku, Finland, 2008, http://users.abo.fi/rzevenho/MineralCarbonationLiteratureReview05-07.pdf.

[31] J. Geerlings, R. Zevenhoven, CO_2 mineralization—bridge between storage and utilization of CO_2, Annual Review of Chemical and Biomolecular Engineering 4 (2013) 103-117.

[32] E. Nduagu, Production of $Mg(OH)_2$ from Mg-silicate rock for CO_2 mineral sequestration, Ph.D. Thesis [Online], Åbo Akademi University/Chemical Engineering, Turku, Finland, 2012, http://www.doria.fi/handle/10024/86170.

[33] C. Aarnio, Production of $Mg(OH)_2$ from serpentinites from the Kuhmo greenstone belt (Produktion av $Mg(OH)_2$ ur serpentiniter från Kuhmo grönstensbälte), BSc Thesis, Åbo Akademi University/Geology and Mineralogy, Turku, Finland, 2013. (in Swedish)

[34] E. Nduagu, T. Björklöf, J. Fagerlund, J. Wärnå, H. Geerlings, R. Zevenhoven, Production of reactive magnesium from magnesium silicate for the purpose of CO_2 mineralization, Minerals Engineering 30 (2012) 75-86.

[35] E. Nduagu, T. Björklöf, J. Fagerlund, E. Mäkelä, J. Salonen, H. Geerlings, et al., Production of reactive magnesium from magnesium silicate for the purpose of CO_2 mineralization, Minerals Engineering 30 (2012) 87-94.

[36] J. Fagerlund, R. Zevenhoven, An experimental study of $Mg(OH)_2$ carbonation, Int. J. of Greenhouse Gas Contro l5 (2011) 1406-1412.

[37] J. Fagerlund, Carbonation of $Mg(OH)_2$ in a pressurised fluidised bed for CO_2 sequestration, Ph.D. Thesis [Online], Åbo Akademi University/Chemical Engineering, Turku, Finland, 2012, http://www.doria.fi/handle/10024/74477.

[38] J. Fagerlund, J. G. Highfield, R. Zevenhoven, Kinetics studies on wet and dry gas-solid carbonation of MgO and $Mg(OH)_2$ for CO_2 sequestration, RSC Advances 2 (2012) 10380-10393.

[39] E. Nduagu, J. Bergerson, R. Zevenhoven Life cycle assessment of CO_2 sequestration in magnesium silicate rock—a comparative study, Energy Conv. & Manage. 55 (2012) 116-126.

[40] W.K. O'Connor, D.C. Dahlin, G.E. Rush, S.J. Gerdemann, L.R. Penner, R.P. Nilsen, Aqueous Mineral Carbonation: Mineral Availability, Pretreatment, Reaction Parametrics, and Process Studies, Albany Research Center, Albany, OR, USA, 2005.

[41] S.J. Gerdemann, W.K. O'Connor, D.C. Dahlin, L.R. Penner, H. Rush, Ex situ aqueous mineral carbonation environ, Sci. Technol. 41 (2007) 2587-2593.

[42] T. Björklöf, R. Zevenhoven, Energy efficiency analysis of CO_2 mineral sequestration in magnesium silicate rock using electrochemical steps, Chem. Eng. Res. & Des. 90 (2012) 1467-1472.

[43] A. Zahra, Carbon dioxide capture from flue gas: Development and evaluation of existing and novel process concepts, Ph.D. Thesis, Delft University of Technology,

Delft, the Netherlands, 2009.

[44] H.H. Khoo, P.N. Sharatt, J. Bu, A. Borgna, T.Y. Yeo, J. Highfield, et al., Carbon capture and mineralization in Singapore: Preliminary environmental impacts and costs via LCA, Ind. & Eng. Chem Res. 50 (2011) 11350-11357.

[45] Nuclear plant units, Olkiluoto 1 and Olkiluoto 2 (in Finnish: Ydinvoimalaitos yksiköt Olkiluoto 1 ja Olkiluoto2) [Online], http://www.tvo.fi/uploads/File/yksikot-OL1-OL2%281%29.pdf (accessed June 13, 2013).

[46] M. Mäkelä, Storing of carbon dioxide by mineral carbonation in Southern Finland, M.Sc Thesis, University of Turku/Geology and Mineralogy, Turku, Finland, 2011.

[47] Hitura—Nickel Database [Online], http://en.gtk.fi/ExplorationFinland/Commodities/Nickel/hitura.html (accessed Feb. 9, 2006).

[48] Stormi—Nickel Database [Online], http://en.gtk.fi/ExplorationFinland/Commodities/nickel/stormi.html (accessed Feb. 9, 2006).

[49] A. Hamalainen, The Postjotnian Diabases of Satakunta, Geological Survey of Finland, Report of Investigation [Online], 1987, http://arkisto.gtk.fi/tr/tr76/tr76_pages_173_178.pdf.

[50] Norilsk Nickel Harjavalta [Online], http://www.nornik.fi/. (in Finnish)

[51] Norilsk Nickel Harjavalta [Online], http://www.nornik.fi/. (in Finnish)

[52] E.J. Anthony, D.L. Granatstein, Sulfation phenomena in fluidized bed combustion systems, Progress in Energy and Combustion Science 27 (2) (2001) 215-236.

[53] H. Gupta, L. Fan, Carbonation-calcination cycle using high reactivity calcium oxide for carbon dioxide separation from flue gas, Ind Eng Chem Res. 41(16) (2002) 4035-4042.

[54] M. Hartman, K. Svoboda, Physical properties of magnesite calcines and their reactivity with sulfur dioxide, Ind. Eng. Chem. Proc. Des. Dev. 24 (3) (1985) 613-621.

[55] K.K. Han, Y. Zhou, Y. Chun, J.H. Zhu, Efficient mgO-based mesoporous CO_2 trapper and its performance at high temperature, J. Hazard. Mater. 203-204 (2012) 341-347.

[56] M.J.H. Snow, J.P. Longwell, A.F. Sarofim, Direct sulfation of calcium carbonate, Ind. Eng. Chem. Res. 27 (2) (1988) 268-273.

[57] P. Elfving, I. Panas, O. Lindqvist, In situ IR study on the initial sulphition and carbonation of Ca $(OH)_2$ and CaO by SO_2 polluted air, Atmos. Environ. 30 (23) (1996) 4085-4089.

[58] H. Chen, C.Zhao, Development of a CaO-based sorbent with improved cyclic stability for CO_2 capture in pressurized carbonation, Chem. Eng. J. 171 (1) (2011) 197-205.

[59] K.S. Lackner, D.P. Butt, C.H. Wendt, Progress on binding CO_2 in mineral substrates, Energy Convers. Mgmt. 38 (Supplement 1) (1997) 259-264.

[60] B.R. Stanmore, P. Gilot, Review—calcination and carbonation of limestone during thermal cycling for CO_2 sequestration, Fuel Process Technol 86 (16) (2005) 1707-1743.

[61] J. Fagerlund, R. Zevenhoven, S.G. Huldén, B. Södergård, Gasometric determination of CO_2 released from carbonate materials, J. Chem. Educ. 87 (12) (2010) 1372-1376.

[62] J. Highfield, J. Bu, J. Fagerlund, R. Zevenhoven, The promoter effect of steam in gas-solid CO_2 mineralisation, in: Proc. ICCDU-XI, Dijon, France, June 27-30, 2011.

[63] H. Lu, P.G. Smirniotis, Calcium oxide doped sorbents for CO_2 uptake in the presence of SO_2 at high temperatures, Ind. Eng. Chem. Res. 48 (11) (2009) 5454-5459.

[64] C. Wang, L. Jia, Y. Tan, Simultaneous carbonation and sulfation of CaO in oxy-fuel CFB combustion, Chem. Eng. Technol. 34 (10) (2011) 1685-1690.

Journal of Energy and Power Engineering 8 (2014) 448-452

Analysis of Energy Saving Achievable through Solar Photovoltaic Systems on School Roofs: A Case of the City of Rome

Livio de Santoli, Gino Moncada Lo Giudice, Fabio Fraticelli, Filippo Fornari and Claudia Calice
Research Center CITERA, University of Rome, Rome 00197, Italy

Received: September 03, 2013 / Accepted: October 18, 2013 / Published: March 31, 2014.

Abstract: Embracing renewable energy technology makes a lot of sense for the public sectors and schools as it meets the government sustainability goals and provides a financially viable means of achieving carbon savings while offering income potential. This study is aimed to quantify the achievable energy saving by spread use of photovoltaic systems on public building stock in the city of Rome. The installation of PV (photovoltaic) systems in the historic center depends on the feasibility conditions, generally more complex compared to the cases examined in the consolidated city, because they require compliance with the formal and aesthetic characteristics of the buildings, so the choice must be made between compatible components, which allow to minimize the transformation. The suburbs are characterized by large plane roofs in bad conditions and belonging to isolated buildings, so the useful surface, according to shading condition, offers a big potential for renewable technologies. The research provides an evaluation of maximum production of solar energy and the subsequent energy saving and reduction of greenhouse gasses, using parametric data, and an evaluation of the cost-effectiveness, with a rough calculation of return on investment.

Key words: Schools, photovoltaic systems, energy saving, solar energy, sustainability.

1. Introduction

The idea of generating electricity with less pollution is becoming more and more attractive. The interest in environmental issues is increasing the use of free solar energy through photovoltaic technologies. Since 1970, the PV price has continuously dropped, encouraging worldwide application of small-scale PV systems [1]. Today these systems can be easily installed on the roof of residential as well as of public buildings at low costs. So the public authorities may undertake investments aimed to make the public stock more sustainable.

The case of school building stock in the city of Rome can be a meaningful example to analyze the potential of a spread use of photovoltaic technologies on public buildings. The objective of this contribution is to quantify the available roof surface area and the benefits in terms of energy and cost saving for large-scale evaluations of photovoltaic energy-potential.

In Europe there is a vast scientific literature related to energy aspects of school buildings, focused primarily on the assessment of the current energy consumption and the individuation of strategies for energy savings in Italy [2-4]. Many papers then are dedicated to the definition of guidelines for the improvement of the indoor air quality and on the impact of indoor conditions on students' performances [5].

However, there is no study in literature focused specifically on the application of solar technologies on school buildings, while solar systems are included only in some publications as possible strategies for energy saving. The only existing article, addresses this issue relatively to the educational potential of solar

Corresponding author: Livio de Santoli, professor, research fields: energy efficiency, plant systems and energy engineering. E-mail: livio.desantoli@uniroma1.it.

technologies [6].

An analysis of the potential applications of photovoltaic systems on a large scale, and of the benefits in terms of energy and cost saving, appears to be completely new in the scientific literature.

2. The Analyzed Sample

The analysis has been focused on Rome's school building stock, composed by 1,296 structures for a total of 13.5 million cubic meters. It is estimated a total electricity consumption for the entire school building stock of 50. 9 GWh per year.[1]

The methodology proposed in this paper allows to estimate the roof area available for solar applications on a sample of 271 schools in Rome, located in 10 administrative districts [7, 8]. The sample under consideration corresponds to the 20% of the total stock, thus it can be considered very significant.

The subdivision on administrative districts allows to diversify the analysis in relation to the types of buildings, considering that buildings located in peripheral districts are often younger than the ones in central areas. Modern buildings are often more suitable for photovoltaic systems because they have large and flat roofs and they receive less cast shadows that may affect the efficiency of the panels because they are often isolated and quite far from surrounding buildings. Historic buildings instead have less available surface, a greater use of pitched roof and more limits and constraints imposed by law for the defense of landscape and historical and architectural values. So, refurbishment and energy retrofit as well as installation of renewable energy systems are easier to undertake in modern buildings than in historic ones.

However, it has been considered the installable power on both historic and modern schools, in order to quantify the potential energy saving and economic advantage in all different conditions, according to the current legal framework.

[1]Data provided by the city of Rome's department for assets management.

3. Legal Framework for Photovoltaic Generation in Italy

In Italy, the system of incentives for photovoltaic generation known as "feed-in tariff" was introduced in 2003 as implementation of EU directive 2001/77/CE and is now in its fifth edition with ministerial decree of July 5, 2012 [9].

According to the actual legal framework, it is possible to enhance the energy produced by the photovoltaic plants in two ways: through feed-in incentives or through net metering. In fact, unlike the previous support schemes, net metering will be no longer a benefit combined to feed-in incentives but will be an alternative to feed-in incentives [10].

Feed-in incentives are sort of operating grants, because they do not provide any supplement for plant's commissioning but only premium tariffs for energy produced during the first 20 years of life of photovoltaic plants. Incentives are composed by an all-inclusive feed-in tariff paid to the share of net electricity injected into the grid and a premium tariff paid to the share of net electricity consumed on site; in addition, users will benefit from energy bill reduction.

The net metering instead is a system for energy exchange for which the electricity generated by a user and injected into the grid can be used to offset the electricity withdrawn from the grid by the same user. Therefore in this case users will benefit only from energy bill reduction, which will be greater than that of the case of feed-in incentives as all of the energy is used to meet the needs of users. In addition, net metering users can benefit from tax deduction for building renovations that are not compatible with feed-in incentives. In this case the grant is configured as a tax discount congruent to the cost of installation, independent of the electricity production of the photovoltaic; the deduction for 2012 is of 50%, for a maximum of 96,000€ [11].

In short, we can consider two alternatives financing for photovoltaic systems, which depend on different intervention strategies:

Feed-in operating scheme, for which it will be necessary to assess whether it is better to maximize the installed power or the gain, considering that the economic favorability increases with the rate of energy consumed on site. In this case also the intervention may be either public or private.

Net metering operating scheme, for which it will be necessary to limit the power installed to actual user needs and to involve private societies called ESCO (Energy Service Companies) that can benefit from the tax deductions.

It is important to remember that both funding schemes provided by law may change over time, the study is based on the current conditions.

It has excluded the hypothesis of energy storage through batteries, for the reduced profitability of such plants, characterized by high costs of installation and maintenance, and low levels of efficiency in the long term.

4. The Methodology

The operating scheme of PV systems under consideration is that of the city of Rome, located at 41.54°N longitude, 12.27°E longitude, 37 m elevation over sea level; the characteristics of solar radiation are shown in Table 1.

Table 1 Characteristics of climate and of solar radiation, source: photovoltaic geographical information system.

Month	H_h	H_{opt}	I_{opt}	D/G
January	1,650	2,600	62	0.54
February	2,270	3,130	53	0.54
March	3,650	4,510	42	0.47
April	4,960	5,410	28	0.43
May	5,970	5,900	15	0.43
June	6,590	6,220	8	0.40
July	6,630	6,400	12	0.38
August	5,780	6,110	24	0.38
September	4,450	5,350	39	0.39
October	3,030	4,170	51	0.44
November	1,870	2,900	60	0.51
December	1,430	2,320	64	0.56
Year	4,030	4,590	33	0.43

H_h—irradiation on horizontal plane (Wh/m^2/day), H_{opt}—irradiation on optimally inclined plane: 33 degrees (Wh/m^2/day), I_{opt}—optimal inclination (deg.), D/G—ratio of diffuse to global irradiation (-), T_D—average daytime temperature (°C).

The sample under analysis was first divided according to the type of buildings to estimate the percentage of area usable for plant installation, single-storey buildings were not considered because of the high level of shadows cast by surrounding buildings. For higher buildings they have been considered usable for plant installation the 40% of surface area in case of flat roofs, and the 20% in the case of pitched roofs. The values are clearly hypothetical and conservative, functional to the scale of the analysis. It was then possible to estimate the installable power of each building, assuming a widespread use of silicon modules having an average efficiency of 14%, corresponding to 1 kW per 8 m^2 of floor space. The costs of the photovoltaic technology have been fixed on the basis of market analysis, at 3,000 €/kW. For the productivity it has been considered an average value of 1,350 kWh/kW for flat roof and 1,100 kWh/kW for pitched roof. On flat roofs in fact there is a greater freedom of installation and it is possible to place the modules with an optimal orientation. These values were obtained by assuming a balance of system average of 80%.

Electric energy consumption, cumulatively provided by the city of Rome's department for assets management was divided by the total usable areas, resulting in an average consumption of 15 kWh/m² per year [12]. This value is congruent to the types in analysis, characterized by a low technological level and a large use of gas heating systems.

The schools are low-tech buildings, it has been considered only the electric consumption due to lighting, neglecting the small amount due to other equipment such as computers, elevators and offices' air conditioning systems.

Assuming therefore to utilize all the available surfaces, it is possible to make a comparison between electric energy consumption and production in each administrative district. The analysis, reported in Fig. 1, shows that the potential contributing to renewable energy exceeds building needs of almost 50%. It is necessary to point out that the calculation of energy

consumption is considered in the kindergartens that being single-storey buildings, do not contribute to the production of electricity. These buildings are the 35% of the total sample by number and 10% by volume. While energy consumption is fairly equal, there is a great difference in energy production between central districts (I, II, III, VI, IX, XVII) and peripheral districts (XI, XII, XIII, XV) that can be justified considering that modern buildings are often located in peripheral districts, which are more suitable for PV.

In a second step, it has been considered the average installable power on buildings, reported in Fig. 2 with two curves showing the maximum power obtainable using all the roofs and the installable power for net-metering. In this case, the installed power in each building has been reduced to the effective building's energy need. The average power installed is 40 kW per building, 22 kW in the case of net metering.

In the end it has been considered the total costs for intervention, related to simple pay-back time, in order to quantify the budgets and the economic advantages of PV systems. The analysis has been performed considering for the case of feed-in incentives of two different strategies. In case 1, it has pursued the maximum gain, reducing the power installed in order to raise the share of energy consumed on site. In fact the feed-in incentive for energy consumed on site added to the bill reduction, provides a gain higher than the feed-in incentive for energy injected into the grid. Table 2 reports the values of feed-in incentives provided by the feed-in scheme for the period between March and July, 2013 and the estimated bill reduction.

To estimate the exact amount of energy consumed on site, it would be necessary to analyze the consumption of each school and the productivity of each plant on an hourly basis. On such a large scale analysis, it have been calculated a percentage of consumption on site of 62%, for the share of energy produced equal to the annual total consumption. This data have been calculated considering the average daily productivity of a standard photovoltaic plant referred to the opening days of school buildings. The value is almost low because school buildings are closed during the summer months in which there is the highest productivity of photovoltaic systems. For the share of energy produced exceeding the annual total consumption it has been considered a percentage of consumption on site of 0%.

Fig. 3 shows the result of the analysis. Net metering is the strategy that provides the best PBT, lower than the one of feed-in incentives cases 1 and 2. Cost value

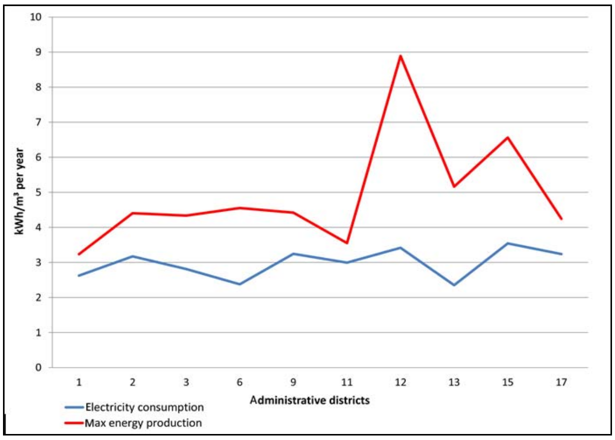

Fig. 1 Electric energy consumption and production for cubic meter and administrative districts.

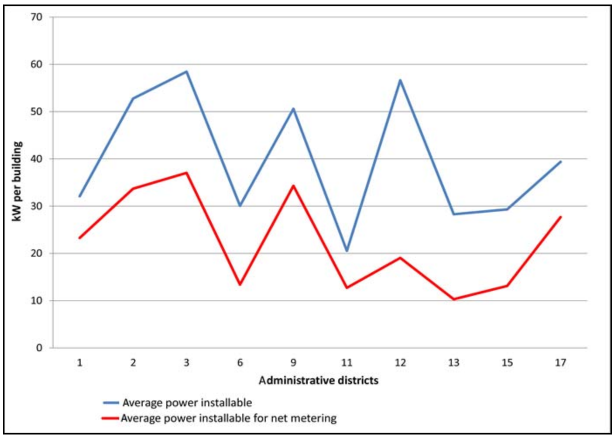

Fig. 2 Average power installable on buildings, related to the administrative districts.

Table 2 Feed-in incentives and bill saving for power installed.

	Energy consumed on site		Energy injected into the grid	
	3 < kWp < 20	20 < kWp < 200	3 < kWp < 20	20 < kWp < 200
Feed-in tariff	0.089	0.075	0.171	0.157
Bill reduction	0.180	0.180	-	-
Total gain	0.269	0.255	0.171	0.157

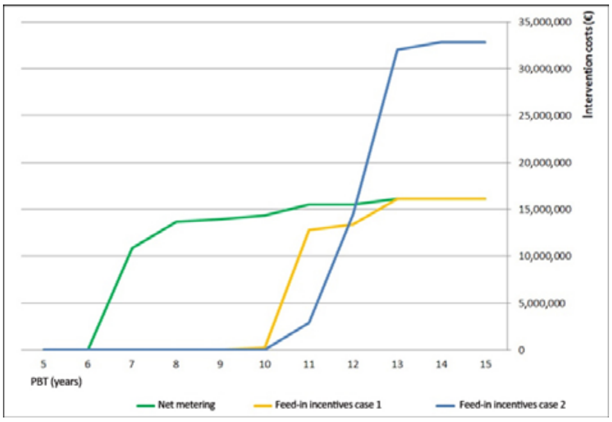

Fig. 3 Simple PBT related to total investment cost.

is indicative of the potential of installation and, consequently, of the potential environmental savings, which will be greater in absolute terms maximizing the available surfaces as in case 2 of feed-in incentives. In the case of net metering the emission saving on 20 years of operability of the plant will be of 4.300 kg of CO_2, in the case of feed-in, utilizing all the available surfaces 8.800 kg of CO_2. In any case the cost of a kg of CO_2 saved is lower than 0.20€. In relative terms environmental savings will be greater in the peripheral municipalities where there is a greater freedom of installation and thus it is possible to optimize the system efficiency.

5. Conclusions

The analysis carried out shows the high potential for photovoltaic installation on Roman school buildings. The energy needs of existing school buildings for the next 25 years could be satisfied with an investment of about 80 million €, equal to the actual budget for nine years of electricity, without taking into account deductions and incentives.

The maximum power installable on the entire school building stock is about 55 MW, sufficient to reduce CO_2 emissions of 763.000 t during twenty years of useful life of the plants. The short PBT (pay-back time) makes these investments profitable for the involvement of private entities, reducing the burden on the public administration. It is thus necessary to have a strong will on the part of the public administration, able to involve private entities in the development of an ambitious and far-sighted project.

References

[1] L. de Santoli, The Community of Energy, Quodlibet, Macerata, 2011, p. 1-191. (in Italian)

[2] U. Desideri, S. Proietti, Analysis of energy consumption in the high schools of a province in central Italy, Energy and Buildings 34 (2002) 1003-1016.

[3] S.P. Corgnati, S. Viazzo, M. Filippi, A method for heating consumption assessment in existing buildings: a field survey concerning 120 Italian schools, Energy and Buildings 40 (2008) 801-809.

[4] F.R. d´Ambrosio Alfano, L. Bellia, A. Boerstra, F. van Dijken, E. Ianniello, G. Lopardo, et al., Indoor Environment and Energy Efficiency in Schools—Part 1 Principles, REHVA, 2010, pp. 1-128.

[5] V.D. Giuli, O.D. Pos, M.D. Carli, Indoor environmental quality and pupil perception in Italian primary schools, Building and Environment 56 (2012) 335-345.

[6] N. Amoroso, D.A. Balladin, O.S.T.C. Headley, I.A. McDoom, A. Parasram, K. Rampersad, et al., Introduction of solar energy devices to secondary schools as teaching aids, Solar Energy 64 (1998) 1-120.

[7] G.M.L. Giudice, F. Fraticelli, F. Fornari, C. Calice, Analysis of energy performance of school building stock in Rome [Online], WIT eLibrary Web site (in press), http://library.witpress.com/pages/PaperInfo.asp?PaperID =25201.

[8] L. De Santoli, F. Fraticelli, F. Fornari, C. Calice, Energy performance assessment and a retrofit strategies in public school buildings in Rome, Energy and Building 68 (2014) 196-202.

[9] Law 387/2003 and Decree 28 July 2005, Implementation of EU Directive 2001/77/CE "on the Promotion of Electricity Produced from Renewable Energy Sources in the Internal Electricity Market", Official Journal [Online], 25 (2004) 5-27, http://www.camera.it/parlam/leggi/deleghe/03387dl.htm.

[10] Ministerial Decree of 5 Jul. 2012, Incentives for energy supplied by PV systems (Incentivi per energia da fonte fotovoltaica), Official Journal [Online], 159 (2012) 1-37, http://www.gazzettaufficiale.it/atto/serie_generale/carica DettaglioAtto/originario?atto.dataPubblicazioneGazzetta =2012-07-10&atto.codiceRedazionale=12A07629&elenc o30Giorni=false.

[11] Law 296/2006 (Italian Financial Act 2007), Official Journal [Online], 299 (2006) 1-341, http://www.camera.it/parlam/leggi/06296l.htm.

[11] M. Bertozzi, M. Casini, F. Leccese, G. Salvadori, Analysis of energy demands for lighting in buildings, Neo-Eubios. 41 (2012) 46-56.

[12] D. Pepe, School Environmentally Friendly: From Kindergarten to High School, Dei, 2009, pp. 1-294. (in Italian)

Journal of Energy and Power Engineering 8 (2014) 453-460

Energy Planning in Small Municipalities Based on Monitoring Results and Demand Side Management

Dagnija Blumberga, Andra Blumberga, Marika Rošā and Aiga Barisa

Institute of Energy Systems and Environment, Riga Technical University, Riga, LV-1010, Latvia

Received: July 24, 2013 / Accepted: September 23, 2013 / Published: March 31, 2014.

Abstract: Recent estimates state that the European Union is on course to achieve only half of the 20% energy consumption reduction target by 2020. As the first governmental stakeholders involved in the implementation of energy saving initiatives, municipalities play a strategic role in the energy planning process. This paper focuses on establishment of an energy planning methodology for small municipalities with numbers of inhabitants in range of 1,000-10,000 which often face common problems associated with low efficient district heat supply systems and decreasing energy consumption in buildings. Particular attention is paid to DSM (demand side management) activities. DSM scheme includes legislative and financial flows with small investments from municipality side. Based on increased information and motivation it promotes reduction of energy consumption in all kinds of buildings. Practical experience has shown that application of DSM measures allows achieving 20% energy savings in municipal buildings during the first year.

Key words: Demand side management, energy efficiency, energy planning.

1. Introduction

EU's (European Union's) climate and energy package, presented in 2009, includes three key climate and energy policy objectives for 2020, known as the "20-20-20" targets. The latest evaluation shows that the EU is on the way towards achieving its targets of reducing greenhouse gas emissions whilst raising the share of renewable energy sources [1]. However, much greater effort is needed to improve energy efficiency. Recent estimates of the European Commission state that the EU is on course to achieve only half of the 20% objective by 2020 [2].

Buildings represent the greatest energy saving potential [2]. On March 8, 2011, the European Commission presented a new energy efficiency plan that aims to improve the energy performance of both public and private buildings and promotes the exemplary role of the public sector. Following on June 22, 2011, the Commission proposed for a new Directive on energy efficiency repealing directives 2004/8/EC and 2006/32/EC. The directive was adopted on October 25, 2012 and established a common framework for promoting energy efficiency in the EU to ensure achievement of agreed 20% primary energy savings target by 2020 [3]. For public sector, which is of the main interest in this paper, the directive makes provision that member states shall encourage public bodies to adopt their energy efficiency plans containing specific energy saving objectives and put in place energy management systems as part of the implementation of these plans. In addition, member states shall ensure that starting from 2014, 3% of the total floor area owned by public bodies is renovated each year to meet at least the minimum energy performance requirements.

1.1 The Role of Public Bodies in Increasing Energy Efficiency

According to Brandoni et al. [4] and Neves et al. [5], local authorities are the first governmental stakeholders involved in the implementation of energy saving

Corresponding author: Dagnija Blumberga, professor, research fields: renewable energy and energy efficiency. E-mail: dagnija.blumberga@rtu.lv.

initiatives. Municipalities therefore play a strategic role in the energy planning process being able to implement several schemes designed to fulfil their exemplary role: (1) develop building codes and issue construction permits responding to high energy efficiency criteria; (2) implement demonstrative energy efficiency initiatives in public properties; (3) launch informative campaigns to increase citizens' knowledge and awareness about energy and environmental issues; (4) adopt new "clean" technologies [4, 6].

A number of authors have discussed aspects of decentralized energy planning [7-9]. Hiremath et al. [7] state that decentralized energy planning is one of the options to meet the rural and small-scale energy needs in a reliable, affordable and environmentally suitable way. Shikha et al. [8] add that decentralized energy planning is in the interest of efficient utilization of resources and takes into account various available resources and energy needs of the region. Eventually Dzene et al. [9] choose decentralized energy planning on a regional level as the most appropriate way to promote renewable energy sources and to reduce negative environmental impacts of energy systems.

1.2 Energy Planning in Small Municipalities

Energy system of a small municipality differs from that of a large one. It is not only about the size but as well technological solutions, financial and management capacity.

Generally more interest has been paid on national and regional energy planning issues than on energy planning at municipal level. However, a number of examples on energy management in municipalities are reviewed in literature. Based on a review of 11 municipal energy plans, Sperling et al. [10] examined to what extent municipal energy planning matches national renewable energy strategies in Denmark. Nilsson and Martensson [11] performed similar study in Sweden analysing whether municipal energy plans have contributed to the development of local energy systems. Cai et al. [12-14] pay attention to long-term renewable energy management in communities within the context of local energy planning and Rezessy et al. [15] discuss the factors that govern local authorities to involve in the market for energy services and energy efficient equipment.

Closer to the topic of this paper, Fiaschi et al. [16] performed a comprehensive investigation on the energy consumption of public buildings and utilities and evaluated the most effective and feasible ways to save energy in a small Italian township with approximately 16,000 inhabitants and Dzene et al. [9] elaborated a screening method for identifying suitable options for improving energy system in an environmentally sound direction in a typical middle-sized rural region in Latvia.

1.3 Energy System of a Municipality

Energy system of a municipality is represented as a network of energy chains consisting of primary energy supply and conversion, energy transmission and distribution and finally the end-use.

The demand for space heating and hot water in buildings is still the major element of the total energy demand for many municipalities in countries with moderate to cold climates [17]. Although district heating offers a number of advantages compared to single house heating systems, the share of individual heating systems is usually larger, mainly due to low density of population in rural areas. Correspondingly, operation of individual heating systems is often associated with lower energy efficiency because of such reasons as technological limitations, lack of owners' knowledge, etc.

On the other hand, also the existing district heating systems face several problems, e.g., decreasing energy consumption due to such reasons as the implementation of energy efficiency measures in buildings, migration of people from rural to urban areas, and shift from district to decentralized renewable energy systems.

Recently an increasing number of studies have analysed possibilities to promote the use of district

heating in the context of decreasing energy consumption in buildings. Thyholt and Hestnes [18] concluded that lowering space heating demand in buildings results in higher costs for district heating. Aberg and Henning [19] add that traditional district heating networks are not designed for low energy buildings because of relatively high distribution heat losses. Meanwhile, Sperling and Möller [17] find that in general substantial reductions of buildings' heat demand can go hand in hand with a continued expansion of the district heating system and can improve the overall efficiency of energy system in the short and long term.

The above mentioned case studies indicate that energy planning in municipalities is a topical question both from side of effective energy production and consumption. Despite the fact that, for example, in Sweden municipal energy planning has been part of energy policy for more than three decades, generally municipalities, especially small ones, lack experience, knowledge and resource to develop qualitative long-term energy plans in their territories. The aim of this paper is to propose a methodology for design of energy plans in small municipalities focusing on DSM (demand side management) measures. The established energy planning model was applied on a case study of Beverina region in Latvia.

2. Methodology

An algorithm for energy planning in municipalities is proposed in Fig. 1. It consists of 11 both directly and indirectly interrelated modules.

Evaluation of the current energy situation in the region is the starting point of energy systems' planning from which it is possible to set relevant objectives and elaborate an adequate action plan. The baseline review is based on existing data on energy system performance in the region and covers both quantitative (energy production and consumption) and qualitative (energy management, knowledge, etc.) aspects. Input data include information on space heating area (m^2), energy consumption for space heating and hot water preparation (MWh/year, kWh/m^2/year), and heat costs (EUR/year, EUR/m^2/year). Data are obtained both directly (from building inventories, accounting, and energy meters) and by calculations if only fuel consumption is measured (frequent for wood fuel applications). In case reliable data are not available several assumptions must be done, e.g., in regard to the length of heating season or energy content of fuels.

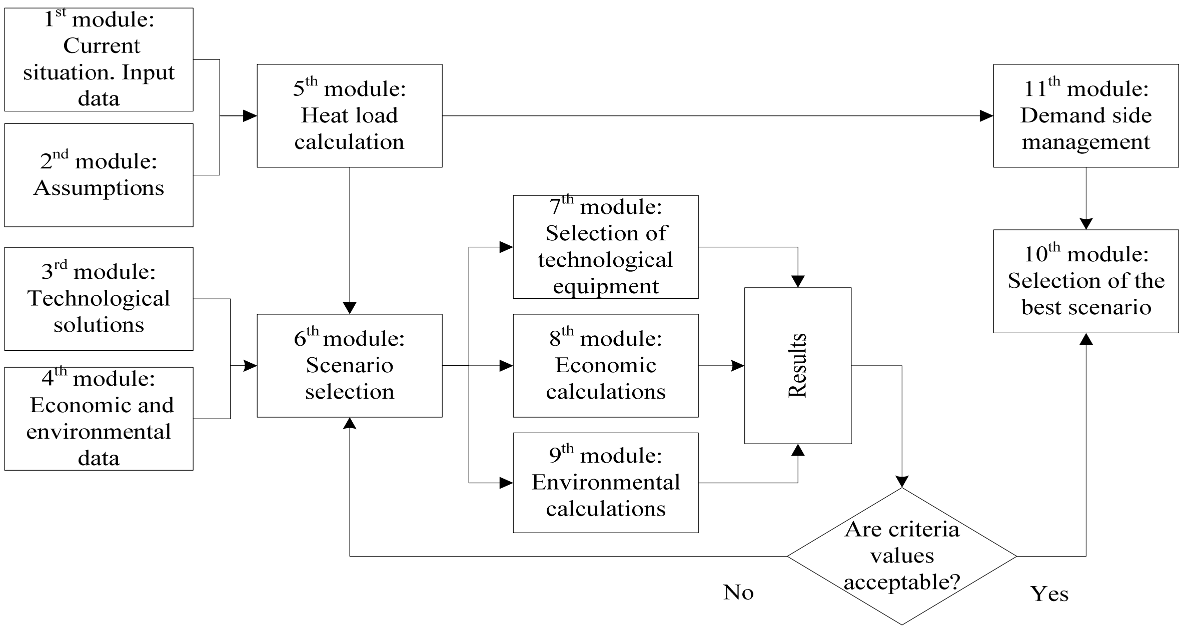

Fig. 1 Algorithm for energy planning in municipalities.

Collected data are further analysed and interpreted. Based on buildings energy consumption characteristics annual heat energy consumption graph is drawn to indicate base and peak loads. Determination of an appropriate heat load is important to ensure high-efficient systems performance.

Based on the data collected, hypothesis for future development of the regional energy system is established. Available technological solutions and economic and environmental considerations are taken into account in this step. Following detailed development scenarios are modelled including selection of technologies and corresponding economic and environmental calculations.

Based on findings of the different scenarios and taking into account specific needs of the region, municipality stakeholders determine the most promising scenario and select measures and actions to be implemented. Finally, implementation of the regional energy strategy is based on previously developed demand side management plan to ensure that planned efficiency improvement is achieved.

3. Results of the Case Study

The proposed algorithm for development of future energy systems was applied to a case study of a small municipality in Latvia. This chapter presents results of the case study.

3.1 Target Region Portrait

Beverina region with its 3,500 inhabitants is an example of a typical small rural area in Latvia, as approximately 70% of regional municipalities in Latvia have less than 10,000 inhabitants based on census data available in Ref. [20]. The municipal area is approximately 301 km^2, resulting in a density of 12 people per square kilometre.

Local administration is responsible for approximately 20 public buildings, including schools and kindergartens, libraries, cultural houses, several social offices and central administration. Household building stock is circa 170,000 m^2, of which 70% are single family houses. Space heating and hot water is mainly supplied by individual heating systems (stoves, furnaces, fire-places or electric heating units) [21].

Further in the paper the authors have chosen to analyse three problematic elements of the energy system of Beverina region:

- Murmuiza boiler house;
- multi-apartment house "Lazdas";
- Trikata Primary School and sports hall.

3.2 Input Data

There is no single source of information on energy situation in Latvian municipalities. Therefore, a comprehensive research was performed to collect the necessary input data characterizing energy supply infrastructure, primary energy resources and energy consumers in Beverina region. All three specific cases covered by this research will be described below.

3.2.1 Murmuiza Boiler House

District heating in Murmuiza community, one of the largest settlements in Beverina region, is supplied by a 1 MW biomass boiler. Fuel consumption was 3,000 m^3 loose volume of wood chips and additional 200 m^3 loose volume of saw dust in 2011. Boiler efficiency is 61.0%.

Data characterizing energy consumers in Murmuiza are illustrated in Fig. 2. Energy consumption in eight monitored buildings varies in range 70 kWh/m^2/year -220 kWh/m^2/year. Building energy performance is the main cause explaining diverse energy consumption though also human factors play a crucial role.

Fig. 2 shows a satisfactory correlation between two variables – normalized energy consumption (converted to standard degree days) in buildings connected to the network of Murmuiza boiler house and heated area of these buildings. In case DSM measures are applied, an empirical equation characterized by a linear function can be used as a benchmark to determine building energy consumption by Eq. (1):

$$Q = -0.083\times F + 222.66 \tag{1}$$

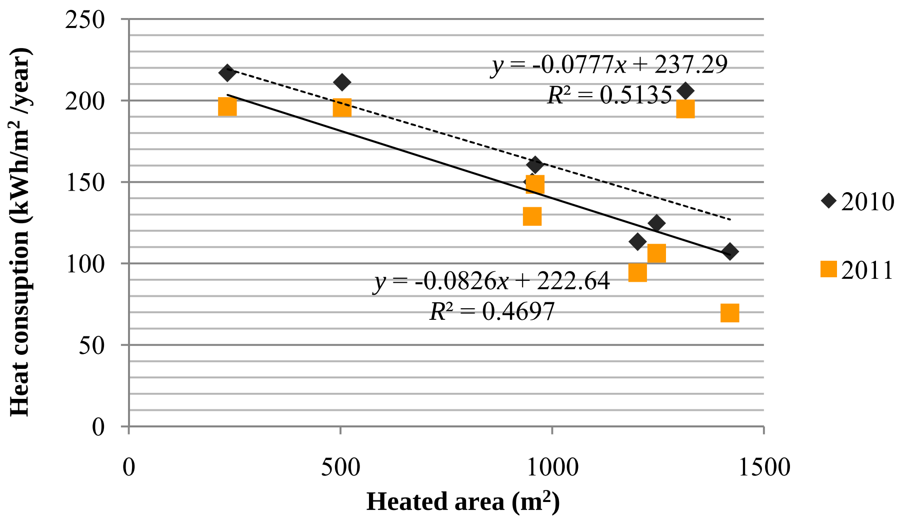

Fig. 2 Specific energy consumption of buildings in Murmuiza community.

where,

Q—annual specific heat consumption, kWh/m^2/year;

F—heated area of the building, m^2.

The benchmark is adjusted each year according to the level of achieved energy savings. Position and slope of the lines describes processes occurring in buildings. Data correlation should improve in line with increased knowledge and awareness of inhabitants about opportunities to reduce heat consumption.

3.2.2 Multi-Apartment House "Lazdas"

Multi-apartment house "Lazdas" in Cempi Community (another settlement area in Beverina region) represents a typical multi-family house in Latvia. Heating area of the building is 1,080 m^2 and specific heat energy consumption is 175 kWh/m^2/year. Heat and hot water is provided by electric heaters.

3.2.3 Trikata Primary School and Sports Hall

Trikata Primary School was built in 1938. A new sports hall next to the school was finished in 2005. Heating space of the school is 2,310 m^2 and of the sports hall—1,075 m^2. In 2007, several energy efficiency measures were implemented in the school including installation of ground heat pumps. Annual electricity consumption to power heat pumps is 144 MWh/year. Annual light fuel oil consumption for heat supply in sports hall is 6.5 t/year.

3.3 Development of Alternative Scenarios

Based on evaluation of current situation, alternative scenarios for each case study were developed. The scenario description are in Table 1 (Murmuiza Boiler House), Table 2 (multi-apartment house "Lazdas"), and Table 3 (Trikata Primary School and sports hall).

4. Discussion

Results of the research have highlighted the main energy management problems in Beverina municipality associated with primary energy purchase, lack of appropriate training of energy operators and building energy management policy. This has led to proposal of a municipality DSM system further applicable for integration in regional level energy planning process. A self-financing scheme can be applied to implement proposed energy efficiency measures (in Fig. 3).

The scheme involves development of a municipality energy management division that is responsible for implementation of energy efficiency related initiatives in the municipality. This includes development of a single documentation for fuel purchase tenders, energy training of building managers and implementation of energy efficiency measures in public buildings. Municipality financing for energy efficiency related projects is secured from two sources: state grants and energy savings. This

Table 1 Alternative scenarios for energy efficiency measures in Murmuiza boiler house.

Alternative	Service	Costs, 1,000 EUR	Payback time, years
A: establishment of an energy management programme	Experts consultation and energy managers salary	3-6	< 1
	Measuring equipment and engineering service purchase	7-10	< 1
	Equipment installation	14-21	< 1
B: installation of effective biomass boilers with flue gas condensing units	Wood pellet boiler (0.4 MW)	57	10
	Wood chips boiler with a flue gas condensing unit (0.4 MW)	71	7
	Wood pellet boiler (0.2 MW) and wood chips boiler (0.2 MW) with a condensing unit	85	10
	Biomass cogeneration unit (0.3 MW_e and 0.4 MW_{th})	1,423	10
C: heat supply decentralization	This is an alternative solution in case installation of new district heating boiler is not technologically and economically feasible. Installation of a pellet boiler in each multi-family house is proposed.		

Table 2 Energy efficiency measures in multi-apartment house "Lazdas".

No.	Measure	Costs, 1,000 EUR
1. District heat supply system		
1	Creation of a new heating system	24
2	Creation of a new hot water supply system	17
3	Creation of a heating unit	7
Total		48
2	Building energy performance improvement	
4	Energy efficiency measures in buildings	171
3	Heat source	
5	Installation of a fully automatized pellet boiler (70-100 kW)	28
Total		248

NB! Repayment time of the alternative is 10.5 years.

Table 3 Alternative energy efficiency measures in Trikata Primary School and sports hall.

No.	Measures at heat supply unit	Costs, 1,000 EUR	Repayment time, years
1	Development of a DSM programme	9	2
2	Development of a DSM programme and installation of a wood pellet boiler in sports hall	33	4.2
3	Development of a DSM programme and installation of a wood pellet boiler to cover the base load	38	3.9

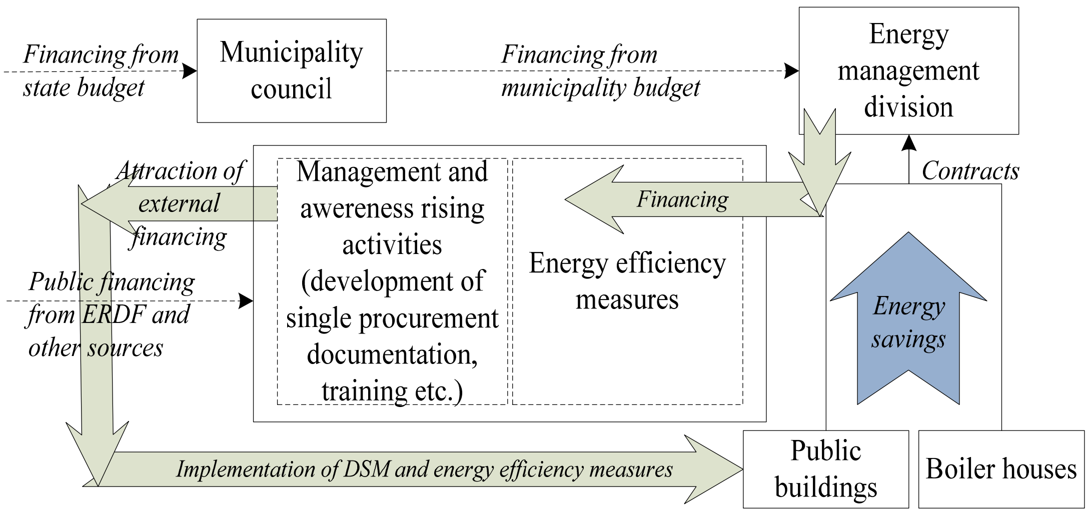

Fig. 3 A partial self-financing scheme for implementaion of energy efficiency and DSM measures in municipalities.

means that municipality invests in both direct energy saving measures in public buildings and in regulatory and awareness rising initiatives that allows achieving maximum planned energy savings. Municipality benefits include reduced fuel purchase and energy costs as well as improved quality of public infrastructure.

5. Conclusions

This study covered three problems typical for small municipalities in Latvia:

• existence of complex heat supply systems consisting of district or partly district heating in community centres and decentralized heat sources in single family houses;

• high energy consumption because of low energy performance of buildings and energy consumers' behavioural traits;

• inability (lack of knowledge, awareness and resource) of local authorities to manage the energy system.

Based on a case study, alternative scenarios were proposed mainly focusing on DSM measures. First results show that introduction of DSM in combination with simple energy efficiency measures in Beverina region has resulted in 20% energy consumption reduction in a half year.

Proposed energy efficiency measures and financing scheme can be considered a representative case study in Latvian scenario and can be applied to other municipalities of a similar size.

Acknowledgments

This research was carried out with support of European Commission's programme Intelligent Energy Europe under the Wood Energy project. The work presented in this paper received support from Beverina municipality.

References

[1] M.G. Carvalho, EU energy and climate change strategy, Energy 40 (1) (2012) 19-22.

[2] Energy Efficiency Plan 2011, European Commission, Brussels, 2011.

[3] Directive 2012/27/EU of the European Parliament and of the Council of 25 October 2012 on Energy Efficiency, Amending Directives 2009/125/EC and 2010/30/EU and Repealing Directives 2004/8/EC and 2006/32/EC, the European Commission, L 315/1, Nov. 14, 2012.

[4] C. Brandoni, F. Polonara, The role of municipal energy planning in the regional energy-planning process, Energy 48 (1) (2012) 323-338.

[5] A.R. Neves, V. Leal, Energy sustainability indicators for local energy planning: Review of current practices and derivation of a new framework, Renewable and Sustainable Energy Reviews 14 (2010) 2723-2735.

[6] G. Comodi¸ L. Cioccolanti, F. Polonara, C. Brandoni, Local authorities in the context of energy and climate policy, Energy Policy 51 (2012) 737-748.

[7] R.B. Hiremath, B. Kumar, P. Balachandra, N.H. Ravindranath, Bottom-up approach for decentralised energy planning: Case study of Tumkur district in India, Energy Policy 38 (2) (2010) 862-874.

[8] R.B. Hiremath, S. Shikha, N.H. Ravindranath, Decentralized energy planning; modeling and application ,Review, Renewable and Sustainable Energy Reviews 11 (5) (2007) 729-752.

[9] I. Dzene, M. Rosa, D. Blumberga, How to select appropriate measures for reductions in negative environmental impact? Testing a screening method on a regional energy system, Energy 36 (4) (2011) 1878-1883.

[10] K. Sperling, F. Hvelplund, B.V. Mathiesen, Centralisation and decentralisation in strategic municipal energy planning in Denmark, Energy Policy 39 (3) (2011) 1338-1351.

[11] J. Stenlund Nilsson, A. Martensson, Municipal energy-planning and development of local energy-systems, Applied Energy 76 (1-3) (2003) 179-187.

[12] Y.P. Cai, G.H. Huang, Z.F. Yang, Q.G. Lin, Q. Tan, Community-scale renewable energy systems planning under uncertainty—An interval chance-constrained programming approach, Renewable and Sustainable Energy Reviews 13 (4) (2009) 721-735.

[13] Y.P. Cai, G.H. Huang, Q. Tan, Z.F. Yang, Planning of community-scale renewable energy management systems in a mixed stochastic and fuzzy environment, Renewable Energy 34 (7) (2009) 1833-1847.

[14] P.A. Østergaard, B.V. Mathiesen, B. Möller, H. Lund, A renewable energy scenario for Aalborg Municipality based on low-temperature geothermal heat, wind power and biomass, Energy 35 (12) (2010) 4892-4901.

[15] S. Rezessy, K. Dimitrov, D. Urge-Vorsatz, S. Baruch, Municipalities and energy efficiency in countries in transition. Review of factors that determine municipal

involvement in the markets for energy services and energy efficient equipment, or how to augment the role of municipalities as market players, Energy Policy 34 (2) (2006) 223-237.

[16] D. Fiaschi, R. Bandinelli, S. Conti, A case study for energy issues of public buildings and utilities in a small municipality: Investigation of possible improvements and integration with renewables, Applied Energy 97 (2012) 101-114.

[17] K. Sperling, B. Möller, End-use energy savings and district heating expansion in a local renewable energy system—A short-term perspective, Applied Energy 92 (2012) 831-842.

[18] M. Thyholt, A.G. Hestnes, Heat supply to low-energy buildings in district heating areas, analyses of CO_2 emissions and electricity supply security, Energy and Buildings 40 (2) (2008) 131-139.

[19] M. Aberg, D. Henning, Optimisation of a Swedish district heating system with reduced heat demand due to energy efficiency measures in residential buildings, Energy Policy 39 (12) (2011) 7839-7852.

[20] Central Statistical Bureau of Latvia, Data on resident population in statistical regions [Online], http://data.csb.gov.lv/Menu.aspx?selection=Sociala__Ikgad%C4%93jie%20statistikas%20dati__Iedz%C4%ABvot%C4%81ji__Iedz%C4%ABvot%C4%81ji%20skaits%20un%20t%C4%81%20izmai%C5%86as&tablelist=true&px_language=en&px_db=Sociala&rxid=992a0682-2c7d-4148-b242-7b48ff9fe0c2.

[21] J. Kaulins, I. Gleizde, I. Paleja, A. Plotkāns, Integrated Development Programme of Beverina Region 2012-2018 [Online], http://www.beverinasnovads.lv/index.php?option=com_content&view=article&id=152&Itemid=170.

Journal of Energy and Power Engineering 8 (2014) 461-469

Selective Adsorption Properties and Stable Solidification of Cs by Insoluble Ferrocyanide Loaded Zeolites

Yuki Ikarashi[1], Rana Syed Masud[1], Tomonori Nakai[1], Hitoshi Mimura[1], Eiji Ishizaki[2], Minoru Matsukura[2] and Yoshinobu Hosoi[3]

1. Department of Quantum Science and Energy Engineering, Graduate School of Engineering, Tohoku University, Miyagi-ken 980-8579, Japan

2. UNION SHOWA K.K., Tokyo 108-0073, Japan

3. Rigaku Corporation, Tokyo 196-8666, Japan

Received: October 29, 2013 / Accepted: November 27, 2013 / Published: March 31, 2014.

Abstract: In Fukushima NPP-1, large amounts of HALW (high-activity-level water) accumulated in the reactor, turbine building and the trench in the facility is treated by circulating injection cooling system. The development of highly functional adsorbents and stable solidification method contributes to the advancement of the decontamination system and environmental remediation. The present study deals with: (1) preparation of insoluble ferrocyanide loaded zeolites; (2) selective uptake of Cs^+ in seawater; and (3) estimation of Cs immobilization ratio and stable solidification. Various kinds of Cs-selective composites loaded with insoluble ferrocyanides (CoFC, NiFC) into the zeolites (zeolite A (A51, A-51J), zeolite X (LSX), chabazite (modified chabazite) and natural mordenite (SA-5)) matrices have been prepared to use successive impregnation/precipitation methods by Tohoku University. As for Cs^+ adsorption, these composites had relatively large uptake (%) over 95%, distribution coefficients (K_d) above 10^3 cm^3/g and excellent adsorption kinetics even in seawater. The immobilization ratio (%) of Cs for the CoFC saturated with Cs^+ was estimated at different calcination temperatures up to 1,200 ºC in advance. The immobilization ratio was less than 0.1% above 1,000 ºC, indicating that the adsorbed Cs^+ ions are completely volatilized and insoluble ferrocyanides had no immobilization ability for Cs. In contrast, the insoluble ferrocyanide-loaded zeolites had excellent Cs immobilization ability; in the case of insoluble ferrocyanide-loaded natural zeolites (NiFC-SA-5, CoFC-modified chabazite), the immobilization ratio was above 99% and 96% even after calcination at 1,000 ºC and 1,100 ºC, respectively, indicating that nearly all Cs ions are immobilized in the sintered solid form. On the other hand, the immobilization ratio for the insoluble ferrocyanide-loaded A and X zeolites (NiFC-A (A51, A51J), NiFC-X) tended to decrease with calcining temperature; for example, the immobilization ratio for NiFC-X at 1,000 ºC and 1,100 ºC was estimated to be 74.9% and 55.4%, respectively, and many spots concentrating Cs were observed on the surface. The difference in immobilization behavior between natural zeolites and synthetic ones is probably due to the phase transformation and surface morphology at higher temperature above 1,000 ºC. The stable solidification of insoluble ferrocyanides was thus accomplished by using the excellent Cs immobilization abilities of zeolite matrices (Cs trapping and self-sintering abilities).

Key words: Cs, Sr, Zeolites, HALW (high-activity-level water), insoluble ferrocyanides, stable solidification.

1. Introduction

In Fukushima NPP-1, large amounts of HALW (high-activity-level water) accumulated in the reactor, turbine building and the trench in the facility is treated by the circulating injection cooling system (in Fig. 1) [1-3]. At present, this system is effectively operated and the cold shutdown is completed. However, large amounts of secondary solid wastes such as zeolites (346 vessels) and insoluble ferrocyanide sludge (581 m^3)

Corresponding author: Hitoshi Mimura, professor, research field: radioactive waste treatment. E-mail: hitoshi.mimura@qse.tohoku.ac.jp.

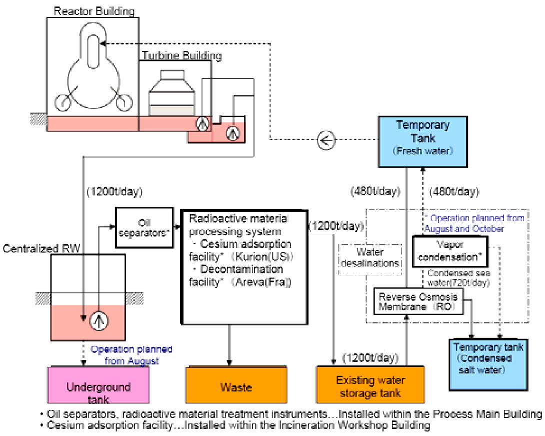

Fig. 1 Decontamination system for high-activity-level water in Fukushima NPP-1 [3].

are generated (on March 14, 2012) [1], and hence the development of effective treatment and disposal methods is very urgent and important issues in Japan. Especially, insoluble ferrocyanide sludge contains high radioactivity of ^{137}Cs and has low thermal stability, and insoluble ferrocyanides tend to release HCN (hydrogen cyanide) above 300 °C under inert and reducing atmosphere [2]. Thus, the development of stable solidification method contributes to the advancement of the decontamination system and environmental remediation. In this study, the stable solidification of insoluble ferrocyanides saturated with Cs^+ ions was examined by utilizing the immobilization abilities of zeolites, i.e., Cs trapping and self-sintering abilities.

The present study deals with: (1) preparation of insoluble ferrocyanide loaded zeolites; (2) selective uptake of Cs^+ in seawater; (3) estimation of Cs immobilization ratio and stable solidification.

2. Experiment

2.1 Materials and Preparation Procedure

Various kinds of Cs-selective composites loaded with insoluble ferrocyanides (CoFC ($K_2[FeCo(CN)_6]$), NiFC ($K_2[FeNi(CN)_6]$)) into the zeolites (synthetic zeolite A (A51, A51J), synthetic zeolite X (LSX), chabazite (modified chabazite) and natural mordenite (SA-5, Ayashi, Sendai)) matrices have been prepared

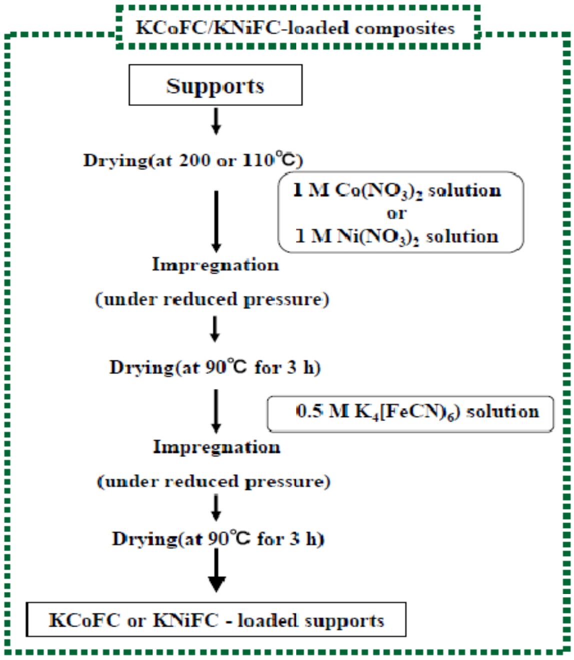

Fig. 2 Preparation procedure of insoluble ferrocyanide-loaded composites.

to use successive impregnation/precipitation methods by Tohoku University (in Fig. 2) [4-9]. For example, NiFC composites were prepared by the repeated impregnation of $Ni(NO_3)_2$ and $K_4Fe(CN)_6$ solutions into the macropores of zeolite matrices under the experimental conditions of zeolite: 3 g, 1 M $Ni(NO_3)_2$ solution: 20 cm^3, 0.5 M $K_4Fe(CN)_6$ solution: 20 cm^3, impregnation time: 3 hours and reaction temperature: 25 °C. The characteristics of zeolites used as matrices are listed in Table 1.

2.2 Determination of Uptake

The distribution of Cs^+ ions for composites was estimated by batch method. An aqueous solution (5 cm^3) containing 10 ppm Cs^+ ions was contacted with 50 mg of composites at 25 ± 1 °C up to 1 day, which was found to be sufficient for attaining equilibrium. The concentrations of Cs^+ ions were measured by atomic absorption spectrometer (AAS, Jarrell AA890). The uptake percentage (R, %) of metal ions removed from the solution and the distribution coefficient (K_d, cm^3/g) are defined as :

$$R = (C_0 - C_t)/C_0 \times 100 \quad (\%) \qquad (1)$$

Table 1 Characteristics of zeolites used as matrices.

Sample	SA-5	4A	LSX	Modified chabazite
Zeolite	Mordenite	A	X	Chabazite
Si/Al ratio	5	1	1	2-2.5
Exchangeable cation	Na, K	Na	Na	Na, Ca
Approximate kinetic diameter (A)	3.9	4	9	5
Cation exchange capacity (Na+, meq/g)	1.2-1.5	5.0-5.5	5.0-5.5	2.0-2.5

where C_0, C_t and C_f (ppm) are the concentration of metal ions at initial, at time *t*, and at equilibrium, respectively; m (g) the weight of composites; V (cm^3) the volume of aqueous phase.

2.3 Characterization and Determination of Cs Immobilization Ratio

The composites were then treated with 0.1 M $CsNO_3$ solution to obtain the Cs saturated composites samples for the immobilization test. The Cs saturated composites were calcined at different temperatures up to 1,100 ºC. Surface morphologies of the calcined specimens were examined by scanning electron microscopy (SEM, HITACHI, Miniscope TM-1,000) and digital microscope (DM, HiROX, KH-1,300). The chemical composition was determined by energy and wavelength dispersive spectrometry (EDS: Swift ED-TM, HITACHI, TM-1000; WDS: Hitachi X-650S) and fourier transform infrared spectroscopy (FT-IR, HORIBA, FT-200). The Cs immobilization ratio (%) was determined from the difference of the Cs content (wt%) before and after calcination. The decomposed gases in inert and active atmosphere (He, He + 20% O_2) were determined up to 400 °C by temperature programmed desorption-photoionization mass spectrometer (TPD-R, Rigaku).

3. Results and Discussion

3.1 Surface Morphology of Composites

Fig. 3 show the SEM images of insoluble ferrocyanide (NiFC, CoFC)-loaded zeolites. In the case of NiFC-A51 composite (Fig. 3b), composite matrices consist of small particles of synthetic zeolite A, and fine NiFC crystals are loaded in these particles. EDS spectra of NiFC-A composites treated with 0.1 M $CsNO_3$ solution indicate the loading NiFC crystals and the uptake of Cs^+ ions.

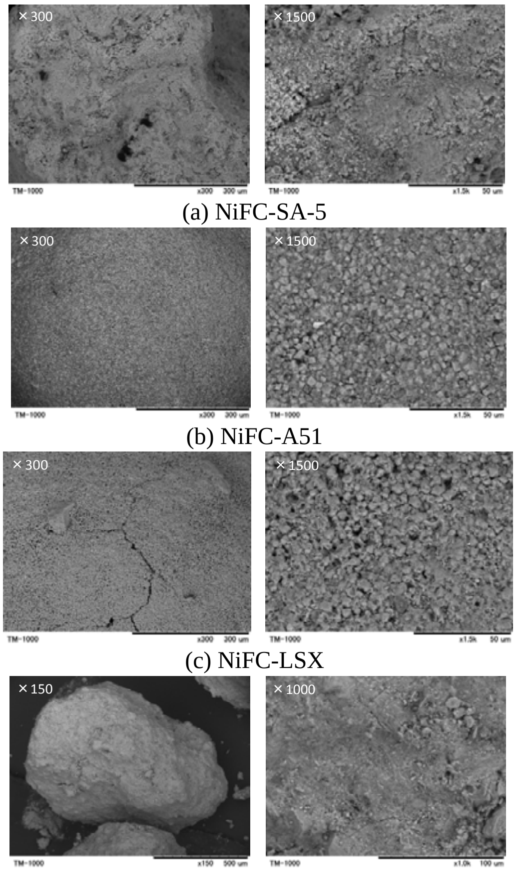

(a) NiFC-SA-5
(b) NiFC-A51
(c) NiFC-LSX
(d) CoFC- modified chabazite

Fig. 3 SEM images of insoluble ferrocyanide (NiFC, CoFC)-loaded zeolites.

3.2 Thermal Stability of Insoluble Ferrocyanides

Prior to the immobilization test for composites, the thermal decomposition of insoluble ferrocyanide itself and gas evolution behavior were examined by instrumental analyses. Surface morphology change of CsCoFC specimens calcined at different temperatures is shown in Fig. 4. In the case of 500 °C calcination, the surface of CsCoFC disk is seen to be thermally decomposed, indicating the decomposed gases (CO_2, NH_3 and NOx, etc.) are released. Fig. 5 shows the immobilization ratio (%) of Cs for CsCoFC at different calcining temperatures up to 1,200 ºC. The Cs immobilization ratio was considerably lowered

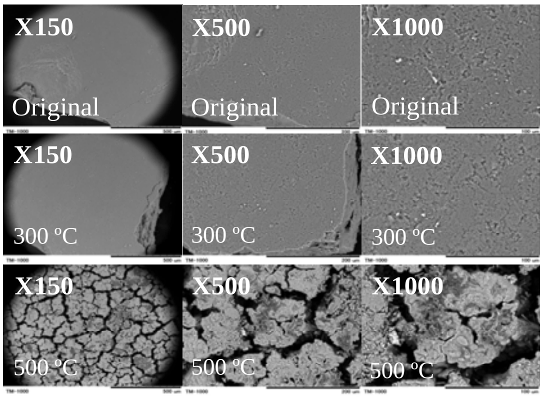

Fig. 4 Surface morphology change of CsCoFC specimens calcined at different temperatures.

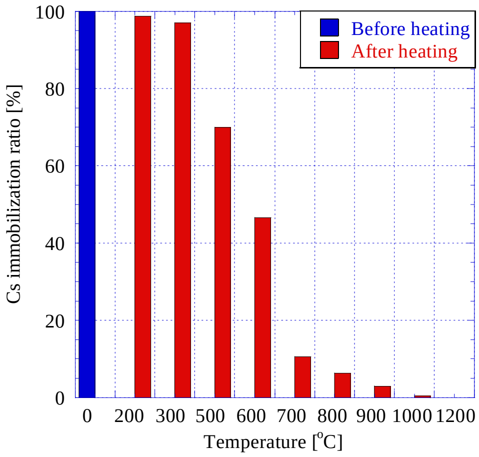

Fig. 5 Immobilization ratio (%) of Cs for CsCoFC at different calcining temperatures in the air up to 1,200 °C.

above 500 °C. This is probably due to the volatilization of Cs_2O gas. Further, the immobilization ratio above 1,000 ºC was estimated to be less than 0.1% (in Fig. 5); the adsorbed Cs^+ ions were completely volatilized, indicating the poor immobilization ability of CoFC for Cs at high temperature. Furthermore, the formation of cyanide is accompanied by thermal decomposition of insoluble ferrocyanides. In order to check the cyanide formation, the thermally decomposed gases from NiFC-A51 composites were analyzed in active and inert atmosphere by mass spectrometer. Mass signal peaks of H_2O, CO_2 and N_2 were detected around 120, 350 and 380 °C in He gas atmosphere, respectively. As shown in Fig. 6, mass signal peaks of HCN were detected twice around 200 °C and 370 °C. On the other hand, in He + 20% O_2 atmosphere, mass signal peaks of H_2O, NH_3, CO/CO_2,

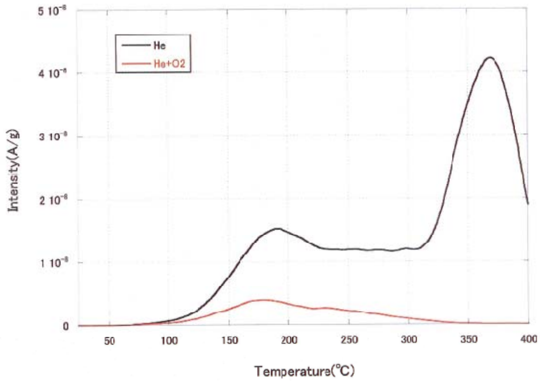

Fig. 6 HCN evolution from NiFC-A51 at different temperatures in inert and active atmosphere.

N_2 and NO were detected around 120, 320, 300-350, 320 and 330 °C, respectively. In active atmosphere, the HCN evolution is considerably lowered as clearly shown in Fig. 6. Thus, the development of stable solidification method for insoluble ferrocyanides is a urgent subject considering the low thermal stability and HCN evolution from insoluble ferrocyanides.

3.3 Selective Uptake of Cs^+ by Composites

In order to check the selectivity and equilibration time of Cs^+ ions for composites, the effect of shaking time on uptake (%) was examined in seawater by batch method. Fig. 7 shows the uptake rate of Cs^+ ions for composites (NiFC-SA-5, NiFC-A51 and NiFC-LSX) in seawater. The uptake rate of Cs^+ for composites was very large in the initial stage within 3 hours. In either case, the uptake equilibrium was attained within 8 hours and relatively large uptake (%) above 95% was obtained. Especially, the uptake of Cs^+ for NiFC-SA-5 had relatively large uptake rate. The uptake (%) of Cs^+ for composites was considerably enhanced compared to that for zeolite matrices (uptake (%): < 90%).

3.4 Immobilization of Cs by Sintering of Composites-Comparison of Immobilization Ratio

Insoluble ferrocyanide-loaded zeolites saturated with Cs^+ ions (CsNiFC-SA-5, CsNiFC-A51, CsNiFC-A51J, CsNiFC-LSX and CsCoFC-IE96) were sintered in electric furnace at high temperature (1,000 °C and

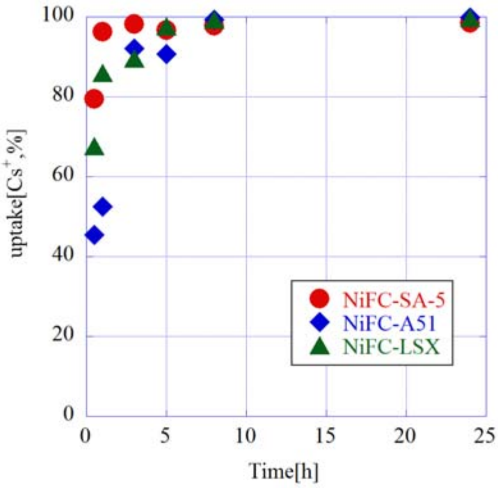

Fig. 7 Uptake rate of Cs^+ ions for insoluble ferrocyanide-loaded zeolites. 1 ppm Cs^+; *V/m* 100 cm^3/g, seawater; 25 °C.

1,100 °C). The Cs content of sintered products was then measured by EDS analysis, and the immobilization ratio (%) of Cs was determined. The immobilization ratios of Cs are compared among four kinds of sintered products as shown in Fig. 8. The immobilization ratio of Cs for CsNiFC-SA-5 sintered at 1,000 ºC and 1,100 ºC was estimated to be above 99% and 95%, respectively, indicating excellent immobilization ability. Similar results were obtained in the case of sintered CsCoFC-modified chabazite. On the other hand, the immobilization ratio for sintered CsNiFC-A51, CsNiFC-A51J and CsNiFC-LSX tended to decrease markedly above 1,100 ºC, and specific Cs concentrated spots were observed on the surface of the sintered products as described later. The order of immobilization ability for the composites was as follows:

NiFC-SA-5 > CoFC- modified chabazite >
NiFC-A51 > NiFC-A51J > NiFC-LSX

3.5 Surface Morphology and Distribution of Cs for Sintered CsNiFC-SA-5

The surface morphology, phase transformation and distribution of Cs for sintered CsNiFC-SA-5 were examined by instrumental analyses (SEM, XRD and WDS). Fig. 9 show SEM images of sintered products. The surface is seen to be porous and begins to melt,

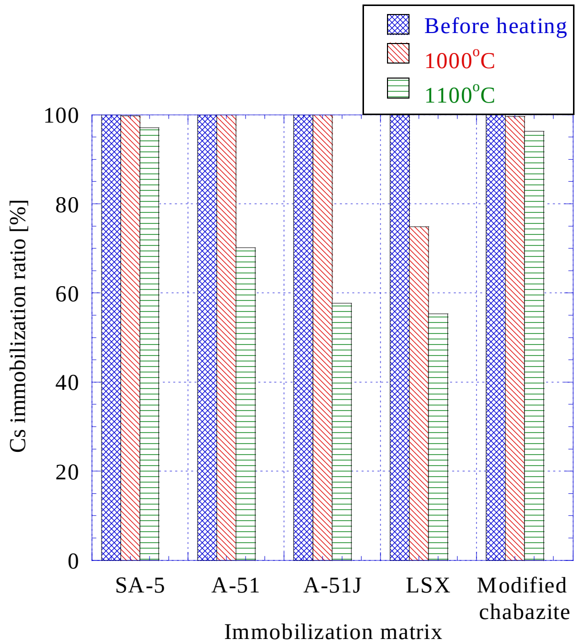

Fig. 8 Immobilization ratio (%) of Cs for insoluble ferrocyanide-loaded zeolites saturated with Cs^+ ions.

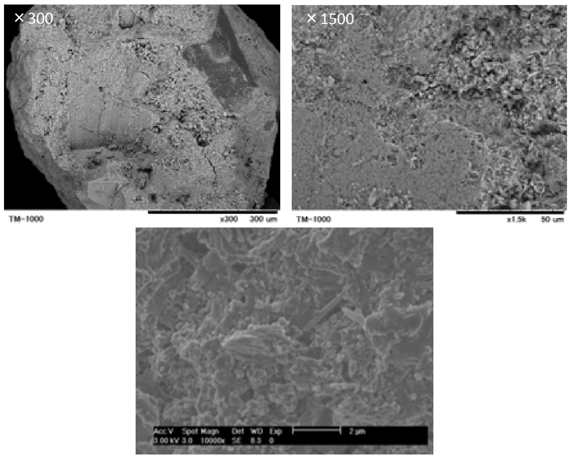

(a) Sintered products at 1,000 ºC

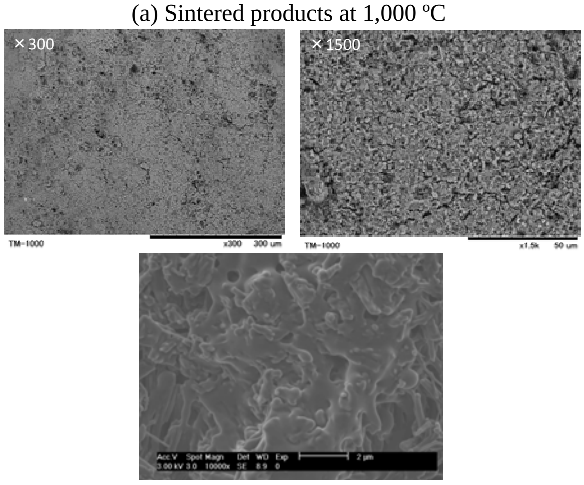

(b) Sintered products at 1,100 °C

Fig. 9 SEM images of sintered CsNiFC-SA-5.

compared to the original sample as shown in Fig. 3a. The XRD patterns of original CsNiFC-SA-5 and sintered products are shown in Fig. 10. The original composite consists of two phases of NiFC ($K_2[FeNi(CN)_6]$) loaded and mordenite matrices. After sintering, these phases were thermally decomposed, and only SiO_2 (Quartz) phase, a coexisting mineral in natural mordenite, was detected. The elemental mapping of Si, Al and Cs in sintered products at 1,000 ºC is shown in Fig. 11. The distribution of Cs was uniform in the sintered products, and the Cs content for sintered products at 1,000 ºC and 1,100 ºC was estimated to be 25.8 wt% and 21.4 wt% by WDS analysis, respectively.

3.6 *Surface Morphology and Distribution of Cs for Sintered CsNiFC-A51J*

The surface morphology, phase transformation and distribution of Cs for sintered CsNiFC-A51J are examined by instrumental analyses (SEM, XRD, WDS). Fig. 12 show the SEM images of sintered products. The surface is seen to be porous and begins to melt. Especially, some Cs-concentrated spots are observed on the surface of sintered products at 1,100 ºC. The XRD patterns of original CsNiFC-A-51J and sintered products are shown in Fig. 13. The original composite consists of two phases of NiFC loaded and zeolite A matrices. After sintering, the NiFC phase were thermally decomposed and zeolite A adsorbing

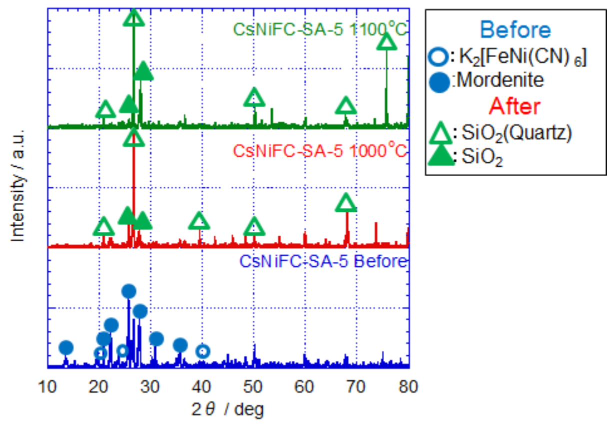

Fig. 10 XRD patterns of original and sintered products of CsNiFC-SA-5.

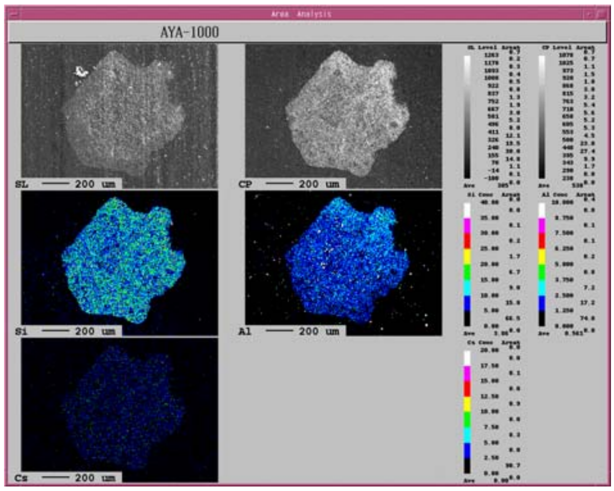

Fig. 11 Elemental mapping of Si, Al and Cs for sintered products of CsNiFC-SA-5 at 1,000 ºC.

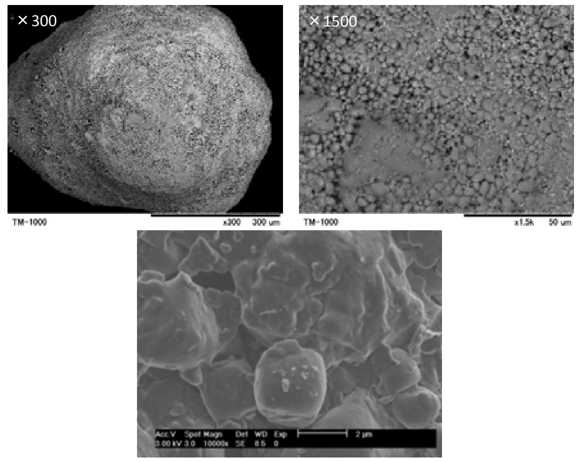

(a) Sintered products at 1,000 ºC

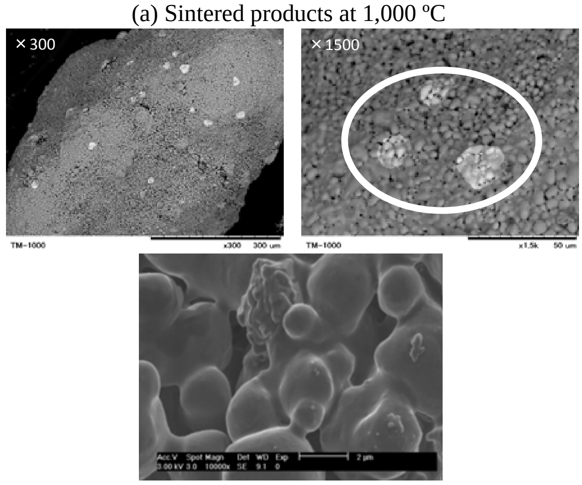

(b) Sintered products at 1,100 ºC

Fig. 12 SEM images of sintered CsNiFC-A51J.

Cs^+ converted to nepheline ($NaAlSiO_4$) and $CsAlSiO_4$ (Fig. 13). Fig. 14 shows the elemental mapping of Si, Al and Cs for the sintered products of CsNiFC-A51J

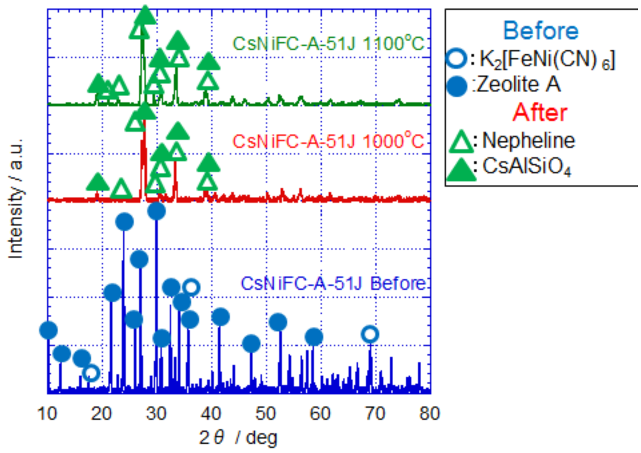

Fig. 13 XRD patterns of original and sintered products of CsNiFC-A51J.

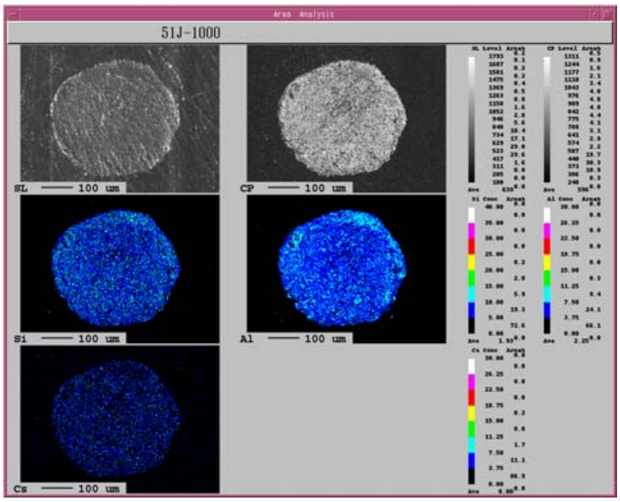

Fig. 14 Elemental mapping of Si, Al and Cs for sintered products of CsNiFC-A51J at 1,000 °C.

at 1,000 ºC. The distribution of Cs was uniform in the sintered products. As for Cs-concentrated spots on the relatively large Cs content was estimated by WDS; the Cs content for the spots and bulk phase was estimated surface (Fig. 12b), to be 28.1 and 14.2 wt%, respectively. These results suggest that the Cs-concentrated spots mainly consist of $CsAlSiO_4$ rich phase.

3.7 *Morphlogy and Distribution of Cs for Sintered CsNiFC-LSX*

The surface morphology, phase transformation and distribution of Cs for sintered CsNiFC-LSX are examined by instrumental analyses (SEM, XRD, WDS). Fig. 15 show the SEM images of sintered products. The surface is seen to be porous and begins to melt. Especially, many Cs-concentrated spots are observed on the surface of sintered products at 1,100 ºC compared to that for the sintered products of CsNiFC-A-51J. Fig. 16 shows the elemental mapping of Si, Al and Cs for the sintered products of CsNiFC-LSX at 1,000 ºC. The distribution of Cs was uniform in the sintered products. As for the Cs-concentrated spots on the surface (Fig. 15b), relatively large Cs content was estimated by WDS (Fig. 17); the Cs content for the spots was estimated to be 43.1 wt%. The formation of Cs-concentrated spots is related to the lowering of Cs immobilization ratio, and the immobilization of Cs can be enhanced in the case of amorphous phase such as the sintered products of natural mordenite (SA-5). The stable solidification of insoluble ferrocyanides was thus accomplished by using the excellent Cs immobilization abilities of zeolites (Cs trapping and self-sintering abilities), and

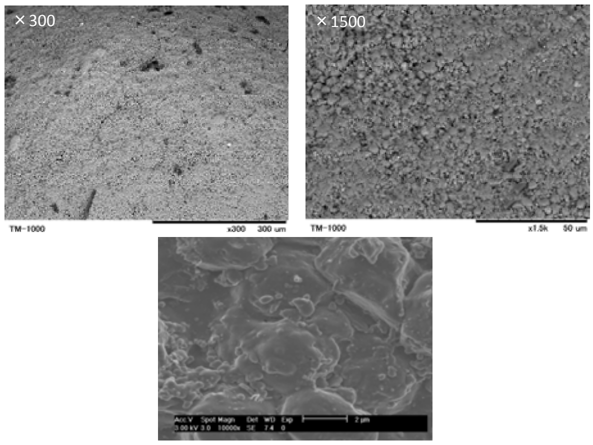

(a) Sintered products at 1,000 ºC

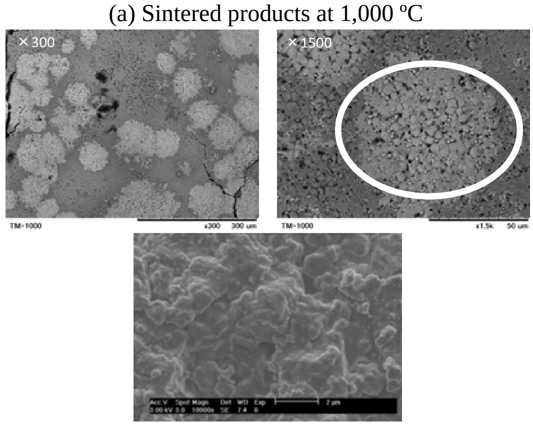

(b) Sintered products at 1,100 ºC

Fig. 15 SEM images of sintered CsNiFC-LSX.

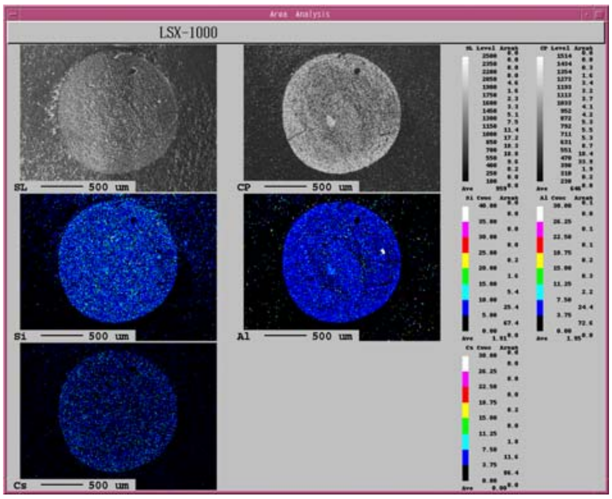

Fig. 16 Elemental mapping of Si, Al and Cs for sintered products of CsNiFC-LSX at 1,000 °C.

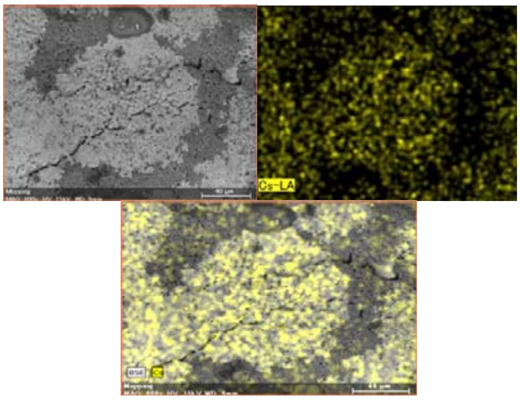

Fig. 17 Elemental mapping of Cs for Cs-concentrated spots of CsNiFC-LSX at 1,100 °C.

the immobilization mechanism and optimal conditions should be clarified in detail. This method can be applied to the stable solidification of the secondary solid wastes such as insoluble ferrocyanide sludge in Fukushima NPP-1.

4. Conclusions

The stable solidification of insoluble ferrocyanides was accomplished by utilizing the excellent immobilizing properties of zeolites such as gas trapping ability and self-sintering properties. The immobilization ratio of Cs for Co ferrocyanides saturated with Cs^+ ions (CsCoFC) was estimated to be less than 0.1% above 1,000 °C; the adsorbed Cs^+ ions were completely volatilized and CoFC had no Cs immobilization ability at high temperature. In contrast, Cs volatilization and cyanide evolution were considerably depressed for the sintered composites of insoluble ferrocyanide-loaded zeolites.

The immobilization ratio of Cs for CsNiFC-SA-5 sintered at 1,000 °C and 1,100 °C was estimated to be above 99% and 95%, respectively, indicating excellent immobilization ability of natural mordenites. Similar results were obtained in the case of sintered CsCoFC-modified chabazite. On the other hand, the immobilization ratio for sintered composites (CsNiFC-A51, CsNiFC-A51J and CsNiFC-LSX) tended to decrease markedly above 1,100 °C, and specific Cs-concentrated spots were observed on the surface of the sintered products. The order of immobilization ability for the composites was as follows:

NiFC-SA-5 > CoFC- modified chabazite >
NiFC-A-51 > NiFC-A51J > NiFC-LSX.

The immobilization of Cs is related to the surface morphology change and phase transformation of zeolite matrices, and the immobilization mechanism and optimal conditions should be clarified in detail. This method can be applied to the stable solidification of the secondary solid wastes such as insoluble ferrocyanide sludge in Fukushima NPP-1.

Acknowledgments

A part of this work was supported by JSPS KAKENHI Grant Number 24226021.

References

[1] Tokyo Electric Power Company, HP: Development of Technologies for the Processing and DIsposal of Radioactive Waste [Online], http://www.tepco.co.jp/en/nu/fukushima-np//fukushima-np/roadmap/images/m120314_03-e.pdf#.

[2] H. Mimura, I. Yamagishi, Characterization and adsorption properties of selective adsorbents for high decontamination of cesium, Journal of Ion Exchange 23 (1) (2012) 6-20.

[3] Tokyo Electric Power Company, HP: Roadmap towards Restoration form Accident at Fukushima Daiichi Nuclear Power Station [Online], http://www.tepco.co.jp/en/nu/fukushima-np/index-e.html

#an-chor00.

[4] H. Mimura, M. Kimura, K. Akiba, Y. Onodera, Preparation of Insoluble Ferrocyanide (KNiFC)-Loaded Silica Gels and Adsorption Properties for Cesium, Bulletin of the Institute for Advanced Materials Processing, Tohoku University, Japan, 1998.

[5] Y. Ikarashi, R.S. Masud, H. Mimura, E. Ishizaki, M. Matsukura, Development of stable solidification method for insoluble ferrocyanides-13170, in: Proc. of WM2013 Conference, Phoenix, Arizona USA , Feb. 24-28, 2013.

[6] H. Mimura, M. Kimura, K. Akiba, Y. Onodera, Ion-exchange properties of potassium nickel hexacyanoferrate (II) Compounds, Solvent Extr. Ion Exch. 16 (1998) 1013-1031.

[7] H. Mimura, M. Kimura, K. Akiba, Y. Onodera, Physicochemical properties of potassium nickel hexacyanoferrate(II)-loaded chabazites, Journal of Nuclear Science and Technology 35 (1998) 392-395.

[8] H. Mimura, M. Kimura, K. Akiba, Y. Onodera, Selective removal of cesium from sodium nitrate solutions by potassium nickel hexacyanoferrate-loaded chabazites, Separation Science and Technology 34 (1999) 17-28.

[9] H. Mimura, M. Kimura, K. Akiba, Y. Onodera, Separation of cesium and strontium by potassium nickel hexacyanoferrate(II)-loaded Zeolite, A Journal of Nuclear Science and Technology 36 (1999) 307-310.

Journal of Energy and Power Engineering 8 (2014) 470-475

Seismic Centrifuge Modelling of Offshore Wind Turbine with Tripod Foundation

Hao Yu, Xiangwu Zeng and Xuefei Wang

Department of Civil Engineering, Case Western Reserve University, Cleveland 44106, OH, USA

Received: August 31, 2013 / Accepted: November 11, 2013 / Published: March 31, 2014.

Abstract: The development of offshore wind energy is fast as it is clean, safe and of high efficiency. The harsh marine environment raises high demand on the foundation design of offshore wind turbine. Earthquake loading is one of the most significant factors which should be considered in the design phase. In this paper, a group of earthquake centrifuge tests were conducted on a physical wind turbine model with tripod foundation. The seismic responses of both wind turbine model and foundation soil were analyzed in terms of the recorded accelerations, pore water pressures, lateral displacements and settlements. The results were also compared with those measured in the previous research on mono-pile foundation. It is demonstrated that the tripod foundation can provide better resistance in the lateral displacement and structural settlement under earthquake loading.

Key words: Centrifuge test, offshore wind turbines, seismic responses, tripod foundation.

1. Introduction

Offshore wind energy has been developed fast in Europe since 1990s. It is estimated that, by the year 2020, at least 40,000 MW of power will be provided by offshore wind energy [1]. In recent years, offshore wind farms have been quickly becoming an attractive proposition worldwide due to the higher quality wind resources at sea, requirement of no land, and less impacts on communities. With the increasing demands on the amount of wind power generation, wind turbines are gradually pushed into deeper sea. The most common turbine size has increased from KW (kilowatt) scale to MW (megawatt) scale. The majority of the modern projects tend to use 5 MW turbines or even larger units.

In addition, the fact that quite a few offshore wind farms are located or planned to be built in seismic active regions has posted greater challenges to the foundation design of offshore wind turbines. Earthquake may cause significant damage to both foundations and wind towers, depending on the performance of constituted system of superstructures, foundations and surrounding soils. The soil of the seabed tends to be softened under earthquake loading which will adversely affect the structure stability. The seismic-induced structural vibration could also reduce the efficiency of power generation. So far, the knowledge about seismic resistance of offshore wind foundations is far from mature yet.

The commonly used foundations for offshore wind turbine include gravity base, monopile, and multipile. Some new types of foundations, such as suction bucket and floating tension leg platform, are also given significant consideration in practice in order to erect wind turbines in deeper water. Gravity base is a traditional foundation which provides stability against the loads transferred either from the superstructure or from the adjacent soil by their massive weight. However, gravity base is susceptible to the water depth and soil conditions underneath the foundation and usually needs pre-treatment of seabed during the installation. This type of foundation might result in

Corresponding author: Xiangwu Zeng, professor, research field: civil engineering. E-mail: xxz16@case.edu.

significant settlement under the earthquake loading. The monopole is considered as an easy and cost-effective foundation in supporting offshore wind turbine. The simply designed steel pipe is able to keep upper structure stable by penetrating into deep soil or even the bedrock. The single pile supporting structures tend to fail in the form of tilting or overturning as soil loses its lateral support during soil liquefaction.

In recent decades, quite a few of studies have been performed on the multipile foundation for offshore structures. McClelland [2] presented the effects of pile size selection on the stability of the deep foundation for offshore structures. Bea et al. [3] analyzed the structural reliability of platform with multipile foundations under extreme environment, i.e., hurricane and earthquake. In 2003, Randolph [4] built an analytical framework for the estimation of design parameters for pile foundations in both onshore and offshore projects. Dynamic model tests were conducted by Li et al. [5] on pile foundations, which provided a qualitative evaluation of the performance of offshore wind turbine. Brandenberg et al. [6] performed earthquake centrifuge tests in order to analyze the responses of group pile foundation during soil liquefaction. Some of recent seismic investigations were conducted on full-scale turbine models [7, 8]. However, the results still need to be calibrated and validated in the design phase.

Tripod foundation, a new adaption of the traditional mono-pile foundation, is the most favorable offshore foundation because of light weight and great stability. It is typically used in water more than 25 m deep, while the mono-pile seems to be the best solution in water depth of 10 m to 25 m and gravity base in less than 10 m [9]. The three legs of tripod are piled to the sea bed supporting the transition piece and turbine. The tripod foundation is thought to be able to limit the deflections of the wind towers [10]. Pile foundation is commonly used as platform foundation. Without sufficient field data and experiences, the seismic evaluation and design of offshore wind turbines with tripod foundation are commonly based on the criteria developed for oil platforms (API [11]; DIN 19901-6 [12]) or general building structures (FEMA450 [13]; IBC [14]; ASCE7-05 [15]). In addition, it may be helpful to refer to the physical experiments or numerical analysis on the seismic behavior of pile foundations for different superstructures [16-21].

In this study, the tripod foundation with three legs was modelled in a group of earthquake centrifuge tests. The earthquake loading was simulated by shaking table located on the geotechnical centrifuge and real earthquake excitation was induced. The seismic responses of both wind turbine and foundation soil were analyzed in terms of the recorded accelerations, pore water pressures, lateral displacements and settlements. Then, the foundation behavior was analyzed simultaneously together with the upper structure. The measured results were also compared with those of the monopile foundation model from previous studies. The conclusions of this study will be helpful in the phase of selecting and designing the offshore wind foundations in seismic areas.

2. Test Program

2.1 Test Facilities and Soil Deposit

The wind turbine model was tested on the geotechnical centrifuge at Case Western Reserve University (Fig. 1). The centrifuge payload capacity is 20 g-ton with a maximum acceleration of 200 g for static tests and 100 g for dynamic tests. The arm has a radius of 1.07 m while the dual platforms lie at a radius of 1.37 m during flight and can carry payloads of up to 182 kg. A hydraulic shaker designed by Team Corporation is mounted on the centrifuge platform. It can generate 1-D earthquake shaking in the flight. The details of the CWRU centrifuge were reported by Figueroa et al. [22]. A rigid container, with internal dimensions of 53.3 (length) × 24.1 (width) × 17.7 cm (height) was utilized in the tests. Different from the laminar container, the rigid side walls allow seismic

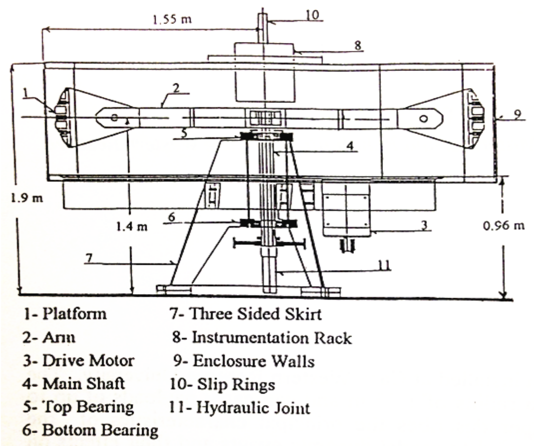

Fig. 1 CWRU centrifuge [22].

energy to be transmitted both from the base and from the side walls. Therefore, the obtained seismic responses of wind turbine models were relatively stronger and might be treated as the upper bound in the design phase.

The soil layer was constructed at 1 g (g = acceleration of gravity) by using the well graded Toyoura sand with D_{50} = 0.17 mm. The soil was uniformly poured from the height of 80 cm to keep the relative density at about 68%. The detailed soil property parameters are listed in Table 1. The thickness of soil deposit was 4.5 m (in prototype scale under 50 g). The saturation process was accomplished by using de-aired water and applying vacuum for at least 24 h. The water table was maintained 1.5 m above the ground surface to simulate the offshore condition.

2.2 Model Configuration and Test Procedures

The centrifuge model was designed by considering the dimensions and masses of prototype wind turbine and foundation. As shown in Fig. 2, the model contained three parts: tower head, wind tower and foundation. The tower head was simplified as a lumped mass, including the mass of the nacelle, generator, gearbox, etc. at the top of the tower rod with large slenderness ratio. This type of structure tended to induce large overturning moment under earthquake loading. Three legs of tripod foundation were modeled by using three aluminum rods integrated by a triangle

Table 1 Toyoura sand property parameters.

Parameter	Value
Particle shape	Angular
C_u	1.59
C_c	0.96
Specific gravity	2.65
D_{50}	0.17 mm
D_{10}	0.16 mm
Maximum void ratio	0.98
Minimum void ratio	0.60

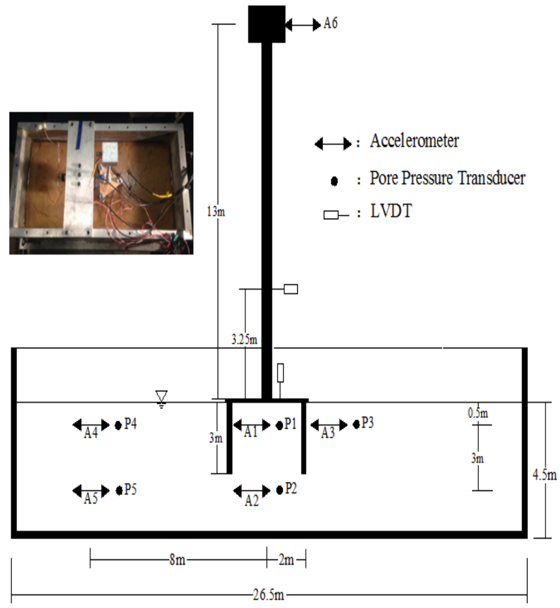

Fig. 2 Model configuration (in prototype unit).

transition piece and driven into the ground by 3 m. The details of each part were shown in Table 1.

The testing model was instrumented by ACC (accelerometers), PPT (pore pressure transducers) and LVDTs (linear variable differential Transducers). The detailed model profile as well as the instrument layout was depicted in Fig. 2 (the dimension was depicted in prototype model under 50 g). A 1-D synthetic earthquake (Fig. 3) was applied along the model base when the soil was consolidated under 50 g gravitational

Table 2 Wind turbine models in the centrifuge tests.

	Dimension (m)	Weight (t)
Tower head	1.75 × 1.75 × 1.25	10.6
Wind tower	L = 13; D = 0.5	6.25
Transition piece	Triangle shape L = 5	6.5
Foundation	L = 3; D = 0.5	1.6/each

(In prototype scale; L = length; D = diameter).

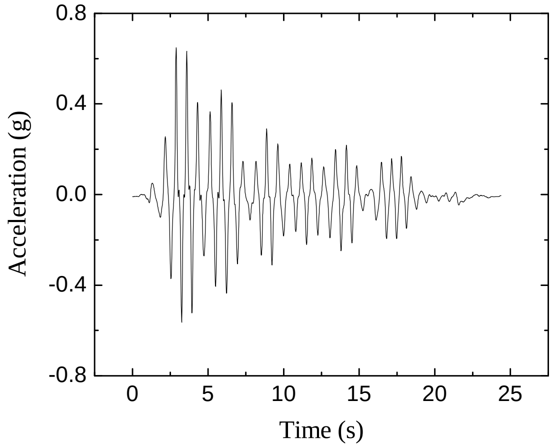

Fig. 3 Typical input acceleration.

field. In the meantime, acceleration and pore pressure time histories were recorded by the installed sensors.

The lateral displacement and settlements of structure were also measured by LVDTs. Centrifuge scaling laws [23] would be employed to evaluate the prototype behavior of the model.

3. Test Result Sand Analysis

3.1 Seismic Response of Soil

In the model tests, the accelerometers and pore pressure transducers were installed in pairs at different locations and depths in the soil. Due to the higher effective stress, quite low excess pore water pressure ratio was obtained at 3.5 m below the ground surface. Accordingly, soil strength remained almost the same under earthquake loading. The shape and magnitude of recorded time histories of acceleration by ACC2 and ACC5 were quite similar to the input motion (Fig. 4).

In the shallow depth of 0.5 m below the ground surface, the transducers were installed under the structure, outside the structure but adjacent to the tripod leg, and far away from the foundation, respectively. The recorded time histories of pore water pressure ratio are compared in Fig. 5. The solid horizontal line indicates that the liquefaction occurs as soon as the pore water pressure ratio is equal to 1. The lowest pore water pressure is generated right beneath the structure. The underlying soil was reinforced by the three legs of tripod foundation and increased confining

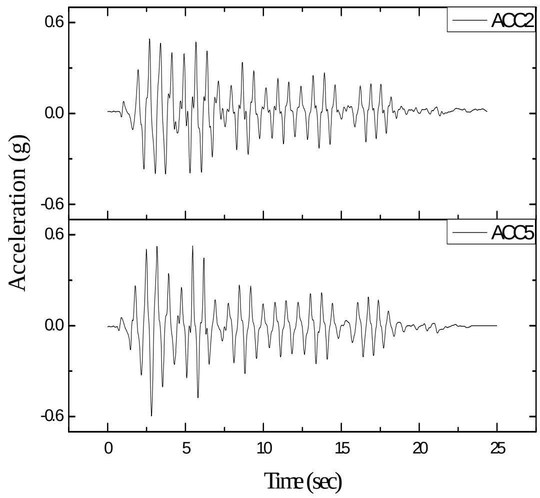

Fig. 4 Recorded time Histories of accelerations in the deep soil.

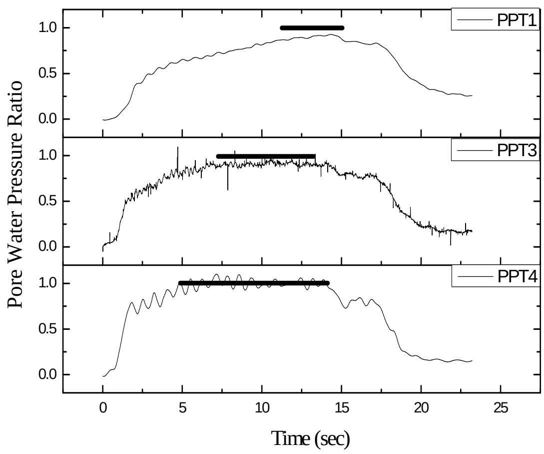

Fig. 5 Recorded time histories of pore pressure ratio in the saturated soil.

pressure. The retained soil strength can be seen from the recorded acceleration in ACC1 (Fig. 6). The soil adjacent to the leg of tripod foundation (ACC3) tended to be liquefied during the strong shaking, however, the softening process lasted quite a short time. The tripod foundation would support the loads both from the superstructure and the surrounding soil. Correspondingly, the seismic behaviors of soils under the structure and adjacent field would be influenced by the tripod foundation. However, the interaction between soil and foundation is quite difficult to measure in the physical experiments. The soil in the free field was not influenced by the structure or the container boundaries. The recorded pore pressure ratio by PPT4 (Fig. 5) indicates the occurrence of intense

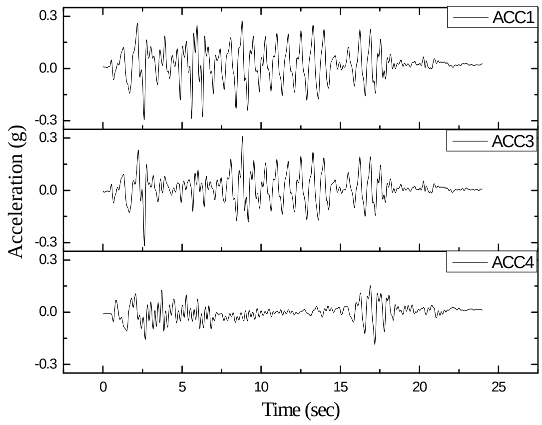

Fig. 6 Recorded time histories of accelerations in the soil.

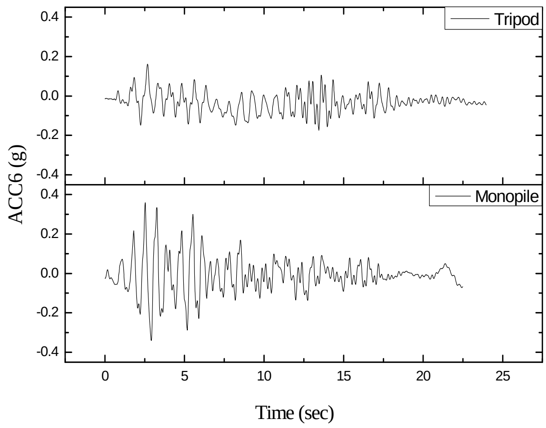

Fig. 7 Recorded time histories of acceleration in tripod model and mono-pile model.

liquefaction starting at the fifth second. The reduction of soil stiffness in ACC4 (Fig. 6) is quite apparent and lasts quite a long time. These different soil responses also illustrated the existence of soil-structure interaction.

3.2 Seismic Response of Wind Turbine

The accelerometer ACC6 was mounted on the tower head. As shown in Fig. 7, the maximum recorded acceleration during the earthquake is less than 0.2 g, which is just half of that measured in mono-pile foundation model in the previous study. The mono-pile model, which had exactly the same superstructure, failed by toppling during the strong shaking when it was penetrated half into the soil. Therefore, the tests were conducted with the mono-pile model standing on the base of container. According to the measurements by LVDTs installed horizontally at 3.25 m above the foundation (Fig. 2), the wind turbine model rotated only 0.6° after the earthquake, which was 50% smaller than the result by using mono-pile foundation (Table 2). The data demonstrates that the tripod foundation has a better resistance to the overturning moment under seismic loading. In addition, the tripod model sunk only 5 cm during the shaking which exhibited a strong resistance to seismic-induced settlement.

From geotechnical engineering point of view, the studies of offshore wind turbine should consider the wind turbine, foundation and surrounding soil in the surrounding area as a system. Appropriate stiffness and damping ratio of the integrated system should be selected in the design phase in order to avoid the damage caused by resonance. This aspect needs to be further studied by combining physical experiments and numerical analysis.

Table 2 Comparison of residual rotation and settlement under earthquake between tripod model and monopile model.

	Residual rotaton	Settlement
Tripod	0.6°	5 cm
Monopile	1.3°	n/a

4. Conclusions

In this paper, a group of earthquake centrifuge tests had been performed on offshore wind turbine model with tripod foundation in order to exam the soil behavior under earthquake loading and the provided structural stability by the tripod foundation. Based on the measured responses in both soil and structure, as well as the comparison with the precious work of mono-pile foundation, the testing results can be concluded as:

(1) The soil underlying the structure was reinforced by the tripod foundation;

(2) Comparing with the monopole foundation, tripod foundation was a better solution for mitigating lateral rotation under seismic loading;

(3) Tripod foundation exhibited good resistance to seismic-induced settlement;

(4) The measurement of interaction between soil and

tripod legs under earthquake was quite difficult in the physical tests. The numerical analysis is needed in the future study.

References

[1] Offshore Wind Technology Overview, AWS Truewind, LLC, Albany, NY, 2009.

[2] B. McClelland, Design of deep penetration piles for ocean structures, J. Geotech. Eng. Div. 100 (7) (1974) 709-747.

[3] R.G. Bea, Z. Jin, C. Valle, R. Ramos, Evaluation of reliability of platform pile foundations, J. Geotech. Geoenviron. Eng. 125 (1999) 696-704.

[4] M.F. Randolph, Science and empiricism in pile foundation design, Geotechnique 53 (10) (2003) 847-875.

[5] Z. Li, S.K. Haigh, M.D. Bolton, Centrifuge modeling of mono-pile under cyclic lateral loads, in: 7th International Conference on Physical Modeling in Geotechnics, Zurich, June 28-July 1, 2010.

[6] S.J. Brandenberg, R.W. Boulanger, B.L. Kutter, D. Chang, Static pushover analyses of pile groups in liquefied and laterally spreading ground in centrifuge tests, J. Geotech. Geoenviron. Eng. 133 (2007) 1055-1066.

[7] I. Prowell, M. Veletzos, A. Elgamal, J. Restrepo, Shake table test of a 65 kW wind turbine and computational simulation, in: 14th World Conference on Earthquake Engineering, Beijing, China, Oct. 12-17, 2008.

[8] I. Prowell, A. Elgamal, Fast simulation of wind turbine seismic response, in: ANCER (Asian-Pacific Network of Centers for Earthquake Engineering Research), Urbana-Champaign, IL, July 25-29, 2010.

[9] Ballast Nedam Offshore Energy, Offshore Foundations and Methods, EWEC, Nov. 2004.

[10] S. Malhotra, Design and construction considerations for offshore wind turbine foundations, in: ASME OMAE, USA, June 2007.

[11] API, Recommended Practice for Planning, Designing and Construction Fixed Offshore Platforms—Load and Resistance Factor Design, American Petroleum Institute, 1993.

[12] DIN EN ISO 19901-6, Petroleum and Natural Gas Industries—Specific Requirements for Offshore Structures, Part 6: Marine Operations, Beuth Verlag GmbH, Berlin, Germany, 2010.

[13] NEHRP Recommended Provisions for Seismic Regulations for New Buildings and Other Structures, Building Seismic Safety Council/National Institute of Building Sciences, Washington DC, 2004.

[14] International Code Council, ICC International Building Code, Country Club Hills, Il, USA, Jan. 1, 2006.

[15] American Society of Civil Engineers, Minimum Design Loads for Buildings and Other Structures, 1801 Alexander Bell Drive, Reston, Virginia, 2006.

[16] R.W. Boulanger, B.L. Kutter, S.J. Brandenberg, P. Singh, D. Chang, Pile Foundations in Liquefied and Laterally Spreading Ground during Earthquakes: Centrifuge Experiments & Analyses, Report, Center for Geotechnical Modeling, Department of Civil & Environmental Engineering, University of California, Davis, CA, 2003.

[17] S. Adhikari, S. Bhattacharya, Dynamic instability of pile-supported structures in liquefiable soils during earthquakes, Shock and Vibration 15 (6) (2008) 665-685.

[18] M.M. Ahmadi, M. Ehsani, Dynamic analysis of piles in sand based on soil-pile interaction, in: 14th World Conference on Earthquake Engineering, Beijing, China, Oct. 12-17, 2008.

[19] R. Dobry, T. Abdoun, Recent studies on seismic centrifuge modeling of liqefaction and its effect on deep foundations, SOAP-3, in: Proc. 4th Intl. Conf. on Recent Advances in Geotechnical Earthquake Engineering and Soil Dynamics, San Deigo, California, Mar. 26-31, 2001.

[20] K. Tokimatsu, H. Suzuki, M. Sato, Effects of inertial and kinematic interaction on seismic behavior of the pile with embedded foundation, Soil Dynamic and Earthquake Engineering 25 (2005) 753-762.

[21] N. Yoshida, H. Hamada, Damage to foundation piles and deformation pattern of ground due to liquefaction-induced permanent ground deformations, in: 3rd Japan-U.S. Workshop on Earthquake Resistant Design of Lifeline Facilities and Countermeasures for Soil Liquefaction, Buffalo, NY, 1991, pp. 147-161.

[22] J.L. Figueroa, A.S. Saada, H. Dief, Development of the geotechnical centrifuge at Case Western Reserve University, Centrifuge 98 (1) (1998) 3-8.

[23] A.N. Schofield, Cambridge geotechnical centrifuge operations, Geotechnique 30 (1980) 227-268.

Journal of Energy and Power Engineering 8 (2014) 476-486

Engineering Design Study on an Innovative Hydrokinetic Turbine with on Shore Foundation

Silvio Barbarelli[1], Gaetano Florio[1], Mario Amelio[1] , Nino Michele Scornaienchi[1], Antonino Cutrupi[2], Manuel Sanchez Blanco[2] and Giacomo Lo Zupone[2]

1. Department of Mechanical, Energy and Management Engineering, University of Calabria, Rende 87036, Italy

2. SintEnergy srl–Technest Incubator, University of Calabria, Rende 87036, Italy

Received: October 19, 2013 / Accepted: November 19, 2013 / Published: March 31, 2014.

Abstract: Tidal currents are a resource of great potentiality and not yet fully explored. Several efforts have been made to exploit these resources, but the costs associated to the deployment of tidal plants in marine environments are usually too high. The aim of this work is to present a system able to handle with the above mentioned problems, through the development of a particular hydrokinetic turbine design. In previous works, the authors described a basic turbine configuration achieving interesting performances, although some operational inconveniences were detected. Those problems have been existing so the solution should be optimized and redesigned. As a result, a new design of the turbine is proposed, consisting of a double rotor spinning in opposite directions in order to balance the induced mechanical torque. From preliminary evaluations related to the Messina Strait tidal cycles (Punta Pezzo site, RC, Italy), a single 12 m diameter turbine can supply a power of about 500 kW with a peak current speed of 3 m/s and deliver up to 450 MWh/year.

Key words: Tidal currents, kinetic turbine, double rotor configuration, equilibrium, pilot plant estimation.

1. Introduction

There are several ways to harness the energy from renewable sources like wind or water, mainly converting the kinetic flow energy into electrical power [1-8].

The main challenges are: high efficiency and low environmental impact, with reasonable costs. Due to their significant dimensions, the wind turbines have a relevant visual impact. In order to reduce this disadvantage, the offshore installations are more often implemented [5], but a good cost/benefits ratio is actually achieved only in shallow waters, not too far from the coast.

A convenient alternative is to shift the attention from wind to water, in order to take advantage of the higher fluid density allowing higher power outputs with smaller size turbines.

These turbines can be interesting for a number of reasons:

- Lower visual impact, since they are installed underwater and just buoys and/or floating structures are visible, also to ensure a safe navigation;
- Reduced risk for fauna: the low rotational speed and number of blades, together with large diameters, allow the fishes and marine species to pass through;
- Predictability of tidal currents speeds and ranges (seasonal intensity and directions) are easy and definitely available, unlike the wind resources;
- Exploitation of the sea energy resource, due to its predictability, may provide an electrical output of better quality, as to be able to balance against the irregularity of wind power.

In literature many examples of marine turbines are present. To date, these turbines are yet under investigation [6] mainly by fluid dynamic calculations

Corresponding author: Silvio Barbarelli, researcher, research fields: hydraulic pumps and turbines, oil dynamic pumps, compressible fluid turbines, marine turbines. E-mail: silvio.barbarelli@unical.it.

and modeling. The state of the art in this field is today at an experimental stage and only a few devices have been assembled and tested in real conditions.

The main challenges are to improve their efficiency and reduce the costs. For the first goal, each solution, depending on the turbine type (horizontal or vertical axis) or geometry (Coiro et al. [7], Kiho et al. [8]) chosen, could be optimized by the theoretical efforts described above and by the possible test in appropriate scale.

The second goal is harder to achieve: the installation of traditional off-shore devices is considerably expensive, time consuming and requires high skilled personnel. The installation of on-shore systems is significantly cheaper, simpler and faster.

In previous works [9-11], a turbine moored to the coast by a steel rope was introduced. Its peculiarity was the use of a deflector which reduces the various hydrodynamic forces involved into a single tensile stress along the rope. Such machine was useful for sites with right bathymetric profile, and high current speeds. Many sites around the world are characterized by the presence of water currents with velocities greater than 3 m/s [3, 4]. The proposed installation is however intended for working at Punta Pezzo, in the Messina Strait.

This paper presented in the European seminar "OWEMES 2012" [12], a further development of this machine is described involving a different torque balancing system together with a visual impact reduction.

2. Single Rotor Tidal Machine: Operating Principle

In previous works [9-11], an innovative tidal machine, able to operate in a power plant whose foundation was designed directly on the coast, has been set up. In the two following sections the main steps summarizing the machine characteristics and its design procedure will be deployed.

2.1 Description of the System

The system has been set up in a simple way considering the possibility to operate with a turbine moored to the coast by a steel rope.

Figs. 1 and 2 show the main views of the single rotor machine. It is moored to the shore by a tensile cable led by a rigid rod. The equilibrium is ensured by a deflector connected to the stator. The forces acting on the deflector (L_r lift and D_r drag) and (T) due to the rotation of the turbine combine in a resultant that tightens the rope (Fig. 1).

Fig. 2 shows the overall machine design (frontal & side views). The torque acting on the turbine rotor is fully counterbalanced by the effect of a buoyant system. The buoyant system is connected to a floating structure which hosts the generator/alternator. The rotational motion is driven to the generating device by a drive shaft with a bevel pinion connected through a sprocket. In addition, a rigid frame (Fig. 2) has been implemented in order to connect the rope to the turbine vertical diameter and ensure the vertical equilibrium.

The turbine weight and the sustaining effect of the buoyant system produce a stabilizing momentum opposing to the one developed by the blades' thrust. The vertical deviation has been estimated in an angle of few degrees, which would not have significant effects on the energy conversion.

The system has been designed to work in sites where the current periodically changes direction. When a tide inversion occurs, a special device rewinds the rope, so that the turbine moves from position 1 (Fig. 3) to the positions 2 and 3 without changing the angle β_1: it allows the rod to rotate, so the turbine passes through the positions 4 and 5. Finally the rope is released, so the machine, passing to the position 6, moves to a new equilibrium in position 7, with an angle β_2.

2.1 Previous Results

In order to design machines able to provide hundreds of kW it is necessary to choose values of diameters between 10 m and 20 m and to ensure that the turbine works at variable rotational speeds and, then, at constant values of λ.

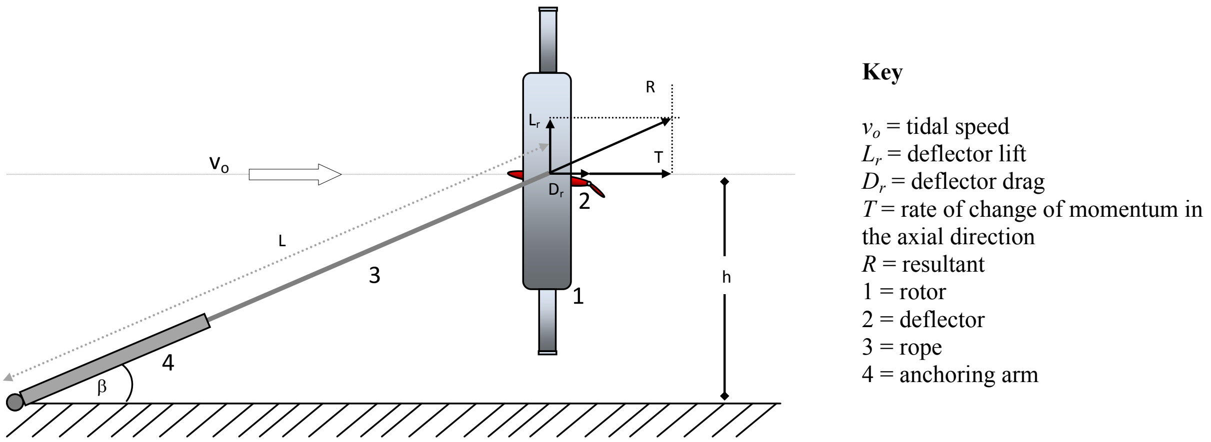

Fig. 1 Scheme of the prototype, showing the balance of forces.

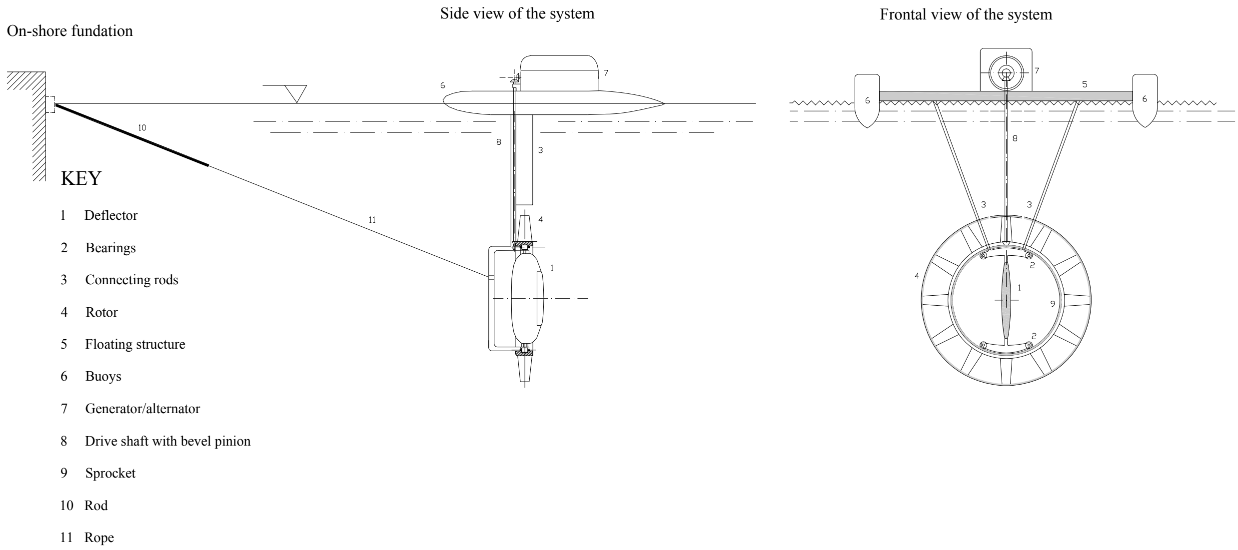

Fig. 2 Scheme of the prototype, showing side and frontal views.

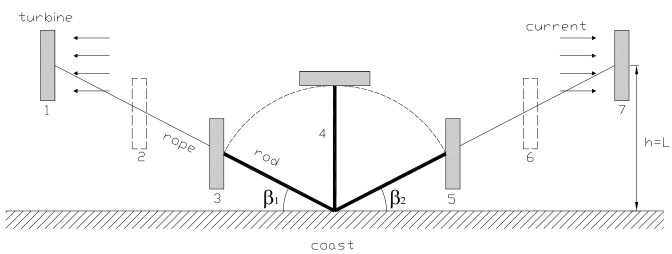

Fig. 3 Turbine equilibrium positions varying with the motion of tides.

According to the Betz theory [13-16] and assuming that the turbine always works at its best operating condition—input (v) and output (v_2) speed equal respectively to 2/3 and 1/3 of the unaltered flow velocity (v_o)—the forces mentioned in Section 2.1 can be calculated through the following equations:

$$T = \rho A_{rot} v(v - v_2) = \frac{4}{9}\rho A_{rot} v_o^2 \tag{1}$$

$$D_r = \frac{1}{2}\rho C_D \left(\frac{2}{3}v_o\right)^2 A_{Defl} \tag{2}$$

$$L_r = \frac{1}{2}\rho C_L \left(\frac{2}{3}v_o\right)^2 A_{Defl} \tag{3}$$

In the previous equations, A_{Defl} indicates the deflector area, A_{rot} is the blade disc area, C_L is the lift coefficient, C_D is the drag coefficient and ρ is the density of the water.

The resultant R assumes the angle β with reference to the coast (Fig. 1). This angle characterizes the system because it never changes, but it depends only on geometrical parameters.

The equilibrium equation of the moments with respect to the hinge, taking into account the length of the rope L, is given by:

$$(T + D_r)L \sin(\beta) = L_r L \cos(\beta) \quad (4)$$

Through Eqs. (1)-(3), the equilibrium equation becomes:

$$\left[\frac{4}{9}\rho A_{rot} v_o^2 + \frac{1}{2}\rho C_D \left(\frac{2}{3}v_o\right)^2 A_{Defl}\right]\tan(\beta) = \frac{1}{2}\rho C_L \left(\frac{2}{3}v_o\right)^2 A_{Defl} \quad (5)$$

Finally, introducing Eq. (5), the deflector efficiency E and developing the rotor area A_{rot}, the position angle β depends only on the geometrical parameters as shown in the next equation.

$$2\frac{\pi}{4}D_e^2\left(1 - \frac{D_i^2}{D_e^2}\right)\tan(\beta) = C_L A_{Defl}\left(1 - \frac{\tan(\beta)}{E}\right) \quad (6)$$

The position angle β is an important design parameter since it allows to set up the turbine internal diameter (D_i), the disc area A_{rot} and then, together with other factors, the electrical power P_e of the turbine once the external diameter D_e, the electrical efficiency η_e, the mechanical efficiency η_m, the power coefficient C_p, are fixed in Eq. (7).

$$P_e = \eta_e \eta_m C_p(\lambda) A_{rot}(\beta)\rho\frac{v_o^3}{2} \quad (7)$$

The power curves, related to four different current velocities, of a turbine with an external diameter equal to 12 m and a C_p coefficient equal to 0.48 change with the β angle as shown in Fig. 4.

The optimal angle associated with the maximum power, is always 11° regardless of the considered velocity range.

The blades design defines the rotor geometry. For this purpose an appropriate blade profile, the value of the tip speed ratio λ and the number of blades z must be chosen. Once the latest parameters are set up, through

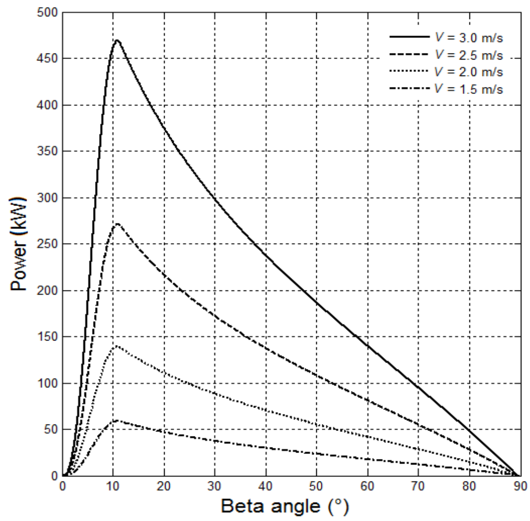

Fig. 4 Power curves.

the relations of optimal blade design in Eqs. (8)-(11), it is possible to obtain the variation along the radius r of two main parameters: the chord c and the angle of attack β_p [15, 16]:

$$c = \frac{1}{z}\cdot\frac{\pi D_e}{\lambda C_{lb}}\cdot\frac{8/9}{\sqrt{\frac{4}{9} + \lambda^2\mu^2\left[1 + \frac{2}{9\lambda^2\mu^2}\right]^2}} \quad (8)$$

$$\beta_p = \phi - \alpha_p \quad (9)$$

In the above equations, the parameter C_{lb} is the lift coefficient of the rotor blades, α_P is the rotor's optimal incidence angle while the factors ϕ and μ are expressed by the Eqs. (10) and (11):

$$\phi = arctg\left(\frac{2/3}{\lambda\mu\left(1 + \frac{2}{9\lambda^2\mu^2}\right)}\right) \quad (10)$$

$$\mu = \frac{2r}{D_e} \quad (11)$$

At this point it is necessary to choose the tip speed ratio λ value and the number of blades z.

For this purpose, the turbine application chart, shown in Fig. 5, Refs. [10, 11] is useful to calculate the best values of λ and z. The area surrounded by the black line is defined considering that:

(1) Very high values of λ indicate too thin blades unable to resist the stresses acting on them;

(2) Very low values of λ indicate an excessive overlapping of the blades profiles placed around the hub;

Fig. 5 Application chart.

(3) The number of blades z must be greater than 2;

(4) A higher number of blades z is profitable (and then allowed) only if it generates incomes higher than the costs.

The area shown in Fig. 5 is discretized in a finite number of cells by changing λ with steps of 0.5.

To calculate the system energy output, it is necessary to know the speed distribution of the streams in the considered site. According to the data supplied in 2008 [17], the hourly current speeds distribution for the Punta Pezzo site has been evaluated, as shown in Fig. 6.

Now it is possible to calculate cell by cell, the C_p [15] value and the $V_{startup}$ value [10, 11], depending on λ and z (in Figs. 7a and 7b).

For each class of velocity represented in Fig. 6, it is possible to calculate the cubic average speed, by considering only values greater than $V_{startup}$, and the turbine power as indicated in Eq. (7).

The energy output yearly produced for any given configuration (λ, z), can be calculated by summing the energy of all the velocity classes v_i displayed in Fig. 6:

$$\sum_{\text{year}} P(v_i)\Delta t_i = \frac{1}{2}\rho\eta_e\eta_m C_P(\lambda,z)\sum_{\text{year}} v_i^3\Delta t_i \qquad (12)$$

$$v_i \geq v_{startup}(\lambda, z)$$

The cell producing the best energy output (among those displayed in the application chart) fixes the design parameters λ and z.

3. Double Rotor Turbine Outline

The new machine (in scheme Fig. 8) is arranged by a circular stator implementing two rotors (inside and outside). The two rotors blades are designed in order to allow:

- the same rotation speed but in opposite directions;
- the same torque acting on each rotor.

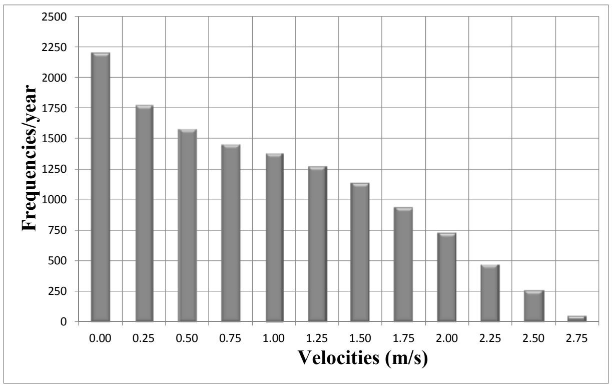

Fig. 6 Hourly currents speeds distribution.

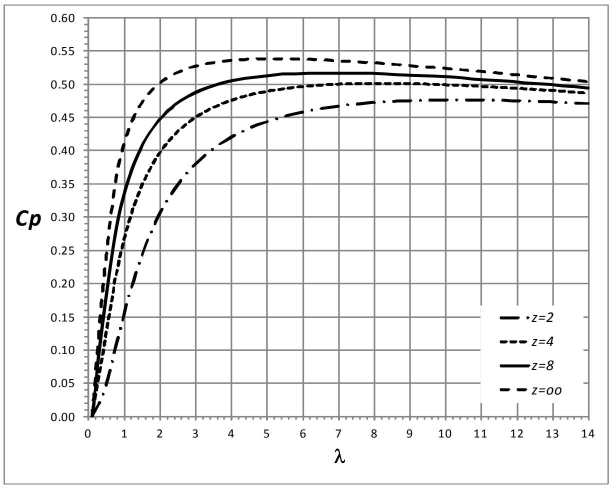

(a)

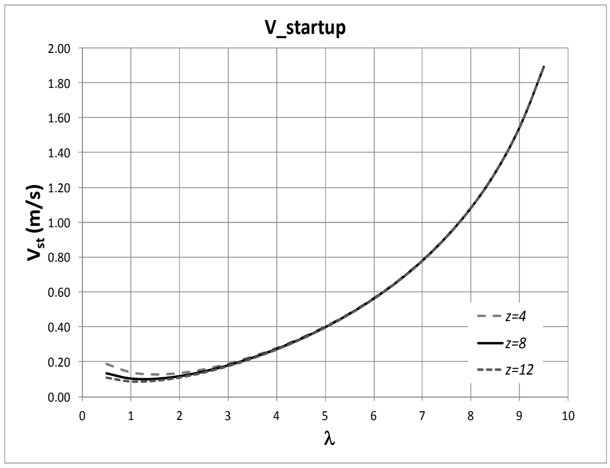

(b)

Fig. 7 (a) Cp curves; (b) Cut in velocities.

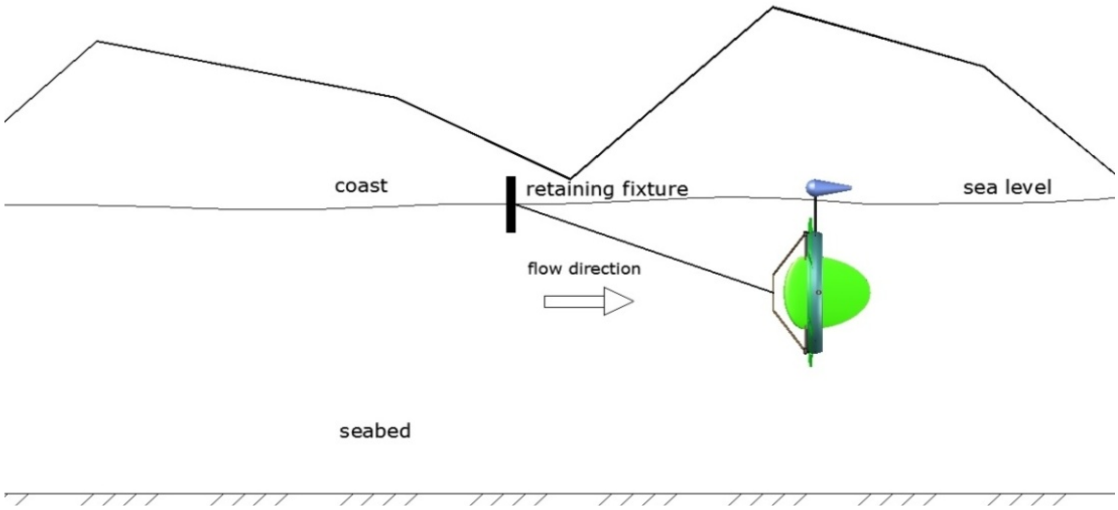

Fig. 8 Working scheme.

3.1 Architecture of the Machine

The two rotor implementation allows a balanced system working without any torsional effects. The compact stabilizer keeps the machine in vertical position at a constant level from the sea surface, as shown in Figs. 9 and 10.

Inside each rotor there are several permanent magnets, coupled with their respective coils located inside the stator, whose movement will generate the magnetic field needed for producing electricity (Fig. 11).

3.2 Improvements Compared to the Old Configuration

Several features have been developed and implemented for this new machine:

(1) The stabilizing system is now easier and lighter, without any wide floating structure (suspended by buoys), as shown in Fig. 2, but just a simple level stabilizer (Figs. 8 and 9);

(2) No mechanical devices are now needed to convert mechanical energy into electrical one: a permanent magnet generator is implemented directly on the machine (Fig. 10);

(3) No mechanical transmission, no pinions or gearboxes needed to transfer the motion for producing electrical energy, and, consequently, no mechanical losses are present. The electrical energy produced is driven to the inverter by cables.

4. Rotors Dimensioning

The calculus procedure is the same defined in the previous works [10, 11]. However, in this specific case the turbine is arranged by two rotors working together to achieve a better equilibrium. Each rotor is designed with the Eqs. (8)-(11) once the parameters λ and z are fixed. Therefore those parameters for both the rotors are to be considered.

4.1 Determination of the Tip Speed Ratios λ_1 and λ_2

In order to design the rotors it is necessary to fix some criteria. With the aim of having two electrical generators rotating at the same speed and considering the mechanical balance above described, the main criteria are as follows:

- The rotors must rotate at the same speed in opposite direction;
- The torques acting on the rotors must be the same.

Therefore the powers developed by the two rotors are the same. In the following equations the above criteria are deployed:

$$P_1 = P_2 \tag{13}$$

$$\frac{1}{2}\rho Cp\,(\lambda_1)\,A_1 v_0^3 = \frac{1}{2}\rho Cp\,(\lambda_2)\,A_2 v_0^3 \tag{14}$$

$$Cp\,(\lambda_1)\,A_1 = Cp\,(\lambda_2)\,A_2 \tag{15}$$

The power coefficient expression comes from the vortex cylinder theory combined with the Prandtl's theory [15, 16]:

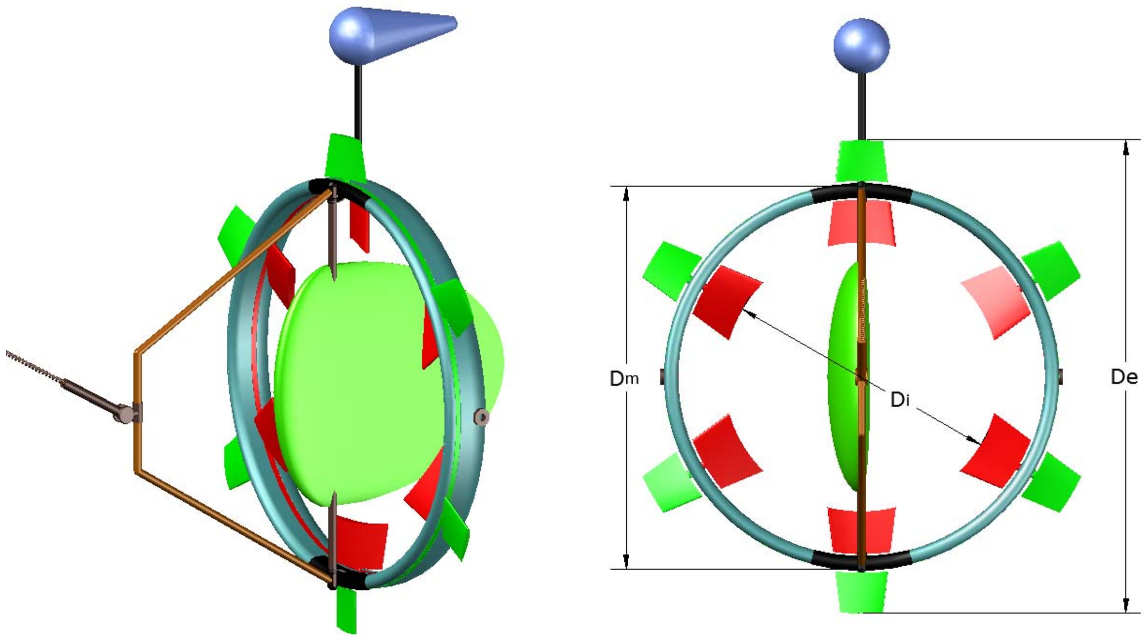

Fig. 9 Views of the new turbine.

1. stator
2. inside rotor
3. inside rotor blade
4. outside rotor
5. outside rotor blade
6. level stabilizer
7. level stabilizer support
8. retaining system stator connector
9. deflector support
10. retaining system connector
11. deflector
12. retaining to rope connector fixture

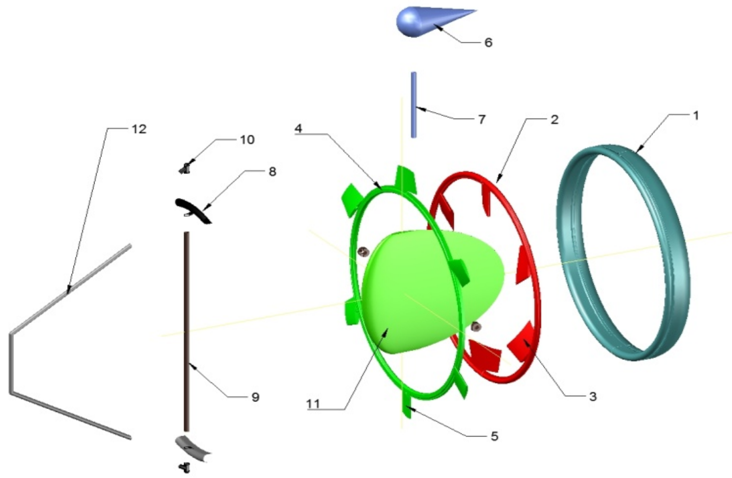

Fig. 10 Main parts of the turbine.

$$\left[\exp(-0.3538\cdot\lambda_1^{-1.2946})-\frac{\lambda_1}{E_P}\right]\left(1-\frac{0.93}{z_1\sqrt{\lambda_1^2+0.445}}\right)^2\cdot\frac{\pi\left(D_e^2-D_m^2\right)}{4}= \left[\exp(-0.3538\cdot\lambda_2^{-1.2946})-\frac{\lambda_2}{E_P}\right]\left(1-\frac{0.93}{z_2\sqrt{\lambda_2^2+0.445}}\right)^2\cdot\frac{\pi\left(D_m^2-D_i^2\right)}{4} \quad (16)$$

By combining Eqs. (15) and (16) and developing the blades areas A_1 and A_2:

$$\left[\exp(-0.3538\cdot\lambda_1^{-1.2946})-\frac{\lambda_1}{E_P}\right]\left(1-\frac{0.93}{z_1\sqrt{\lambda_1^2+0.445}}\right)^2\cdot\frac{\pi\left(D_e^2-D_m^2\right)}{4}= \left[\exp(-0.3538\cdot\lambda_2^{-1.2946})-\frac{\lambda_2}{E_P}\right]\left(1-\frac{0.93}{z_2\sqrt{\lambda_2^2+0.445}}\right)^2\cdot\frac{\pi\left(D_m^2-D_i^2\right)}{4} \quad (17)$$

Considering that:

$$\frac{\lambda_1}{\lambda_2}=\frac{\dfrac{u_1}{v_0}}{\dfrac{u_2}{v_0}}=\frac{\dfrac{\pi n D_e}{v_0}}{\dfrac{\pi n D_m}{v_0}}=\frac{D_e}{D_m} \quad (18)$$

or developing with respect to the intermediate diameter D_m:

$$D_m=\frac{\lambda_2}{\lambda_1}D_e \quad (19)$$

and taking into account the design diameter ratio:

$$\frac{D_i}{D_e}=r \quad (20)$$

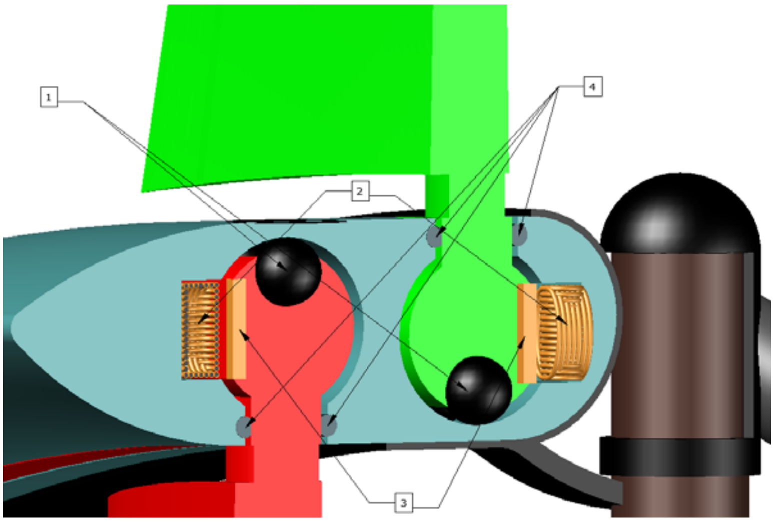

1. ball bearing;
2. coils;
3. permanent magnet;
4. o-ring;

Fig. 11 Permanent magnet generator.

or:

$$D_i = rD_e \tag{21}$$

the Eq. (17) becomes:

$$\left[\exp(-0.3538\cdot\lambda_1^{-1.2946})-\frac{\lambda_1}{E_P}\right]\left(1-\frac{0.93}{z_1\sqrt{\lambda_1^2+0.445}}\right)^2\cdot\frac{\pi D_e^2\left(1-\frac{\lambda_2^2}{\lambda_1^2}\right)}{4}= \tag{22}$$

$$\left[\exp(-0.3538\cdot\lambda_2^{-1.2946})-\frac{\lambda_2}{E_P}\right]\left(1-\frac{0.93}{z_2\sqrt{\lambda_2^2+0.445}}\right)^2\cdot\frac{\pi D_e^2\left(\frac{\lambda_2^2}{\lambda_1^2}-r^2\right)}{4}$$

Once the value of λ_1 (external rotor), the blades number z_1 and z_2, the external diameter D_e, the internal diameter D_i and thus the ratio r are fixed, through the last equation it is possible to calculate the value of λ_2 (internal rotor).

The couple of values of λ, z, through the Eqs. (8)-(11), determines the design of the blades for each rotor.

The input of the design procedure is then: the tip speed ratio of the external rotor λ_1, the number of blade z of each rotor (normally chosen z_1=z_2), the external diameter D_e, the diameter ratio r which depends on the position angle β.

The external diameter D_e is a free parameter: it is chosen according to the possibility to install the turbine near the coast in deep waters.

For the choice of the internal diameter it is necessary to calculate the power curves shown in Fig. 4: the best power implies an optimal position angle β and then an optimal diameter ratio D_i/D_e in Eq. (6).

Finally on the application chart of the double rotor machine it is possible to look for the cell to produce the maximum energy output in order to determine the blade design parameters (λ, z).

5. Results

The turbine design starts from the choice of the parameters (λ, z) on the application chart (Fig. 12).

The above mentioned constrains (geometric, structural and economic) cancel the inadmissible configurations (λ, z).

In this chart [18], the geometric constrain is fixed by considering that:

- The chord variation occurs without excessive gradient between the blades tip related to the internal rotor and the blades hub related to the external rotor;
- Only a difference of 0.3 m between the two chords above can be allowed.

The structural constraint defines a knock out area for all configurations (λ, z) inducing stresses on the blades higher than the admissible limits for a given material.

The economic constraint is deduced by evaluating if the costs increase required for producing one more blade, involving a higher energy output, is covered by higher incomes.

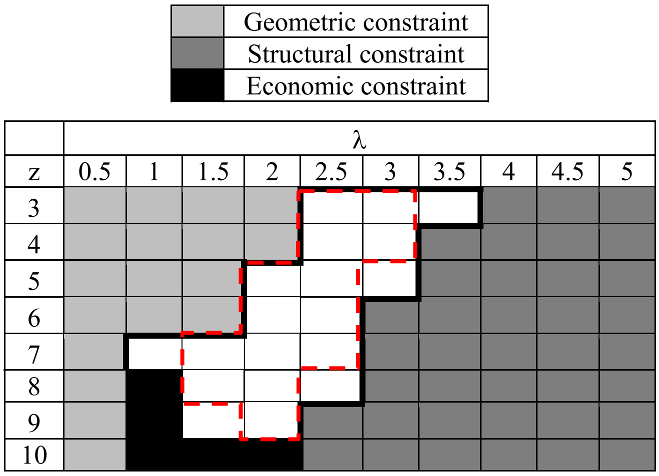

Fig. 12 Application chart double rotor turbine.

The chart is drawn up by considering the operating cells of both rotors. The black lines surround the white cells of the external rotor while the dashed gray lines surround the white cells of the internal rotor (Fig. 12). It is necessary to determine the best energy output among the cells pertinent to the internal rotor and among the cells pertinent to the external rotor.

The energy output is calculated cell by cell by integrating in a year the value of the power $P(v)$ relative to the speed ranges of the considered site:

$$E(\lambda, z) = \int_{year} P(v)dt \qquad v \geq v_{startup} \qquad (23)$$

The tidal velocities change with the time t according to the following harmonic series [17]:

$$V(t) = A_1 sen\omega_1 t + A_2 sen\omega_2 t + A_3 sen\omega_3 t + A_4 sen\omega_4 t + A_5 sen\omega_5 t + A_6 sen\omega_6 t + A_7 sen\omega_7 t + A_8 sen\omega_8 t \qquad (24)$$

where, the values A_i and ω_i depend on the chosen site. The calculus of the integrate (23) is done by considering values of velocity greater than the turbine startup velocities which depend on the values (λ, z) as shown in Fig. 7.

Fig. 13 shows the energy output level curves obtained for the Calabrian site of Punta Pezzo, located in the Messina Strait. Each curve represents a specific energy level per unit of blade area. The curves are useful to point out the best values (λ_1, z_1) for the external rotor.

Obviously the value of λ_2 (internal rotor) depends on the value of λ_1 (external rotor) according to the Eq. (22). Then, by imposing the same number of blades ($z_1 = z_2$), it is possible to determine the optimal energy output of the whole machine.

In Fig. 13, these values are highlighted. The best value of λ_1 (external rotor) is equal to 2.5 and the best number of blade z_1 is equal to 7. The energy output related for this configuration is 5,996 kWh/m^2. Therefore the values for the internal rotor are: $\lambda_2 = 2$, $z_2 = 7$ with an energy output of 5,685 kWh/m^2.

Once the value of C_p is known, regarding to the best configuration above calculated, it is possible to draw the power curves by changing the position angle β.

Fig. 14 shows the power curves of the two rotors (internal and external) by considering an overall turbine dimension of 12 m. The area of each rotor is calculated by estimating the intermediate and internal diameter according to Eqs. (19) and (21).

In this last figure it is possible to see that the maximum value, corresponding to a power of 430 kW, is obtained for a β equal to 11°. The optimal value of β allows to calculate the diameter ratio r, and then the internal diameter D_i and the value of each disc area. Table 1 reports the main parameters related to the turbine focused in this work.

The plant to be installed with the parameters above is able to produce 464,000 kWh/year with an economical revenue of 150,000 €/year. By considering an initial investment of 700,000 € the payback time is equal to 5 years.

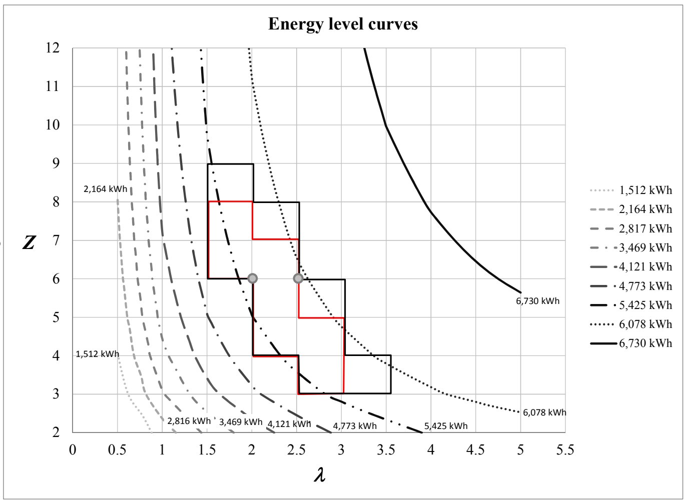

Fig. 13 Contour plot.

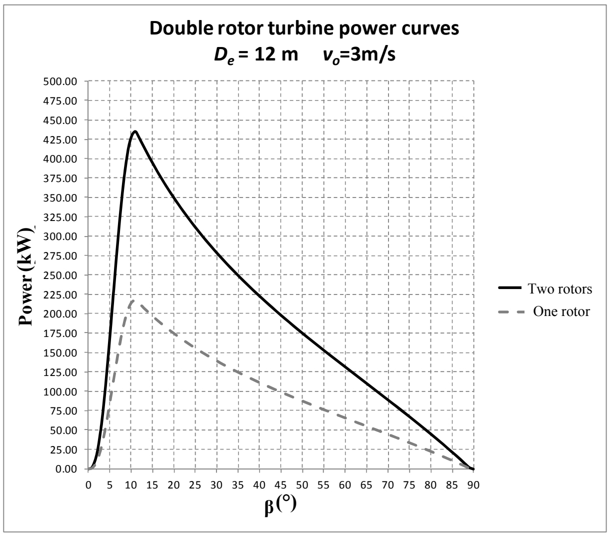

Fig. 14 Power curves.

Table 1 Design parameters.

parameter	Symbol	Value
External diameter	D_e	12.00 m
Intermediate diameter	D_m	9.73 m
Internal diameter	D_i	6.63 m
External rotor area	A_e	38.74 m^2
Internal rotor area	A_i	39.83 m^2
External rotor tip sped ratio	λ_1	2.5
Internal rotor tip speed ratio	λ_2	2
External rotor number of blades	z_1	7
Internal rotor number of blades	z_2	7
Position angle	β	11°

6. Conclusions

An important step in the development of a tidal kinetic machine prototype has been achieved. Unlike the first model the new turbine is lighter, easier to operate and it does not need an excessive maintenance. The operating principle is the same as the previous configuration: The turbine is moored to the shore by an extensible steel rope and it can reach an equilibrium condition thanks to the presence of a central deflector able to convert all the forces acting on the turbine into a single resultant force aligned with the rope.

The implementation of the two rotors is an innovative element that allows equilibrium in the vertical plane by counterbalancing any torsional effect.

In addition, the built-in permanent magnet generator eliminates further complexity. This way, the system becomes simpler, with even lower environmental impact and fewer economic resources for its implementation and maintenance required.

Further studies will be carried out to improve mechanical features such as bearings, seals, materials, connections and so on.

Anyway, the energetic evaluation relative to a pilot plant at the pier of Punta Pezzo (strait of Messina—Italy) does not substantially change referred to the one carried out in the previous works. The energy output is estimated around 464,000 kWh/year with annual incomes of 150,000 € and payback time of 5 years.

References

[1] M. Esteban, D. Leary, Current developments and future prospects of offshore wind and ocean energy, Applied Energy 90 (1) (2012) 128-136.

[2] M.J Khan, G. Bhuyan, M.T Iqbal, J.E Quaicoe, Hydrokinetic energy conversion systems and assessment of horizontal and vertical axis turbines for river and tidal applications: a technology status review, Applied Energy 86 (10) (2009) 1823-1835.

[3] F.O. Rourke, F. Boyle, A. Reynolds, Tidal energy update 2009, Applied Energy 87 (2) (2010) 398-409.

[4] D.P. Coiro, Clean energy with micro-wind and with marine and river current: innovative, technological and economical aspects, in: European Conference "POSIT.IVE Changes" in the framework of DG Education and Culture Community Action Programmed to Promote Active European Citizenship, Positano, Italy, Oct. 26-28, 2007.

[5] M.D. Esteban, J.J. Diez, J.S. López, V. Negro, Why offshore wind energy?, Renewable Energy 36 (2) (2011) 444-450.

[6] F.O. Rourke, F. Boyle, A. Reynolds, Marine current energy devices: Current status and possible future applications in Ireland, Renewable and Sustainable Energy Reviews 14 (3) (2010) 1026-1036.

[7] D.P. Coiro, F. Nicolosi, Numerical and experimental tests for the kobold turbine, in: Proceedings of Sinergy Symposium, Hangzhou, China, Nov. 24-27, 1998.

[8] S. Kiho, M. Shiono, K. Suzuki, The power generation from tidal currents by darrieus turbine, Renewable Energy 9 (1-4) (1996)1242-1245.

[9] M. Amelio, S. Barbarelli, G. Florio, N.M. Scornaienchi, A. Cutrupi, A. Interdonato, Innovative turbine recovering energy from tidal currents with central deflector and mechanical arm connected to the coast, in: Proceedings of "65° Congresso Nazionale ATI" Symposium, Cagliari, Italy, Sept. 13-17, 2010.

[10] M. Amelio, S. Barbarelli, G. Florio, N.M. Scornaienchi, A. Cutrupi, G. Minniti, M. Sanchez Blanco, Innovative tidal turbine with central deflector for the exploitation of river and sea currents in on-shore installations, Applied Energy 97 (2012) 944-955.

[11] M. Amelio, S. Barbarelli, G. Florio, N.M. Scornaienchi, A. Cutrupi, G. Minniti, et al., Innovative tidal turbine exploiting river and sea currents in on-shore installations, in: Proceedings of 66° Congresso Nazionale ATI, Italy, Sept. 5-9, 2011.

[12] M. Amelio, S. Barbarelli, G. Florio, N.M. Scornaienchi, A. Cutrupi, M. Sanchez Blanco, et al., Engineering design study of an innovative hydrokinetic turbine with on shore foundation, in: Proceedings of European Seminar OWEMES 2012 Offshore Wind and Other Marine Renewables Energies in Mediterranean and European Seas, Rome, Italy, Sept. 5-7, 2012.

[13] J. Anderson, Fundamental of Aerodynamics, McGraw Hill Higher Education, USA, 2006.

[14] I.H. Abbott., A.E.V. Doenhoff, Theory of Wing Sections: Including a Summary of Airfoil Data, Dover Books on Physics, the McGraw Hill Book Company, Inc., NY, USA, 1949.

[15] R. Pallabazzer, Wind Energy Conversion Systems, 1st ed., Rubbettino Editor, Italy, 2011, p. 116.

[16] T. Burton, D. sharpe, N. Jenkins, E. Bossanyi, Wind Energy Handbook, 1st ed., John Wiley & Sons, Ltd, 2001.

[17] Tide Tables, Hydrographic Institute of the Navy, 2008, editorial office, Genoa, Italy, 2007.

[18] R. Osso, Study of a tidal stream generator with contra-rotating double turbine, Dr. Thesis, Department of Mechanical, Energetic and Management Engineering, University of Calabria, Italy, Feb. 2013.

Journal of Energy and Power Engineering 8 (2014) 487-494

Assessment of the Wind Field in the East Coast Algerian Regions for the Installation of Wind Farms

Abdelouaheb Benretem, Dalila Khafa and Naziha Zerari

Electromechanical Systems Laboratory, Badji-Mokhtar Annaba University, Annaba 23000, Algeria

Received: September 04, 2013 / Accepted: November 04, 2013 / Published: March 31, 2014.

Abstract: The available electricity generated by a wind power generation system depends on mean wind speed, standard deviation of wind speed and the location of installation. Since year-to-year variation on annual mean wind speed is hard to predict, wind speed variations during a year can be well characterized in terms of a probability distribution function, as well Weibull distribution has been one of the most commonly used, accepted and recommended distribution to determine wind energy potential. In this study, the two Weibull parameters of the wind speed distribution function (the shape parameter k (dimensionless) and the scale parameter c (m/s)), were computed from the wind speed data for Algerian east coastal regions, recording over a 11-year period (1995-2005). It was found that the numerical values of both Weibull parameters (k and c) vary over a wide range. The yearly values of k range from 1.20 to 1.94, while those of c are in the range from 4.31 to 1.94. To minimize the uncertainties of statistical calculation, a spatial representation indicating distribution and occurrence frequency the direction from which the wind comes, appears a very primordial step. Over the whole valid data during the study period, the compass shows that there is no dominant direction marked. However, we can identify a preferred wind direction. The statistical results correspond to the analysis of the rose compass.

Key words: Wind energy, Weibull parameters, compass rose, statistical analysis.

1. Introduction

Renewable energy is abundant and its technologies are well-established to provide complete security of energy supply. It is now evident that renewable energy technologies play a strategic role in achieving the goals of sustainable economical development and environmental protection. With winds fairly constant all year and with availability of large amount of credit and other financial incentives, there is a growing trend for new wind energy installations in the coastal areas of the Algeria, it is has considerably high level of renewable energy resources that can be a part of the total energy network in the country [1].

In practice, it is very important to describe the variation of wind speeds for optimizing the design of the systems resulting in less energy generating costs.

Corresponding author: Abdelouaheb Benretem, professor, research fields: electromechanical system and renewable energy. E-mail: benretem_a@yahoo.fr.

To attract more and more investors to install new wind farms, conditions are created for a large scale source of renewable electric power generation in the regions. To get a clear assessment of the wind power potential in Algeria, it is necessary to make long meteorological observations in the area.

However, wind as a source of energy is not sufficient to provide continuous electricity because even in the best location wind is variable. If there is no wind blowing no energy can be generated. So, the amount of power that can be harvested from the wind will depend on wind frequency and wind direction (since wind turbines are most efficient when facing into the wind).

Among such observations, the wind speed is an important random variable which affects the most accurate results on the energy potential of the site. The wind speed in a given period may be represented by a probability density function. In recent years, the Weibull distribution has been one of the most widely

used and recommended tool to determine the potential of wind energy. Moreover, it is used as a benchmark to estimate the wind energy commercially viable.

In this study, the methodology that we implement for the calculation of wind power parameters is based on the study of meteorology over 11 years with a daily rate. At first glance weather given by power and direction of wind "Alger Airport" has a good coverage of observations over the territory, the regions concerned in this study is named: Annaba, Skikda, Jijel, Chlef and Oran are situated in east coast of Algeria. In order to find a suitable location it is necessary to know spatial distribution of wind. For this reason and improved allocation data, frequencies of wind direction are presented in this work by a rose compass.

2. Temporal and Spatial Wind Variation

The main objective of the wind data analysis is a clearer knowledge of the temporal and spatial variation.

Temporal variation includes:

- low frequency (annual variations and seasonal, monthly);
- medium frequency (changes daily and hourly);
- high frequency (changes to the second or higher frequency above 1 Hz) typical of wind turbulence.

Spatial variation: mainly the vertical variation of the field and wind directions.

3. Temporal Variability and Numerical Methods for Estimating Weibull Parameters

The wind speed is a random variable and to determine the wind potential of a region it is necessary to use statistical analysis [2-4].

This requires the existence of time series records of wind speed. Such records are the wind data. Based on the wind speed data collected, the Weibull distribution can be described as a probability density function and a cumulative distribution function, determined by the following equations [5, 6]:

$$f(v) = \frac{k}{c}\left(\frac{v}{c}\right)^{k-1} \exp\left[-\left(\frac{v}{c}\right)^{k}\right] \tag{1}$$

$$F(v) = \int_0^{-\infty} f(v)\,dv = 1 - \exp\left[-\left(\frac{v}{c}\right)^{k}\right] \tag{2}$$

where, k and c are the Weibull parameters and v is the wind speed, the k values range from 1.5 to 3.0 for most wind conditions. The Rayleigh distribution is a special case of the Weibull distribution in which the shape parameters are 2.0, for estimating the parameters of Weibull distribution many numerical methods are used.

3.1 Graphical Method

The graphical method is achieved through the cumulative distribution function. In this distribution method, the wind speed data are interpolated by a straight line, using the concept of least squares, the equation for this method can be represented by a double logarithmic transformation [7] as follows:

$$\ln\left\{-\ln\left[1-F(v)\right]\right\} = k\ln(v) - k\ln(c) \tag{3}$$

$$\bar{v} = c\Gamma\left(1+\frac{1}{k}\right) \tag{4}$$

The gamma function is:

$$\Gamma(x) = \int_0^{\infty} \exp(-t)t^{x-1}\,dt$$

3.2 Maximum Likelihood Method

The maximum likelihood estimation method is difficult to solve, since numerical iterations are needed to determine the parameters of the Weibull distribution.

In this method, the parameters k and c are determined according to the equations below [8, 9]:

$$k = n\left[\frac{\sum_{i=1}^{n} v_i^k \ln(v_i)}{\sum_{i=1}^{n} v_i^k}\right] \tag{5}$$

$$c = \left[\frac{1}{n}\sum_{i=1}^{n} v_i^k\right]^{\frac{1}{k}} \tag{6}$$

where, n is the number of observations performed and v_i is the wind speed measured at the interval i.

3.3 Moment Method

The moment method can be used as an alternative to the maximum likelihood method [10] and, in this case, the parameters k and c are determined by the following equations:

$$c = \bar{v} / \Gamma\left(1 + \frac{1}{k}\right) \tag{7}$$

$$\delta = c\left[\Gamma\left(1 + \frac{2}{k}\right) - \Gamma^2\left(1 + \frac{1}{k}\right)\right]^{\frac{1}{2}} \tag{8}$$

where, $\bar{v}$ and δ are the mean wind speed and the standard deviation of the observed data of the wind speed, respectively.

3.3 Empirical Method

The empirical method is considered a special case of the moment method, where the Weibull parameters k and c are given by the equations shown below [11]:

$$k = \left(\frac{\alpha}{\bar{\bar{V}}}\right)^{-1,086} \tag{9}$$

The scale parameter c is given by Eq. (7).

4. Spatial Variability

4.1 Vertical Wind Speed Variation

Very often, measuring wind speeds is taken at a different height at which wind turbines are installed. It is therefore necessary to determine a relationship between wind speeds varying heights, the formula expressing the speed gradient is logarithmic but normally approached by a potential form:

$$v_2 = v_1\left(\frac{Z_2}{Z_1}\right)^{\alpha} \tag{10}$$

The wind profile indicates the average wind speed based on the height Z_2 above the ground. v_1 is the reference speed at the height Z_1, and α is the empirical parameter of the law potential. This parameter varies on the same site 1/7 during days and 1/2 during the night, it takes the value of 0.2 according to IEC 2005 61400-1 [12].

4.2 Wind Direction

Wind roses are circular and graphical displays of wind speed, direction and frequency based on a simple compass rose. Wind direction is shown by the length of a line representing a number of wind collection events.

The length of the line from the outer circle to the center of the rose shows the percentage of total wind measurements where the wind blows from that compass direction-incorporating both frequency and direction data. Wind speeds are shown using a number of different techniques.

Indeed, during the wind turbines installation on a site, it is necessary to know where the principal directions of the wind is in order to limit the negative interaction between several wind and obstacles. Therefore, the wind roses give more information.

5. Topography

The topographic study over the years “1995-2005” has given practical information on meteorological conditions and specific wind condition of various cities of Algeria; we are interested only in this work on Algerian east coast regions such as “Annaba, Skikda, Jijel, Alger, Chlef, and Oran”.

6. Results and Discussion

6.1 Parameters Weibull Results

Figs. 1-6 show the Weilbull distribution, described by its probability function, versus the mean wind speed, for data collected on an annual basis from 1995 to 2005, for the cities of East Cost of Algeria, based on parameters calculated using the Weibull methods presented in previous section.

The annual parameters Weibull k and c as well as the standard deviation data observed in the all cities over 11 years are shown in Table 1.

Furthermore, from Figs. 1-6 it is possible to verify how the curves representing the yearly Weibull probability density function, for each of the six cities “Annaba, Skikda, Jijel, Alger, Chlef, and Oran” along 10 years :1995 to 2005.

The probability density distribution shape develops the real data set around the average speed for small values of shape factor k, the Weilbull distribution is wide curve. However, for high values of shape factor k the data distribution is very narrow, and beyond k = 3 the distribution obeys a normal law.

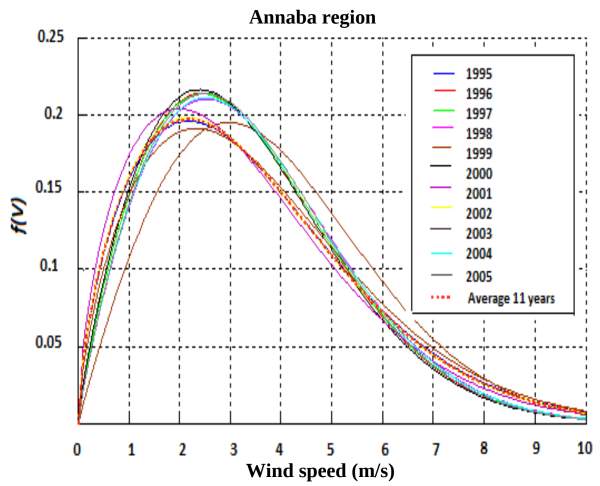

Fig. 1 The Weibull probability density of Annaba.

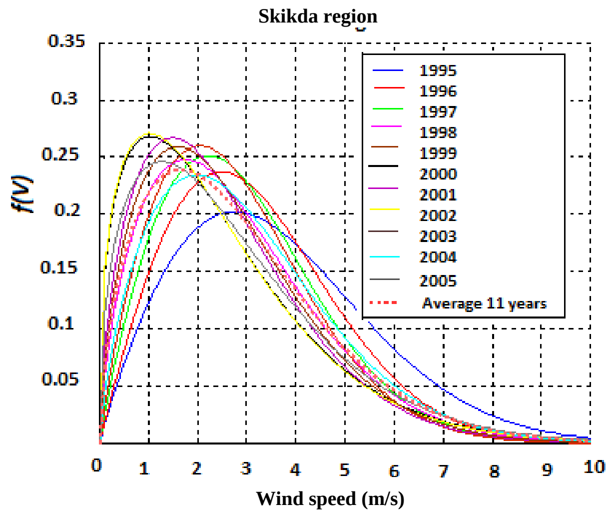

Fig. 2 The Weibull probability density of Skikda.

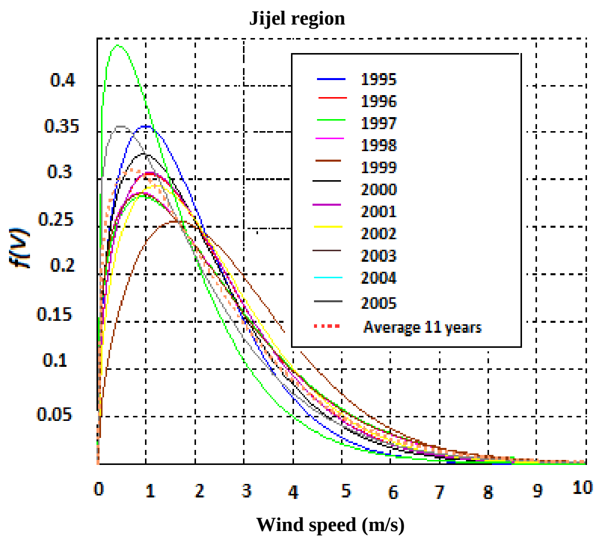

Fig. 3 The Weibull probability density of Jijel.

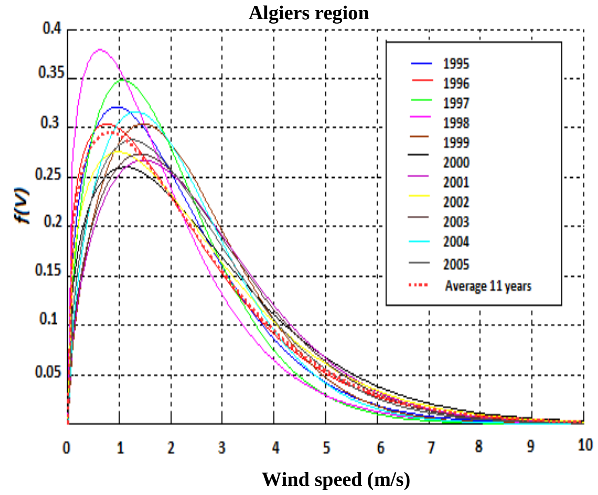

Fig. 4 The Weibull probability density of Algiers.

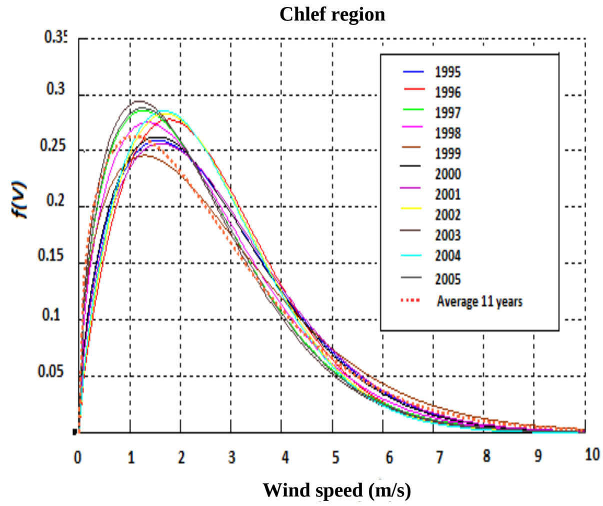

Fig. 5 The Weibull probability density of Chlef.

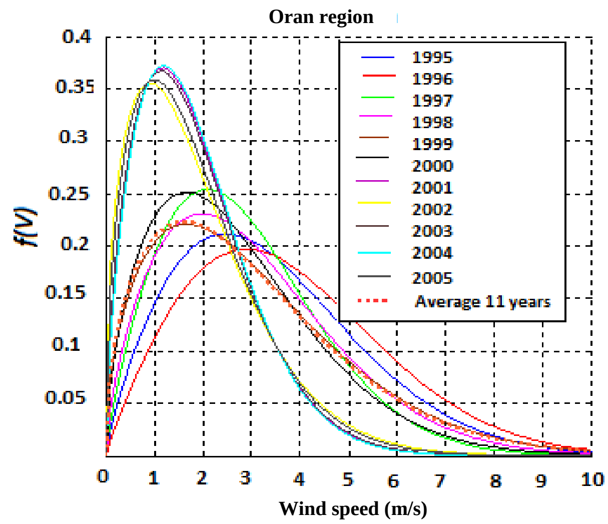

Fig. 6 The Weibull probability density of Oran.

Table 1 The coefficients values *k* and *c*.

Regions	Annaba		Skikda		Jijel		Algiers		Chlef		Oran	
	k	*c*	*k*	*c*	*k*	*c*	*k*	*c*	*k*	*c*	*k*	*c*
1995	1.63	3.91	1.89	4.09	1.48	2.08	1.41	2.29	1.59	2.93	1.82	3.83
1996	1.82	3.78	1.96	3.57	1.44	2.41	1.29	2.42	1.76	2.86	1.92	4.25
1997	1.82	3.79	1.89	3.29	1.33	2.60	1.53	2.15	1.51	2.61	1.84	3.21
1998	1.84	3.87	1.64	3.10	1.32	2.56	1.30	1.94	1.53	2.72	1.69	3.38
1999	1.94	4.31	1.84	3.13	1.61	2.97	1.66	2.54	1.43	3.00	1.52	3.39
2000	1.81	3.73	1.36	2.74	1.41	2.25	1.38	2.82	1.59	2.89	1.61	3.04
2001	1.59	3.72	1.57	2.83	1.45	2.40	1.56	2.82	1.61	2.97	1.64	2.08
2002	1.63	3.87	1.36	2.71	1.48	2.53	1.35	2.66	1.74	2.79	1.44	2.08
2003	1.66	4.04	1.60	2.94	1.32	2.57	1.55	2.75	1.49	2.53	1.61	2.08
2004	1.84	3.86	1.70	3.33	1.22	1.69	1.61	2.41	1.73	2.76	1.66	2.08
2005	1.85	3.82	1.42	2.99	1.20	2.11	1.50	2.59	1.51	2.59	1.50	2.08
Average	1.63	3.89	1.57	3.16	1.27	2.38	1.30	2.49	1.38	2.79	1.50	3.34

Generally the average wind speed is between 1.5 to 4 m/s for all the regions studied.

The average Weibull parameters estimation for 11 years (1995 to 2005), the shape factor in this case varies between 1 and 2. This is why there is a little wide distribution data around the average wind speed, which is between 1 m/s and 3.5 m/s.

6.1 Wind Compass Results

To improve knowledge idea of the wind speed distribution and directions, rose compasses were studied from meteorological data to the six regions mentioned previously.

The compass rose of Annaba region (Fig. 7) shows that wind directions are distributed on almost similarity in all regions and with equal percentages (Fig. 8), however the wind almost neglected in the direction north-west and south-east, with a calm wind 20.3% in the south-south.

The winds have the most frequent wind speed between 1 m/s and 6 m/s (55. 3% Occurrences), but these winds are 30% of the south side.

The annual compass rose of the Skikda region (Fig. 9) in the period (1990-2007) shows the prevailing wind direction is south-south and the second dominant direction is north-south, while other directions are neglected. All directions have a low speed varied between 1 m/s and 6 m/s. With higher wind speed, they

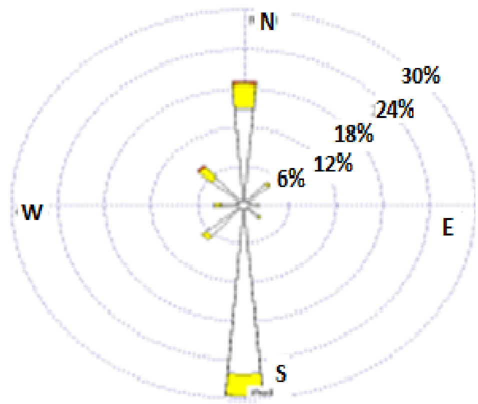

Fig. 7 Annaba compass rose.

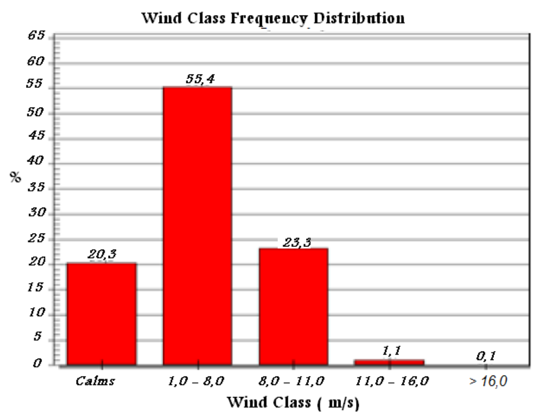

Fig. 8 Annaba wind class frequency distribution.

have a very low rate of occurrence (Fig. 10).

Figs. 11 and 12 show the compass rose speed and the percentage classes in the Jijel region. It was found that:

• The winds are the most frequent wind speed equal to 1 m/s and 6 m/s (40. 3% of occurrences) and between

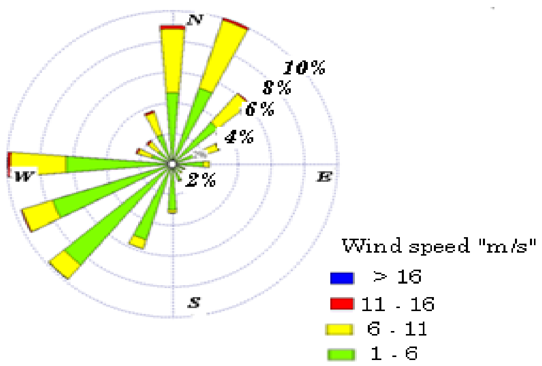

Fig. 9 Skikda compass rose.

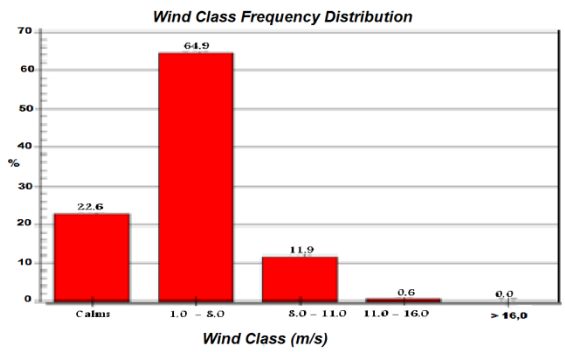

Fig. 10 Skikda wind class frequency distribution.

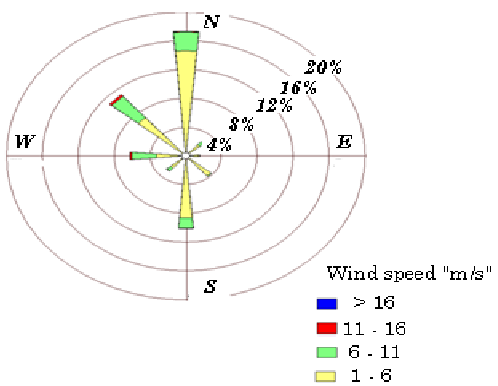

Fig. 11 Jijel compass rose.

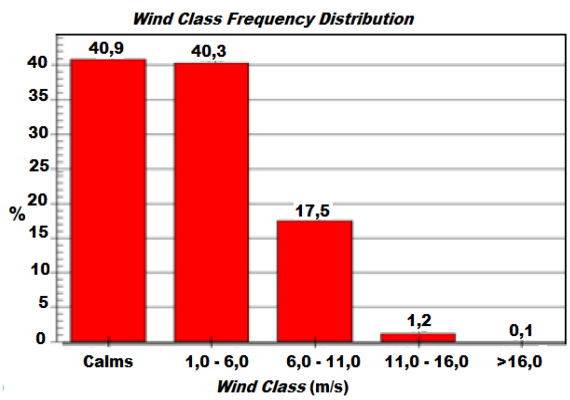

Fig. 12 Jijel wind class frequency distribution.

6 m/s and 11 m/s (17.5% of the occurrences), these winds are from the north-west;

• The calm winds have a percentage of 40.9% in all directions;

• Strong winds (speed exceeding 16 m/s) were not observed during this period.

Figs. 13 and 14 show the compass rose speed and the percentage classes in Alger region. It was found that:

The winds are the most frequent wind speed equal to 1 m/s and 6 m/s (40. 3% of occurrences) and between 6 and 11 m/s (17.5% of the occurrences). These winds are mostly from the south-west.

• The calm winds have a percentage of 40.9% in all directions;

• Strong winds (speed exceeding 16 m/s) were not observed during this period.

The both histograms of wind class frequency distribution (of Jijel and Algiers) have the same distribution.

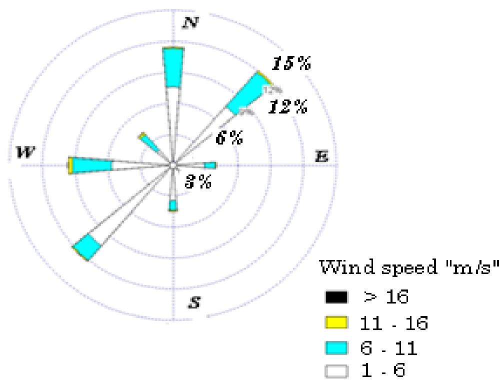

Fig. 13 Algiers compass rose.

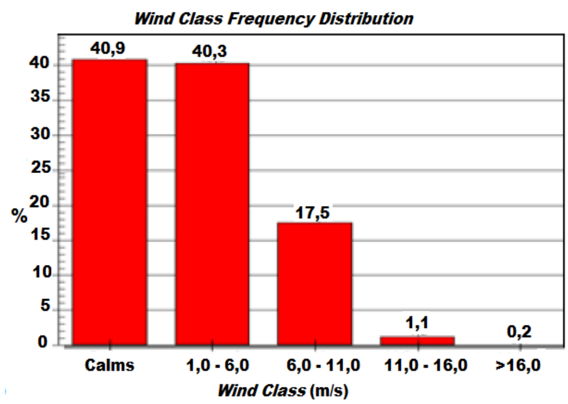

Fig. 14 Algiers wind class frequency distribution.

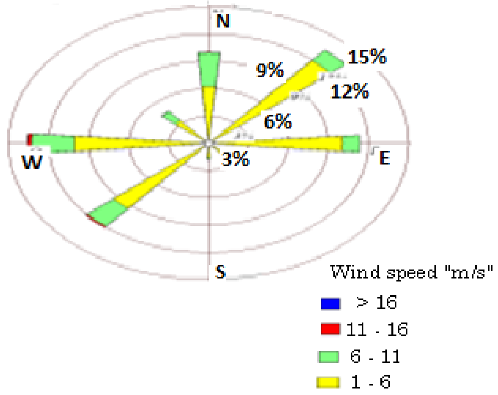

Fig. 15 Chlef compass rose.

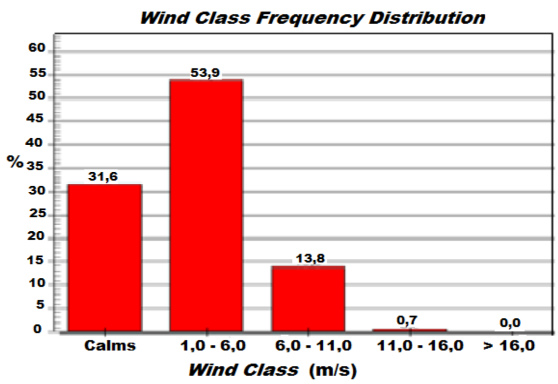

Fig. 16 Chlef wind class frequency distribution.

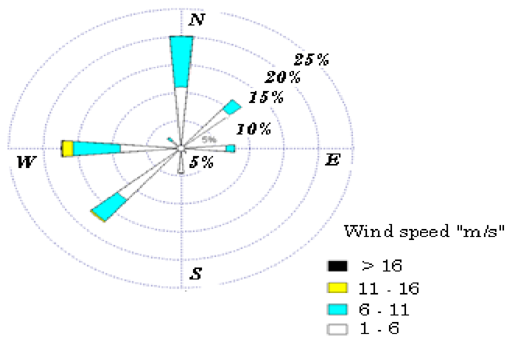

Fig. 17 Oran wind compass.

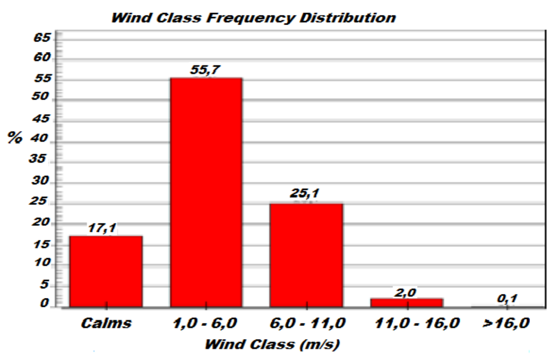

Fig. 18 Oran wind class frequency distribution.

Figs. 15 and 16 show the compass rose speed and the percentage classes in Chlef region, we find that:

The winds are still the most frequent wind speed equal to 1 m/s and 6 m/s (53.8% of occurrences) between 6 m/s and 11 m/s (13.8% of occurrences) and they are almost in all directions.

- The weak winds (speed less than 1 m/s) have no preferred direction;
- High winds (speed exceeding 16 m/s) represent 0.6% of the data and come, mostly from west and south-west.

Figs. 17 and 18 show the compass wind speed and the percentage classes in Oran region, we find that:

The winds are always the most frequent wind speed equal to 1 m/s to 6 m/s (55.7% of occurrences) between 6 m/s and 11 m/s (25.1%). These winds are mostly from all directions and northern west for wind between 6 and 11 m/s.

- The feeble winds (speed less than 1 m/s) have no preferred direction;
- High winds (speed exceeding 16 m/s) represent 3% of the data and come mostly in the south.

7. Conclusions

This work focuses on the estimation of wind power in east coastal region of Algerian which must drive the development of wind power in Algeria. The research consists of the study of a phase prior to providing effective assistance to all those who have to make decisions about the planning and implementation of projects wind power. In this perspective, we began by determining various parameters related to the wind, such as the mathematical modeling of the frequency distribution of wind, Weibull distribution, treatment simulation and real data collected on the wind over 10 years to size a wind farm on a cities. It has estimated wind power potential, meanwhile relying on the automatic determination of the direction of the wind sites in study subjects.

The measured parameter using the rose compass are very close to approximation of the parameter obtained

by mathematical modeling of Weibull distribution, which validates our study.

References

[1] H. Bensaid, The Algerian program on wind energy, Proceeding of WEAC, Oxford, 1985, pp. 21-27.

[2] A. Celik, A statistical analysis of wind power density based on the Weibull and Rayleigh models at the southern region of Turkey, Renew Energy 29 (4) (2003) 593-604.

[3] D.M. Deaves, I.G. Lines, On the fitting of low mean wind speed data to the Weibull distribution, Wind Eng. Indus. Aerodynamic 66 (3) (1997) 169-178.

[4] A.N. Celik, A. Makkawi, T. Muneer, Critical evaluation of wind speed frequency distribution functions [Online], http://dx.doi.org/10.1063/1.3294127 (accessed Mar. 31).

[5] O.S. Ohunakin, M.S. Adaramola, O.M. Oyewola, Wind energy evaluation for electricity generation using WECS in seven selected locations in Nigeria, Applied Energy 88 (9) (2011) 3197-3206.

[6] A. Ucar, F. Balo, Evaluation of wind energy potential and electricity generation at six locations in Turkey, Applied Energy 86 (10) (2009) 1864-1872.

[7] T.P. Chang, Estimation of wind energy potential using different probability density functions, Applied Energy 88 (5) (2011) 1848-1856.

[8] T.P. Chang, Performance comparison of six numerical methods in estimating Weibull parameters for wind energy application, Applied Energy 88 (1) (2011) 272-282.

[9] P.A. Costa Rocha, R.C.D. Sousa, C.F.D Andrade, Comparison of seven numerical methods for determining Weibull parameters for wind energy generation in the northeast region of brazil, Applied Energy 89 (1) (2012) 395-400.

[10] M.J.M. Stevens, P.T. Smulders, The estimation of the parameters of the Weibull wind speed distribution for wind energy utilization purposes, Wind Eng. 3 (2) (1979) 132-145.

[11] C.G. Justus, A. Mikhail, Height variation of wind speed and wind distribution statistics, Geophys Reslett 3 (5) (1976) 261-264.

[12] C. Nichita, D. luca, D. Dakyo, E. Eeanga, Large bande simulation of wind speed for real time wind simulators, IEEE Transaction on Energy Conversion 17 (4) (2002) 523-529.

Journal of Energy and Power Engineering 8 (2014) 495-501

Mathematical Modelling of Charge/Discharge Process in Seasonal Heat Storage Tank

Ladislav Böszörményi, Emese Šiváková, Roman Vodička and Peter Kapalo

Faculty of Civil Engineering, Technical University of Košice Vysokoškolská, Košice 404 02, Slovakia

Received: September 13, 2013 / Accepted: November 07, 2013 / Published: March 31, 2014.

Abstract: The seasonal heat storage tank is the most important component of the SDH (solar district heating) system, which allows significant increase in the share of solar energy in heat supply in comparison with conventional solar systems with short-term accumulation of heat. The adverse impact of their investment sophistication on competitiveness may be compensated by the increased use. For example: Cooperation with heat pump allows to increase the accumulation capacity of the seasonal heat storage tank and causes the direct use of heating energy and accumulation of cooling energy produced by heat pump. In the final stage of the heating period, it can be used to remote cooling supplied buildings. Experimentation on mathematical model is possible to obtain valuable insights about the dynamics of the processes of charging and discharging in the seasonal storage tank and subsequently used in the design, implementation and operation.

Key words: One seasonal heat storage, temperature stratification.

1. Introduction

The major part of the materials originating from not renewable natural resources (i.e., metal, building materials, etc.) can be recycled after the use. Contrarily to that, the fossil energy sources cause environment pollution after utilisation besides the accelerated decrease of the reserve of the earth. Consequently the rational use of fossil energy sources is one of the basic conditions of the sustainable development, however, sustainability of energy supply is very limited also in the case of the most economic utilisation. The gas and oil resources will be depleted in this century according to most of the scenarios. There are also more optimistic scenarios available but the fact cannot be changed: the mankind has to face the very inconvenient fact of the depletion of fossil energy resources. The replacement of the fossil renewable energy sources cannot happen from one day to the other. This is a long process through decades. We are now in the initiative phase where renewable energy sources—like the forms of solar energy and geothermal energy give alternative solutions.

2. The Solar District Heating System with Seasonal Heat Storage

The environmental load caused by the primer-energy consumption in the building's heat supply is the lowest by using solar energy or geothermal energy. Slovakia has high geothermal potential eligible for heat supply of buildings, however, for that purpose it is used only in a small scale. The interest for utilizing of that heat is always growing especially because of the gas crises; however, only in some region it can be taken into account as a realistic approach.

The solar energy can be used everywhere in smaller or bigger scale and in an unlimited time scale because the hourly incoming solar radiation to the earth is more than the annual energy demand for more than 4 milliard years. The supply covered only by solar energy is theoretically possible and practically can be realized but

Corresponding author: Ladislav Böszörményi, associate professor, research fields: energy engineering, energy systems of buildings. E-mail: ladislav.boszormenyi@tuke.sk.

it has high investment cost. The research of the possibilities of the effective heat supply based on the combination of solar energy and biomass is very important. Principally all of them are solar energy as the biomass is also solar energy stored in a chemical form.

The active use of solar energy is mostly about producing DHW (domestic hot water) or water heating for swimming pools. Only about 15% of the yearly heat consumption can be covered by solar energy in such systems. The heat demand is the higher in winter when the heat produced by solar energy is the lowest, and the proportions are the opposite for summer. The support of space heating from solar energy is also very limited in time—just in the very short time in the beginning of the spring and autumn period—also in the dedicated systems if the solar heat can be stored only for short time for several days. In these systems only about 30% of the yearly heat demand can be covered. This proportion can be extended with a consequent system-planning, however, the real development is the seasonal storage.

In the SDH (solar district heating) systems based on a seasonal storage the proportion of the utilised solar energy can reach 40%-70%. These systems are in the initial phase of the research and development but good experiences from more demonstration projects are already available. These projects have been realised mainly in Germany, in Denmark and in Sweden [1-6]. The scheme of the system is illustrated in Fig. 1. with the main parameters of the Friedrich shafen project in Germany.

The useful heat energy is produced from the solar energy in the solar collectors. This heat energy captured in antifreeze liquid is transported through pumps and heat exchanger in a seasonal heat storage tank in the summer period. In the heating period in winter, the heat consuming equipments of the building are supported with the heated water from the storage tank through heat exchanger and pumps. The system normally is extended with a fossil fuel boiler.

The aim of the seasonal accumulation is to place the heat from the solar collectors by solar thermal conversions in the period with a maximum intensity of sunlight and minimal need of heat in the supply of a building or group of buildings in the period with a minimum intensity of solar radiation and the maximum heat demand.

The most important feature of the seasonal storage tanks is the ability to keep the heat in the storage tanks as long as possible and with minimum heat losses to the surroundings. Over time, they have developed various new technologies and materials used for the construction of seasonal storage tanks. Gradually, the demands have increased on their properties, durability and construction technology, too.

Technologies of heat accumulation are the subject of intensive research and development in many renowned research institutes and universities. Nevertheless, currently the best solution seems to be the easiest, namely accumulation in water, which is the cheapest of the working substances and has the largest specific thermal capacity.

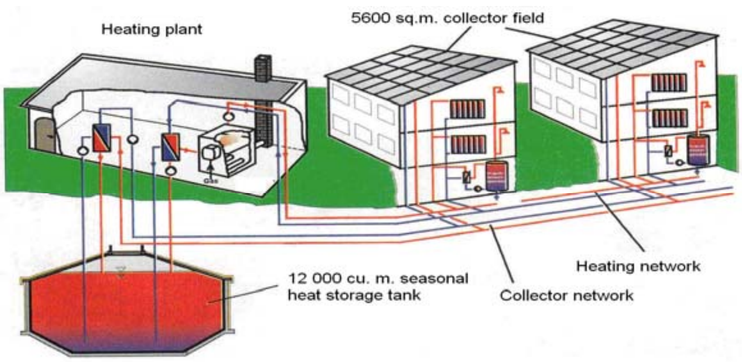

Fig. 1 The principle of the solar district heating system based on the seasonal heat storage [3].

The heat from the storage tank can be used directly for heating up to temperature around 35 °C, according to the return water temperature from the consumer system. For existing systems it generally takes no more than 3-4 months. In the rest of the heating period it can significantly cool down by heat loss to surroundings. An innovative measure can be based on the replacement of spontaneous cooling of the storage tank by forced cooling with heat pump. The storage tank will discharge at the temperature of 5-10 °C at the end of the heating period, while the heat power is used for heating support.

Such integration of heat pump to the system allows increasing the capacity of the storage tank and its transformation on a seasonal storage tank of cold. Finally, the SDH system can become SDH/C system (solar district heating/cooling).

Such use of the seasonal storage tank puts increased demands on the quality of the preparation and implementation of the project of the entire system in comparison with the standard, thermal properties of the construction materials used in the construction and application to structures.

The use of the seasonal storage tanks is not yet known. We do not have experiences with them, which could be used in the preparation, implementation and operation. The results of temperature stratification measurements in water were published with default used seasonal storage tank [5, 6]. Knowledge would be necessary to experiment with the physical model of the storage tank. The experiment would be financially difficult as well as time consuming. Therefore, it is advisable to use the method of mathematical modeling instead of physical modeling.

3. The Mathematical Description of Temperature Stratification in the Heat Storage Tank

Among the most important steps in the development of a mathematical model stands the mathematical description of the stratification of the water temperature when the seasonal reservoir is charging or discharging. A simplified solution is mentioned [7] for a short-term accumulation of solar heat into the water. In such storage tank the pressured water fills its whole volume. Seasonal storage tanks are built principally as pressureless, thus with the free surface over which the air layer is associated with the atmosphere. This fact and the partial failure provide the relation with thermodynamic essence of processes and limit the possibility of extrapolating the results of [7] for our case. Therefore, the development of the mathematical description of temperature stratification in a seasonal storage tank was necessary. We assume temperature stratification of water in the pressureless seasonal storage tank according to Fig. 2.

The modeling of the time evolution temperature in different layers of the water filling in the storage tank can be used to the I. law of thermodynamics which can be expressed by general balance Eq. (1) for non-stationary process in an open thermodynamic system [8]:

$$\frac{dE}{dt} = \dot{Q} + P + \sum_{in} \dot{m}_{in} \left(h + \frac{v^2}{2} + gz\right)_{in} - \sum_{out} \dot{m}_{out} \left(h + \frac{v^2}{2} + gz\right)_{out} \quad (1)$$

where,

E —total energy of the system, (J);

$\dot{Q}$—heat flow transferred across the borders of the system, (W);

P —mechanical interaction between system and surrounding, (W);

$\dot{m}_{in}$—substance flow incoming to the system, (kg/s);

$\dot{m}_{out}$—substance flow outgoing from the system, (kg/s);

$\dot{h}_{in} / \dot{h}_{out}$—specific enthalpy of incoming/outgoing substance flow, (J/kg);

$\left(\frac{v^2}{2}\right)_{in} \Big/ \left(\frac{v^2}{2}\right)_{out}$ —specific kinetic energy of incoming/outgoing substance flow, (J/kg);

$(g \cdot z)_{in} / (g \cdot z)_{out}$ —specific potential energy of incoming/outgoing substance flow, (J/kg).

Any i-th layer of water in the storage tank can be considered as an open thermodynamic system, which

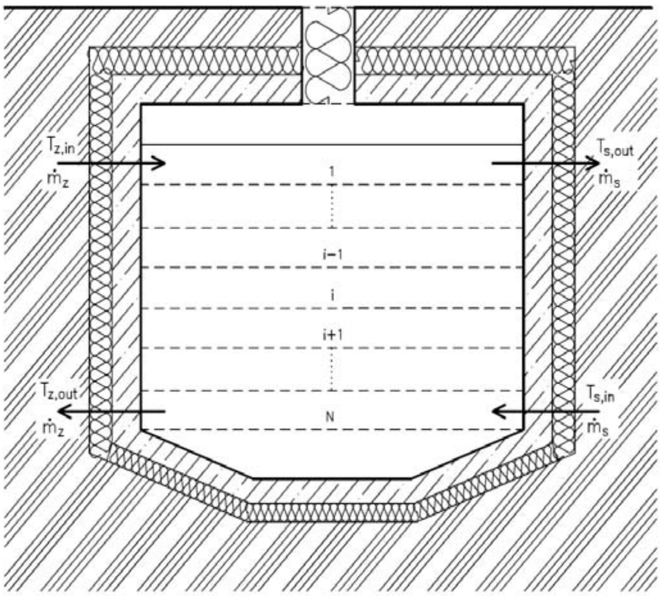

Fig. 2 Calculation scheme of the seasonal heat storage tank.

can be applied to this balance equation. Mechanical interaction between this system and its surrounding does not exist, so $P = 0$.

The individual forms of mechanical energy system, the kinetic and potential energy, respectively their changes compared with the internal energy can be ignored:

$$dE = dU = m \cdot c_v \cdot dT$$

$$\left(\frac{v^2}{2}\right)_{in} = \left(\frac{v^2}{2}\right)_{out} = 0$$

$$(g.z)_{in} = (g.z)_{out} = 0$$

Balance Eq. (1) can be expressed in the form:

$$m \cdot c_v \cdot \frac{dT}{dt} = \dot{Q} + \sum_{in} (\dot{m} \cdot h)_{in} - \sum_{out} (\dot{m} \cdot h)_{out} \quad (2)$$

The specific enthalpy of water depends on temperature:

$$h = c_p \cdot T$$

Specific heat capacity at constant volume c_v and constant pressure c_p are the same.

$$c = c_v = c_p$$

The distribution of water volume in storage tank to N effective layers applies to all layers of the same mass balance in the form:

$$\sum_{in} \dot{m}_{in} = \sum_{out} \dot{m}_{out} = \dot{m}_z + \dot{m}_s$$

Substance flow is incoming and outgoing to layers 1 and N through the supply and sampling equipments and this also spreads over the cross section A_q. Other layers 2 to $N - 1$ have input and output of substance flows distributed only cross-section.

The thermal interaction of the system with the surrounding is manifested by heat loss into the surrounding through the walls of the storage tank and by conductive heat transfer between the layers. Balance Eq. (2) of any i-th layer can be expressed in the form:

$$\dot{m}_i \cdot c \cdot \frac{dT_i}{dt} = \dot{Q}_{hflowmi} + \dot{Q}_{mflow,i} \quad (3)$$

where,

m_i—water mass in the i-th layer (kg/s);

T_i—water temperature in the i-th layer, (K);

t— time, (s);

$\dot{Q}_{hflow,i}$—the thermal interaction of i-th layer with surrounding and near layers through the heat flow (inlet eventually outlet of heat in time unit), (W);

$\dot{Q}_{mflow,i}$—the thermal interaction of i-th layer with surrounding and near layers through the mass flow (inlet eventually outlet of heat in time unit), (W).

Eq. (3) can be arranged by expressing $\dot{Q}_{hflow,i}$ and $\dot{Q}_{mflow,i}$ according to the laws of thermodynamics into a form:

$$\dot{m}_i \cdot c \cdot \frac{dT_i}{dt} = A_q \cdot \frac{\lambda_{ef}}{z} \cdot (\Delta T_{cond})_i - (U.A)_i (T_i - T_0) + \dot{m}_z.c.(\Delta T_{cha})_i - \dot{m}_s.c.(\Delta T_{dcha})_i \quad (4)$$

The first term on the right side of the Eq. (4) represents the thermal interaction between the i-th layer and the surrounding layers by means of conductive heat flow, where:

λ_{ef}—effective heat conductivity coefficient of the water or accumulation fluid respectively, (W/mK);

z—water layer height, (m);

$(\Delta T_{cond})_i = T_i - T_{i-1}$ if $i = 1$

$(\Delta T_{cond})_i = T_{i-1} + T_{i+1} - 2.T_i$ if $i \neq 1$

The second term on the right side of the Eq. (4) represents the heat transfer from the i-th layer to the surroundings. Unlike in the case of the first term, this one expresses the heat loss from the respective layer per time unit, where:

$(U \cdot A)_i$—specific heat loss to the surroundings per time unit (W/K);

U—heat transfer coefficient of the heat storage tank's wall, (W/(m^2.K));

A—heat storage wall surface through which heat flows from the i-th layer to the surroundings (m^2);

T_0—surrounding temperature, (K).

In case of a simplified first approach, the surrounding temperature is considered to be constant in time and place, the heat transfer coefficient U can be looped upon as constant and then $(U \cdot A)_i$ shall only be a function of the surface A through which the heat is transferred to the surroundings. The surface can have different values for $i = 1$, $i = 2 \div N$ and $i = N + 1$.

The third term on the right side of the Eq. (4) represents the heat transferred to the i-th layer by means of charging mass flow rate $\dot{m}_z$. The change of the temperature of the charging mass flow rate at the inlet and outlet is:

$$\Delta T_{char} = T_{z,in} - T_{i+1} \quad \text{if } i = 1$$

$$\Delta T_{char} = T_{i-1} - T_{i+1} \quad \text{if } i \neq 1$$

The fourth term on the right side of the Eq. (4) represents the heat that is taken away from the i-th layer by means of discharging mass flow rate $\dot{m}_s$. The temperature change of the discharging mass flow rate $\dot{m}_s$ between the inlet and outlet is:

$\Delta T_{dchar} = T_{i.1} - T_{s1}$ if $i = N$

$\Delta T_{dchar} = T_{i.1} - T_{i+1}$ if $i = 2 \div N - 1$

$\Delta T_{dchar} = T_i - T_{i+1}$ if $i = 1$

Applying the Eq. (4) for each of the surfaces enables us to simulate the temperature stratification of the seasonal heat storage in time during:

- the charging process, when $\dot{m}_z \neq 0$, $\dot{m}_s = 0$;
- the discharging process, when $\dot{m}_s \neq 0$, $\dot{m}_z = 0$;
- simultaneous charging and discharging, when $\dot{m}_z \neq 0$, $\dot{m}_s \neq 0$.

4. Seasonal Hat Storage Tank Charging and Discharging Simulation

In order to identify the water temperature stratification of the seasonal heat storage in time, a solution needs to be found to the simple differential Eq. (4), for instance by means of differential method for all of the layers by time step $\Delta t = t_{j+1} - t_j$. The temperature in the i-th layer in time t_{j+1} shall be:

$$T_{i,j+1} = T_{i,j} + (\Delta T_i)_{\Delta t} \tag{5}$$

where,

$T_{i,j}$—water temperature in the i-th layer in time t_j;

$(\Delta T_i)_{\Delta t}$—change in water temperature in the i-th surface in time interval Δt.

By taking the Eqs. (4) and (5) into consideration, for the water temperature in any i-th layer in time t_{j+1} follows:

$$T_{i,j+1} = T_{i,j} + \frac{\Delta t}{\dot{m}_i.c}[A_q \cdot \frac{\lambda_{ef}}{z} \cdot (\Delta T_{cond})_i - (U.A)_i(T_i - T_0) + \dot{m}_z.c.(\Delta T_{char})_i - \dot{m}_s.c.(\Delta T_{dchar})_i] \tag{6}$$

The first functional version of the simulation software on the water stratification in a seasonal heat storage in time according to the Eq. (6) and agreed simplifications was carried out in MATLAB. Some of the graphic outputs of the charging and discharging process simulation are shown in Figs. 3 and 4.

5. Perspectives of the Simulation Software Improvement

The first functional version of the simulation software represents the output of the first stage of a research project carried out at the Technical University of Košice. It can be further improved by:

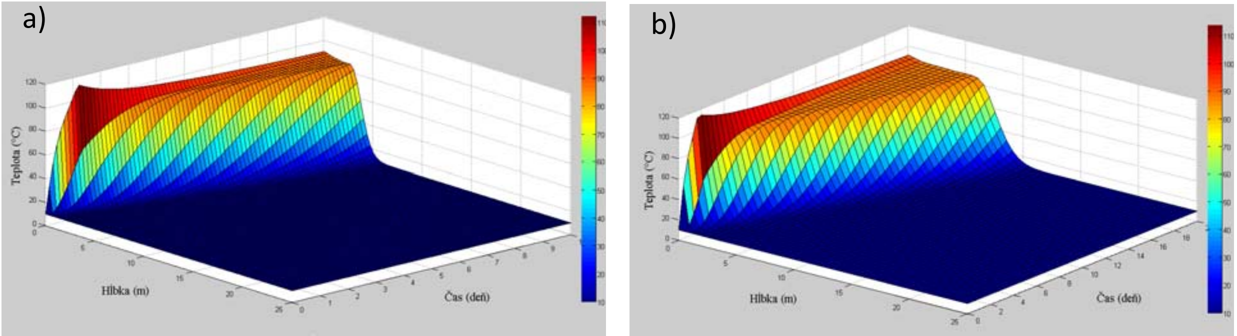

Fig. 3 Graphical output of the heat storage charging (a) after 10 days, (b) after 20 days.

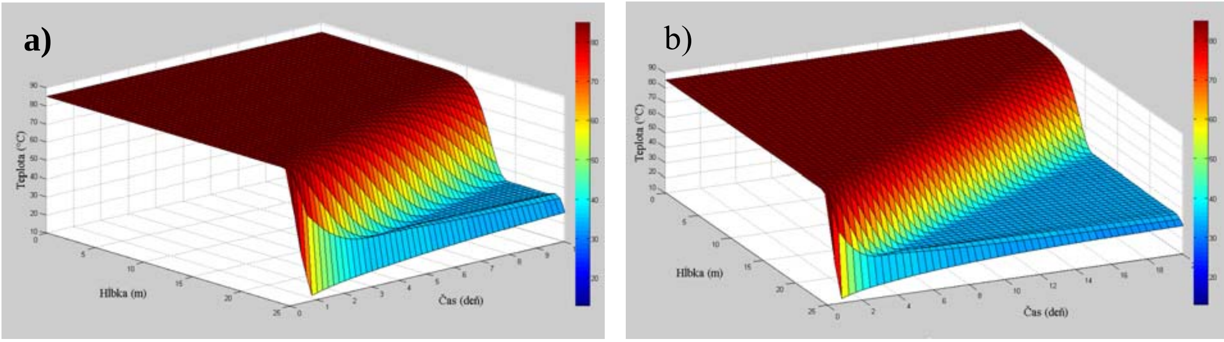

Fig. 3 Graphical output of the heat storage discharging (a) after 10 days, (b) after 20 days.

- taking the dependency of the surrouding temperature and/or charging and discharging mass flow rate on time and/or weather conditions into account;
- taking into account the temperature dependency of the water density, i.e., adjusting the water mass in each of the layers or adjusting the water volume by keeping the mass constant;
- taking into account the possibility of the charging and/or discharging mass flow through the stratification tube directly into the layer of identical temperature;
- innovating the algorithm for automatic correction of time step in order to speed up or slow down the simulation in case it is justified in case of minor temperature changes;
- innovating the algorithm in order to increase the clearness of the graphical output by means of result saving only in case of rather major temperature changes;
- innovating the algorithm in order to extend its applicability for simulating the time dependency of the energy balance of the heat storage;
- verification of the mathematical model results on a physical model of the heat storage tank, whose build-up has already started at the Technical University of Košice.

6. Conclusions

The described concept of a mathematical model is a simplified description of complex processes, which take place during the charging and discharging of the seasonal heat storage tank. This is the first approximation of the solution. After the development of computer implementation to simulate of the dynamics processes it will be possible to apply the obtained results in practice.

Acknowledgments

This publication is the result of the projects implementation: Research centre for efficient integration of the renewable energy sources, ITMS: 26220220064 supported by the Research & Development Operational Programme funded by the ERDF and Research and development of quasi fully

solar heat supply systems of buildings, VEGA 1/0976/11.

References

[1] D. Mangold, T. Schmidt, The next generations of seasonal energy storage in Germany [Online], http://www.solites.de/download/literatur/07-Mangold_ESTEC%202007.pdf.

[2] D. Mangold, T. Schmidt, The new central solar heating plants with seasonal heat storage in Germany, EuroSun [Online], Glasgow, UK, June 27-30, 2006, http://www.solites.de/download/literatur/06-Eurosun.pdf/.

[3] T. Schmidt, D. Mangold, P.A. Sorensen, Large-scale heat storage, in: 6th International Renewable Energy Storage Conference, Eurosolar, Berlin, Germany, Nov. 28-30, 2011.

[4] T. Schmidt, O. Miedaner, Solar district heating guidelines: Storage, SDH fact sheet 7.2 [Online], http://www.solar-district-heating.eu.

[5] M. Banner, M. Rodmann, D. Mangold, J. Nußbicker, S. Raab, T. Schmidt, et al., Solar Assisted District Heating and Seasonal Heat Storage, Research Report 1998-2003 [Online], http://www.solites.de/download/literatur/AB-SUN%20IV%20FKZ%200329606S.pdf.

[6] D. Mangold, M. Riegger, T. Schmidt, Technical-Economic Analyse and Development of Seasonal Storage of the Solar Heat, Research Report 2005-2007 [Online], http://www.solites.de/download/literatur/AB-SUN%20VI%20FKZ%200329607L.pdf.

[7] U. Eicker, Solar Technologies for Buildings, John Wiley and Sons, West Sussex, England, 2003, p. 336.

[8] H.D. Baehr, Thermodynamik, Springer-Verlag Berlin, Heidelberg, New York, 1992, p. 460.

Journal of Energy and Power Engineering 8 (2014) 502-507

Energetic and Environmental Optimization of the Biomass Using

František Hrdlička and Jan Hrdlička

Department of Energy Engineering, Faculty of Mechanical Engineering, Czech Technical University in Prague, Technicka 4166 07 Prague 6, Czech Republic

Received: July 17, 2013 / Accepted: October 14, 2013 / Published: March 31, 2014.

Abstract: Biomass energy conversion can be done in several ways–combustion, gasification, pyrolysis or anaerobic fermentation (biogas production). Each of these technologies has certain advantages and disadvantages from the point of view of energy generation for final consumption. In parallel, each of them has certain environmental impact in terms of emissions. The proposed EU directive prefers utilization of primary energy sources by application of highly efficient co-generation. Such change in assessment of energy effectiveness also means a completely new approach in assessment of current technologies. This report presents a guide for optimization of biomass energy conversion technologies assuming application of this new condition and minimal environmental impact. Specific values of emissions from particular technologies are used for the evaluation.

Key words: Road map 2050, biomass energy utilization, directive of energy efficiency, power heat ratio, indirect dryer.

List of Symbols

ΔQ^{T}_{pv} Fuel savings
E Annual electricity production
Q_d Annual production of useful heat
E Power/heat ratio
Δq^{T}_{pv} Relative fuel saving
Q^{E+V}_{pv} Annual fuel consumption for separate production of power and heat
η_E Default condensing electricity production efficiency
η_V Heat production efficiency according to national standards
η_T Gross efficiency of the cogeneration source

1. Introduction

Biomass with high moisture content is the most common type of biomass available for energy conversion purposes, including wooden chips from forestry, bark and sawdust from non-dried wood from wood processing industry and pulp and paper production. Study of available sources regarding utilization of such kinds of biomass for effective CHP (combine heat and power) production shown that the work is focused mostly on pyrolysis and gasification processes. These processes allow production of higher share of electricity in relation to heat production. This solution is economically feasible for large scale applications. However, in distributed energy systems is used either biomass drying by air or by flue gas. Both approaches result either in lower efficiency of the combustion system (water vapor increases stack loss) or in decrease of electricity share and increase of heat in CHP production.

2. Change of Energy Policy

In November, 2012 a new version of the Energy Efficiency Directive (2012/27/EU) [1] was published. This directive is one of the basic tools of the European energetics, which should enable to fulfill Union's ambitious targets on energetic efficiency, included in the road map 2050 [2]. From the wide range of milestones of the Road map 2050, we consider the

Corresponding author: František Hrdlička, professor, research fields: combustion technologies, fossil fuels, renewable energy, industrial and district energy sources. E-mail: frantisek.hrdlicka@fs.cvut.cz.

following two ones to be the most important for the energetic policy and strategy:

• emission CO_2 decrease by about 85% to 90% compared to year 1990;

• primary energy resources exploitation decrease by about 380 Mtoe compared to year 2005 (peak of consumption);

The second predicted goal is shown in Fig. 1 [2], which describes assumed development of savings of primary energy resources in the EU.

To reach this target it is of course necessary to start the change of energetic policy immediately.

The essence of the intent is the change of the energy savings policy from reduction of the final gross energy consumption to savings of the primary energy resources. The new energetic policy, also included in targets of the "Horizon 2020", is also expressed through the particular targets of the primary energy resources savings in the explanatory report of the new directive, where it is compared to the development of the expected consumption of the primary resources as shown in the following Fig. 2.

It is clear that such an ambitious energetic policy must be supported by appropriate tools. These tools can be summarized as follows:

• Fundamental increase of the share of electricity on the final consumption according to the road map 2050 [1, 2] as shown in Fig. 3.

• Increase of the share of electricity should be done especially using power sources, which in the EU nomenclature (not physically) have a conversion factor between primary energy and electricity equal to "1". This in fact means strict preference of water, wind and solar (not only photovoltaic) power plants.

3. New EU Energy Policy and Biomass

How to understand the new European legislation from the point of view of the only significant renewable primary energy source in CR—i.e., biomass? Biomass is still an environmentally acceptable source in terms of greenhouse gases production, but its

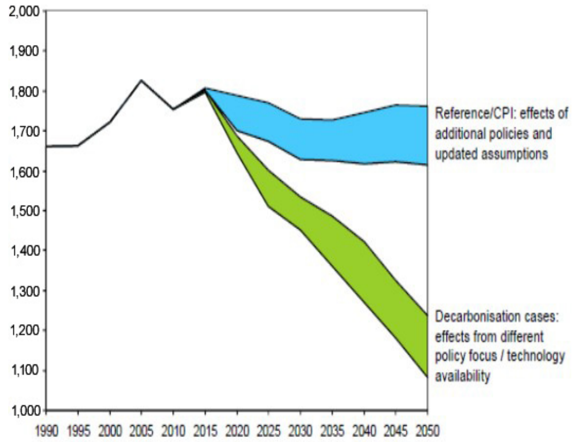

Fig. 1 Decrease of primary energy resources exploitation.

utilization is not easy in terms of planned primary energy sources savings. It is necessary to divide the look at the biomass utilization in two aims:

• direct conversion of the biomass to electric power and heat (+ cooling as an additional product, although EU does not mention it);

• production of biofuels for final consumption in transportation;

Utilization of the biomass [3] for biofuels production in terms of energetically realistic conversions between the primary energy and the final consumption is not mentioned at all by EU, the only mention is that the efficiency of technologies for conversion to first-generation biofuels is about 0.7 and conversion to second-generation biofuels will be much higher-up to 0.9. The real net yield of the bioproduct in terms of energetic transformations and own consumption of the technologies is not stated. And this brings us to the subject of the paper. How to handle the energy facilities utilizing biomass as the primary energy resource for the next planning period, so that they meet the new EU targets?

There are no direct restrictions for energetic sources with heat input up to 20 MW (The EU Industrial Emissions Directive). The consequences of their utilization will show only in final balances of the country. In chapter "greenhouse gases production" positively, in chapter "energetic transformation: primary fuel—final consumption" negatively.

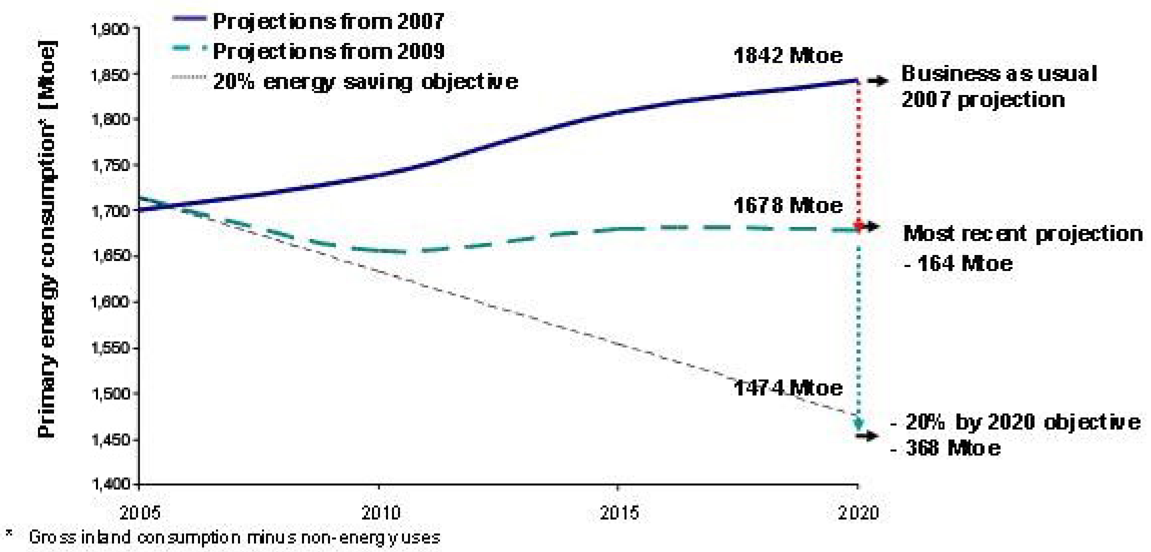

Fig. 2 Primary energy savings as presented in the explanatory report EU.

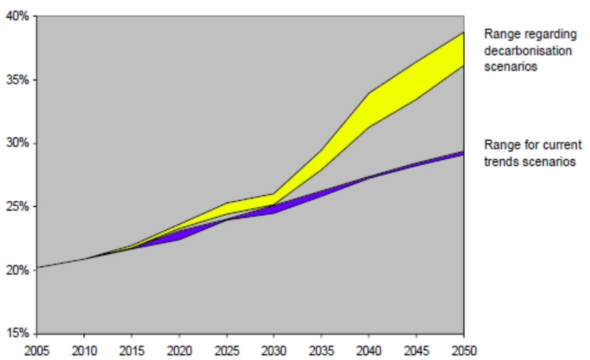

Fig. 3 The increasing share of electricity on final consumption.

4. Energy Sources with the Heat Input above 20 MW

For energetic sources with heat input over 20 MW is necessary to take into account all factors, which are stated in the new EU legislation, so that we can define an area of positive impact of the biomass utilization for energetic purposes in terms of energy management.

4.1 The Analyzed Cases of Plants Operation

The EU directive 2012/27/EU [1] states the following conditions for power sources with heat input over 20 MW.

The power source will utilize cogeneration with high efficiency, which saves at least 10% of the fuel annually, compared to heat generation from power plants and heating plants. The reference electricity production efficiency is $\eta_E = 0.4$ and the reference heat production efficiency is according to national standards and the fuel (biomass) $\eta_V = 0.8$ to 0.85.

The annual average gross efficiency of the power source will be 75% and the power/heat ratio $e = E/Q_d$ is 0.45. E is annual electricity production at the generator terminals and Q_d is annual production of useful heat. With these boundary conditions it is now possible to assess the design of the power source and whether is it possible to operate it as a high-efficiency co-generation in the conditions of Czech Republic.

To obtain a fuel saving ΔQ^T_{pv} by cogeneration, we can use the following equation [4]:

$$\Delta q^T_{pv} = \frac{\Delta Q^T_{pv}}{Q^{E+V}_{pv}} = 1 - \frac{\dfrac{1+e}{\eta_T}}{\dfrac{e}{\eta_E} + \dfrac{1}{\eta_V}} = 1 - \frac{\eta_E \cdot \eta_V}{\eta_T} \cdot \frac{1+e}{e.\eta_V + \eta_E} \quad (1)$$

And the resulting equation of the wanted quantity η_T is:

$$\eta_T = \frac{\eta_E \cdot \eta_V \cdot (1+e)}{(1 - \Delta q^T_{pv}).(e.\eta_V + \eta_E)} \quad (2)$$

This seemingly simple equation gives an array of results for input values e = 0.1 to 0.5, relative fuel saving 0.1 to 0.25 and two variants of the national gross

efficiency of the biomass heating plant 0.8 and 0.85. The results are summarized in Tables 1 and 2 [5].

The calculation results show the following conclusions:

- The majority of considered combinations of modules "*e*" (power and useful heat ratio) and primary fuel savings are unacceptable. The first reason is the low gross efficiency of the power production (yellow results) and the second reason is a high annual power heat ratio (blue results and very probably purple as well).
- The real operating combinations (white results) are few and in the case of the national standard heating plant efficiency 85% they lay rather in the lower range of the power/heat ratio. These are acceptable (reachable) thermal concepts in terms of implementation of the cogeneration unit, but they rely on a high proportion of annual heat supply, which is unrealistic without technology that would require such heat consumption.
- For Czech Republic and the local ordinary types of biomass for concept of direct combustion (wood chips and straw) it is necessary to require a lower reference value of efficiency of the heating plant (max. 80%). This value allows acceptable values of the power/heat ratio in terms of annual share of supplies of useful heat for district heating systems.

Table 1 Results of calculation for η_{VI} = 0.85.

Relative savings qp		0.1	0.15	0.2	0.25
e=0.2	0.2	0.80	0.84	0.89	0.95
e=0.25	0.25	0.77	0.82	0.87	0.93
e=0.3	0.3	0.75	0.79	0.84	0.90
e=0.35	0.35	0.73	0.77	0.82	0.88
e =0.4	0.4	0.71	0.76	0.80	0.86
e =0.45	0.45	0.70	0.74	0.79	0.84
e =0.5	0.5	0.69	0.73	0.77	0.82

Table 2 Results of calculation for η_{VI} = 0.80.

Relative savings qp		0.1	0.15	0.2	0.25
e=0.2	0.2	0.76	0.81	0.86	0.91
e=0.25	0.25	0.74	0.78	0.83	0.89
e=0.3	0.3	0.72	0.76	0.81	0.87
e=0.35	0.35	0.71	0.75	0.79	0.85
e =0.4	0.4	0.69	0.73	0.78	0.83
e =0.45	0.45	0.68	0.72	0.76	0.81
e =0.5	0.5	0.67	0.71	0.75	0.80

The performed analysis shows that the new EU directive was completely focused on natural gas as the primary fuel for cogeneration facilities. The natural gas allows a very high power/heat ratio of the cogeneration plant.

5. Solution for Biomass

Biomass, especially the type commonly used in the Czech Republic for combustion, with a high water content (Fig. 4 [6]) has a low calorific value and a high stack losses (due to loss of the vaporization heat in the flue gases leaving the stack), which is disadvantageous or unacceptable when considering higher power/heat ratios. Effective way of improving the parameters of biomass as a fuel is biomass drying. Indirect drying of the biomass by a waste heat from the power generation process appears to be an appropriate drying concept for achieving a high power/heat ratio and also a high gross efficiency of the thermal cycle [7]. The design of CHP plant cycle [8] with integrated steam heated indirect biomass dryer is shown in Fig. 5 [6]. The increase of the power/heat ratio through the indirect biomass dryer heated by an extracted steam is shown in Fig. 6.

To summarize, analysis of the above mentioned cases with aim to increase the value of power/heat ratio "e" leads to proposal of indirect drying of biomass fuel by using a waste heat from steam R-C cycle. This design allows a positive valuation of primary energy in biomass into a higher production of electricity in small- and medium-scale systems where are the specific costs of machines in steam cycle much lower than costs for gas turbine and gas cleaning in gasification and pyrolysis systems [6]. This is also in agreement with EU policy targets documented in Refs. [1, 2].

6. Conclusions

The new European directive "on Energy Efficiency" brings an entirely new principles for assessment of the preferred so-called "high-efficiency cogeneration". In

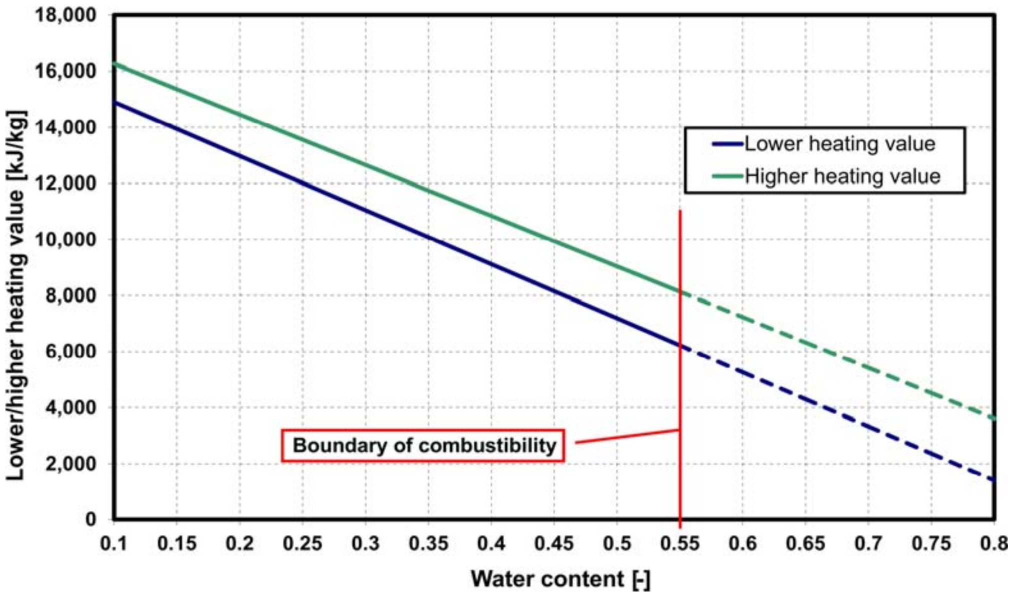

Fig. 4 Function of heating value of biomass on its water content.

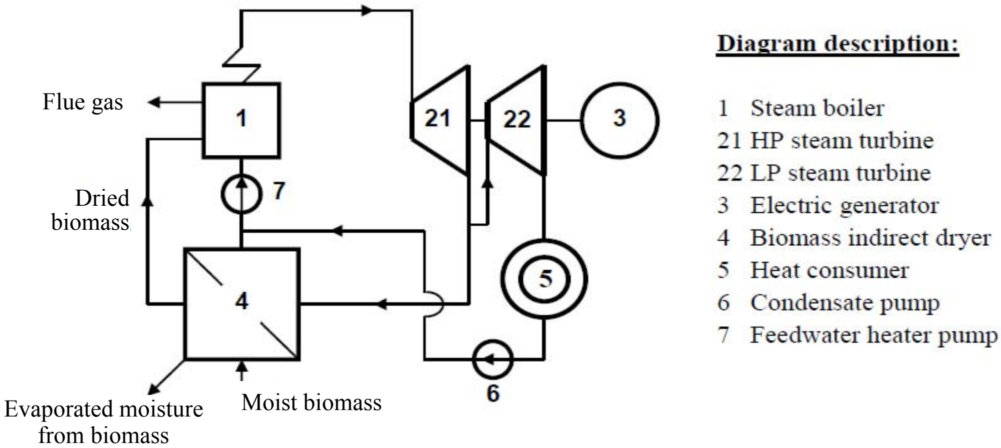

Fig. 5 Connection diagram of district heating plant with integrated indirect dryer.

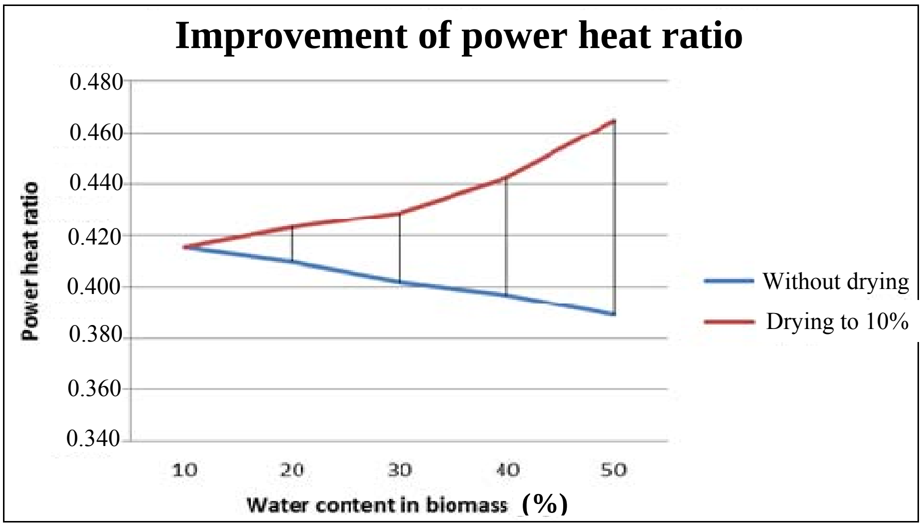

Fig. 6 Improvement of power/heat ratio by biomass drying to 10% water content value.

the Czech Republic these matters significantly affect a substantial segment of renewable sources with low greenhouse gas emissions—biomass district heating plants. The calculations and considerations clearly show that it is necessary to negotiate the national reference efficiency of biomass heating plants to acceptable value for the Czech Republic—i.e., max. 0.8.

For design of new cogeneration biomass sources it is necessary to use the concept of controlled indirect biomass drying, which is essential for achieving high power/heat ratio of the power generation and simultaneously sufficiently high value of the average gross annual efficiency of the district heating plant units [8]. Analysis of results of indirect biomass drying by waste heat show significant increase of power/heat production ratio “e” for biomass with high water content.

Acknowledgments

This paper was created using results from a research project MSM6840770035 supported by the ministry of education, Youth and Sports of the Czech Republic.

References

[1] Directive 2012/27/EU on Energy Efficiency Home Page, http://ec.europa.eu/energy/efficiency/eed/eed_en.htm.

[2] Energy roadmap 2050，European Commission Web site, 2011. http://ec.europa.eu/energy/energy2020/roadmap/index_en.htm (accessed Sept. 30, 2013).

[3] P. Skopec, J. Hrdlička, M. Kaválek, Specific emissions from biomass combustion, Acta Polytechnica. 54 (1) (2014) 74-78.

[4] T. Dlouhý, F. Hrdlička, F. Hrdlička, M. Kolovratník, Industrial energy sources, CTU in Prague, Prague, 2004.

[5] F. Hrdlička, J. Hrdlička, Energetics and environmental optimization of the biomass using, in: Clima 2013-11th REHVA World Congress & 8th International Conference on IAQVEC, Prague, Czech Republic, June 16-19, 2013.

[6] T. Dlouhý, J. Havlík, M. Vitvarová, J. Dlouhý, Use of biomass indirect dryer in power and heating plants, in: Proceedings of Impacts of Fuel Quality on Power Production and Environment, Puchberg am Schneeberg, Austria, Sept. 23-27, 2012.

[7] V. Plaček, C. Oswald, J. Hrdlička, Optimal combustion conditions of a small-scale biomass boiler, in: Proceedings of the ERIN Prague, Czech Republic, Oct. 30-Nov. 1, 2012, pp. 183-187.

[8] J. Hrdlička, P. Skopec, Possibility of biomass utilization in a district heating system, Journal of Slovak University Technology in Bratislava 4 (4) (2011) 21-26.

Journal of Energy and Power Engineering 8 (2014) 508-514

The Influence of Surge Arrester Location on Over-Voltages Caused by Direct Lightning Strikes to MV Lines

Alexandre Piantini[1], Thaís O. de Carvalho[1], Paulo F. Obase[1], Jorge M. Janiszewski[2], Gilnei J. G. Santos[3] and Donorvan R. Fagundes[3]

1. *Institute of Energy and Environment, University of São Paulo, São Paulo 05508-010, Brazil*

2. *Polytechnic School, University of São Paulo, São Paulo 05508-010, Brazil*

3. *AES SUL, Coordination of Planning and Engineering, São Leopoldo 93010-060, Brazil*

Received: August 06, 2013 / Accepted: September 27, 2013 / Published: March 31, 2014.

Abstract: In the period 2003-2011, lightning over-voltages accounted for about 47% of the total number of distribution transformer failures observed in the service area of AES Sul, a power company that operates in the state of Rio Grande doSul, in South Brazil. This paper presents the results of an investigation on the influence of the distance between transformer and MV arresters on the surges at the transformer windings caused by direct strikes to the MV network. The analysis, performed through simulations using the Alternative Transients Program, shows that in general higher voltages are produced by subsequent strokes. Although in relation to the primary side the surges transferred to the secondary are much less affected by the distance between transformers and primary arresters, such distance should always be kept as short as possible in order to reduce the probability of occurrence of transformer failures due to over-voltages at the MV bushings.

Key words: Distribution transformer, lightning surges, overvoltages.

1. Introduction

Distribution transformer failures can often be caused by lightning overvoltages, especially in regions characterized by high lightning activity. This is the case of the western part of the state of Rio Grande do Sul, in south Brazil, where the ground flash densities in some cities exceed 9 flashes/(km²·year). In this region, the distribution transformer failure rate of AES Sul, one of the power companies of the state, is approximately 6%/year. Lightning accounts for most of the transformers' damages in the period 2003-2011 (8 years), causing approximately 47% of the total number of failures. This high failure rate motivated the development of a research project in cooperation with the Lightning and High Voltage Research Center of the University of São Paulo.

A possible measure to reduce the transformer failure rate refers to the installation of LV (low-voltage) arresters [1-5]. In order to evaluate the effectiveness of such measure, two regions of the AES Sul service area characterized by high failure rates and high ground flash densities were selected and LV arresters were installed at the secondary terminals of more than 50% of the transformers. After two years of implementation of this protection scheme (2008-2010), the number of failures did not reduce significantly, a result which has been explained by the fact that the great majority of the observed lightning-caused transformer failures are associated with direct strikes to the MV

Corresponding author: Alexandre Piantini, professor, research fields: power quality, electromagnetic transients and modeling of lightning phenomena, with particular reference to the lightning interaction with power systems. E-mail: piantini@iee.usp.br.

(medium-voltage) network. This is in accordance with the analysis of the failed transformers and with the investigation conducted in Ref. [6], which showed that, for the distance of about 1.5 m commonly adopted between the transformer and the MV arresters, the amplitudes of the over-voltages associated with direct strikes to the line can frequently exceed the CFO (critical impulse flashover voltage) at the transformer terminals.

AES Sul has changed its practice in view of the results and a new configuration has been adopted, with the arresters installed at distances not larger than 0.4 m from the transformer. The installation of LV arresters is recommended in the case of exposed LV lines longer than 500 m. Simulations using models of typical AES Sul distribution transformers, surge arresters, insulators, structures, and line configurations have shown that such measure should lead to a substantial reduction of the lightning-caused failures.

The aim of this paper is to evaluate, through simulations performed using the ATP (Alternative Transients Program) [7], the effect of the variation of the distance between transformer and surge arresters on the surges at the transformer primary and secondary sides in the case of direct strikes to the MV line.

2. Methodology

In order to obtain reliable results it is essential to use, in the simulations, models that represent adequately the behavior of the most important equipment—namely distribution transformers, insulators, and surge arresters, when subjected to lightning surges.

Transformers were represented by quadripoles whose parameters were determined from the analysis of the voltages and currents were measured at their terminals when impulsive voltages were applied to the primary and secondary windings, according to the procedure presented in Ref. [8]. The frequency response curves of the quadripole were obtained from the application of the fast fourier transform to the measured waveforms. The values of the resistive, inductive and capacitive parameters of the circuit were then adjusted to obtain a good agreement between the frequency response curves of the quadripole and those obtained from measurements. To validate the model, comparisons were made between measured and calculated voltages transferred from the primary to the secondary winding when the standard lightning impulse voltage (1.2/50 μs waveform) was applied to the primary terminals. These tests were performed with the transformer secondary either loaded or in open circuit. In the former case, lumped resistive, inductive or capacitive loads, with different values, were considered. Models were obtained for the most common transformers used in the AES Sul distribution network and good agreements were found between measured and calculated results in all comparisons, thus confirming the appropriateness of the developed models for the analysis of transferred surges.

MV insulators were represented by switches that are close when a certain condition—defined by the "Disruptive Effect Model" [9] is reached. Although the project includes simulations of 15 kV and 25 kV three-phase and single-phase lines with pin and pillar porcelain insulators and wooden and concrete poles, the results presented in this paper refer to the 25 kV single-phase network, pillar type insulator, considering both concrete and wooden poles.

MV surge arresters were represented through their voltage-current characteristic (V-I curve) provided by the manufacturer. The residual voltage was approximately 80 kV.

Different values were considered for the soil resistivity and ground resistance (R_g); the effect of soil ionization was taken into account according to the procedure presented in Ref. [10]. The calculations of lightning over-voltages were performed considering a specific section of the 25kV network, shown in Fig. 1, whose LV line is exposed to direct lightning strikes.

The transformer labeled SFR-58, with power and voltage ratings of 10 kVA and 25 kV, respectively, has arresters installed only at the MV terminals. It was

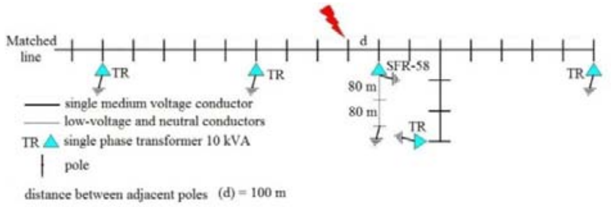

Fig. 1 Distribution line configuration considered in the analysis. SFR-58 indicates the transformer under analysis.

damaged once during the period 2008-2010. Its model obtained according to the procedure described above, is shown in Fig. 2. The model was validated through tests performed in different load conditions. The impulse shown in Fig. 3a was applied to the primary terminal and the comparisons between some measured and calculated secondary voltages, for different load conditions, are shown in Figs. 3b-3d.

In all simulations, lightning was supposed to hit the MV line 100 m away from transformer SFR-58. The distances *a* and *b* between the arrester terminals and the transformer, indicated in Fig. 4, were varied so as to investigate their influence on the over-voltages at the transformer windings. Although in most of the simulations the stroke current was represented by the Heidler function [11], the results presented in the next section were obtained considering for both the first and subsequent strokes a triangular wave shape with tail time equal to 100 μs. Different values were adopted for the current front time (t_f).

Unless otherwise indicated, the following conditions were adopted in the simulations:

- lightning strike point at a distance of 100 m from transformer SFR-58 (as shown in Fig. 1);
- single-phase transformers rated 10 kVA, 13,337 V - 220 V, protected by surge arresters only at the primary side, as shown in Fig. 4;
- ground resistances of 20 Ω at the transformers' poles, 220 Ω at both the neutral groundings and consumers' poles, and 440 Ω at the other poles;
- soil resistivity equal to 500 Ω·m;
- spans of 100m (MV line) and 80 m (LV line);
- wires: 4 ACSR for both the primary (only one phase) and secondary (phase and neutral) networks;

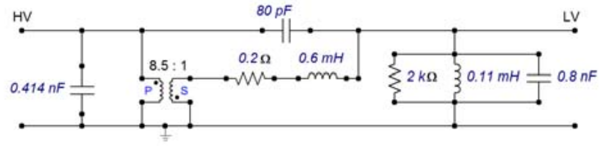

Fig. 2 10 kVA, 25 kV transformer model.

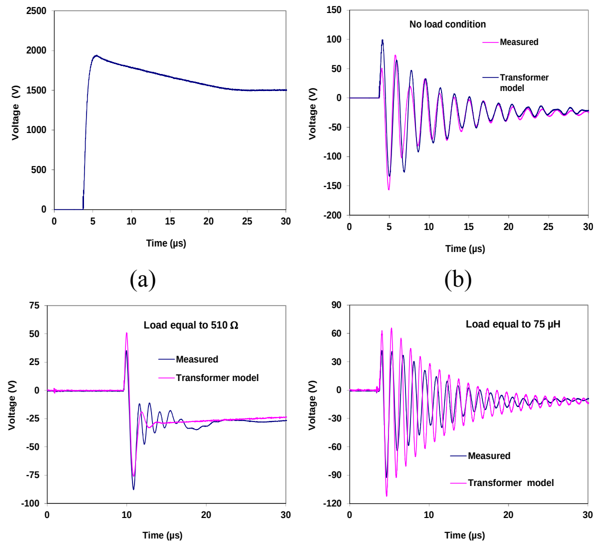

Fig. 3 Voltages at the transformer terminals. (a) Standard impulse applied to the primary; (b) Measured and calculated transferred voltages (no-load condition); (c) Measured and calculated transferred voltages (load: 510 Ω); (d) Measured and calculated transferred voltages (load: 75 μH).

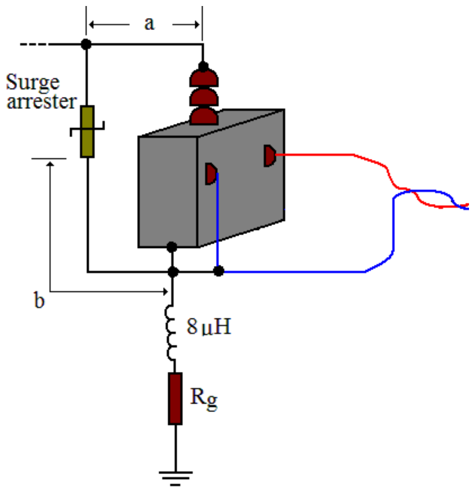

Fig. 4 Distances *a* and *b* between the transformer and arrester terminals.

- 6 consumers connected to the SFR-58 transformer, each one represented by an inductive load of 60 μH;

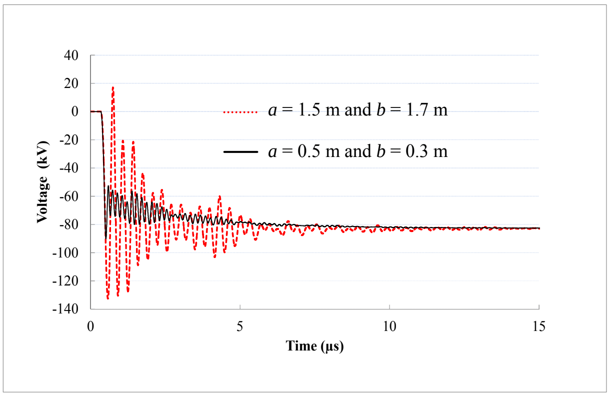

(a)

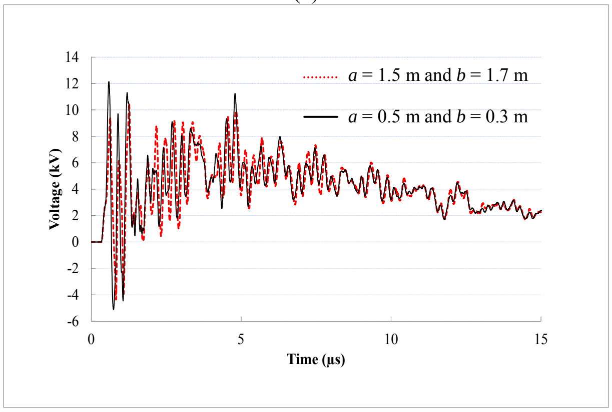

(b)

Fig. 5 Phase-to-neutral voltages. First stroke (I = 31.1 kA and t_f = 3.8 μs), concrete poles. (a) primary (b) secondary.

- 30 m long service drop (twisted conductors configuration): 1 × 10 + 10 mm² aluminum conductor.

Two situations were considered regarding the distances a and b indicated in Fig. 4a a = 1.5 m, b = 1.7 m and Fig. 4b a = 0.5 m, b = 0.3 m. Both for the first and subsequent stroke currents the front time was varied, in the simulations, in a range whose limits correspond to the probabilities of 97.5% and 2.5% of being exceeded. For each front time, the current amplitude was increased till the voltage between the LV terminal and the transformer tank exceeded 30 kV—which is a typical CFO of the LV transformer terminals [12] or values larger than 200 kA or 30 kA were reached for the first or the subsequent stroke current, respectively. In other words, the idea was to determine the lightning current amplitude that, in combination with a certain front time, to yield a voltage equal to the CFO at the transformer LV terminal.

3. Results and Analysis

For both situations considered for the distances a and b, stroke current front times with the same probability of being exceeded were assumed for the first and subsequent strokes and the corresponding current amplitudes required to produce phase-to-neutral voltages exceeding 30 kV at the transformer LV side were obtained. For instance, the front times with 80% probability of being exceeded are 2.5 μs and 0.2 μs for the first and subsequent strokes, respectively [13].

The simulations have shown that, due to the higher steepness of their currents, subsequent strokes are more likely to cause failures on the LV windings, even though the amplitudes are in general lower than those of first strokes.

Figs. 5a-5b and Figs. 6a-6b present examples of results obtained for different distances between the transformer and surge arrester for typical first and subsequent stroke currents (I = 31.1 kA and t_f = 3.8 μs

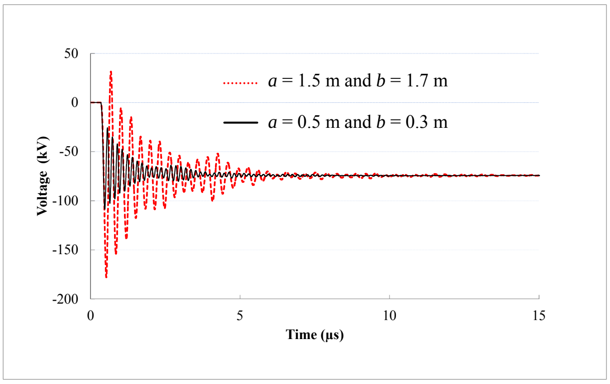

(a)

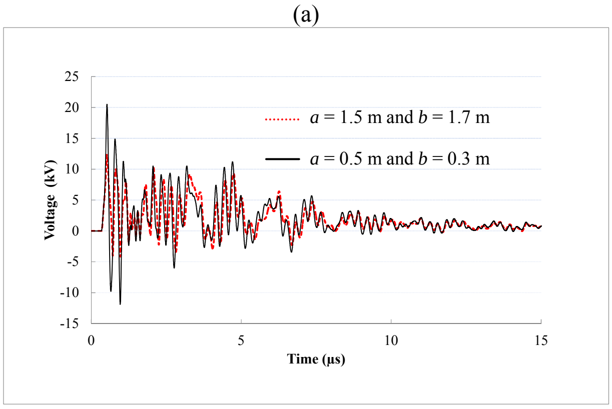

(b)

Fig. 6 Phase-to-neutral voltages. Subsequent stroke (I = 12.3 kA and t_f = 0.7 μs), concrete poles. (a) primary (b) secondary.

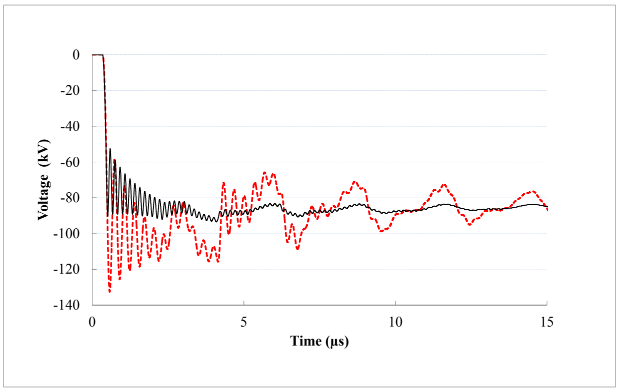

(a)

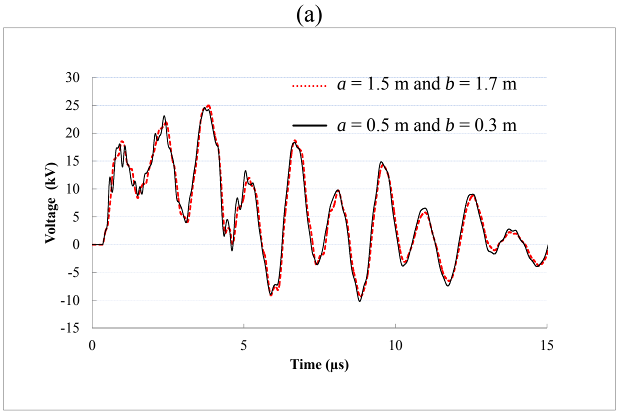

(b)

Fig. 7 Phase-to-neutral voltages. First stroke (I = 31.1 kA and t_f = 3.8 µs), wooden poles. (a) primary (b) secondary.

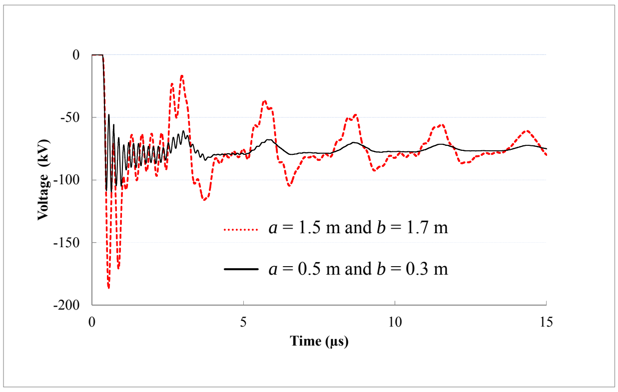

(a)

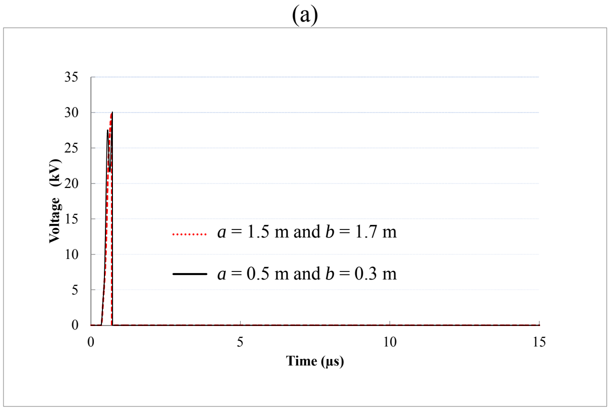

(b)

Fig. 8 Phase-to-neutral voltages. Subsequent stroke (I = 12.3 kA and t_f = 0.7 µs), wooden poles. (a) primary (b) secondary (a flashover occurred across the transformer bushing).

and I = 12.3 kA and t_f = 0.7 µs, respectively), for the case of concrete poles. These amplitudes and front times have a 50% probability of being exceeded [13].

The corresponding voltage waveforms relevant to the case of wooden poles are presented in Figs. 7 and 8.

For the cases relative to concrete poles, flashovers were observed to occur along the MV line as well as in the secondary line. As a consequence of the resulting power dissipation, the surges present in general a shorter duration than those related to wooden poles.

The particular voltage waveform shown in Fig. 8b, which refers to simulations run for the case of wooden poles and subsequent stroke current, is the result of a flashover that occurred across the transformer secondary bushing.

Figs. 5-8 show that the over-voltages at the MV bushing vary significantly with the distance between the transformer and the surge arrester. The shorter the distance is, the lower the voltage is. For example, in the case of concrete poles and a subsequent stroke (Fig. 6a), a reduction of about 40% on the peak value is obtained when the distances a and b are reduced from 1.5 m and 1.7 m to 0.5 m and 0.3 m, respectively.

On the other hand, the voltages on the secondary side are much less affected by the position of the MV surge arrester in relation to the transformer. As shown in Fig. 7b and Fig. 8b, corresponding to wooden poles, the differences between the voltages calculated for the two distances are negligible. In some conditions the secondary voltages may even have the opposite behavior, i.e., reach higher values for smaller distances, as for example in the case of concrete poles illustrated in Figs. 5b and 6b. The influence of the distance on the behavior of the secondary voltages depends on the transformer transfer characteristics, network configuration, ground resistance, and possible occurrence of flashovers.

In order to illustrate how the value of the ground resistance affects the voltage at the secondary transformer terminal for the two distances considered between the transformer and the surge arrester, Figs. 9 and 10 present the results of simulations performed with R_g = 20 Ω and R_g = 60 Ω. The transferred voltages were calculated for the same subsequent stroke current (I = 15 kA and t_f = 0.4 μs), for the case of concrete poles.

It can be readily seen, by comparing Figs. 9 and 10, that the voltages at the secondary transformer side have a very similar behavior. The difference between the peak values corresponding to the two distances reduces with the increase of the ground resistance—from about 50% in the case of R_g = 20 Ω. to 35% for R_g = 60 Ω. A comparison between Figs. 9 and 10 show also that, at

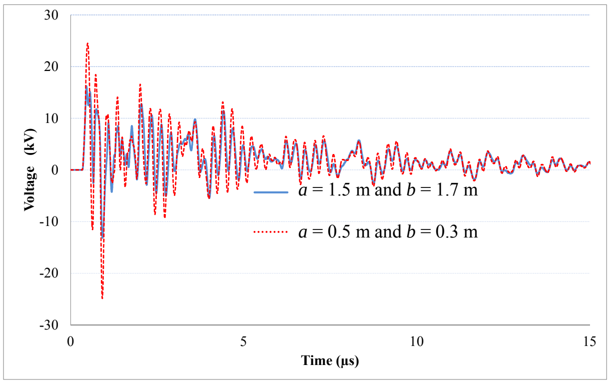

Fig. 9 Phase-to-neutral voltages at the secondary transformer terminal for I = 15 kA, t_f = 0.4 μs (subsequent stroke) and R_g = 20 Ω and two distances between the transformer and the surge arrester.

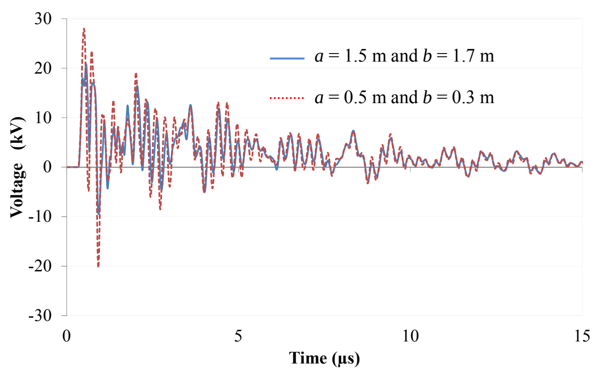

Fig. 10 Phase-to-neutral voltages at the secondary transformer terminal for I = 15 kA, t_f = 0.4 μs (subsequent stroke) and R_g = 60 Ω and two distances between the transformer and the surge arrester.

the LV terminal, the increase of the voltage peak value with the ground resistance is more pronounced for longer distances between the surge arrester and the transformer. The difference, which is about 14 % for the case of a = 0.5 m and b = 0.3 m, increases to 28 % for a = 1.5 m and b = 1.7 m.

4. Conclusions

The relatively long distance between transformers and MV surge arresters has been shown to be the main reason for the high failure rate of distribution transformers in the western part of the state of Rio Grande do Sul, in south Brazil. The analysis revealed that most of the lightning-caused failures were associated with over-voltages at the MV bushings caused probably by subsequent strokes, and that the reduction of this distance would lead to a significant decrease in the failure rate.

The influence of the distance between transformers and MV surge arresters on the surges transferred to the low-voltage side was investigated. The analysis, performed through ATP simulations using models representative of the most important equipment of the distribution network, showed that in general higher voltages are produced by subsequent strokes, and that first strokes are less likely to provoke surges with amplitudes higher than the insulation strength of the transformer LV windings. The effect of the distance has been shown to be more important in the case of low ground resistance.

Although in relation to the primary side the surges transferred to the secondary are much less affected by the distance between transformers and primary arresters, such distance should always be kept as short as possible in order to reduce the probability of occurrence of transformer failures due to over-voltages at the MV bushings.

References

[1] M. Darveniza, D.R. Mercer, Lightning protection of pole mounted transformers, IEEE Trans. Power Delivery 4 (2) (1989) 1087-1095.

[2] M. Darveniza, Lightning arrester protection of distribution transformers – revisited, in: Proc. 6th Int. Symp. Lightning Protection (SIPDA), São Paulo, Brazil, Nov. 2001.

[3] R.C. Dugan, S.S.J. Kershaw, S.D. Smith, Protecting distribution transformers from low-side current surges, IEEE Trans. Power Delivery 5 (4) (1990) 1892-1901.

[4] M.B. Marz, S.R. Mendis, Protecting load devices from the effects of low-side surges, IEEE Trans. Industry Applications 29 (6) (1993) 1196-1203.

[5] Secondary (low-Side) Surges in Distribution Transformers, Task Force Report, IEEE Transformers Committee, 1992, pp. 746-755.

[6] T.O. de Carvalho, A. Piantini, P.F. Obase, J.M. Janiszewski, E.L. Batista, Analysis of lightning-caused distribution transformer failures, in: Proc. 11th Int. Symp. Lightning Protection (SIPDA), São Paulo, Brazil, Oct. 3-7, 2011.

[7] ATP: Alternative Transients Program Rule Book, Leuven EMTP Center, 1987.

[8] A. Piantini, A.G. Kanashiro, A distribution transformer model for calculating transferred voltages, in: Proc. 26th ICLP (Int. Conf. Lightning Protection), Cracow, Poland, 2002, pp. 429-434.

[9] M. Darveniza, A.E. Vlastos, The generalized integration method for predicting impulses volt-time characteristics for non-standard wave shapes—a theoretical basis, IEEE Trans. Electrical Insulation 23 (3) (1988) 373-381.

[10] IEEE Std. 1410-2010, IEEE Guide for Improving the Lightning Performance of Electric Power Overhead Distribution Lines, Jan. 21, 2011, pp. 1-73.

[11] F. Heidler, J.M. Cvetić, B.V. Stanić, Calculation of lightning current parameters, IEEE Trans. Power Deliver 14 (2) (1999) 399-404.

[12] A. Piantini, Lightning protection of overhead power distribution lines, in: Proceedings of the 29th Int. Conf. Lightning Protection (invited lecture), Uppsala, Sweden, June, 2008.

[13] R.B. Anderson, A.J. Eriksson, Lightning parameters for engineering application, Electra 69 (1980) 65-102.

Journal of Energy and Power Engineering 8 (2014) 515-522

Deduction of Design Equations for Durability Performance Improvement of Voice Coil Type Linear Actuator for Servo Valve Operation

Baek Ju Sung

Department of System Reliability, Korea Institute of Machinery & Materials, Daejeon 305-343, Korea

Received: July 31, 2013 / Accepted: November 04, 2013 / Published: March 31, 2014.

Abstract: The precise hydraulic valve is widely used in various industrial fields like aircraft, automobile and general machinery. Linear actuator is the most important device for driving the precise hydraulic valve. The reliable operation of linear actuator has effects on the overall hydraulic system. The performance of linear actuator relies on frequency response and step response according to arbitrary input signal. In this paper, the analysis for the components of linear actuator is performed to satisfy the reliable operation and response characteristics through the reliability analysis, and also deducted the design equations to realize the reliable operation and fast response characteristics of voice coil type linear actuator for servo valve operation through the empirical knowledge of experts and electromagnetic theories. The design equations are suggested to determine the values of design parameters of linear actuator as like bobbin size, length of yoke and plunger and turn number of coil, and calculated the life test time of linear actuator for verification of reliability of the prototype. In addition, for reducing the life test time, the acceleration model of linear actuator is proposed and the acceleration factor is calculated considering the field operating conditions. And then, the achieved design values are verified through accelerated life test and performance tests using some prototypes of linear actuators adapted in servo valve.

Key words: Linear actuator, failure analysis, design equation, accelerated life test, attraction force, frequency response.

1. Introduction

Modern electric controlled valves are demanded that its linear actuator should be smaller size, lighter weight, lower consumption power and higher response time. The linear actuator is a very economical motion converter due to its simple structure as electromagnetic energy converting to kinetic energy. And the linear actuator is used as key components in automobile and aircraft industry. For having higher response time and product reliability, two kinds of different techniques are needed. One is the optimal design method for linear actuator. A regarded point for design of linear actuator is flux density analysis, determination of plunger shape and mass, optimal bobbin design, selected magnetic analysis, determination of duty ratio, and calculation of coil turn number which is regarded temperature rising. For the optimal design of the linear actuator, theoretical and empirical knowledge are simultaneously needed. Theoretical knowledge governs the operational characteristics of the linear actuator, and empirical knowledge compensates for the theoretical limitation obtained from the designer's design and manufacturing experiences for various kinds of linear actuator [1]. They can not be determined solely by calculation or simulation because the empirical knowledge is more essential than theoretical knowledge for determination of the plunger shape and value of the space factor. When designer's accumulated experiences and expertise are added to these, the most proper shape and value of them can then be obtained.

Corresponding author: Baek Ju Sung, Ph.D., research fields: linear actuator, system reliability and FEM analysis. E-mail: sbj682@kimm.re.kr.

In this study, the design equations for design of linear actuator are derived by a combination of electromagnetic knowledge and empirical knowledge. And also, to establish the reliability assessment technology of linear actuator, the failure analysis considering the literature, failure data of manufacturing companies and the opinion of experts is performed, and the reliability parameters for design and test are produced. As the data of failure analysis, the FMEA (failure modes effect analysis), 2-stage QFD (quality function deployment), FTA (fault tree analysis) are draw out, also analyzed failure causes and effects of linear actuator and decided test items. Then the no-failure test time of linear actuator is calculated. In particular, for reducing of the no-failure test time, the acceleration model of linear actuator is proposed and the acceleration factor is calculated with the reality. The validity of the proposed design method and deducted reliability parameters are proved by accelerated life test and performance test.

2. Linear Actuator

Fig. 1 represents the structure of a linear actuator for servo valve operation. It is composed of an excitation coil for generation of magnetic field, yoke for flux path, plunger for creation of mechanical stroke, stationary for attraction of the plunger, permanent magnet for assistance of attractive force and reduction of consumption power, and centering spring [2].

Fig. 2 presents the structure of a simple linear actuator to the exclusion of permanent magnet. Permanent magnet independently compensates the electromagnetic force of linear coil, and it contributes to the reduction of consumption power and increase of operational speed in comparison with the case only used linear coil for generation of the same attraction power.

3. Failure Analysis Documents

3.1 Failure Modes and Effects Analysis

Failure mode and failure mechanism analysis represents the main failure mode of component parts, and the effect on total system and failure cause which was generated by analyzing failed component parts. Table 1 represents the result of failure mode and failure mechanism analysis [3, 4]. Critical matrix analysis represents the severity and failure frequency as a matrix form according to the procedures of MIL-STD-882D such as Table 2 in order to mark qualitatively distribution of severity at each failure modes, failure modes and critical analysis represents failure modes and failure mechanism analysis result and critical matrix analysis result which is performed previously with representing quantitative value such as Table 3. Linear actuator used in automobile and aircraft industry is required to have long life time as well as its stable performance which is suitable for various usage situation, which has recently been an active area of research [5, 6].

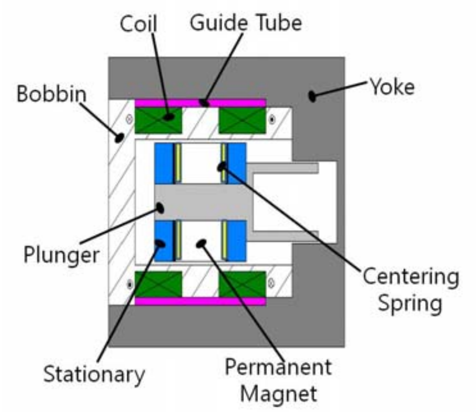

Fig. 1 Structure of voice coil type linear actuator.

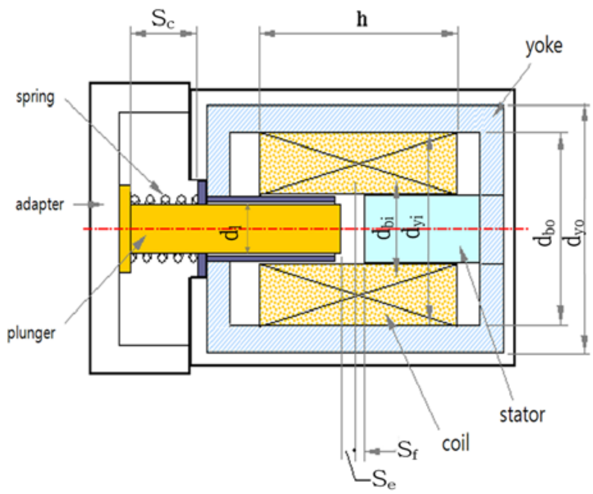

Fig. 2 Simple structure of linear actuator.

Table 1 Failure modes and failure mechanism analysis results.

#	Part	Function	Failure mode	Failure effect		Failure mechanism	
				Local effect	High level effect	Mechanism	Load factor
1	Frame	Structure, magnetic flux passage	Crack, strain, wear	Force loss	Infelicitous motion	Corrosion, fatigue	Humidity, pollution, vibration
2	Plunger	Motion	Jam, constraint	Current rise	Inoperable, Infelicitous motion	Scratch, corrosion, pollution	Temperature, humidity, pollution
3	Stationary	Structure, magnetic flux passage	Strain, wear	Noise rise	Infelicitous motion	Wear, scratch	Repeated motion
4	Sealing	Seal	Crack, strain	Infelicitous motion	Leakage	Stress, wear	Infelicitous assembly, repeated motion
5	Spring	Return force generation	Fracture	Returning power loss	Infelicitous motion	Fatigue	Repeated motion
6	Coil	Force generation	Cut	Stoppage current	Inoperable	Fatigue	Temperature
7	Coil	Force generation	Short	Force loss	Inoperable	Dielectric breakdown	Temperature
8	Guide tube	Friction reduction	Pollution	Current rise	Infelicitous motion	Pollution	Dust, temperature

Table 2 Critical matrix analysis results.

Severity	High	III	5.8	II	2	I	6.7
	Medium	IV	4	III	1	II	
	Low	V	3	IV		III	
		Low		Medium		High	
		Failure frequency					

Table 3 Failure modes, effects and severity analysis results of linear actuator.

#	Part	Function	Failure mode	Failure effect		Failure mechanism		Criticality		
				Local effect	High level effect	Mechanism	Load factor	Frequency	Severity	Criticality
1	Frame	Structure, magnetic flux passage	Crack, strain, wear	Force loss	Infelicitous motion	Corrosion, fatigue	Humidity, pollution, vibration	Medium	Medium	5
2	Plunger	Motion	Jam, constraint	Current rise	Inoperable, Infelicitous motion	Scratch, corrosion, pollution	Temperature, humidity, pollution	Medium	High	7
3	Stationary	Structure, magnetic flux passage	Strain, wear	Noise rise	Infelicitous motion	Wear, scratch	Repeated motion	Low	Low	1
4	Sealing	Seal	Crack, strain	Infelicitous motion	Leakage	Stress, wear	Infelicitous assembly, repeated motion	Low	Medium	3
5	Spring	Return force generation	Fracture	Returning power loss	Infelicitous motion	Fatigue	Repeated motion	Low	High	5
6	Coil	Force generation	Cut	Stoppage current	Inoperable	Fatigue	Temperature	High	High	9
7	Coil	Force generation	Short	Force loss	Inoperable	Dielectric breakdown	Temperature	High	High	9
8	Guide tube	Friction reduction	Pollution	Current rise	Infelicitous motion	Pollution	Dust, temperature	Low	High	5

3.2 Fault Tree Analysis

In Fig. 3, contents in the circle are causes of the detailed failure and contents in the rectangular are phenomena of failure which are generated by causes of the detailed failure.

In case there are many causes of detailed failure, the causes of failure are combined by OR gates and then linked to triangle having a connection character. By analysis of Fig. 3, linear actuator is unable to operate by causes of failure linked under A, and occur partial

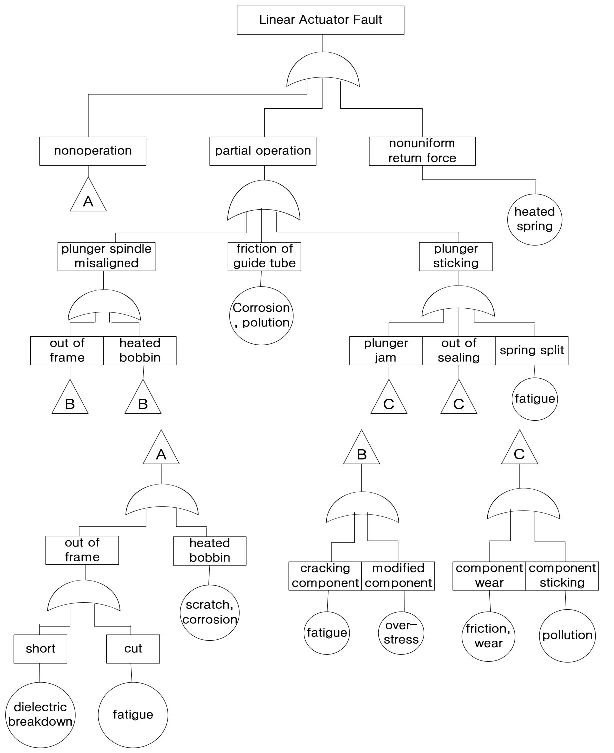

Fig. 3 Fault tree analysis of linear actuator

fault such as shaft bending of plunger, friction of guide tube, and plunger sticking by B, C, corrosion or pollution, fatigue, and also know that return force can be non-uniform by spring wearing.

3.3 Quality Function Deployment

Table 4 represents QFD (I) which expresses the failure modes corresponding to each required quality function. And the importance grade of each failure modes converted to scores, as it were, higher score means more important failure mode. Table 5 represents QFD (II). It is made by the use of the analysis results of QFD (I) and determines the reliability test items.

4. Design Equations

For optimal design, theoretical and empirical knowledge are simultaneously needed. Theoretical knowledge governs the operational characteristics of the linear actuator, and empirical knowledge compensates for the theoretical limitation obtained from the designer's design and manufacturing experiences for various kinds of linear actuator. In this chapter, the derived design equations are presented in Table 6.

We obtained the results of design in Table 6 through the design equations and input parameters. The prototype linear actuator represents Fig. 4. Besides, Fig. 4 represents the servo valve which is adopted the linear actuator prototype.

5. Acceleration Model of Linear Actuator

Domestic industries surveyed integral servo valve operating conditions the lifetime of the field by considering the 90% confidence level B_{10} life of 1.0×10^7 cycles that were guaranteed. According to the survey of the literature, shape parameter of 1.1 Weibull distributions follows. Reliability standards for the evaluation of servo valve in the prescribed lifetime

Table 4 QFD (I) of linear actuator.

Failure mode requirement	Frame crack & strain	Sealing wear	Plunger jam & constraint	Stationary strain & Wear	Spring strain & fracture	Coil cut	Coil short	Guide tube pollution
Smoothing function of plunger	○	○	◎	○	◎	◎	◎	◎
Low consumption power	△			○			◎	○
High attraction force	△		○	◎	△	◎	◎	△
Low temperature rise of coil	○		◎	○	○	◎	◎	○
High insulation resistance						◎	◎	
Low pollution		◎	△					
Low noise					◎			△
Prevention of corrosion		◎	○		△		○	○
High durability	◎	△	○	△	◎	◎	◎	△
Failure risk	25	26	36	27	38	45	59	33
priority	8	7	4	6	3	2	1	5

Very important ◎:9, Important ○:5, Normal △:3

Table 5 QFD (II) of linear actuator.

Failure mode/ risk test item	Frame crack & strain 25	Sealing wear 26	Plunger jam & constraint 36	Stationary strain & wear 27	Spring strain & fracture 38	Coil cut 45	Coil short 49	Guide tube pollution 33	status	priority
Structure test	○							△	224	13
Noise test		△	△	◎					429	10
Consumption power test			○			○	○		650	6
Maintain power test			○	○			○		560	9
Starting power test			○			○			405	11
Attraction force test	○		△	○	○		○	○	968	2
Temperature rising test			△			◎	○		758	4
Insulation resistance test						◎	○		650	6
Voltage test						◎	○		650	6
High temperature test		○				○	◎		706	5
Low temperature test		○				△			265	12
Humidity test			△		△	△	○	◎	899	3
Lift test	○	◎	◎	○	◎	◎	◎	○	2171	1

Very important ◎:9, Important ○:5, Normal △:3

Table 6 Design equations.

Items	Equations	Items	Equations
Attraction force	$F = \dfrac{B^2 \bullet S}{2\mu_0}[N]$	Rising temperature	$T_f = \dfrac{q \bullet \rho}{d \bullet \lambda \bullet X_i \bullet w} \bullet \left(\dfrac{N \bullet W}{h \bullet V}\right)^2$
Design coefficient	$K_f = \dfrac{\mu_0 \bullet S \bullet U_m^2}{2}$	Coil height	$h = \sqrt[3]{\dfrac{(q \bullet \beta \bullet \rho \bullet U^2)}{2 \bullet \lambda \bullet X_i \bullet T_f}}$
Maximum attraction force	$F_{\max} = \dfrac{K_f}{S_f^2}$	Coil mean length	$l_m = \dfrac{\pi(d_{bo} + d_{bi})}{2}$
Minimum attraction force	$F_{\min} = \dfrac{K_f}{d^2}$	Diameter of bare wire	$d_s = \sqrt{\left(\dfrac{2 \bullet \rho \bullet (d_{bo} + d_{bi}) \bullet U}{V}\right)}$
Magnetic flux density	$B = 2 \bullet \dfrac{\sqrt{2 \bullet \mu_0 \bullet F_{\min}}}{d_l \bullet \sqrt{\pi}}$	Total turn number	$N = n_c \bullet m_c$
Magnetic motive force	$U = \dfrac{C_m \bullet B \bullet d}{\mu_0}$	Equivalent resistance	$R_t = \dfrac{2 \bullet \rho \bullet (d_{bo} + d_{bi}) \bullet N}{\pi d_s^2}$
Inner diameter of yoke	$d_{yi} = d_{bo} + C_g$	Coil current	$I = \dfrac{V}{R_t}$
Outerdiameter of yoke	$d_{yo} = \sqrt{d_{yi}^2 + C_p \bullet d_l^2}$	Consumption power	$W = V \bullet I$

where,

F :	Attraction force	U :	Actual magnetic motive force	W :	Consumption power
B :	Magnetic flux density	C_m :	Empirical compensation coefficient	N :	Total turn numbers
S :	Cross sectional area of plunger	d_{yi} :	Inner diameter of yoke	h :	Coil height
μ_0 :	Permeability in the air	d_{yo} :	Outer diameter of yoke	V :	Supply voltage
K_f :	Design coefficient	d_{bo} :	Outer diameter of bobbin	l_m :	Coil mean length
U_m :	Theoretical magnetic motive force	C_g :	Empirical constant	m_c :	Total layer number of coil in the radial direction

$F_{\max}$:	Maximum attraction force	C_p :	Empirical constant	n_c :	Total turn number in shaft direction
$F_{\min}$:	Minimum attraction force	T_f :	Rising temperature	d_s :	Diameter of bare wire
S_f :	Sum of fixed air gap	q :	Duty ratio	R_t :	Equivalent resistance
d :	Maximum distance between plunger and stationary	ρ :	Relative resistance	I :	Coil current
d_l :	Radius of plunger	λ :	Dissipation coefficient		

[1, 7-9].

Table 6 Results of design.

Parameters	Values	Magnetic flux density	2.3~2.4 (T)	Coil turn number	330 (No.)
Attraction force	150 (N)	Permanent magnet width	8 (mm)		

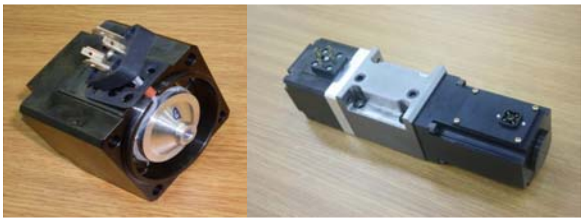

Fig. 4 Prototype of linear actuator & servo valve assembly.

of 1.0×10^7 cycles (B10 life) means to guarantee the following:

- lifetime distribution: Shape parameter (β) 1.1 Weibull distribution [10];
- insurance life: 1.0×10^7 cycles (B_{10} lifetime);
- confidence level : 90%;
- prototype: 3ea.

At this point, no-failure test time was calculated (1) using, the result is $6.1 \cdot 10^7$ cycles.

$$t_n = B_{100p} \bullet \left[\frac{\ln(1-CL)}{n \bullet \ln(1-p)} \right]^{\frac{1}{\beta}} \quad (1)$$

$$t_n = 1.0 \times 10^7 \bullet \left[\frac{\ln(1-0.9)}{3 \bullet \ln(1-0.1)} \right]^{\frac{1}{1.1}} \cong 1.0 \times 10^7 cycles$$

where,

t_n : no failure test time;

B_{100p} : assurance life;

CL : confidence level;

n : number of prototype;

p : unreliability (if B_{10}, $p = 0.1$);

β : shape parameter.

However, because no-failure test time is too long to accelerate the model chosen and accelerated life test of time should be calculated. Failure modes related to the pressure and flow of the servo valve. Pressure and flow are chosen to acceleration stress. Considering the pressure and flow general log-linear acceleration model applied to the test conditions. So the acceleration factor calculates acceleration time fault-tolerance test. 7.0 MPa, 50 L/min and acceleration, conditions 25.2 MPa, 88 L/min was chosen as the acceleration factor calculation. Thus, Eq. (2) is 22.8096.

$$AF = \left(\frac{P_{test}}{P_{field}} \right)^m \times \left(\frac{F_{test}}{F_{field}} \right)^l \quad (2)$$

$$= \left(\frac{25.2}{7.0} \right)^2 \times \left(\frac{88}{50} \right)^1 = 22.8096$$

where,

AF : acceleration factor;

P_{test} P_{field} : acceleration & field pressure (MPa);

ω_{test} ω_{field} : acceleration & field flow (L/min);

m,l : Acceleration index ($m = 2$, $l = 1$).

Calculated acceleration factor Eq. (3) by substituting the acceleration test, time (t_{na}) is produced.

$$t_{na} = \frac{t_n}{AF} = \frac{61{,}000{,}000}{22.8096} \cong 2.7 \times 10^6 cycles \quad (3)$$

6. Life Test and Performance Test

6.1 Accelerated Life Test

The propriety of the design equations has been proven through the accelerated life test. The three unit valve assembly adopting the linear actuator is used in this test. Fig. 5 shows the accelerated life test.

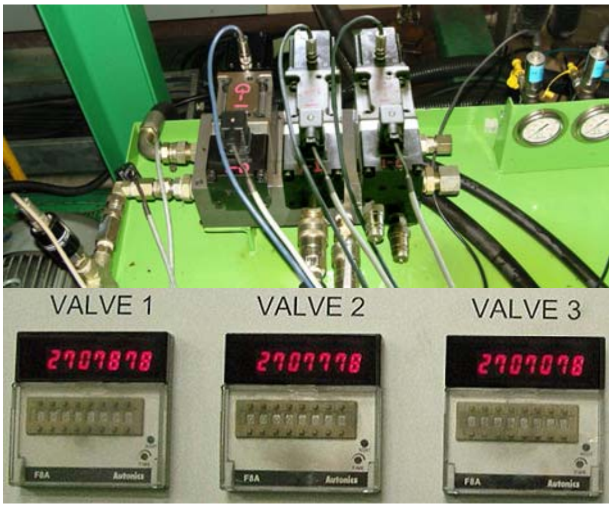

Fig. 5 Accelerated life test.

6.2 Attraction Force and Linearity Test

For attraction test, firstly, the prototype linear actuator is to be fastened to the attraction force test equipment, which is connected to load cell by mechanical coupling. When the work of coupling connection is done, the plunger must be surely tightened not to result in the eccentric phenomenon, and also it must be checked that the value of load cell is 0. The attraction force should be measured by changing the value of current form 0 to +3 A and form 0 to -3 A. Fig. 6 represents the measuring result of the attraction force. From Fig. 6, the attraction force is about 200 N at maximum current ±3 A and about 153 N at rated current ±2.2 A. In addition, the linearity is almost approaching to the first order function, $f(x) = 3.5\ x$. At this time, for overall region, the error rate of linearity is 1.90%, and the error rate of symmetrical characteristic is 3.05% ~ -2.00%. These mean that the test results for attraction force and linearity are generally satisfactory.

6.3 Test of Step Response

This test is to measure the time difference between supplying time of input step signal and reaction time of plunger. Here, the 80% control signal (8 V) to controller is used as input step signal and reaction of plunger is detected by output signal of LVDT. Referring

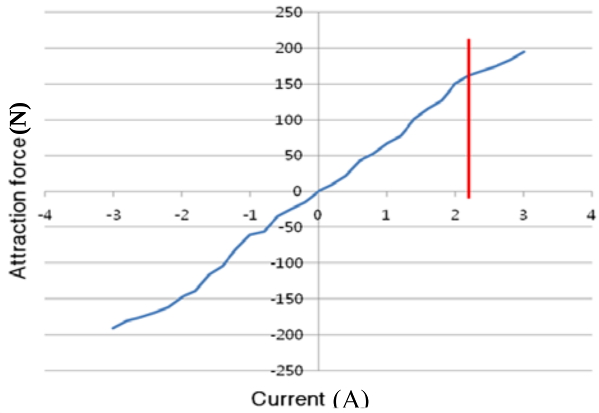

Fig. 6 Results of attraction force test.

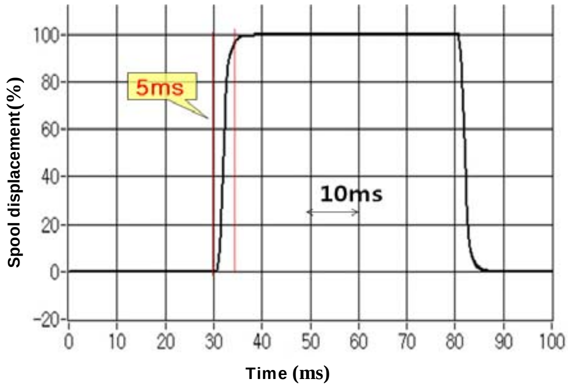

Fig. 7 Results of step response test.

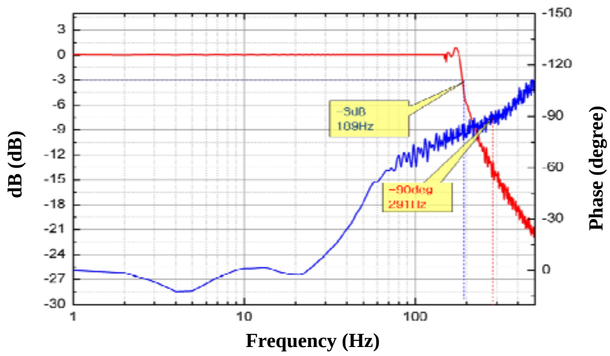

Fig. 8 Results of frequency response test.

to Fig. 7, the control signal 8 V is applied to controller at point of time 30 ms, and the reaction signal 5 V of LVDT is detected at point of time 35 ms. So, the step response time is 5 ms.

6.4 Test of Frequency Response

This test is similar to the test of step response. The input is control signal of controller and output is reaction signal of LVDT. This test performed at 25%

and 100% magnitude of input signal with 0.01 Hz ~200 Hz carrier frequency region. Fig. 8 is the test results for 25% control signal of controller. It shows that the -3dB frequency is about 189.

7. Conclusions

In this paper, as a reliability assessment study of linear actuator for valve operation, detailed analysis is performed about potential failure modes of linear actuator, and the effects and converting the importance grade of each failure modes into score, and determine test items for prior check the failures observed through failure analysis. And also, design equations of linear actuator for valve operation was composed.

(1) The high speed linear actuator reliability assessment techniques were established. In addition, the failure analysis data such as FMEA, CMA, FTA, 2-Stage QFD was written;

(2) The design equations are induced for design using between electromagnetic theories and empirical knowledge;

(3) The major test items of servo valve takes a long time for the accelerated life test. 3ea samples were calculated for the accelerated life test of time.

As a result of experiments, the step response of prototype linear actuator approaches 5 ms in Fig. 7, the operating frequency is about 189 Hz in -3dB gain and 291 Hz in -90 degree at 25% input signal in Fig. 8.

References

[1] C. Roters, Electro Magnetic Device, John Wiley & Sons, Inc., Canada, 1970, p. 213.

[2] B.J. Sung, E.W. Lee, H.E. Kim, Development of design program for on and off type solenoid actuator, in: Proceedings of the KIEE Summer Annual Conference, Jeju, Korea, July 10, 2002.

[3] C. Liu, Y.W. Yi, Micromachined magnetic actuators using electroplated permalloy, IEEE transactions on Magnetic 35 (3) (1999) 1976-1985.

[4] A. Steck, Modeling the magnetic propertics and dynamic behaviour of MRF-valves in flow mode, in: 8th International Conference on New Actuators & 2nd International Exhibition on Smart Actuators and Drive Systems, Bremen, Germany, June 10-12, 2002.

[5] Reliability Assessment Technology of High-Speed and Intelligent System, Ministry of Knowledge Economy, 2002.

[6] T. Arakawa, S. Niimi, Optimization technology of magnetic circuit for linear solenoid, SAE Technical Paper Series [Online], Mar. 4, 2002, http://papers.sae.org/2002-01-0565/.

[7] Hydraulic and Pneumatic Lap. of KIMM, Development of Low Consumption Power Type Solenoid Valves: KIMM-CSI Annual Report, Dec. 2001.

[8] J.S. Baek, E.W. Lee, H. Kim, Characteristics of non-magnetic ring for high-speed solenoid actuator, in: The Eleventh Biennial IEEE Conference on Electromagnetic Field Computation, Seoul, Korea, June 6-9, 2004.

[9] K. Kunio, Design Concept for DC Solenoid of Pneumatic Valve, KIMM Research Reporter, 1997.

[10] Barringer Associates, Inc., Weibull Database, 1994.

Journal of Energy and Power Engineering 8 (2014) 523-529

Single-Phase Inverter Synchronized to the Grid by Linear Kalman Filter in Microgrids

Oscar Carranza, Rubén Ortega, Gilberto Sánchez and Rubén Galicia
Instituto Politécnico Nacional, Escuela Superior de Cómputo, México D. F. 07738, México

Received: September 17, 2013 / Accepted: November 12, 2013 / Published: March 31, 2014.

Abstract: This paper presents the analysis and implementation of a synchronizer to the grid using a linear Kalman filter. The synchronizer is used in a single-phase inverter, which is applied in an environment of microgrids. The inverter converts the energy that comes from renewable energy sources (photovoltaic, wind, fuel cell, etc.). The main objective of obtaining the phase of the grid is to achieve a power factor close to unity in the inverter. For this reason it is vital that the phase difference between the synchronizer and the grid zero. To obtain synchronizer algorithm using LKF (linear Kalman filter) is necessary to know the EKF (extended Kalman filter). This allows to analyze the operation of the filter, which allows to reach reduce linear Kalman filter or also known as simplified Kalman filter. It is necessary to generate an orthogonal signal in order to obtain a stationary reference frame from a single-phase grid because the linear Kalman filter works with a stationary reference frame. Orthogonal signal is created with an all-pass filter.

Key words: Inverter, lineal Kalman filter, microgrids, synchronized.

1. Introduction

At present, renewable energy sources have a great impact on society because they are energy sources that do not pollute the environment and the cost of oil is becoming more expensive, which affects the cost of electric energy, also producing a high pollution. The renewable energy sources currently have a major impact on both the commerce and researches are about the photovoltaic, wind and hydrogen among others. These may be added to the power contribution of the grid and can work autonomously if necessary, providing power directly to the user. Under this perspective, power distribution schemes should be more flexible than existing ones. These new generation schemes are called DG (distributed generation) [1]. In this context, generation systems are divided into two types: generation systems that inject directly into the grid (grid connection operation) and generation systems with isolated loads from the grid (island mode operation). These systems are known as microgrid [2, 3].

In systems based on renewable energy generation, energy is obtained in AC or DC, but in most cases it is never constant. Therefore, the systems require one or more stages to inject the energy generated to the grid. One of the stages, it is a converter AC/DC or converter DC/DC that maintain constant voltage. Then place a DC/AC converter (inverter), which provides the appropriate values of voltage, current and frequency so that the energy is delivered to the grid in the best conditions. Given this condition, the inverter is responsible for regulating the voltage of the DC link, so as to regulate the current that is injected to the grid, and that is in phase with the grid [4, 5]. In order to reduce the switching frequency at the output signal of the inverter, a low-pass filter is placed, typically L filters are used, however, the trend is to use LCL filters having a higher order, the problem with these filters is its resonance frequency which can cause stability problems, so that it requires a more delicate control design [6].

Corresponding author: Oscar Carranza, Ph.D., research field: power electronics. E-mail: ocarranzac@ipn.mx.

To achieve a factor close to unity power, it is necessary to use a synchronization stage. This stage allows the synchronization of the output current of the inverter with grid voltage. The most used method is a PLL (phase locked loop) [6]. However, this paper presents the study of synchronization to the network using a linear Kalman filter to analyze its characteristics and set it as a highly viable alternative in synchronization with the grid. The EKF (extended Kalman filter) [7, 8] and the LKF (linear Kalman filter) have been widely used in estimates of speed and position in permanent magnet synchronous motors [9, 10] and permanent magnet synchronous generators [11, 12]. This paper presents the analysis of the EKF to understand its full operation. This allows reduction algorithm to obtain the LKF to be used as a method of synchronization to the grid.

The stages of the current control loop, the control loop voltage and grid filter are outside the scope of the paper and these stages are discussed in Ref. [4].

2. Single-Phase Inverter

The inverter that injects energy into the grid is a single-phase inverter with bipolar polarization and LCL output filter. Fig. 1 shows the schematic of the inverter with LCL output filter and the control structure is implemented. The control structure is constituted by synchronization to the grid, the current control loop to the grid and voltage control loop of the DC-Link.

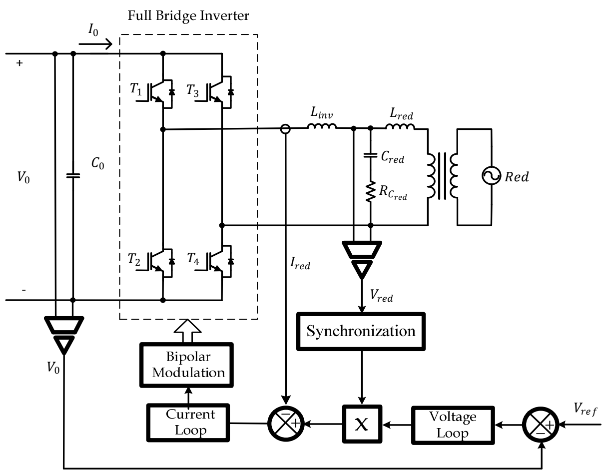

Fig. 1 Diagram of Inverter with LCL output filter and control structure.

3. Stationary Reference Frame

Synchronization techniques are based on the synchronous reference frame (dp), which is established from stationary reference frame $(\alpha\beta)$ of a three-phase system. However, in this particular case the system is single phase so that it should create a signal that allows complete orthogonally signals stationary reference frame. Therefore, it is obtained by:

$$V_{grid} = V_{alpha} \quad (1)$$

To create orthogonal signal is performed by:

$$V_{\beta} = G_{ort}(s) * V_{\alpha} \quad (2)$$

Where,

$$G_{ort}(s) = \frac{\omega - s}{\omega + s} \quad (3)$$

$G_{ort}(s)$ is an all-pass filter with a phase shift of the signal from 90° to the set frequency (ω), for this case, the signal has a frequency (f) of 50 Hz, therefore, ω is 314.159 rad/s. The Bode diagram of the all-pass filter is shown in Fig. 2.

Fig. 3 shows the scheme is used to create the stationary reference frame.

4. Linear Kalman Filter

EKF is analyzed to understand and implement the algorithm as a method of synchronization LKF to the grid.

EKF [10] is based on the discrete-time lineal dynamic systems, which can be expressed in the form of vectors in the discrete state space, as expressed by Eq. (4).

$$x(k+1) = A_k x(k) + B_k u(k) + \sigma(k)$$
$$y(k) = C_k x(k) + \mu(k) \quad (4)$$

where, y is the output vector and u is the vector of inputs, whereas x is called the state vector. A_k, B_k y C_k are system matrices, which in most cases are obtained from time-varying systems. A system model in discrete time can be obtained by discretization of the continuous time model [13]. $\sigma(t)$ and μ(t) represent noise and measurement process, with covariance matrices $Q(k)$ and $R(k)$, respectively, noise levels are unknown and act as disturbances of the system, white

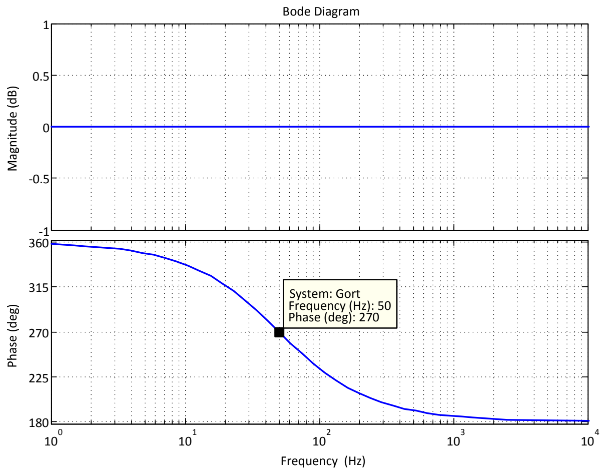

Fig. 2 The bode diagram of the all-pass filter, $G_{ort}(s)$.

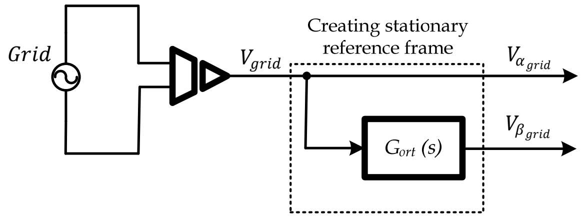

Fig. 3 Scheme for creating stationary reference frame.

noise and a stochastic nature. $Q$and $R$are regarded as adjustment parameters instead of actual measurements of the noise, which in most cases are constants chosen as diagonal until the filter works satisfactorily through trial and error. A third matrix is employed $P(K)$, which represents the error covariance of the state vector.

The EKF algorithm has two steps: estimation and correction. The first step sets a prediction of the state estimation (x_p) and of its covariance matrix (P_p). This is implemented by means of the following recursive relationships:

$$x_p(k) = A_k\tilde{x}(k) + B_k u(k)$$
$$P_p(k) = F(k)\tilde{P}(k)F^T(k) + Q \tag{5}$$

where, $F(k)$ is expressed by Eq. (6).

$$F(k) = \frac{\partial[A_k\tilde{x}(k)+B_k u(k)]}{\partial x}\Big|_{x=\tilde{x}(k)} \tag{6}$$

The second step corrects the prediction of the state estimation and that of its covariance matrix by feedback of the measured quantities. This is performed by means of the following recursive relationships.

$$\tilde{x}(k+1) = x_p(k) + K(k)\big[y(k) - C_k(k)x_p(k)\big] \tag{7}$$
$$\tilde{P}(k+1) = P_p(k) - K(k)H(k)P_p(k) \tag{8}$$

where Eq. (8) is determined by the Riccati equation of differences (EDR) and $K(k)$ is the gain of the Kalman filter matrix, which is defined by Eq. (9).

$$K(k) = P_p(k)H^T(k)\big[H(k)P_p(k)H^T(k) + R\big]^{-1} \tag{9}$$

where, $H(k+1)$ is determined by Eq. (10):

$$H(k) = \frac{\partial[C_k x(k)]}{\partial x}\Big|_{x=\tilde{x}(k)} \tag{10}$$

With this set of recursive equations is implemented EKF. The EKF used as the synchronization method of the grid is technically feasible. However, it requires a high computation when implemented in a digital signal processor, therefore, it is not used in practice, but provides a basis for analyzing the linear Kalman filter.

5. Linear Kalman Filter

To eliminate the problem of high computation, the EKF can be reduced to LKF or also known as Kalman filter simplified by a number of conditions. The LKF requires a little computation. The EKF calculates a variable gain matrix K(9) which requires a high computational cost. It is an important point in the implementation on a digital signal processor. However, if the filter structure is known, the calculation of K may be reduced to calculate a fixed gain matrix [14], this results in the LKF.

In the LKF, the state vector is defined by Eq. (11).

$$x = \begin{bmatrix} \theta \\ \omega_e \\ \acute{\rho} \end{bmatrix} \tag{11}$$

where, θ is the phase angle of the network, ω_e is the angular frequency of the grid and $\rho(k)$ is the process noise with Gaussian distribution with zero mean [15, 16]. In what is considered the following model to calculate the phase angle and the angular frequency, it is expressed by Eq. (12):

$$\theta(k+1) = \theta(k) + T_s\omega_e(k)$$
$$\omega_e(k+1) = \omega_e(k) + \acute{\rho}(k)$$
$$\acute{\rho}(k+1) = \acute{\rho}(k) + \rho(k) \tag{12}$$

For analysis of this synchronization method, variables are output from the grid voltages in the stationary reference frame, as shown by Eq. (13).

$$\begin{bmatrix} y_1(k) \\ y_2(k) \end{bmatrix} = \begin{bmatrix} V_\alpha \\ V_\beta \end{bmatrix} \tag{13}$$

The LKF synchronizer extracts the frequency information from the fundamental component of the grid voltages, whereas other harmonic components are considered as measurement noise. Note that this approach is suitable for this application, because the output voltages contain both low frequency harmonics.

Output variables are sine and cosine of the phase angle, expressed in normalized form to simplify the model and mainly Kalman gain, as shown by Eq. (14).

$$\begin{bmatrix} y_1(k) \\ y_2(k) \end{bmatrix} = \begin{bmatrix} \cos\theta(k) \\ \operatorname{sen}\theta(k) \end{bmatrix} + \begin{bmatrix} \mu_1(k) \\ \mu_2(k) \end{bmatrix} \quad (14)$$

where, both $\mu_1$and μ_2 represent switching noise and high-order low frequency harmonics. Considering the state space representation (11) and the input $u(k) = 0$, the state space system are rewritten as shown by Eq. (15).

$$\begin{aligned} x(k+1) &= A_s x(k) + \rho(k) \\ y(k) &= C_s x(k) + \mu(k) \end{aligned} \quad (15)$$

The expressions of the matrices A_s and $C_s x(k)$ are given by Eqs. (16) and (17):

$$A_s = \begin{bmatrix} 1 & T_s & 0 \\ 0 & 1 & 1 \\ 0 & 0 & 1 \end{bmatrix} \quad (16)$$

$$C_s x(k) = \begin{bmatrix} \cos\theta(k) \\ \operatorname{sen}\theta(k) \end{bmatrix} \quad (17)$$

Applying Eq. (10) to Eq. (17) it results Eq. (18).

$$H_s(k) = \frac{\partial C_s x(k)}{\partial x} = \begin{bmatrix} -\operatorname{sen}\theta(k) & 0 & 0 \\ \cos\theta(k) & 0 & 0 \end{bmatrix} \quad (18)$$

However, to simplify $H_s(k)$ uses the dq to transform matrix (T) shown by Eq. (19).

$$T(\theta) = \begin{bmatrix} \cos\theta & -\operatorname{sen}\theta \\ \operatorname{sen}\theta & \cos\theta \end{bmatrix} \quad (19)$$

$T(\theta)$ is an orthogonal matrix, ie, $T^T(\theta)T(\theta) = I$. As $H_s(k)$ can be expressed by Eq. (20):

$$H_{LKF}(k) = \begin{bmatrix} \cos\theta & \operatorname{sen}\theta \\ -\operatorname{sen}\theta & \cos\theta \end{bmatrix}^T \begin{bmatrix} 0 & 0 & 0 \\ 1 & 0 & 0 \end{bmatrix} \quad (20)$$

Where,

$$H_s = \begin{bmatrix} 0 & 0 & 0 \\ 1 & 0 & 0 \end{bmatrix} \quad (21)$$

Applying Eq. (20) to Eq. (9), it can obtain simplified filter gain $K_s(k)$, which is shown in Eq. (22).

$$K_s(k) = \begin{bmatrix} 0 & K_{s1} \\ 0 & K_{s2} \\ 0 & K_{s3} \end{bmatrix} \begin{bmatrix} \cos\theta(k) & -\operatorname{sen}\theta(k) \\ \operatorname{sen}\theta(k) & \cos\theta(k) \end{bmatrix} \quad (22)$$

K_{s1}, K_{s2} and K_{s3} are LKF gains that are calculated using the Matlab command DLQE (A_s,G_s, H_s, Q_s, R_s) [17], with the input matrices shown in Eq. (23).

$$G_s = R_s = \begin{bmatrix} 0 & 0 & 0 \\ 0 & 0 & 0 \\ 0 & 0 & 1 \end{bmatrix}; \; Q_s = \delta \begin{bmatrix} 1 & 0 \\ 0 & 1 \end{bmatrix} \quad (23)$$

In Eq. (23), the parameter δ allows to adjust the noise rejection ability, being chosen by trial and error.

With previous development LKF is expressed by Eq. (24).

$$\begin{aligned} \varepsilon(k) &= V_\beta(k)\cos\tilde{\theta}(k) - V_\alpha(k)\operatorname{sen}\tilde{\theta}(k) \\ \tilde{\theta}(k+1) &= \left[\tilde{\theta}(k) + T_s\tilde{\omega}_e(k) + K_{s1}\varepsilon(k)\right]_{-\pi}^{\pi} \\ \tilde{\omega}_e(k+1) &= \tilde{\omega}_e(k) + \acute{\rho}(k) + K_{s2}\varepsilon(k) \\ \acute{\rho}(k+1) &= \acute{\rho}(k) + K_{s3}\varepsilon(k) \end{aligned} \quad (24)$$

Notably LKF gains are independent of the characteristics of the grid and can be used in different grid conditions. Another advantage of using LKF synchronizer is that the algorithm is very efficient in terms of computation and can be implemented in a digital signal processor without any difficulty.

Fig. 4 shows the scheme of using LKF synchronizer.

6. Results

Synchronization method to the grid under study has been evaluated by means of accurate PSIM™ 7.0.5 simulations [18].

Fig. 5 shows there is no phase shift between the real phase and the phase obtained by using PLL and LKF synchronizers.

This is also demonstrated in Fig. 6, which shows the behavior of the grid voltage and the sinusoidal voltage that is obtained through synchronizer using PLL and synchronizer using LKF.

One way to evaluate the response of the synchronizers is applying frequency steps so that the steps are applied to grid frequency of 60 Hz to 50 Hz

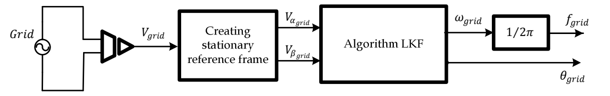

Fig. 4 Scheme of synchronizer using a Kalman filter Linear.

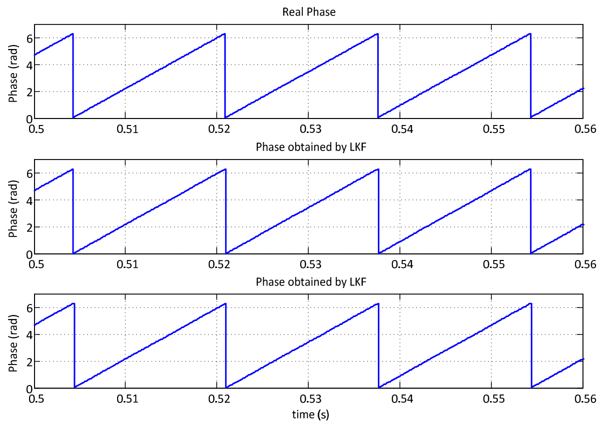

Fig. 5 Behavior of the phase angle of synchronization methods to the grid (60 Hz).

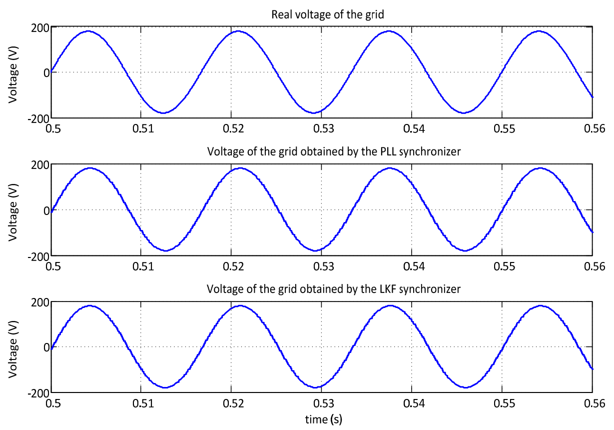

Fig. 6 Behavior of the grid voltage of synchronization methods (60 Hz).

and 60 Hz to 50 Hz, which can obtain the response time of each of synchronizers. Fig. 7 shows the phase behavior of the two synchronizers. When a frequency step is applied to the grid of 60 Hz to 50 Hz, it is observed that the response time of the synchronizer using PLL is 165 ms, corresponding to eight cycles of the grid signal and the response time of synchronizer using LKF is 125 ms, which corresponds to six cycles of the grid signal.

Fig. 8 shows the response of the grid voltage when applying a frequency step of the grid of 60 Hz to 50 Hz.

Fig. 9 shows the phase behavior of the two synchronizers. When a frequency step is applied to the

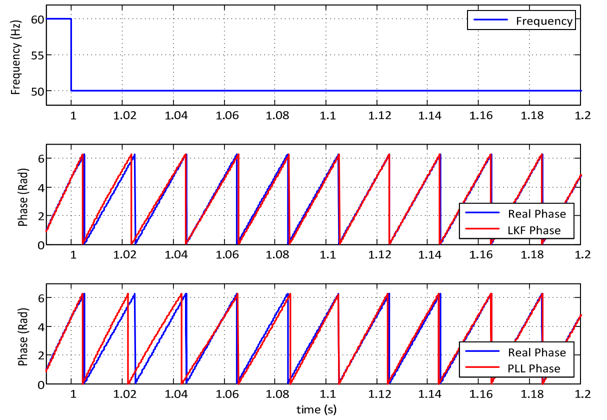

Fig. 7 Behavior of the phase of a step to the grid frequency of 60 Hz to 50 Hz.

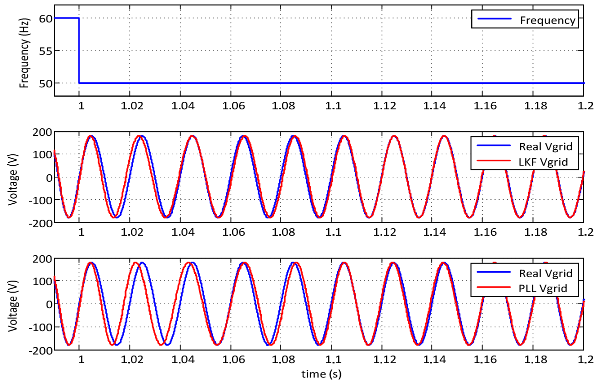

Fig. 8 Behavior of the grid voltage of a step to the grid frequency of 60 Hz to 50 Hz.

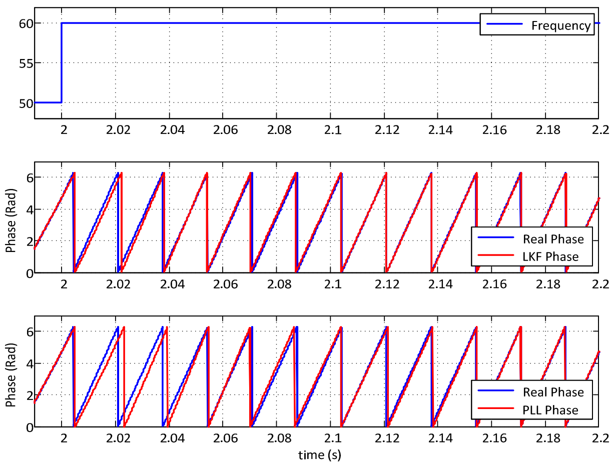

Fig. 9 Behavior of the phase of a step to the grid frequency of 50 Hz to 60 Hz.

grid of 50 Hz to 60 Hz, it is observed that the response time of the synchronizer using PLL is 171 ms, corresponding to ten cycles of the grid signal and the response time of synchronizer using LKF is 120 ms, which corresponds to seven cycles of the grid signal.

Fig. 10 shows the response of the grid voltage when applying a frequency step of the grid of 50 Hz to 60 Hz, which yields the same results as in Fig. 9. In both cases it is observed that the synchronizer using LKF has a lower response time in comparison with synchronizer using PLL, which in the worst case is 120 ms, and always in six cycles of the network signal.

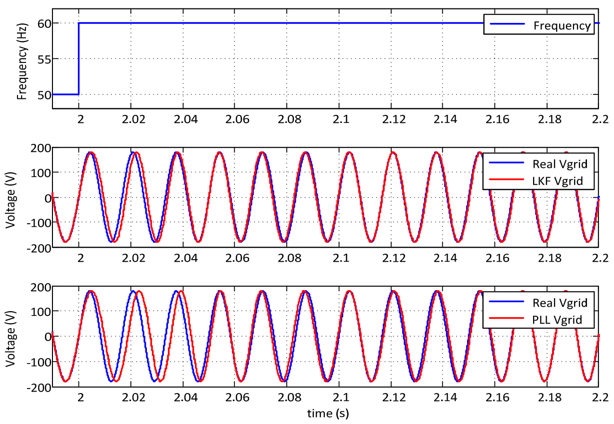

Fig. 10 Behavior of the grid voltage of a step to the grid frequency of 50 Hz to 60 Hz.

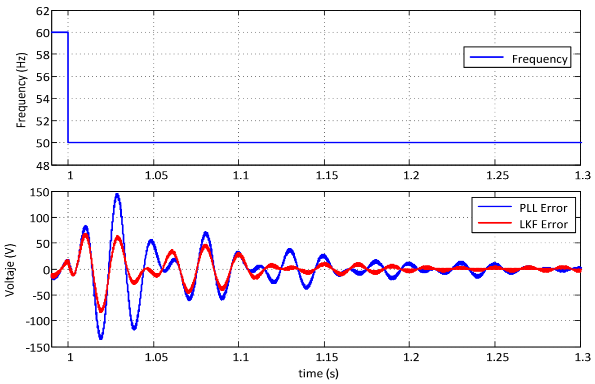

Fig. 11 Behavior of the grid voltage of a step to the grid frequency of 60 Hz to 50 Hz.

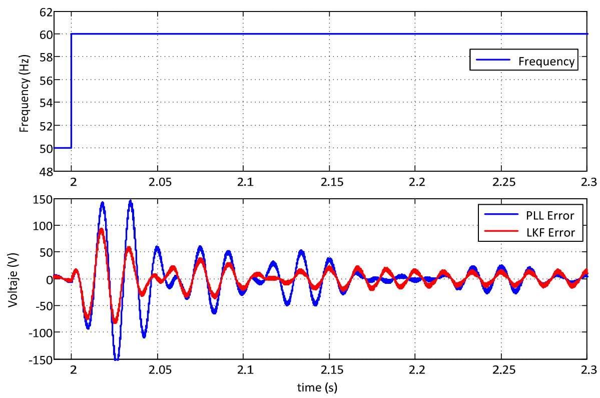

Fig. 12 Behavior of the grid voltage of a step to the grid frequency of 60 Hz to 50 Hz.

Figs. 11 and 12 show the grid voltage behavior of the synchronizer. It is observed that the response time synchronizer using LKF is 125 ms, which corresponds to six cycles of the grid signal.

7. Conclusions

The synchronizer to the grid using a linear Kalman filter has been designed and evaluated in this paper. A stage of creating an orthogonal signal is implemented. Orthogonal signal allows to use the stationary reference frame. To evaluate the synchronizer using LKF is deployed to a synchronizer using PLL, because it is the most widely used. The synchronizer using LKF has a lower response time in comparison with synchronizer using PLL, which in the worst case is 125 ms, and always in six cycles of the grid signal. Synchronizers were developed in C, in the PSIMTM 7.0.5 simulations.

References

[1] Renewable 2009, Global Status Report, REN21 Steering Committee, World Watch Institute, Washington, DC, 2009.

[2] H.B. Puttgen, P.R. MacGregor, F.C. Lambert, Distributed generation: Semantic hype or the dawn of a new era?, IEEE Power and Energy Magazine 1 (1) (2003) 22-29.

[3] R. Lasseter, A. Akhil, C. Marnay, J. Stephens, J. Dagle, R. Guttromson, et al., White paper on integration of distributed energy resources, The CERTS microgrid concept, Consortium for Electric Reliability Technology Solutions, 2002, pp. 1-27.

[4] E. Figueres, G. Garcera, J. Sandia, F. Gonzalez-Espín, J. Calvo, Sensitivity study of the dynamics of three-phase photovoltaic inverters with an LCL grid filter, IEEE Transactions on Industrial Electronics 56 (3) (2009) 706-717.

[5] M. Liserre, R. Teodorescu, F. Blaabjerg, Stability of photovoltaic and wind turbine grid-connected inverter for a large set of grid impedance values, IEEE Transactions on Power Electronics 21 (1) (2006) 263-272.

[6] M. Ciobotaru, R. Teodorescu, F. Blaabjerg, Control of single-stage single-phase PV inverter, in: 11th European Conference on Power Electronics and Applications, Dresden, Sept. 2005.

[7] S. Bolognani, L. Tubiana, M Zigliotto, Extended Kalman filter tunning in sensorless PMSM drives, IEEE Transactions on Indfustrial Applications 39 (6) (2003)

1741-1747.

[8] A. Qiu, W. Bin, H. Kojori, Sensorless control of permanent magnet synchronous motor using extended Kalman filter, in: Canadian Conference on Electrical and Computer Engineering, Canada, May 2-5, 2004.

[9] S. Bolognani, R. Oboe, M. Zigliotto, Sensorless full-digital PMSM drive With EKF estimation of speed and rotor position, IEEE trans. on Industrial Electronics 46 (1) (1999) 184-191.

[10] T.F. Chan, P. Borsje, W.M. Wang, Application of unscented Kalman filter to sensorless permanent-magnet synchronous motor drive, IEEE International Electric Machines and Drives Conference, Miami, FL, May 3-6, 2009.

[11] L.G. González, E. Figueres, G. Garcerá, O. Carranza, Maximum-power-point tracking with reduced mechanical stress applied to wind-energy-conversion-systems, Applied Energy 87 (7) (2010) 2304-2312.

[12] O. Carranza, E. Figueres, G. Garcerá, L.G. González, Comparative study of speed estimators with highly noisy measurement signals for wind energy generation systems, Applied Energy 88 (3) (2011) 805-813.

[13] K. Ogata, Discrete-Time Controls System, Prentice Hall, NJ, USA, 1995.

[14] L. Harnefors, Speed estimation from noisy resolver signal, in: Proceedings of the Sixth International Conference on Power Electronics and Variable Speed Drives, Nottingham, UK, Sept. 23-25, 1996.

[15] M.C. Huang, A.J. Moses, F. Anayi, X.G. Yao, LKF (linear Kalman filter) sensorless control for permanent magnet synchronous motor based on orthogonal output linear model, in: International Symposium on Power Electronics, Electrical Drives, Automation and Motion, Taormina, Italy, May 23-26, 2006.

[16] L. Yong, Z.Q. Zhu, D. Howe, Instantaneous torque estimation in sensorless direct-torque-controlled brushless DC Motors, IEEE Transactions on Industry Applications 42 (5) (2006) 1275-1283.

[17] Matlab 7.6, User’s Guide (2008), Math Works Inc., Feb. 2008.

[18] User´s Guide (2006), Powersim Inc., Mar. 2006.

Journal of Energy and Power Engineering 8 (2014) 530-542

Step-Loading Characteristics of Gas Engine Cogeneration System Using Doubly-Fed Induction Generator in Stand-Alone Operation

Tetsuji Daido[1], Yushi Miura[1],Toshifumi Ise[1] and Yuki Sato[2]

1. Division of Electrical, Electronic and Information Engineering, Graduate School of Engineering, Osaka University, Osaka 565-0871, Japan

2. Energy Technology Laboratory, Osaka Gas Co., Ltd., Osaka 554-0051, Japan

Received: October 31, 2013 / Accepted: November 27, 2013 / Published: March 31, 2014.

Abstract: Application of a DFIG (doubly-fed induction generator), which is one of adjustable speed generators, to a gas engine cogeneration system has been investigated. To operate during a blackout as an emergency power supply is one of important roles for the gas engine cogeneration system. In the case of conventional constant speed of synchronous generator, the amount of the allowed step load is limited to around 30% of the rated power. On the other hand, DFIG is expected to increase the amount of step load during the stand-alone operation. In this paper, it has been demonstrated that an increase in the gas engine speed resulted in an increase in the maximum amount of step load using experimental equipment with a real gas engine. It has been concluded that the proposed system can improve the performance of an emergency power supply at step-loading.

Key words: Step load change, doubly-fed induction generator, gas engine cogeneration system, stand-alone operation.

1. Introduction

In recent years, a lot of attention has been paid to cogeneration which utilizes natural resources efficiently to reduce CO_2 emission. A conventional gas engine cogeneration whose rated power is more than three hundred kilowatt has used a constant-speed synchronous generator directly connected to loads and grid. However, the efficiency of the gas engine operating at a constant speed is deteriorated in part-load condition due to the gas engine characteristics [1, 2]. Refs. [1, 2] show the decrease of part-load efficiency in the schematic diagram of the steady-state efficiency according to the rotational speed. In addition, the gas engine is incapable of operating in overloaded condition because the output torque of the gas engine reaches to the upper limit. Moreover, when it comes to operating as a stand-alone system, the permitted frequency deviation restricts the maximum amount of step load change.

Employment of an adjustable speed generator can effectively solve the above-mentioned problems. Therefore, in this study, application of a DFIG (doubly-fed induction generator) to the gas engine cogeneration system as one of the ways to enables the gas engine to operate at adjustable speed regardless of grid frequency has been investigated. An advantage of DFIG is to require less converter power capacity, which is only the maximum amount of the DFIG secondary side power depending on the operational speed range, compared with other adjustable speed ac generators that require converting full output power [3, 4]. The adjustable speed operation makes the gas engine more efficient thanks to operating at an optimal

Corresponding author: Tetsuji Daido, master, research fields: power electronics and distributed generation. E-mail: daido@pe.eei.eng.osaka-u.ac.jp.

speed according to the load ratio. In addition, the adjustable speed operation enables the gas engine to operate in overloaded condition for a short time. Furthermore, an increase in the amount of step-loading during the stand-alone operation is expected because the DFIG is prevented from causing the frequency excursion by controlling the secondary side frequency.

To operate during a blackout as an emergency power supply is one of the important roles for the gas engine cogeneration system. In the preceding literatures [5-7], the authors have proposed the start-up method of the DFIG with a charged capacitor during a blackout because the DFIG requires an excitation source for the startup. Moreover, the authors have investigated stand-alone operation in the case of applying and disconnecting loads following the blackout start. Refs. [8-11] also investigated the response to application and disconnection of loads in the stand-alone operation. Ref. [8] dealt with stand-alone wind-diesel generation using DFIG and showed the optimal control method of diesel genset. In addition, the control method to keep constant voltage and constant frequency irrespective of load variation was proposed and verified by experiment. Ref. [9] showed the indirect stator-flux-oriented vector control for stand-alone operation and a simplified diesel engine model. Moreover, they have investigated the response to step load change. Ref. [10] proposed another control method of stand-alone DFIG which referred to reference voltage space vector control. In this literature, step-loading and step-unloading have been done at a constant rotational speed by experiment. Ref. [11] also investigated step-loading and step-unloading of the stand-alone operation of a DFIG by experiment. In this reference, the stator-flux-oriented vector control has also been used. Although these preceding literatures investigated step load change at stand-alone operation, operation continuity of stand-alone genset with DFIG did not investigate.

In terms of improving the gas engine performance, various approaches have been addressed [12-14]. Recent mainstream of medium size gas engine is to adopt lean-burn and miller cycle technologies to realize high electrical efficiency at the expense of the response performance to the load changes. Therefore, in the case of a conventional constant speed gas engine genset in the stand-alone operation, the amount of step load to the gas engine is limited to approximately 30% of the rated power so as to make the frequency excursion within approximately ±15%. On the other hand, the DFIG is expected to increase the amount of step load in the stand-alone operation because the DFIG is able to keep constant output frequency in spite of change of rotational speed during load change.

In this paper, stand-alone operation of a DFIG driven by a real gas engine at step load change has been investigated by both a computer simulation and experiment. In the study, the amount of step load and the reference of the rotational speed were changed in order to investigate the operation continuity when the loads were applied and disconnected. The experimental results have revealed that the maximum amount of step load in which the genset was capable of continuing its operation increased as the operational speed became faster, which resulted in improvement of the step-loading characteristics of the gas engine genset. Based on the experimental results, a simplified simulation model of the gas engine has been developed to investigate the operation continuity at step-loading. These experimental and simulation results have revealed what factor determines the maximum amount of step load in the case of a genset with a DFIG.

2. Main Circuit and Control System

2.1 Circuit Configuration

A main circuit configuration of the proposed system is shown in Fig. 1. Voltages v_s, v_r, currents i_r and i_g are defined as follows: stator phase voltage $v_s = (v_{sa}, v_{sb}, v_{sc})$, rotor phase voltage $v_r = (v_{ra}, v_{rb}, v_{rc})$, rotor side converter output current $i_r = (i_{ra}, i_{rb}, i_{rc})$ and grid side

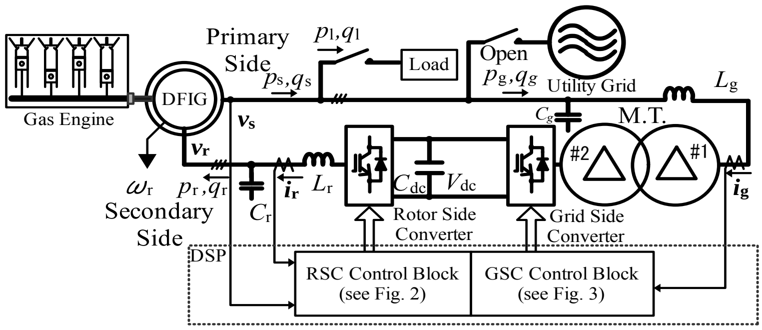

Fig. 1 Schematic diagram of the main circuit.

converter output current $i_g = (i_{ga}, i_{gb}, i_{gc})$. Parameters of the main circuit are summarized in Table 1. The DFIG was coupled with the gas engine directly. The DFIG parameters are summarized in Table 2. In this study, all equipment were scaled down compared with the size of a practical system. In the main circuit, two power converters were installed between the DFIG primary and secondary sides with a common dc link. These converters are called "RSC (rotor side converter)" and "GSC (grid side converter)", respectively. These converters function as ac-to-ac power conversion. In the experiment, the rated output voltages of the RSC and GSC are both 220 V and the rated output currents of the RSC and the GSC are 24 A and 11 A, respectively. The large converter ratings compared with the DFIG rating (1.1 kW) were chosen so as not to be lack of the converter capacity at the various experimental conditions. LPFs (LC low-pass filters) were connected to each converter's ac output side. Loads and a utility grid can be connected to the DFIG primary side. In this paper, it was assumed that the DFIG was disconnected from the utility grid. A load equipment which has constant impedance characteristics was used. An electrolytic capacitor which was initially charged was connected to the dc link part. A M. T. (matching transformer) was installed between the GSC and the DFIG primary side to match the voltage level. The parameters of the M. T. are shown in Table 3.

2.2 Control System

The converters are controlled based on the following three control blocks.

Table 1 Circuit parameters.

L_r	4 mH	L_g	4 mH
C_r	10 μF	C_g	10 μF
C_{dc}	11.8 mF		

Table 2 DFIG parameters.

Rated		Parameter	
Power	1.1 kW	Stator resistance	0.536 Ω
Frequency	60 Hz	Rotor resistance	2.377 Ω
Number of pole	6	Leakage reactance	1.256 Ω
Stator voltage	210 V	Magnetizing reactance	26.99 Ω
Stator current	6.3 A	Iron resistance	3.658 Ω
Rotor voltage	32.9 V	Stator/rotor turn ratio	6.38
Rotor current	20.3 A		

Table 3 Parameters of matching transformer.

Phase	3	Primary side voltage	460 V
Capacity	10 kVA	Secondary side voltage	230 V
Frequency	60 Hz	Primary side current	12.6 A
Connection	Δ-Δ	Secondary side current	25.2 A
% Impedance	1.54%	Magnetizing current	4.10%

The RSC control block diagram is shown in Fig. 2. The RSC controls the primary side voltage and frequency. Superscript * indicates reference values. The control system employs PI (proportional and integral) control, and the transfer function $G_{PI}(s)$ is defined as follows:

$$G_{\mathrm{PI}}(s) = K\left(1 + \frac{1}{s\tau}\right) \quad (1)$$

where, K and τ represent a gain and an integral time constant, respectively. The phase angle of the RSC output current is represented in θ_{slip} and is calculated by $\int (\omega_1^* - \omega_r)\, dt$, where ω_1^* is a reference of the grid electrical synchronous angular speed, which is given by $2\pi f_0$. The value of f_0 is 60 Hz in this study. The DFIG

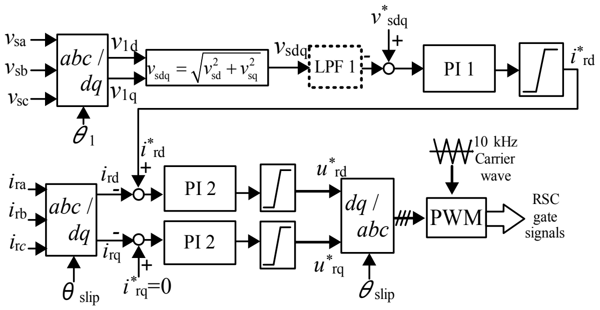

Fig. 2 RSC control block diagram.

rotational angular speed in electrical angle ω_r is obtained by a speed encoder. The *rms* value of the primary side line voltage is equal to v_{sdq} which is shown in Fig. 2. Ripples on the voltage v_{sdq} are eliminated by the LPF1. A current control is used in the RSC control block diagram based on the *dq* rotational coordinates with the reference of the RSC q-axis output current $i_{rq}{}^* = 0$.

A GSC control block diagram is shown in Fig. 3. GSC controls both the dc link voltage to keep it constant and the reactive current i_{gq} to supply the excitation current from the primary side. In this control, the d-axis current corresponds to the active current and the q-axis current corresponds to the reactive current. In order to avoid interfering with the d and q axes current control, a decoupling control is used. In addition, the primary side voltages in the dq rotational coordinates v_{sd} and v_{sq} are used for feed-forward control so as to improve the response speed of the current control.

A PLL (phase locked loop) control block diagram is shown in Fig. 4. The PLL is used to acquire the phase angle of the primary side voltage θ_1. A steady-state output frequency is represented by f_0. The primary side q-axis voltage is controlled to be zero so that the d-axis is aligned with the primary side a-phase voltage.

The reference values used in the control blocks are summarized in Table 4. The parameters of PI controllers and LPFs are shown in Tables 5 and 6, respectively.

2.3 Sharing Excitation Current Control

In the case of our experimental equipment, the excitation current from the secondary side became excessive when the DFIG was excited only from the secondary side. Therefore, we excited the DFIG from the primary side using the reference of the GSC q-axis current i^*_{gq}, and shared the excitation current between the primary and secondary sides to suppress the secondary current. From no load test of the DFIG and computer simulation results, we tentatively determined that the reference value of the excitation current from the primary side $i_{gq}{}^*$ was 5 A [3]. This means that the GSC outputed 1 kilo-var (leading).

3. Experimental Results of Stand-Alone Operation

In this chapter, results of application and disconnection of step loads in the stand-alone operation are shown.

3.1 Experimental Conditions

Fig. 5 shows the appearance of the DFIG directly coupled with a gas engine. The gas engine used in the experiment was converted from a general-purpose diesel engine (producted by Yanmar, type: NFAD6). The reference of the gas engine rotational speed was changed from 1,000 rpm to 1,600 rpm by 100 rpm. The following constant impedance loads were used for application and disconnection to the genset: 100, 200, 400 and 600 W.

3.2 Application of Step Load

In this paper, the two results under the following conditions are shown as typical responses of application of the loads:

- load: 400 W, the reference of the rotational speed: 1,300 rpm (rotational frequency in electrical angle is 65 Hz);
- load: 400 W, the reference of the rotational speed: 1,400 rpm (rotational frequency in electrical angle is 70 Hz).

The former and latter results are shown in Figs. 6 and 7, respectively.

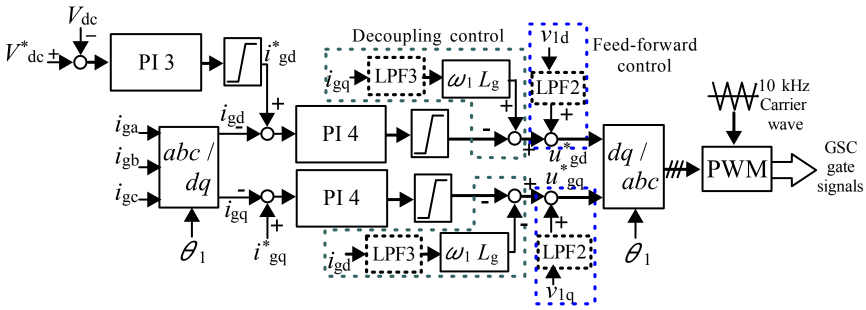

Fig. 3 GSC control block diagram.

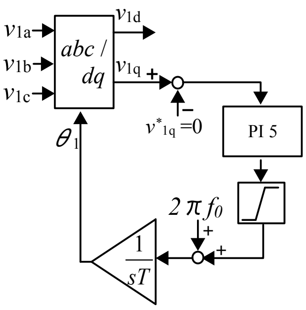

Fig. 4 Phase locked loop block diagram.

Table 4 Reference values.

$v_{sdq}{}^*$	200 V	$i_{rq}{}^*$	0 A
$V_{dc}{}^*$	200 V	$i_{gq}{}^*$	5 A

Table 5 PI parameters.

	Gain	Time constant (s)	Cutoff frequency (Hz)
PI 1	200 V	0.1	
PI 2	25.2	0.0597	1,000
PI 3	0.05	0.05	
PI 4	25.2	0.0597	1,000
PI 5	0.1	0.06	

Table 6 LPF parameters.

	Time constant (s)	Cutoff frequency (Hz)
LPF 1	0.01	15.9
LPF 2	0.031	5.13
LPF 3	0.031	5.13

Fig. 5 Appearance of DFIG coupled with gas engine.

Before application of the load, the primary side voltage was controlled to be constant and any load was not connected. At that time, the generated power circulated between the primary and secondary sides. Then, the 400 W load was applied as indicated by the first dotted line with blue in Figs. 6 and 7.

Fig. 6 shows that the genset was incapable of continuing its operation after the 400 W step-loading as shown in Fig. 6a when the reference of the rotational speed was 1,300 rpm because the primary side voltage shown in Fig. 6b went to zero after the step-loading. Fig. 6c genset lagged behind the increase in the load. As a result, the slip of the DFIG increased and the output current of the RSC increased as shown in Figs. 6d and 6e because the circulating power from the primary side to the secondary side increased. At the same time, Fig. 6f shows that the GSC d-axis current, which corresponds to the active current and is used for controlling the *dc* link voltage shown in Fig. 6g to constant, increased as the speed went down. Finally, the RSC tripped due to overcurrent when the DFIG rotated at around 950 rpm as indicated by the second dotted line with red in Fig. 6. At this time, the peak value of the RSC output current was 40 A and the slip of the DFIG was 0.21. In addition, the GSC d-axis output current was 5 A, which means that 1,000 W of active power flowing from the primary side to the dc-link part. This power provided the secondary side power. In addition, this was also consumed in the power conversion stage as energy loss. After the RSC tripped, the stored energy in the generator reactance and the filter capacitances resonated. Then the primary

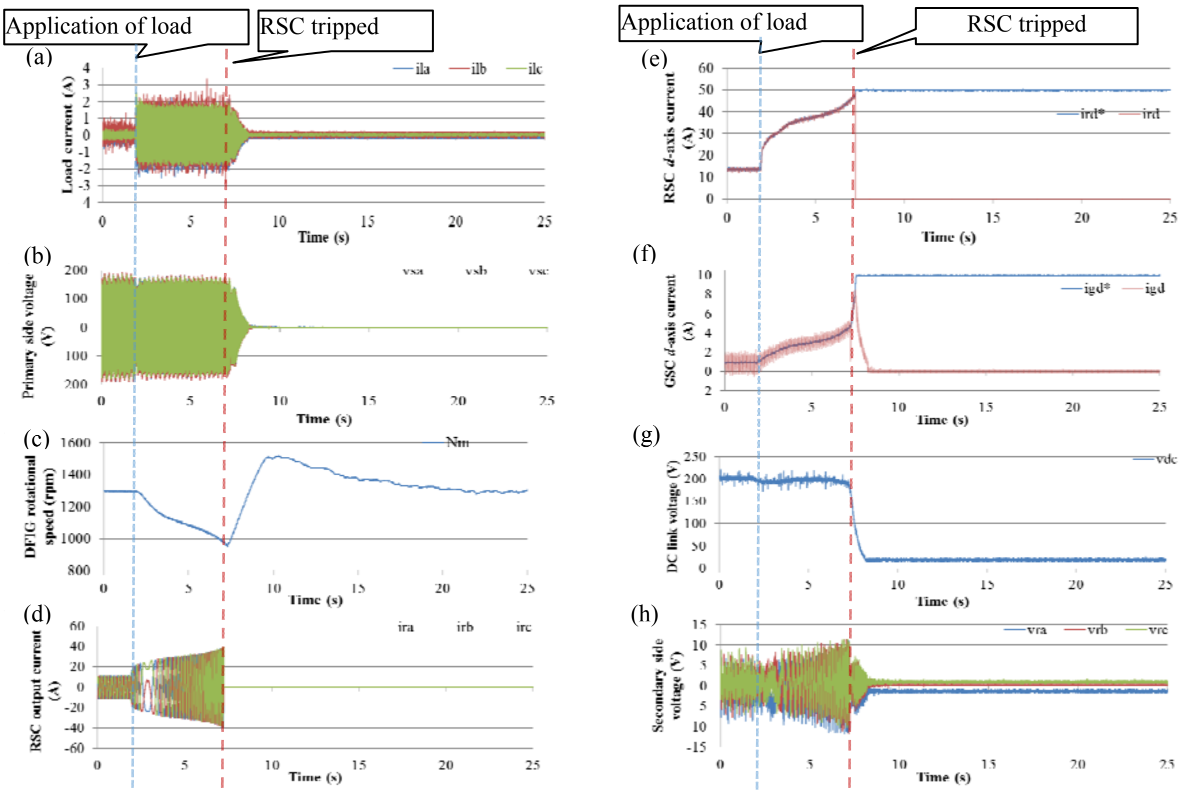

Fig. 6 Waveforms of application of step load (400 W, P.F. = 1) when the reference of the rotational speed was 1,300 rpm. (a) Primary side phase voltage v_{sa}, v_{sb}, v_{sc}; (b) Secondary side phase voltage v_{ra}, v_{rb}, v_{rc}; (c) RSC output current i_{ra}, i_{rb}, i_{rc}; (d) RSC d-axis output current i_{rd} and its reference i_{rd}^*; (e) Load current i_{la}, i_{lb}, i_{lc}; (f) DFIG rotational speed; (g) GSC d-axis output current i_{gd} and its reference i_{gd}^*; (h) dc-link voltage v_{dc}.

and secondary side voltages exponentially decreased to zero as shown in Figs. 6b and 6h. Eventually, the 400 W load was not able to be applied to this system.

On the other hand, Fig. 7 shows that the genset successfully continued its operation after the 400 W step-loading as shown in Fig. 7a when the reference of the rotational speed was 1,400 rpm because the primary side voltage was kept constant as shown in Fig. 7b regardless of the step-loading. Fig. 7c shows that the lowest speed of 1,260 rpm was higher than the previous experiment after application of the load since the initial rotational speed was higher. In other words, the stored energy in the inertia of the DFIG and the gas engine was higher than the previous case. Therefore, the delay of the gas engine response was compensated by the inertia energy. When the rotational speed went down, the secondary side phase voltage shown in Fig. 7d decreased because the absolute value of the slip decreased as shown in Fig. 7c and the internal induced voltage at the rotor side decreased. On the contrary, the RSC output current shown in Figs. 7e and 7f and the GSC d-axis output current increased in Fig. 7g when the rotational speed went down. That is because the active power flowing from the primary side to the dc-link increased due to the loss of the power conversion stage between the primary and secondary sides when the rotational speed slowed down. Then the active power at the primary side increased. That led to increase in the RSC output current. Fig. 7h shows that the dc-link voltage was kept constant regardless of the step-loading.

These results have revealed that the rating of the RSC output current and the lowest rotational speed have limited the maximum amount of step load in which the genset is capable of continuing its operation. However, the secondary side current can be suppressed by redesigning the DFIG stator/rotor turn stator/rotor turn ratio. Then the secondary side voltage

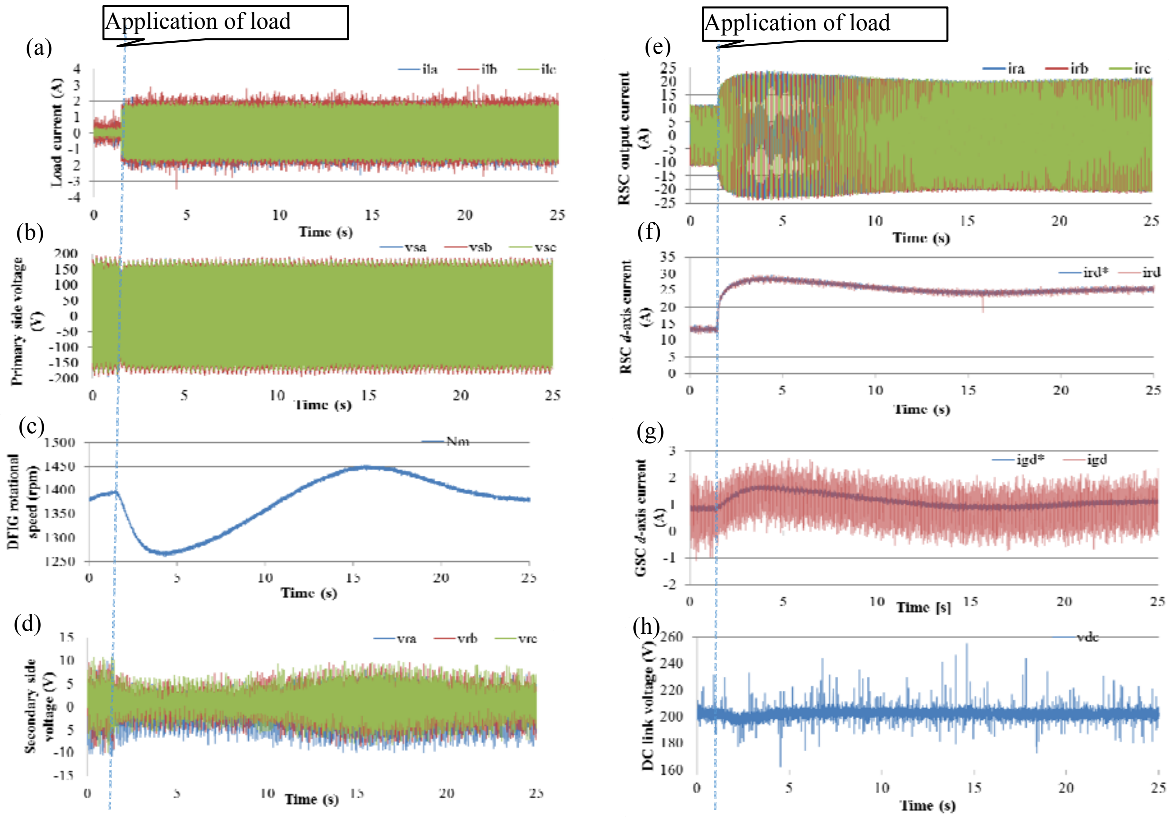

Fig. 7 Waveforms of application of step load (400 W, P.F. = 1) when the reference of the rotational speed was 1,400 rpm. (a) Primary side phase voltage v_{sa}, v_{sb}, v_{sc}; (b) Secondary side phase voltage v_{ra}, v_{rb}, v_{rc}; (c) RSC output current i_{ra}, i_{rb}, i_{rc}; (d) RSC d-axis output current i_{rd} and its reference i_{rd}^*; (e) Load current i_{la}, i_{lb}, i_{lc}; (f) DFIG rotational speed; (g) GSC d-axis output current i_{gd} and its reference i_{gd}^*; (h) dc link voltage v_{dc}.

would become an issue for the rotor side converter instead of the secondary side current when loads are applied.

3.3 Operation Continuity Performance to Step-Loading

Table 7 shows the operation continuity performance of the genset when the step loads were applied. The power factor of these loads was unity. The system behavior after the step-loading is categorized into four. Each of the behavior is represented by the symbols shown as follows:

○: Step load is able to be applied to the genset;

△: The load is able to be gradually applied to the genset. However, the step-loading leads to the RSC trip owing to the drop of the rotational speed;

□: When the load is gradually applied to the genset, the RSC does not become overcurrent. However, the gas engine hits its maximum output torque and the gas engine ends up stalling;

×: The load is not able to be applied to the genset even though the load is gradually increased because of both the RSC overcurrent and upper limit of the gas engine output torque.

Table 7 The operation continuity to step-loading.

The amount of applied load	Reference of the rotational speed (rpm)						
	1,000	1,100	1,200	1,300	1,400	1,500	1,600
100 W	○	○	○	○	○	○	○
200 W	△	○	○	○	○	○	○
400 W	□	□	□	△	○	○	○
600 W	×	×	□	□	□	□	○

Overall, the higher the reference of the rotational speed was, the more amount of load we were able to apply to the genset.

The cause of most of the stop of the operation was that the RSC tripped due to overcurrent. There are two

cases for the trip in terms of the initial rotating speed and the lowest speed after the step-loading. The first case is that the higher the rotational speed became, the less the RSC output current became. That was because the higher the rotational speed was, the less the active power flowing from the primary side to the secondary side became. Therefore, the first case of the trip is that the RSC tripped due to overcurrent even though the rotational speed did not go down after the step-loading. In this case, the reference of the rotational speed should be increased in order to avoid overcurrent of the RSC. The second case of the trip is that the RSC tripped after the step-loading because the gas engine speed went down. In this case, the response speed of the gas engine affected the drop of the gas engine speed. Therefore, if the response speed of the gas engine becomes faster, more amount of step load can be applied to the genset because the drop of the gas engine speed becomes smaller.

3.4 Disconnection of Step Load

Results under the following conditions are shown as typical responses to disconnection of the loads.

- load: 400 W, the reference of the rotational speed: 1,300 rpm (rotational frequency in electrical angle is 65 Hz);
- load: 400 W, the reference of the rotational speed: 1,400 rpm (rotational frequency in electrical angle is 70 Hz).

The former and latter results are shown in Figs. 8 and 9, respectively.

At first, the 400 W step load was connected to the genset. The moment of disconnecting the load is indicated by a dotted line in both Figs. 8 and 9. After the disconnection, there was no load connected to the genset. Unlike application of the load, disconnection of the load was successfully done with the reference speeds of both 1,300 rpm and 1,400 rpm.

When the reference of the rotational speed was 1,300 rpm, the rotational speed shown in Fig. 8a went up to 1,430 rpm due to disconnection of the load shown in Fig. 8b. Regardless of that, the primary side voltage was kept constant as shown in Fig. 8c. The amplitude of the secondary side voltage increased as shown in Fig. 8d. On the contrary, before disconnecting the load, the rms value of the RSC output current was 15.6 A. Then this current decreased to 7.1 A after disconnection of the load. Figs. 8e and 8f show that the output current of the RSC was almost constant irrespective of the rotational speed after disconnection of the load. In addition, Fig. 8g shows that i_{gd} decreased from 1.5 A to 1.0 A after disconnection of the load because the active power flowing from the primary side to the dc-link part decreased. Additionally, the dc link voltage went up temporarily at disconnection of the load as shown in Fig. 8h. The peak value of the dc-link voltage was approximately 210 V.

On the other hand, when the reference of the rotational speed was 1,400 rpm, the rotational speed shown in Fig. 9a went up to 1,510 rpm at disconnection of the load. Regardless of the speed, the primary side voltage was kept constant shown in Fig. 9b. Then the amplitude of the secondary side voltage increased after disconnection of the load as shown in Fig. 9c. On the contrary, Figs. 9d and 9e show that the output current of the RSC decreased significantly after disconnection of the load. In addition, Fig. 9f shows that i_{gd} decreased from 1.1 A to 0.9 A after disconnection of the load, which is smaller than the previous results. This means the decrease in the active power flowing from the primary side to the secondary side. In this case, the dc-link voltage shown in Fig. 9g slightly increased when the load was disconnected. Load current is shown in Fig. 9h.

These results show that the secondary side current did not become overcurrent when the load was disconnected. However, the rotational speed rose due to lag of the gas engine response performance when the load was disconnected. That makes the amplitude of the secondary side voltage higher. Therefore, when the reference of the rotational speed is high, the secondary

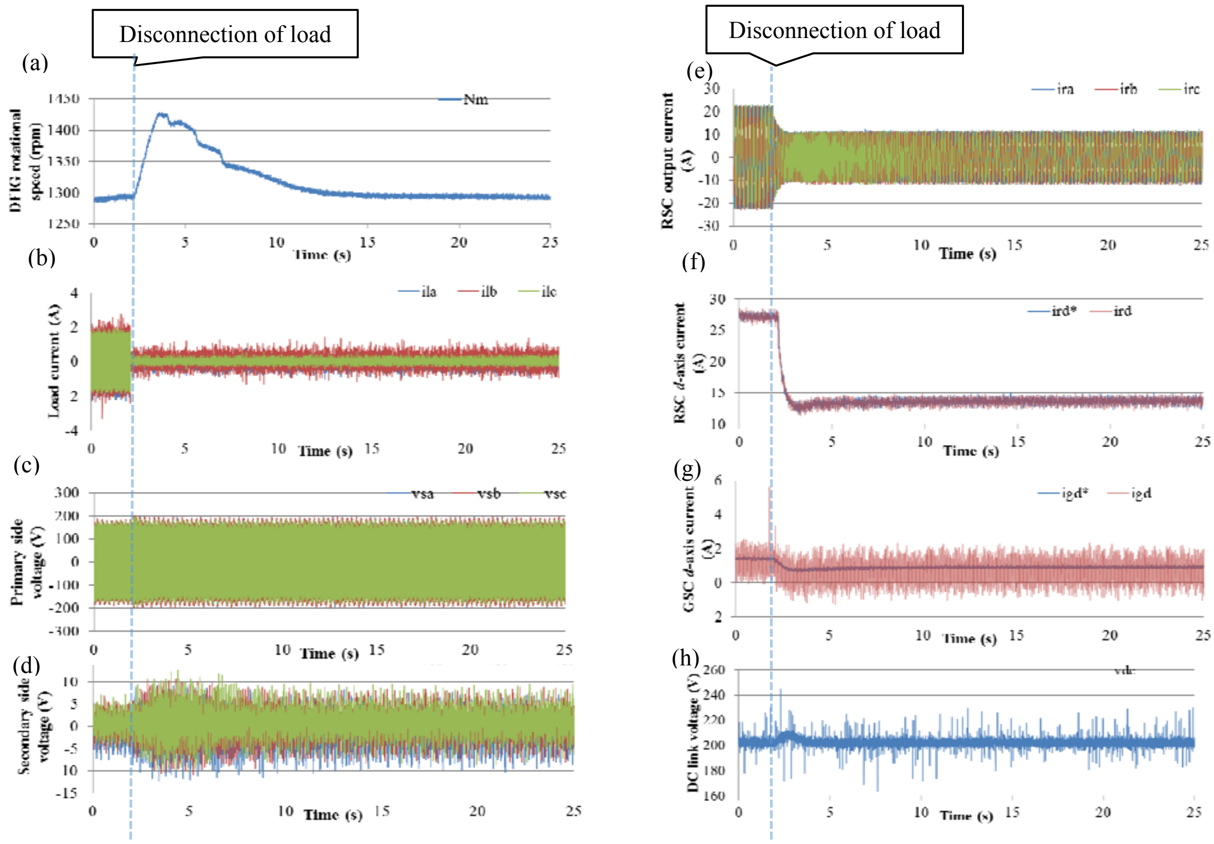

Fig. 8 Waveforms of disconnection of load (400 W, P.F. = 1) when the reference of the rotational speed was 1,300 rpm. (a) primary side phase voltage v_{sa}, v_{sb}, v_{sc}; (b) secondary side phase voltage v_{ra}, v_{rb}, v_{rc}; (c) RSC output current i_{ra}, i_{rb}, i_{rc}; (d) RSC d-axis output current i_{rd} and its reference i_{rd}^*; (e) load current i_{la}, i_{lb}, i_{lc}; (f) DFIG rotational speed; (g) GSC d-axis output current i_{gd} and its reference i_{gd}*. (h) dc-link voltage v_{dc}.

side voltage can become high after disconnection of the load. That may lead to fail the current control of the RSC due to lack of the RSC output voltage.

Eventually, disconnection of the loads is not a serious issue to continue its operation of the genset. Therefore, application of step loads has been merely verified by a computer simulation in the next chapter.

4. Simulation Results of Stand-Alone Operation

In this chapter, the proposed control system has been validated at step-loading by computer simulation using software PSCAD/EMTDC. In addition, a gas engine has been expressed as a simple control block diagram.

4.1 Gas Engine Simulation Model

A gas engine model can be divided into an energy conversion part and a mechanical part. The energy conversion model is referred to as a combustion model. In addition, the mechanical model is referred to as a governor model. In the governor model, using the error between a reference speed and the actual speed, a PID controller outputs the fuel flow rate f_g. On the other hand, in the combustion model, the fuel is converted to the mechanical shaft torque. The thermodynamics of the combustion process is quite complex. However, for the purpose of simulating dynamic response, the essential features of the combustion part can be fully described by the simple transfer function:

$$T_{\mathrm{d}} = K_{\mathrm{g}} \frac{e^{-\tau_{\mathrm{d}} s}}{1+\tau_{\mathrm{c}} s} f_{\mathrm{g}}$$

where, T_d is the average shaft torque, K_g is the gain, τ_d is the time delay of combustion and τ_c is a time constant

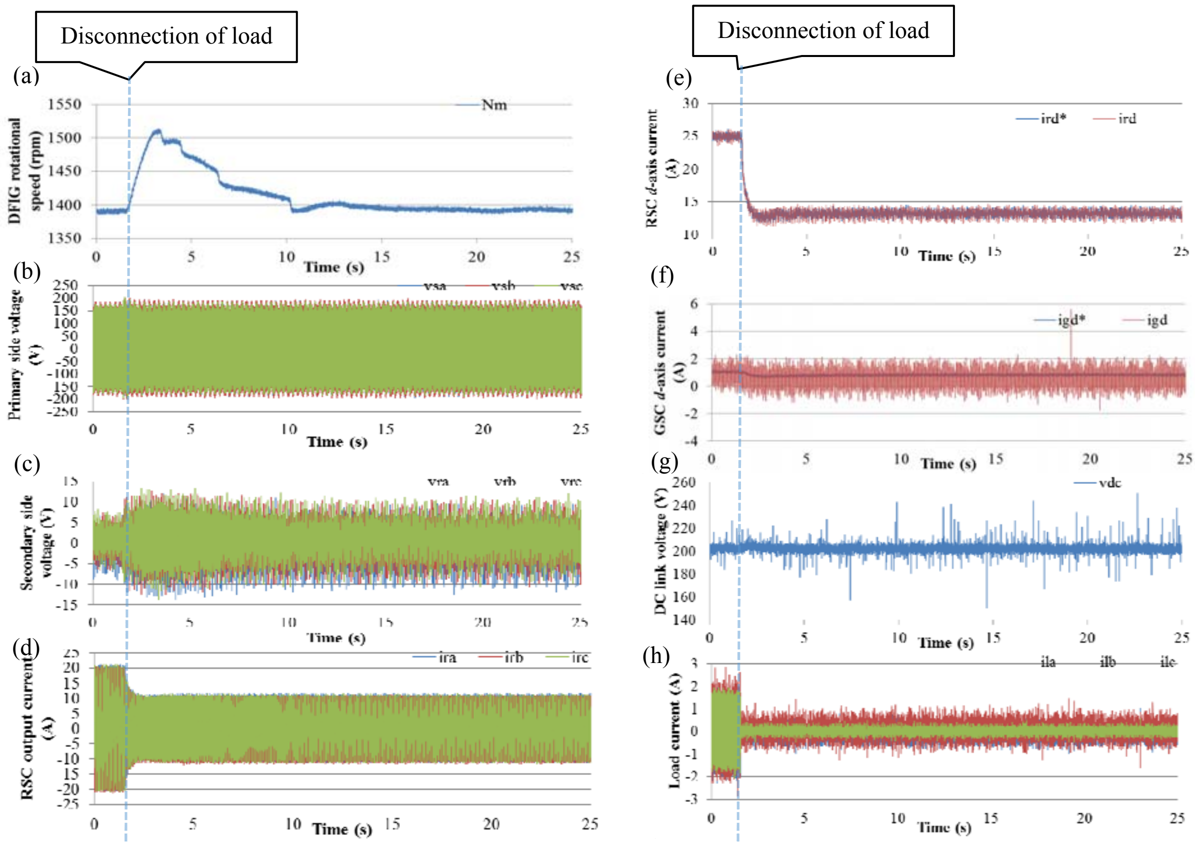

Fig. 9 Waveforms of disconnection of load (400 W, P.F. = 1) when the reference of the rotational speed was 1,400 rpm. (a) primary side phase voltage v_{sa}, v_{sb}, v_{sc}; (b) secondary side phase voltage v_{ra}, v_{rb}, v_{rc}; (c) RSC output current i_{ra}, i_{rb}, i_{rc}; (d) RSC d-axis output current i_{rd} and its reference i_{rd}^*;. (e) load current i_{la}, i_{lb}, i_{lc}; (f) DFIG rotational speed; (g) GSC d-axis output current i_{gd} and its reference i_{gd}*. (h) dc link voltage v_{dc}.

representing the governor and combustion process dynamics. The PID controller is expressed as the following form:

$$G_{\mathrm{PID}} = K_1 \frac{(1+sT_2)(1+sT_3)}{sT_1}$$

The block diagram of the PID controller and gas engine is shown in Fig. 10.

When T_3 is tuned to be equal to τ_c and T_1 is set to be equal to T_2, the open loop transfer function becomes:

$$G_{\mathrm{ol}} = K\left(1+\frac{1}{T_1 s}\right)e^{-\tau_d s}$$

where, K is the product of K_1 and K_g. Then the block diagram shown in Fig. 10 is simplified to Fig. 11.

Then the parameters were tuned referring to the experimental result shown in Fig. 7f. All values are in p.u. system. Referring to the rate of the speed decrease

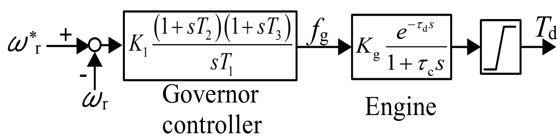

Fig. 10 Block diagram of PID controller and gas engine.

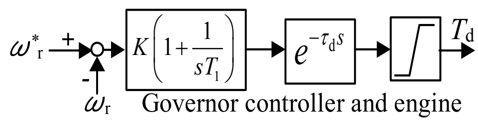

Fig. 11 Simplified model of gas engine and its controller.

after the step-loading, the angular moment of inertia was roughly estimated to 5 s. Other parameters were tuned by cut-and-try approach to agree with the actual response to the step-loading. The parameters were determined as follows:

τ_d: 40 ms;

K: 2.1;

T_1: 3.15.

In this study, it was assumed that the maximum output torque of the gas engine is 1.2 pu (10.5 Nm). Therefore, a limiter was set in Figs. 10 and 11.

4.2 Simulation Conditions

System configuration and parameters in the simulation were set to be same as the experimental setup. Steady-state losses were represented by 2 kΩ resistance connected in parallel to the primary side to agree with the experimental results. The reference speed of the engine was set to a constant value at each simulation. The reference value was changed from 1,000 rpm to 1,600 rpm by 100 rpm. The following constant impedance loads were used for the purpose of investigating the response to step load change: 100, 200, 400 and 600 W.

4.3 Application of Step Load

Typical two simulation results are shown in the same way as the previous experimental results.

- load: 400 W, the reference of the rotational speed: 1,300 rpm;
- load: 400 W, the reference of the rotational speed: 1,400 rpm.

The former and latter results are shown in Figs. 12 and 13, respectively.

In the case of the reference speed of 1,300 rpm, the genset was incapable of continuing its operation at 400 W step-loading as shown in Fig. 12. Since the engine torque shown in Fig. 12a lagged behind the DFIG load torque shown in Fig. 12b, the DFIG rotational speed shown in Fig. 12c went down abruptly. The more the rotational speed went down, the more the losses in the genset increased because the increase in the circulating power between the primary and secondary sides caused much loss in energy conversion part. Eventually, the DFIG load torque exceeded the maximum torque of the engine. The RSC output current shown in Fig. 12d reached to the limit, which resulted in losing the excitation of the DFIG. Then the primary side voltage shown in Fig. 12e

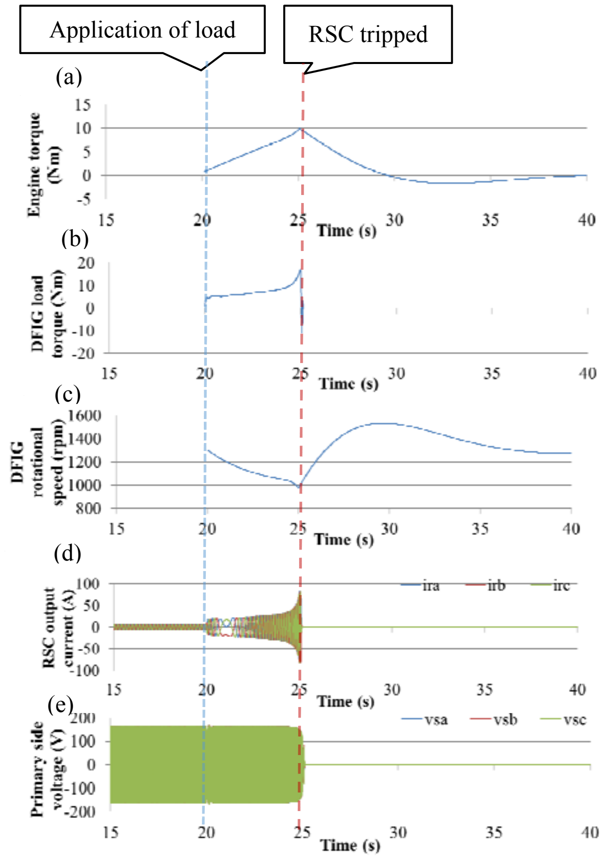

Fig. 12 Simulation waveforms of application of step load (400 W, P.F. = 1) when the reference of the rotational speed was 1,300 rpm. (a) primary side phase voltage v_{sa}, v_{sb}, v_{sc}; (b) RSC output current i_{ra}, i_{rb}, i_{rc}; (c) DFIG rotational speed; (d) engine torque; (e) DFIG load torque.

went to zero and the genset stopped supplying the electric power.

On the other hand, in the case of the reference speed of 1,400 rpm, the genset successfully continued its operation after 400 W step-loading as shown in Figs. 13a and 13b. The DFIG load torque is shown in Fig. 13c. The engine torque shown in Fig. 13d was able to prevent from the large decrease in the rotational speed shown in Fig. 13e because of the high reference speed. Therefore, the RSC was capable of continuing to excite the DFIG.

4.4 Discussion about Simulation Results

In the simulation, the torque dynamics that was difficult to observe in the experiment was emulated. The operation continuity after step-loadings can be

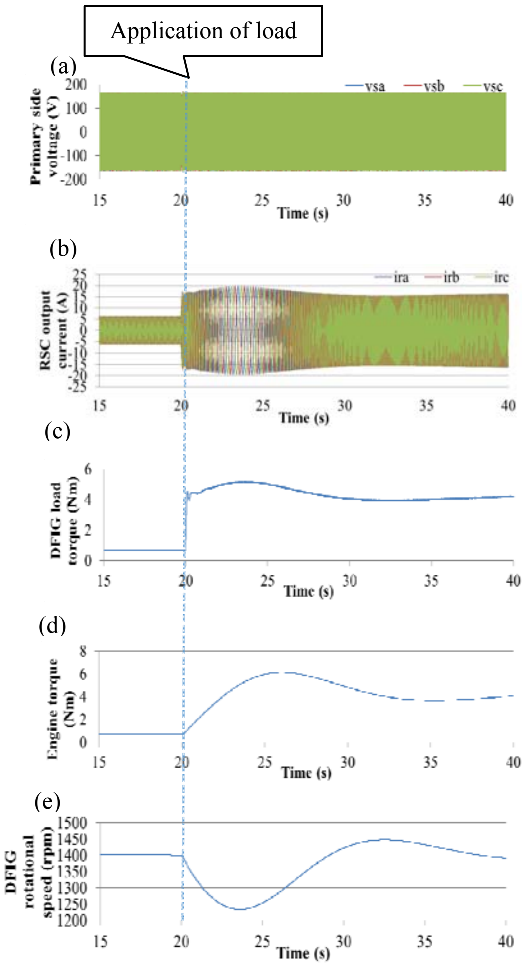

Fig. 13 Simulation waveforms of application of step load (400 W, *P.F.* = 1) when the reference of the rotational speed was 1,400 rpm. (a) primary side phase voltage v_{sa}, v_{sb}, v_{sc}; (b) RSC output current i_{ra}, i_{rb}, i_{rc}; (c) DFIG rotational speed; (d) engine torque; (e) DFIG load torque.

investigated by the computer simulation. In addition, the torque dynamics can be observed in the simulation. It was found that when a step load was applied, the required transient gas engine torque was larger than the steady-state torque. It can be concluded that the engine model is enough to simulate the actual dynamics of the rotational speed as shown in Fig. 7f.

5. Discussions

In our study, the DFIG whose stator/rotor turn ratio is 6.38 has been used. Due to this high ratio, the secondary side voltage became small. Therefore, the RSC output current became quite large when loads were applied. In this case, upper limit of the RSC output current was a problem. On the other hand, the upper limit of the RSC output voltage did not matter. However, the stator/rotor turn ratio of the DFIG can be designed to be smaller than that of our DFIG. Then the secondary side internal induced voltage would become higher than that of our DFIG. In this case, the RSC could fail the current control for lack of the output voltage. Therefore, the upper limit of the RSC output voltage will be an issue. On the other hand, the upper limit of the RSC output current does not matter.

6. Conclusions

In this paper, transient response to step load changes of the DFIG applied to gas engine cogeneration system in stand-alone operation have been investigated.

The experimental results show quantitatively that the higher the rotational speed was, the more amount of step load the genset was capable of being applied. As a typical example, two experimental results were shown in this paper. When the reference of the rotational speed was 1,300 rpm, the RSC tripped due to overcurrent after the step-loading of 400 W. That was because the rotational speed went down due to lag of the gas engine response to the load changes. On the contrast, when the reference of the rotational speed was 1,400 rpm, the load was successfully applied to the genset because the lowest speed became higher than the previous case. The RSC did not become overcurrent. Therefore, it has been concluded that the maximum amount of step load is determined by the reference of the rotational speed, the rating of the RSC output current and the response performance of the gas engine.

On the other hand, when the load was disconnected, the RSC did not become overcurrent. However, because of the increase in the slip at disconnection of the load, the secondary side induced voltage became higher. That could lead to fail the RSC control due to lack of the RSC output voltage.

In the simulation, the gas engine that was used in the experiment was modeled by the simple transfer function. It can be concluded that the simple model

developed based on the experimental results is sufficient to investigate the dynamics of the rotational speed when step load is applied. The simulation results show that the simulation can investigate the operation continuity performance at step-loading.

A DFIG driven by a gas engine at stand-alone operation will increase the maximum amount of allowed step load compared with a conventional constant speed synchronous generator because the DFIG is capable of keeping the constant output frequency regardless of the rotational speed. In this paper, the operation continuity after the step-loading at each reference speed has been fully investigated and verified that the maximum amount of allowed step load increased by operating at a high rotational speed. Therefore, it can be proposed that before applying a large amount of step load, speeding up the rotational speed is effective to continue the gas engine genset operation after the step-loading. Thus, the required gas engine capacity will be smaller than a conventional constant speed gas engine genset.

References

[1] J. Lee, S. Lee, S. Sul, Variable-speed engine generator with supercapacitor: Isolated power generation system and fuel efficiency, IEEE Trans. Ind. Appl. 45 (6) (2009) 2130-2135.

[2] G. Iwanski, W. Koczara, Power management in an autonomous adjustable speed large power diesel genset, in: Proceedings of 13th Int. Power Electronics and Motion Control Conf. EPE-PEMC, Poznan, Poland, Sept. l-3, 2008.

[3] W. Koczara, N. Al-Khayat, R. Seliga, J. Al-Tayie, Variable speed integrated generating set an emerging technology for distributed power generation, in: Proceedings of Power Tech Conference, Bologna, Italy, June 23-26, 2003.

[4] N. Al-Khayat, J. Al-Tayie, R. Seliga, Stand alone adjustable speed power generating set, in: International Conference on Harmonics and Quality of Power, Rio de Janeiro, Brazil, Oct. 6-9, 2002.

[5] T. Daido, Y. Miura, T. Ise, Y. Sato, A study on start-up method during a blackout of a doubly-fed induction generator applied to gas engine cogeneration system, in: Proceedings of 8th Int. Conf. Power Electronics—ECCE Asia, Jeju, Korea, May 30-Jun. 3, 2011.

[6] T. Daido, Y. Miura, T. Ise, Y. Sato, Characteristics on stand-alone operation of a doubly-fed induction generator applied to adjustable speed gas engine cogeneration system, Journal of Power Electronics 13 (5) (2013) 841-853.

[7] T. Daido, Y. Miura, T. Ise, Y. Sato, Transient characteristics for load changes of a doubly-fed induction generator applied to gas engine cogeneration system in stand-alone operation, in: Proceedings of Energy Conversion Congress and Exposition (ECCE), Raleigh, NC, Sept. 15-20, 2012.

[8] R. Pena, R. Cardenas, J. Proboste, J. Clare, G. Asher, Wind-diesel generation using doubly fed induction machines, IEEE Trans. Energy Convers 23 (1) (2008) 202-214.

[9] D. Wang, C. Nayer, C. Wang, Modeling of stand-alone variable speed diesel generator using doubly-fed induction generator, in: Proceedings of 2nd IEEE Int. Symp. Power Electronics for Distributed Generation Systems, Hefei, China, June 16-18, 2010.

[10] G. Iwanski, W. Koczara, Sensorless stand alone variable speed system for distributed generation, in: Proceedings of 35th Annu. Power Electronics Specialists Conf., Aachen, Germany, June 20-25, 2004.

[11] D. Forchetti, G. Garcia, M. Valla, Vector control strategy for a doubly-fed stand-alone induction generator, in: Proceedings of 28th IEEE IECON, Sevilla, Spain, Nov. 5-8, 2002.

[12] T. Ito, T. Watanabe, T. Monai, S. Nii, Development of cooperative control between lean-burn gas engine and power storage devices at grid-independent operation, the Journal of the Institution of Electrical Installation Engineering of Japan 30 (4) (2010) 318-325.

[13] T. Ito, T. Tsukada, S. Sato, S. Nii, Improvement of islanded operating stability for lean-burn gas engine by effective use of power storage device, in: Proceedings of 2nd IEEE Int. Conf. Smart Grid Communications, Brussels, Belgium, Oct. 17-20, 2011.

[14] T. Ito, T. Watanabe, Y. Ishibashi, T. Tsukada, T. Monai, S. Nii, et al., A high-efficiency, high-quality power supply implemented with a lean-burn gas engine and a power storage device, Proceedings of IEEE Power and Energy Society General Meeting, Mineapolis, MN, July 25-29, 2010.

Journal of Energy and Power Engineering 8 (2014) 543-550

Fault Detection and Isolation for Low Hardware Redundancy Flight Control System

Yongliang Du[1] and Yakui Gao[2]

1. Department of Flight Control and Hydraulic system, AVIC the First Aircraft Institute, Xi' an 710089, China

2. Department of Chief Engineer's office, AVIC the First Aircraft Institute, Xi' an 710089, China

Received: September 26, 2013 / Accepted: November 14, 2013 / Published: March 31, 2014.

Abstract: The problems of current highly redundant flight control system are analyzed in this paper. Our study gives methods of utilizing other information to reduce physical components on the condition of meeting the reliability requirements for flight control system. The strategies presented in this paper mainly include information redundancy, multi-thread, time redundancy, geometry space redundancy, etc.. Analysis and simulation show these non-hardware based methods can reduce the requirement of system hardware level and thus reduce the system complexity, weight, space, costs and R&D (research and development) time.

Key words: Low hardware redundancy, multi-thread, wavelet analysis.

1. Introduction

It is without an exception that it always uses highly redundancy system components when designing fly-by-wire flight control system for big aircraft. Such as Boeing 777 primary flight control system adopted 3 identical computer control channels with each including 3 dissimilar lanes in each channel, and a total of four ACE boxes, each of them drives one actuator on either of the two elevators, ailerons and rudders [1, 2]. A330/A340 has adopted 3 primary computers and two secondary computers to control the surfaces. Each computer has two lanes, and failure of one lane will result in that computer shutting down, or at least be removed from the execution task. The redundancy comes from the fact that each control surface can be driven by up to four computers [2]. C-17 military aircraft flight control system has introduced standard input-computer-output quadrupled architecture, in which every computer has a dual processor module [3]. It ensures the reliability by introducing high redundancy of hardware configuration. But it is not to say the bigger redundancy number, the better performance. With redundancy number increasing, the corresponding detection, isolation and transition device would also increase. Because the effects of tandem relationship, it has become the bottleneck of system reliability, and thus downgraded the system reliability. At the same time, redundancy number and reliability do not have a linear relationship after the redundancy gets to a certain number, and then the increase of the reliability with the increase of the redundancy gradually becomes slower.

The current highly redundant fly-by-wire flight control system hardware architecture put forward a challenge to electrical flight control system design for small aircraft. It is urgently needed to reduce the flight control system weight, costs and design cycle based on the satisfaction of system reliability requirements. The purpose of this paper is to study the methods which utilize appropriate redundancy management, fault detection strategy and non hardware redundancy strategy to reduce system hardware redundancy, making it possible for less hardware to develop higher

Corresponding author: Yongliang Du, Ph.D., research fields: flight control and hydraulic system. E-mail: duyliang@163.com.

benefit, and provide a reference for the design of low hardware redundancy flight control system.

2. Redundancy Design of Low Cost Flight Control System

2.1 Considerations of Redundancy Design

Redundancy number mainly depends on reliability index, weight, volume, power consumption, cost and the level of redundancy management. The increasing number of replicas of system components will increase the system complexity, weight, space, costs and development time. The increased complexity will accentuate unplanned task, increase maintenance task, and reduce the system reliability. Therefore, reliability, weight, space, cost, maintainability and design cycle should all be taken into consideration. As long as the system requirements are met, system redundancy architecture should be as simple as possible.

2.2 Reliability Comparison between n Select 1 and 2 System

If a system successfully performs the task need at least k out of n redundancy components, this system is called k/n (G) structure. The paper only compares the theoretic reliability between 1/n and 2/n system.

Suppose the probability of failure for every channel is q, then chance of good working condition is $1-q$, According to Newton's binomial distribution, then:

$$[q+(1-q)]^n = C_n^0 q^n + C_n^1 q^{n-1}(1-q) + \cdots + C_n^k q^{n-k}(1-q)^k + \cdots + C_n^n (1-q)^n \tag{1}$$

It needs at least 2 subsystem effectively for simple parallel systems such as 5 redundancy system (2/5 (G)), quadrupled redundancy system (2/4 (G)), triple redundancy system (2/3 (G)) and dual redundant system (2/2 (G)) work properly. Reliability expressions are shown as follows:

$$R_5^2 = C_5^0 q^5 + C_5^1 q^4 (1-q) + C_5^2 q^3 (1-q)^2 + C_5^3 q^2 (1-q)^3 \tag{2}$$

$$R_4^2 = C_4^0 q^4 + C_4^1 q^3 (1-q) + C_4^2 q^2 (1-q)^2 \tag{3}$$

$$R_3^2 = C_3^0 q^3 + C_3^1 q^2 (1-q) \tag{4}$$

$$R_2^2 = C_2^0 q^2 \tag{5}$$

It needs only 1 subsystem effectively for simple parallel systems such as 5 redundancy system (1/5 (G)), quadrupled redundancy system (1/4 (G)), triple redundancy system (1/3 (G)), dual redundancy system (1/2 (G)) and single channel system work properly. Reliability expressions are shown as follows:

$$R_5^1 = C_5^0 q^5 + C_5^1 q^4 (1-q) + C_5^2 q^3 (1-q)^2 + C_5^3 q^2 (1-q)^3 + C_5^4 q (1-q)^4 \tag{6}$$

$$R_4^1 = C_4^0 q^4 + C_4^1 q^3 (1-q) + C_4^2 q^2 (1-q)^2 + C_4^3 q (1-q)^3 \tag{7}$$

$$R_3^1 = C_3^0 q^3 + C_3^1 q^2 (1-q) + C_3^2 q (1-q)^2 \tag{8}$$

$$R_2^1 = C_2^0 q^2 + C_2^1 q (1-q) \tag{9}$$

$$R_2^1 = C_1^0 q \tag{10}$$

The general expression of reliability function is:

$$R(t) = \exp[\int_0^t \lambda(t)\, d\, t] \tag{11}$$

For electronic equipment, it generally takes $\lambda(t) = \lambda$ (constant failure rate), then Eq. (11) becomes $R(t) = e^{-\lambda t}$, then take $q = e^{-\lambda t}$ into the above expression it would get the result which is shown in Fig. 1.

2.3 Redundancy Management Strategy, Number Selection and Problems to being Solved

As can be seen from Fig. 1, to 2/n system, reliability increases significantly between two to triple redundancy, but when it increases to four or five redundancy configurations, the increase of reliability becomes more and more slowly; to 1/*n* system, the largest reliability increase rate is when a single channel changes to two redundancy channels. As it can also be found that, the reliability of 1/*n* system is far higher than 2/*n* system, the reliability of 1/2 system can achieve even higher than that of 2/4 system. From the above analysis, a conclusion can be drawn that 1/2 redundancy configuration is the best choice for low cost flight control system design.

However, the current flight control system of all uses the idea of comparison monitoring, which includes 2/*n* of *n* × 1 structure and 1/n-2/k of *n* × k (*k* is 2 or 3) structures. This is mainly because it is very easy to detect faults through the comparison of two similar parts. So to achieve 1/2 of 2 × 1 system architecture, the fault detection and diagnosis problems of two redundancy or non redundancy components must be

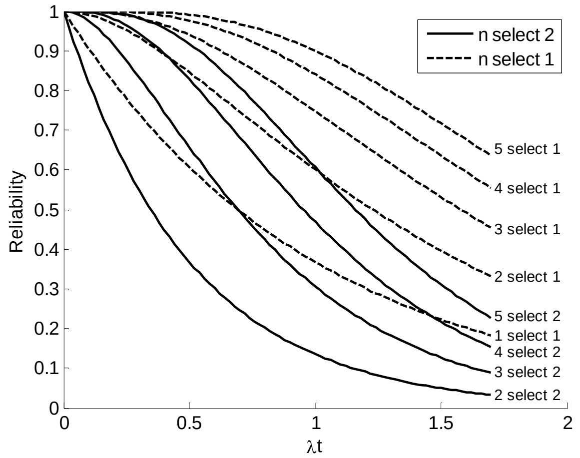

Fig. 1 Redundancy number vs. reliability.

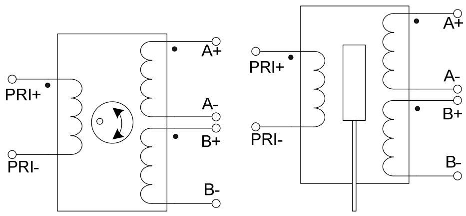

(a) RVDT (b) LVDT

Fig. 2 The principle of displacement sensor.

solved. The following text will study fault detection and isolation of the flight control system based on electrical characteristics of part types.

3. Typical FCS Components Electrical Characteristic Analysis

3.1 Typical FBW FCS Components and Usage

The electric/electronic components of general Fly-by-wire flight control system consist of cockpit command sensor, surface position sensor, aircraft motion sensor, flight control computer and actuator, in which flight control computer also cross-links with other system through analogue wire and data bus. Cockpit command sensors are mainly used to feel three-dimensional commands which come from pilots. Cockpit command sensor, surface position sensor and the rod sensor of the actuator all belong to displacement measurement devices. For RVDT (rotary variable differential transformer) and LVDT (linear variable differential transformer) adopt a non-contact structure, which have noiselessness, high sensitivity, high repeatability, high reliability, infinite resolution, theoretical infinite life and good high frequency response characteristics [4]. Therefore, they are almost used for all displacement measurements of the flight control system. Aircraft motion sensors includes rage gyro and acceleration sensors, rate gyro is used to measure the aircraft angular rate and acceleration sensor is used to feel the acceleration of the aircraft along axis. The flight control computers receive all signals from sensors and cross-linked systems, and then compute command to control actuator according to control law. Due to actuator redundancy always close connection with control surface, therefore its redundancy simplification is not considered here.

3.2 Analysis of the Characteristics of Flight Control System Components

3.2.1 Displacement Sensor

Two types of displacement sensor are always used in flight control system, namely: RVDT and LVDT. The principle of RVDT is similar to transformer. As shown in Fig. 2a, when inputting sine excitation signal to the original edge, in the two second coils which generally have the same circle number that would produce the same frequency alternating sine signals. When turning the core of the sensor, the coupling between the two vice parts changes, thus the amplitude of the two parts changes too. When the zero point of the iron core moves to the center, induced electromotive force of the two parts are equal. The farther the iron core turns, the bigger induced electromotive force. For the proportion relationship between the turn angle and the output voltage, therefore the displacement or angle is detected. The working principle of LVDT and RVDT is basically the same, which is shown in Fig. 2b.

With the position of displacement sensor changing, the amplitude of voltage of two second coil changes too. When the amplitude of the second coil A increases, the amplitude of the second coil B will decrease. The difference in the voltage of two second coil is working voltage of the sensor. The output of the voltage

summing of the two second coil is always constant and it does not have any connection with the position of the iron core.

3.2.2 Aircraft Motion Sensors

Aircraft motion sensor includes rate gyro and acceleration sensor. Rate gyro is a single degree-of-freedom gyroscope which has flexible constraints and damping constraints. The precession motion of gyro is used to feel aircraft angular rate which is around the aircraft body axis, and output electrical signals which is proportional to angular rate. The basic principle of acceleration rate is changing a certain mass linear accelerating into displacement aroused by force measurement or inertia moment, and then output electric signals which are proportional to linear acceleration.

3.2.3 Flight Control Computer

The flight control computer is the core of flight control system, it is a computing device for system comprehension and control, which receives a variety of sensors and other system input signals, completes control law calculation and then controls actuator movement. Traditional flight control system generally uses 3 to 4 redundancy centralized flight control computer through the comparison of redundancy processor or computer to achieve health monitor of flight computers. When any of the processor modules or servo control module fault, the whole computer source would be lost.

4. Fault Diagnosis of Low Redundancy Flight Control Computer

4.1 Modular Computer Architecture

Modular and open architecture is a basic characteristic of new generation fault tolerated airborne computer system. The modular structure, which is based on a high-speed serial backplane bus or system bus, enhances the system's fault isolation ability, improves tolerance and anti-destroying ability of the system, and also achieves high degree sharing of information. The open structure, which makes testability, maintainability and expansibility function get to a new level.

The new generation of airborne fault tolerant computer system has the redundancy backup reconstruction and slowly degradation reconstruction ability and general module resources are consumed. It can arrange the surplus resources in the highest priority function according to the flight mission requirement. The whole flight control system functions present slow degradation and would not be lost completely, which can make the system reliability largely improved when compared to traditional computer architecture.

4.2 Multi-thread Fault Diagnosis

False alarm has always been a tough issue for fly-by-wire flight control system. The application of national and international on-board BIT devices shows that transient fault is one of the main causes of false alarm of BIT.

The N version program is a more effective and cheaper way to detect transient faults in airborne computers than other fault-tolerant solutions that use some form of hardware redundancy, but for the real-time requirement that it is not a good choice for flight control computers. This problem can be solved by a recent micro architecture innovation called simultaneous multi-threading. Simultaneous multi-threading leverages the fine-grain scheduling flexibility and highly parallel micro architecture of superscalar processors. Often there are phases of a single program that do not fully utilize the micro architecture, so sharing the processor resources among multiple programs will increase overall utilization. Improved utilization reduces the total time required to execute all program threads [5].

5. Fault Detection for Low Redundancy Sensors and Actuators

5.1 Information Redundancy

For displacement sensor of flight control system, monitoring the constant voltage summation of second

two output coil can be used. Wire disconnected or excitation decreased will make the summation V1 + V2 decreased too, if the difference of sum voltage and benchmark voltage exceeds a certain threshold which will be taken as a failure (fault coverage could reach 98%~99%) [6]. LVDT sensor signal acquisition and online monitoring are shown in Fig. 3.

Normally, self checking ability would design for rate gyro too. For ground testing, DC movement circuit should be exerted to gyro framework detector (namely torque generator), which is used to check the function of inner device, the flexible rotation degree of the framework, the good working condition of signal sensor and torque winding. For continuous monitoring or set gyro motor speed detector in the air, AC signals which frequency are much higher than the system response frequency should be exerted, and supply speed and direction of motor movement to the monitor, then shut off motor power when gyro motor fails.

5.2 Geometry Space Redundancy

Because some system has some inner link, as long as the sensors are installed in the system according to certain relationships, no matter whether these sensors are the same type or not, the output of these sensors then can consist of a certain relationship, which is called parity equation. If one or more sensor failed, the relationship of the output signals between those sensors would be destroyed.

For example, the parity equation of angular rate gyro signals *p*, *q* and *r* can be expressed as [7]:

$$\begin{aligned} & p-(\dot{\phi}+\dot{\psi}\sin\theta)\approx 0 \\ & r-(\dot{\psi}\cos\theta\cos\phi+\dot{\theta}\sin\phi)\approx 0 \\ & q-(\dot{\theta}\cos\phi-\dot{\psi}\cos\theta\sin\phi)\approx 0 \end{aligned} \tag{12}$$

Among them, ψ is course angle signal, θ is pitch angle signal, ϕ is roll angle signal.

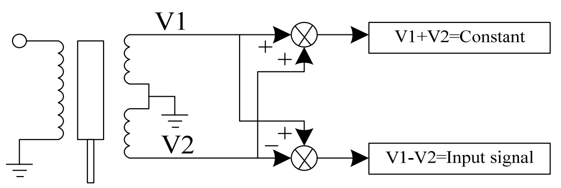

Fig. 3 LVDT online monitor.

For dual hardware redundant system, the difference between of the two output signals is taken as a parity equation.

Also, for the gyroscope and acceleration sensors, etc., this can construct the analytical equation according to the installation of the sensors in geometry space.

As shown in Fig. 4, four single-degree-of-freedom gyros, 3 is installed along the body axis, and another is installed which have a same angle $\alpha = 45^{\circ}$ with these 3 ones, thus forming the lowest geometry space redundancy architecture, and then the parity equation can be expression as:

$$s_1\cos\alpha + s_2\cos\alpha + s_3\cos\alpha - s_4 \approx 0 \tag{13}$$

It gives a way to detect a failure among the four sensors, but this method cannot achieve failure isolation.

Different installation relationship would produce different parity equations. An optimal installation of six single freedom direction sensitive sensors are given in Ref. [8], which insures that all three axis information can be provided so long as any 3 of the 6 sensors is working in good conditions. One or two times' failure works, three times' failure safety can be satisfied by the fault detection method of pure hardware comparison.

5.3 Time Redundancy

5.3.1 Redundancy Information Based on Extra-Time

Sensor faults commonly represent as the signal abruptly changes, which can be divided into sensor open-circuit fault, offset fault, short circuit fault, locked

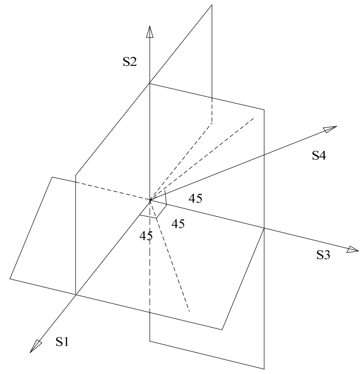

Fig. 4 The installation relationship between 4 single-degree-of-freedom gyros.

fault. When sensors do not have the online monitor function, the fault detection and isolation to dual redundancy or single sensor can be achieved through the continuous monitoring sensor signals during a certain time period.

It is very suitable for detecting signal mutations due to wavelet function has local time-frequency analysis ability. Research, analysis and simulation results show that wavelet analysis method has strong ability of detecting failures for low frequency and nonstationary signals, which do not need the supports of sensor models. It is a weak model based fault detection method, very suitable for online sensor fault monitor. In this paper, FIFO buffer is used to store a particular period of sensor data, and then fault is detected from these data based on wavelet analysis method.

5.3.2 Wavelet Analysis

5.3.2.1 Principium

Wavelet function is defined as: support $\psi(t) \in L^2(R)$, if the Fourier transform $\psi(\omega)$ meet the conditions,

$$c_\psi = \int_R \frac{|\psi(\omega)|^2}{|\omega|} d\omega < \infty \tag{14}$$

Then $\psi(t)$ is called a basic wavelet or wavelet generating function, Eq. (14) is called the allowed condition of wavelet function.

The continuous wavelet transformation for signal $s(t)$ is defined as:

$$WT_s(a,b) = \frac{1}{\sqrt{a}} \int_{-\infty}^{\infty} s(t)\psi^*(\frac{t-b}{a})dt = < s(t), \psi_{a,b}(t) > \tag{15}$$

In the expression: *---complex number conjugate.

Among them, $\psi_{a,b}(t) = a^{-\frac{1}{2}}\psi(\frac{t-b}{a})(a > 0, b \in R)$ is the results of window function $\psi(t)$ shifted time b and scale flexed a.

In practical applications, especially when implementing in computers, continuous wavelet must be discretized. It must be pointed out that the so-called discretization is not for time variable t, but for the parameters of scale and displacement.

If scale factor and displacement factor is discrete according to power index, namely take as $a = a_0^m$, $b = nb_0a_0^m$ (a_0 , b_0 is constant number, $a_0 > 1$, $b_0 > 0$). Discrete wavelet transformation is:

$$DWT_S(m,n) = \int s(t)\psi^{m,n}(t)dt \tag{16}$$

The discrete mother wavelet function is:

$$\psi^{m,n}(t) = a^{-m/2}\psi(\frac{t - nb_0a_0^m}{a_0^m}) \tag{17}$$

Mallat algorithm is a fast algorithm of wavelet transformation, which has the same status as FFT algorithm in Fourier transformation. For any signal on the space $L^2(R)$, it can be divided into low frequency part of 2^{-N} and high frequency part of 2^{-j} （$j = 1$，2, … N resolution ratio.

Take $c_0(n)$ as discrete signal of a sensor for a certain period time. The signal of the sensor one dimension Mallat pyramidal decomposition is shown in Fig. 5.

The decomposition formula of Mallat algorithm is:

$$c_{j+1}(n) = \sum_k h(k-2n)c_0(k) \tag{18}$$

$$d_{j+1}(n) = \sum_k g(k-2n)c_0(k) \tag{19}$$

The function of low pass filter H is to realize the approximation of function $f(t)$ to C_j , the role of high-pass filter G is to extract the detail of $f(t)$.

It can be known from above that wavelet analysis technique can decompose any signal (stationary signal or non-stationary signal) into a basic function which is based on the escalation of wavelet, and in which the information is integrated, it can get decomposition series in the whole frequency which is distributed in different frequency band, and has a local analysis function both in time domain and frequency domain. Therefore, it is useful and effective to analyze the singularity and singularity position of signals based on wavelet transformation.

5.3.2.2 Simulation of Wavelet Based Fault Detection

Sensor faults generally include locked fault, gain changed fault, offset fault, all of which are performer as signal mutation. For the length reason, only one situation is simulated here.

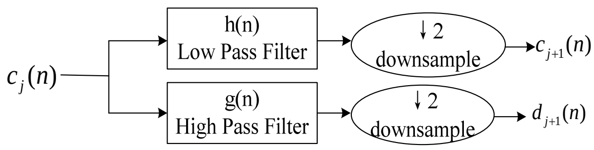

Fig. 5 Multiscale analysis.

A kind of four single-degree-of-freedom gyro space configuration is given in Fig. 4. Three gyros are installed according to three vertical axis and another sensor is installed which has a same angle with each of them. This kind of configuration can get a parity equation.

First, assuming that s1 occurs offset fault at 100 s. Fig. 6 is shown that through parity equation the fault is detected at 100 s, but it cannot be isolated and orientated. Fig. 7 shows through the application of wavelet analysis, which degrades sensor signals into level 1 or 2 and can judge s1 suffering a fault at 100 s. Then, the faulted sensor can be positioned and be isolated.

Discrete wavelet transform analyzes the stored sensor data then judge whether the sensor is fault or not. It does not need the hardware redundancy of sensor itself. It is very important to select the length of the data storage buffer. The lesser of the selected data length, the shorter of the calculating time it would use. At the same time, correctness is also decreased with the decrease of data length. The length should be selected based on computer calculation ability and its control security time interval. It can be known from the simulation that 16 data length can be used to judge fault easily based on the condition of no interference and smaller noise, so the bigger number should be selected in practical application, such as 32.

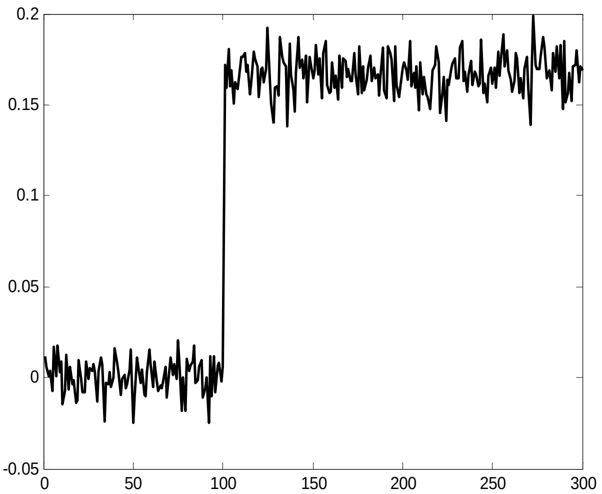

Fig. 6 Offset fault is detected by parity equation.

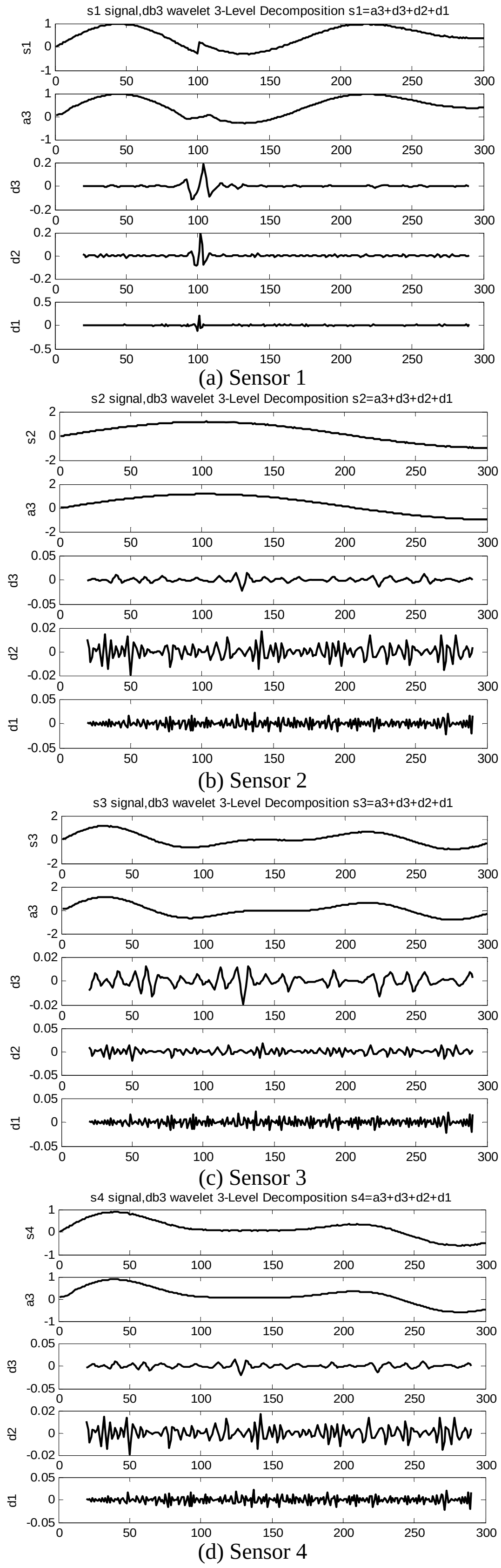

Fig. 7 Offset fault is detected by wavelet analysis.

5.3.2.3 Analysis of Wavelet Based Fault Detection

Simulation shows that wavelet analysis to low frequency nonstationarity signal fault detection has a strong ability of diagnosis. Its characteristic is to realize the signal of the multi-resolution analysis, and is convenient for the overall and local signal to score, this regarding the fault diagnosis of great practical significance. And, the wavelet analysis method for sensor fault diagnosis provides an effective way, and does not need mathematic model of the system. Moreover, wavelet analysis method not only can be realized by using software, but also can be realized by using hardware, so it can be applied in real-time demanding occasions, and it provides the fault detection and diagnosis algorithm suitable for applications in all kinds of airplanes, which is with a great practical value and extensive applicability.

6. Conclusions

The above analysis and simulation shows flight control system redundancy number can be reduced by making the best use of every redundancy component, and thus fault detection and isolation for low hardware redundancy is becoming very important. The methods which mentioned in this paper can easily achieve flight control system components fault detection and isolation for low hardware redundancy configuration, thus improving flight control system reliability at the same time reducing the hardware redundancy number. The most important thing is that these methods are all mathematic model independent, therefore they are suitable for all kinds of aircraft, so they have great value in practice and can be widely used.

References

[1] M. Jim, Development of the 777 flight control system, in: AIAA Guidance, Navigation, and Control Conference and Exhibit, Austin, Texas, Aug. 11-14, 2003.

[2] J. Gautrey, Flight Control System Architecture Analysis and Design For Fly-by-Wire Generic Regional Aircraft, University Press, Cranfield Bedford, USA, 1996.

[3] D.J. Popp, R.L. Kahler, C-17 flight control systems software design, in: Proceedings of 11th IEEE/AIAA Digital Avionics Systems Conference, Seattle, USA, Oct. 5-8, 1992.

[4] S.J. Bai, R.B. Zhang, H.Y. Hu, C.Z. Yin, Design of angular displacement sensor with a large range and a high precision based on LVDT, Transducer and Micro system Technologies 25 (11) (2006) 12-14.

[5] E. Rotenberg, AR-SMT: A microarchitectural approach to fault tolerance in microprocessors, in: 29th International Symposium on Fault-Tolerant Computing, Madison, Wi, USA, Mar. 15-18, 1996.

[6] Handbook of Aircraft Design Editorial Board, Handbook of Aircraft Design, Aviation Industry Press, Beijing, China, 2003.

[7] C.Y. Wen, Modern Flight Control, Beijing University of Aeronautics and Astronautics Press, Beijing, China, 2004.

[8] X. Yan, Navigation System, Aviation Industry Press, Beijing, China, 1993.

Journal of Energy and Power Engineering 8 (2014) 551-559

Current Situation and Perspective of Second Generation Solid Biofuels Production: Case Study—CMR (Campinas Metropolitan Region), Sao Paulo, Brazil

Walfrido Alonso Pippo[1], Gilberto García del Pino[2] and Sergio Duvoisin Junior[2]

1. Alternative Fuels Group /DFA/IFGW, Estate University of Campinas, CEP 13083-970, SP, Brazil

2. Higher School of Technology, Estate University of Amazon, Manaus, CEP 69065-020, AM, Brazil

Received: October 09, 2013 / Accepted: November 26, 2013 / Published: March 31, 2014.

Abstract: This proposal aims to assess the market introduction of advanced technologies for the production of 2nd generation solid biofuels, specifically technologies for the production of briquettes and pellets from agro-industrial wastes. The development of this project will evaluate the socio-environmental and techno-economical feasibility and use of 2nd generation solid biofuels in the CMR (Campinas Metropolitan Region). The successful introduction of second generation briquettes and pellets to market depends, mainly, on two aspects: logistics in supply chains which generate waste, and the efficiency of production technologies. The study of logistics (supply chain) is based on survey data of the main productive supply chains, analysis, and modeling to optimize the facility location in the network for each case. The evaluation of the efficiency of production technology is provided by testing specially designed waste compacting devices, and comparing these results with the resulting power consumption during the production, in demonstration-scale, of a round of briquettes. The costs and consumption during the demonstration-scale production of briquettes are used for validation and correction of an optimization model. This project was approved in late 2012 with a period of two years for its implementation. Later in 2013, it was decided also to extend its implementation to the Metropolitan Region of Manaus, Amazon. Due to its recent beginning, the results shown here are only preliminary.

Key words: Supply chain management, energy efficiency, environmental management, logistic, renewable energy, biofuels.

1. Introduction

Today Brazil is the world leader in the use of renewable energy, specifically biofuels. A simple comparison between the composition of the Brazilian and the world's energy matrices is enough to confirm this statement. The percentage of renewable energy in the world is 15% (Fig. 1), but in Brazil it is 43%. The percentage of bioenergy in the composition of the global energy matrix is only 12% while in Brazil it is 30%. Brazil is the second leading ethanol producer in the world, and it has approximately 30 million FFVs (flex-fuel vehicles), which is the largest fleet in the world today [1]. With its national program for the production and use of biodiesel [2], Brazil became the first Latin American country to implement this kind of program. This privileged situation represents a great opportunity for Brazilian enterprises to expand the use of biofuels in social practice, and export not only commodities, but also biofuel production technologies.

2. Importance of Second Generation Solid Biofuels

Just a cursory look at agribusiness in Brazil and one can quickly identify at least nine supply chains with vast potential to convert solid waste residues into briquettes and pellets (second generation solid biofuels). These agribusinesses include sugar cane, corn, cassava, citrus, wheat, rice, coffee, timber, soy and coconut. All of them must be studied in detail in

Corresponding author: Walfrido Alonso Pippo, associate senior researcher, research field: biofuels. E-mail: pippo177@yahoo.com.

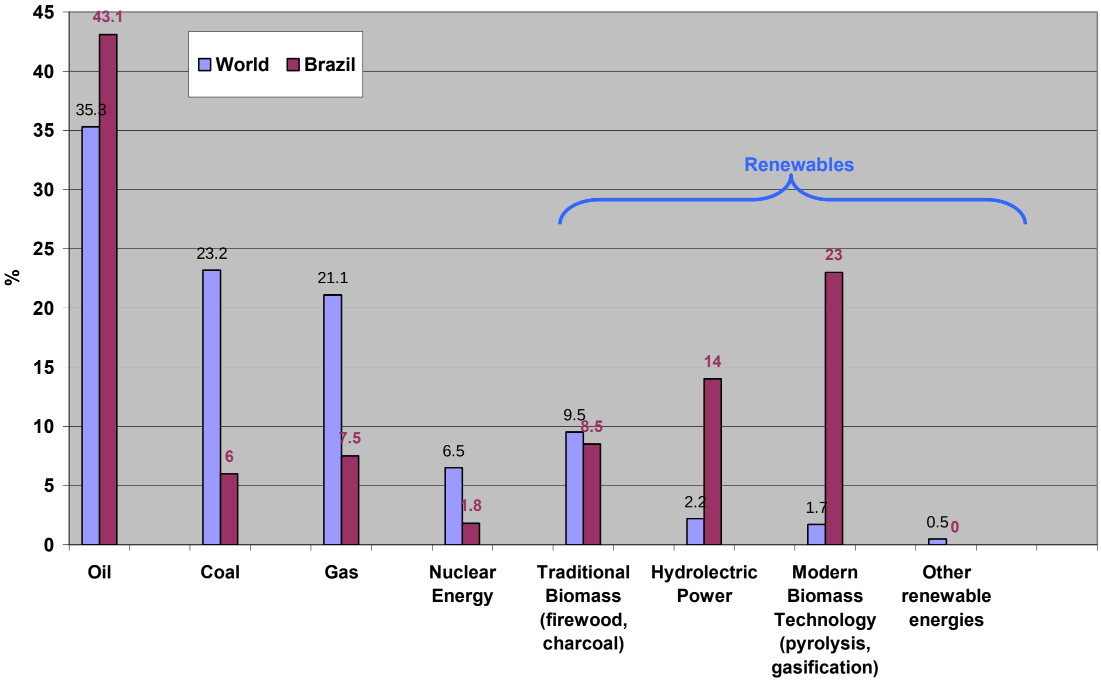

Fig. 1 Energy matrix composition utilized by the world vs. Brazil.

order to decide whether it is possible to utilize the energy or not, and to adopt the adequate logistics strategies for those which are feasible. The total agricultural waste produced in Brazil in 2008 was as follows [3]: corn: 70.814×10^6 tons; cassava: 56.887×10^6 tons; wheat: 1.354×10^6 tons; citrus: 10.384×10^6 tons; sugarcane-trash: 220.651×10^6 tons. According to the survey, which contained data collected on solid waste from Brazilian states, most of these residues are not adequately treated. As a rule, their disposal is done by using inappropriate procedures [4]. In most cases, the waste is deposited in landfills untreated, or simply left to accumulate, often polluting the water, air and soil. If the residues mentioned above were used in solid biofuels production, many new jobs would be generated in supply logistic, manufacturing, and distribution logistic, meanwhile, simultaneously avoiding the negative environmental impacts. Moreover, the gas, firewood and charcoal can be substituted by briquettes and pellets produced from agricultural residues, creating the possibility of self-financial management concerning relevant carbon credits. A ton of firewood has a price between $300.00-$325.00 USD. These figures make it easy to see that even without considering the possibility of carbon credits each year, Brazil is throwing away millions, perhaps tens of millions of USD.

2.1 Context of the Problem

The CMR is composed of 19 municipalities (Fig. 2), and it has an area of 3,673 km² and a population of 2,798,477 inhabitants. In the CMR there are over 9,362 companies which are potential consumers of briquettes, either for cooking food or for kilns factories which produce different types of ceramic materials. In Campinas there are more than 272 facilities with the capacity to supply feedstock for the production of briquettes and pellets [5]. These enterprises have a staff of 48,272 employees and their annual salary budget is more than $265 million USD. In Campinas alone (the largest municipality of the CMR), which has an excellent road network, there are 3,346 hotels, restaurants and small food stores registered with 16,089 employees and a wage budget of $68,062 million USD [6]. Currently, most of these enterprises use fossil fuels, firewood, or charcoal for cooking and

Fig. 2 CMR administrative division map.

water heating (the latter two are derived from wood from deforestation). The option to use these types of fuels is derived from a historical practice which has proven its environmental unsustainability, and persists due to a lack of competitive renewable fuel alternatives in Brazil. The government of the state of Sao Paulo and also the municipality of Campinas are interested in improving and preserving the environment [7, 8]. Moreover, the state of Sao Paulo is the largest producer of agricultural waste. In the CMR alone there are over 297 companies that produce agricultural waste (excluding pulp mill facilities). Of these, 272 are timber facilities and they generate 149,676,000 tons/year of waste. The remaining 25 companies are rice mills that produce between 720 and 2,400 tons/year of rice husk. In Sao Paulo City there are two large industries that produce 4,320 tons/year of rice husk, while 4,520 t of this product are produced in Campinas each year [9]. Currently, most of these companies do not have a proper system for solid waste disposal, and in many cases soil and water contamination and air pollution have occurred. Taken together, this means that annually a vast number of residues, with high energy content, are generated in the CMR, and they could be used to manufacture briquettes/pellets, and thus replace the use of fossil fuels, wood, and charcoal in consumer enterprises in Campinas.

3. The Solution and Limits to the Supply Chain Problem

Given the multitude of factors concerning the issue and their complicated interrelationships within the framework of this project, it is impossible to claim a total and definitive solution. Therefore, this project aims through the study and analysis of the supply chains that generate agro-industrial residues in the CMR to identify which of them are better for the production of solid biofuels. This project also aims to carry out a feasibility study of manufacturing second generation briquettes, which can be substituted for fossil fuels, wood, and charcoal in consumer enterprises in the CMR. Filling the gaps in expertise on the feasibility of the use of solid biofuels in the CMR,

the publication and dissemination of research results from this work will undoubtedly help to eliminate the distrust of investors, and justify and encourage the sustainable development of this region.

3.1 Working Hypotheses and Prediction of Impacts

Considering the results of preliminary studies carried out during the development of this proposal, and the experience of over twenty years of work on the subject, the following working hypotheses were prepared:

(1) Given the geographic, demographic, technological and logistic facilities existing in the CMR: it is feasible to use the agro-industrial waste from the existing supply chains of major commodities for the production of 2nd generation solid biofuels.

(2) Given that the materials and processes utilized in this study are low cost, also considering the geographic, demographic, technological and logistic facilities of the CMR:

Optimal locations can be found for the production facilities for 2nd generation solid biofuels in those supply chains, which aid in their techno-economical feasibility.

(3) Although the amount of waste generated by businesses in the CMR is large, more than 90% of companies in the CMR are micro, small and medium enterprises. This is translated to inherent losses due to the seasonal nature of most crops. Overcoming this contradiction is not always understood by investors, who generally do not have or are unaware of the technological possibilities existing in Brazil. This indicates the necessity of a study of each supply chain, taking into consideration the location of new developments and technologies for the production of briquettes, and then adapting the reality of the production scale to small businesses: It is possible to overcome the constraints of raw material availability in the supply chain for the production of briquettes, through the use of extrusion technology proposed in this project, and simultaneously to guarantee high efficiency in the production process.

3.2 Prediction of Impacts

Because the product engineering (briquetting and pelletization) is known, and considering that the raw material is safe to use from the point of view of greenhouse gases emissions, it is not expected that the manufacture of briquettes/pellets starting from agro-industrial residues will introduce new negative impacts, beyond those already existing today. The practical implementation of the knowledge generated by this project, in addition to the environmental benefits, will insure the following positive impacts: (1) increased technological energy efficiency and improved combustion in boilers and furnaces due to the lower moisture content of the briquettes/pellets; (2) techno-economic benefits including the possibility to extend the use of agricultural waste energy in the off-season; (3) financial savings by the replacement of fossil fuels; (4) socioeconomic benefits including job creation for the collection and transportation of biomass, construction of production facilities, and direct employment in the manufacturing of briquettes/pellets.

4. General Project Objective

To assess the techno-economic feasibility and socio-environmental sustainability of solid biofuels production from agro-industrial waste in the CMR, taking into consideration the main supply chains existing in this region.

4.1 Project Specific Objectives

This general objective can be broken down to eight more specific objectives that would together achieve the overall goal of the project as follows:

(1) to study the potential suppliers of agro-industrial residues of the main supply chains in the CMR (rice husk, coffee husk, sawdust, bagasse and sugarcane-trash);

(2) to analyze and select the three supply chains with

the largest potential and superior conditions for the collection of waste. This involves the physical-chemical characterization of residues from selected supply chains, and their conversion to briquettes and pellets;

(3) short and medium term forecast for the demand for briquettes/pellets in the selected companies of the CMR. Determine the long-term forecast for the demand for briquettes in the best of the analyzed companies., from the feasibility point of view;

(4) development of profit optimization models (operational research);

(5) experimental determination of energy consumption during the production of briquettes and pellets from residues from the selected supply chains;

(6) comparison of the results obtained during the compaction assays under ideal conditions with the results obtained during the production of a round of briquettes in the demonstration scale, to evaluate the efficiency of the technology and validate the optimization model;

(7) estimation of the technical and economic feasibility of briquette production in commercial scale, in the supply chains of the CMR;

(8) publication of partial and final results in specialized journals on the issue.

5. Solution Algorithm: Its Steps and Particularities

The solution algorithm is shown in Fig. 3. Basically the algorithm is composed of four steps.

In the 1st step, which also includes the physical–chemical characterization and quality control, the assessment concerning techno-economical requirements is carried out by using the formula (1):

$$GrPM = \sum \mathrm{Price}_{Sales} - \left(\sum_{1}^{m} P_f + \sum_{1}^{n} T_{\cos t} + \sum_{1}^{\ell} TR + \sum_{1}^{\varphi} C + \sum_{1}^{\nu} CR\right) \quad (1)$$

where, $GrPM$ = Average Gross Profit (profit before tax discount); Price_{Sales} = sale price of the main product in the supply chain; P_f = price of feedstock suppliers; T_{cost} = transportation costs of the main products in the supply chain; TR = costs of transporting the residues; C = costs related to manufacturing and distribution of the main product of the supply chain; CR = costs related to manufacturing and distribution of biofuels starting from residues; m = quantity of feedstock suppliers; n = number of travels to guarantee feedstock for main product; ℓ = number of travels to guarantee residues; φ= total quantity of costs concerning manufacturing of the main product; ν= total quantity of costs concerning biofuels production starting from residues.

The analyses used in the physical-chemical characterization of the residues in the 1st step and their relevant standards are shown in Table 1.

Because there are not yet Brazilian standards on the quality of briquettes and pellets, as a rule these parameters are assessed by using standards from the European Union [9].

The optimization model developed in the 2nd step is a Linear Programming method (Simplex Method; in formula 2). The comparison is based on Ref. [9].

The constrictions related to the Linear Program system Eq. (2) are specific for each type of residue studied.

$$\begin{aligned} & Min \sum_{i=1}^{n} f_i y_i + \sum_{i=1}^{n}\sum_{j=1}^{m} D_j c_{ij} x_{ij} \\ & ST \\ & \sum_{i=1}^{n} x_{ij} = 1 \_\_ \ para \ \_\_ \ j = 1,\ldots,m \\ & \sum_{j=1}^{m} D_j x_{ij} \le K_i y_i \ \_\_ \ para \ \_\_ \ i = 1,\ldots,n \\ & x_{ij}, y_i \in (0,1) \end{aligned} \quad (2)$$

where, n = number of locations for briquettes/pellets facilities construction; m = number of clients; D_j = year demand of the market j; K_i = annual capacity of the facility i; f_i = fixed operational costs if facility i is open; c_{ij} = production and handling costs from i facility to j market (costs including production cost, stocks cost, and transportation); y_i = 1 if facility y is localized in i, otherwise 0; x_{ij}= 1 if market j is stocked by the facility i, otherwise 0.

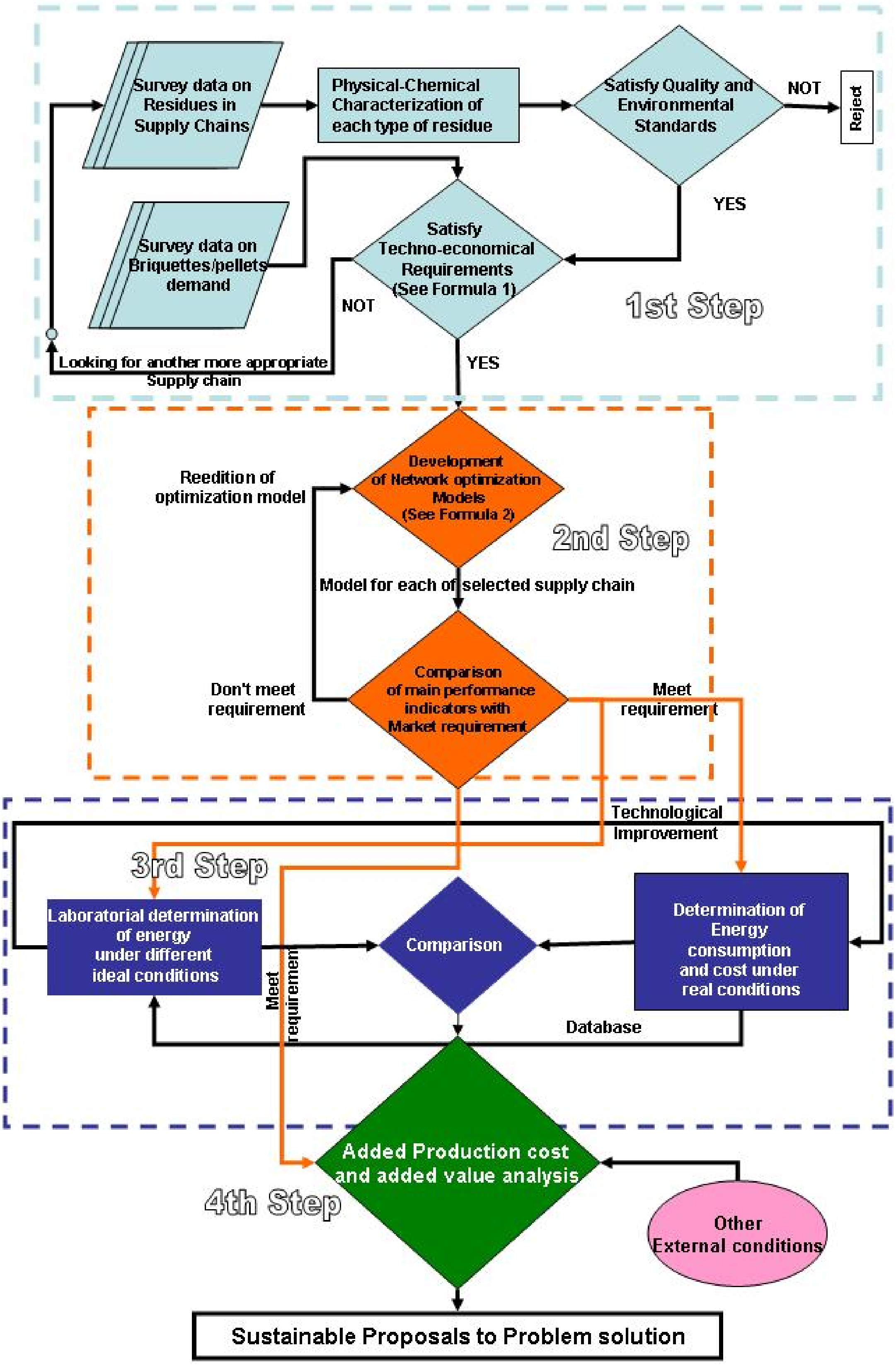

Fig. 3 Algorithm for problem solution.

Table 1 Analyses used in the physical-chemical characterization of the residues.

Tested residues	Characterization technique	Measuring and control equipment used	References
Residues from selected supply chain	Elemental analysis	Device: Perkin Elmer–Series II 2400. Laboratory glassware	[10]
	Moisture content	Analytical balance type (AB204). Max Capacity-220 g. Min-10 mg. Read -1 mg, precision 0.01 mg. Muffle 1,200 °C, precision -10 °C, Furnace 600 °C. Laboratory glassware. Set of tyler sieves	[11]
	Proximate analysis	90-4070-27, Parr oxygen bomb 1,108P	[12]
	Test methods for gross calorific value bomb calorimeter		[13]
	Bulk density		Author experimental procedure adapted from [14]
		Calibrated recipient 0.005 m^3; analytical balance; laboratory glassware	

Fig. 4 Compression-traction testing station.

During the 3rd step laboratorial experiences are carried out to determine the theoretical limits of energy consumption. Figs. 4 and 5 show the equipment and the procedure used.

During the 3rd step, the production in demonstration-scale of a round of briquettes is made using an extrussion briqueting machine (Fig. 6).

In the 4th step, the techno-economical assessment is carried out through added value/added cost analysis. In this step, the main techno-economical performance indicators are determined: Cash flow analysis; Payback time, Profitability Assessment by means of NPV (net present value) and IRR (investment return ratio).

6. Expected Results

• estimation of potential demand of briquettes/pellets for the CMR businesses in the short, medium and long terms.

Fig. 5 Compression of biomass residues in the briquetting test device.

Fig. 6 Extrussion briqueting machine.
Source: Courtesy of alternative fuel group UNICAMP

• detailed survey of potential feedstock suppliers for the production of briquettes/pellets from waste in the CMR.

• determination and classification of supply chains with greater feasibility potential for energy recovery from agro-industrial residues in the CMR.

• development of optimization models, specific for the selected supply chains.

• development of new knowledge about the process of waste compaction, and the costs involved with this physical phenomenon.

• determination of the efficiency of reserves that can still be exploited by the extrusion technology.

• estimation of the technical and economic feasibility and socio-environmental production of briquettes in the CMR.

• publication of partial and final results in the specialized indexed journals.

7. Conclusions

The development of this project will evaluate the socio-environmental and techno-economical feasibility and use of 2nd generation solid biofuels in the CMR.

The practical implementation of the knowledge generated by this project, in addition to the environmental benefits, will insure the following positive impacts: (1) increased technological energy efficiency and improved combustion in boilers and furnaces due to the lower moisture content of the briquettes/pellets; (2) techno-economic benefits including the possibility to extend the use of agricultural waste energy in the off-season; (3) financial savings by replacement of fossil fuels; (4) socioeconomic benefits including job creation for the collection and transportation of biomass, construction of production facilities, and direct employment in the manufacturing of briquettes/pellets.

Acknowledgments

The authors want to thank the Brazilian National Council for Scientific and Technological Development (CNPq)-Process No. 150604/2009-2, the Sao Paulo Research Foundation (FAPESP) (Process 12/50730-2), and the Amazon Research Foundation (FAPEAM) for the financial support of this work.

References

[1] R. França, L.A.H. Nogueira, Seventy questions to

understand the ethanol (Setenta questões para entender o etanol), Revista Veja 1 (2052) (2008) 104-114. (in Portuguese)

[2] Law 11.097, 2005 (Common Law) 01/13/2005, LEI 11.097/2005 Provides for the Introduction of Biodiesel in Brazilian Energy Matrix (LEI ORDINÁRIA) 13/01/2005 (Original in Portuguese) [Online], President of Brazilian Federative Republic, http://www.planalto.gov.br/ccivil_03/_ato2004-2006/2005/Lei/L11097.htm. (2005) (accessed Oct. 12, 2012).

[3] IBGE Brazilian Institute of Geography and Statistic (Instituto Brasileiro de Geografia e Estatística) [Online], http://www.ibge.gov.br. (accessed Oct. 19, 2009)

[4] ABNT, Brazilian Association of Standard and Technical Norms, Solid Residues (Resíduos Sólidos Classificação NBR 10004: 2004, p. 71) [Online], http//www.aslaa.com.br/legislacoes/NBR%20n2010004-2004.pdf (accessed Nov.30, 2012).

[5] IBGE System for Automatic Recovery of Information (Sistema IBGE de Recuperação Automática-SIDRA) (Original in Portuguese) [Online], http://www.sidra.ibge.gov.br/bda/tabela/listabl.asp?z=t&o=1&i=P&e=l&c=1734(accessed 04/04/2012).

[6] IBGE—Central Register of Enterprises (Cadastro Central de Empresas) [Online], http://www.sidra.ibge.gov.br/bda/tabela/listabl.asp?c=1735&z=t&o=12). (Accessed 09/02/2012)

[7] Organic Law of Campinas County (Lei Orgânica de Campinas e Lei Complementar nº15 de 27/12/2006 sancionada e promulgada pelo Prefeito Municipal) [Online], Sept. 2, 2012, http://www.campinas.sp.gov.br/bibjuri/lom.htm (accessed 09/02/2012).

[8] Database of Industries Federation of São Paulo Estate (A indústria Paulista: Banco de dados de Empresas do Estado de São Paulo), 1st ed., Sao Paulo Federation of Industries, Brazil, 2003, pp. 235-250.

[9] European Pellets Center–Pellets@las Project, Disponívelem [Online], http://www.pelletcentre.info/cms/site.aspx?p=878 (acesscessed Dec. 12, 2008).

[10] ASTM (D 3178-84), Standard Test Methods for Carbon and Hydrogen in the Analysis of Coal and Coke, USA, 1984.

[11] ASTM (D 3286-85), Standard Test Methods for Gross Calorific Value of Coal and Coke by the Isoperibol Bomb Calorimeter, USA, 1985.

[12] T.A. Miene, A.H. Brennan, B.H. Glenn, Sourcebook of Methods of Analysis and Biomass Conversion Processes. Elsevier Applied Science, Elsevier Science Publisher, 1990, pp. 166-527.

[13] ASTM E872-82, Standard Test Method for Moisture Analysis of Particulate Wood Fuels ASTM International [Online], West Conshohocken, PA, 2006, http://www.astm.org (accessed Sept. 2, 2012).

[14] N. Chevanan, A.R. Womac, V.S. Bitra, Loose-filled and tapped densities of chopped switchgrass, corn stover and wheat straw, ASABE 8 (20) (2008) 15-30.

Journal of Energy and Power Engineering 8 (2014) 560-567

Least Squares Fitting Based Fault Classification in Distribution Systems

Omar A. Saraereh[1], Qais Alsafasfeh[2], Anas Al Tarabsheh[1], Aouda Arfoa[2] and Issa Etier[1]

1. Department of Electrical Engineering, Hashemite University, Zarqa 13115, Jordan

2. Electrical Engineering Department, Tafila Technical University, Tafila 66110, Jordan

Received: October 26, 2013 / Accepted: December 23, 2013 / Published: March 31, 2014.

Abstract: Power systems are the largest and most complex human made systems, consisting of thousands of electrical sources, loads, transmission and distribution lines, power transformers, circuit breakers, etc. where faults always occurred. Faults can cause personnel and equipment safety problems, and can result in significant disruption to power supply and thus financial losses. In this paper we will present comprehensive mathematical suite to detect and classify fault dependent models of various types of power systems. This work will extract fault unique signatures by using polarization ellipse during the healthy condition and the polarization will be circular shape with radius equal the rated voltage of the system, but during the fault condition the polarization will be ellipse shape and the fault signature will be defined according the ellipse parameters major axis, minor axis, ellipticity and orientation angle, by using least squares criterion will define the ellipse parameters this system will identify and classify. This paper will be a milestone for extended paper based on the proposed mathematical modelling and applying it to identify, classify and localize with simulation model.

Key words: Distribution systems, major axis, minor axis, ellipticity, fault, ellipse, least squares criterion.

1. Introduction

There is a trend that the power distribution systems now served by large power generators will be enhanced with more DG (distributed generator) architectures are less restrictive. Fault detection has been a focal point in the research of power systems area since the establishment of electricity transmission and distribution systems. The objectives of a power system fault analysis is to provide enough information to understand the reasons that lead to an interruption and to, as soon as possible, restore the handover of power, and perhaps minimize future occurrences if possible at all. Analysis should indeed provide us with an understanding of the network that can lead to producing a set of preventive measures which can be implemented to reduce the likelihood of equipment damage. Circuit breakers and other control elements are designed to help protective relays to take appropriate actions [1, 2] and thus minimize damage and length of interruption. Prompt detection of a fault will have a significant impact on the equipment safety since it will engage the circuit breakers instantaneously and before any significant damage occurs. In recent years, with an increase in the number of power system networks within one control center, the behavior and effect of faults became more complex and as a result, fault impacted area has expanded. Researchers in applied mathematics and signal processing have developed many techniques for the detection and classification of faults in traditional electrical power distribution systems and used them in conjunction with relaying and protection devices. Recent tools include ANN (artificial neural network) and Wavelets among other powerful pattern recognition and classification tools. ANN based algorithms depend on indentifying the different patterns of system variables using impedance information. The proposed neural network

Corresponding author: Omar A. Saraereh, Ph.D., research fields: renewable energy and RF energy harvesting. E-mail: eloas2@hu.edu.jo.

architectures suffer from a large number of training cycles and a high computational burden. Another significant drawback for using ANN is that the resolution is not efficient since it can be a very sparse network with the need for a large size training data adding an additional burden on its computational complexity [3-6]. Wavelet transform has been proposed by many to decompose voltage and current waves in an effort to identify a fault. It has been reported that wavelet transform based methods for fault detection are fast and effective analysis methods [7]. Others incorporated wavelet transform with other methods such as PNN (probabilistic neural network), adaptive resonance theory, adaptive neural fuzzy inference system and support vector machines [8-11]. Fuzzy logic was also combined with discrete Fourier transform, adaptive resonance theory, principles of estimation and independent component analysis to enhance performance [11-16]. In comparison with ANN, fuzzy logic systems are subjective and heuristic and in general, they are simpler than the wavelet transform or the neural network based techniques. Unfortunately, most of the available tools for fault detection and classification are not efficient and are not investigated for real time implementation [4]. There is a need for new algorithms that have high efficiency, general applicability, and suitable for real time usage especially for power distribution system with high penetration of renewable energy. This research proposes a protection scheme to classify the fault in a distribution network with renewable energy DG penetration.

2. The Polarization Ellipse

2.1 Introduction

Rotary-spectrum and polarization analysis are widely used in a number of research areas, including optics, geophysics, meteorology, oceanography and radar [17]. These techniques were originally developed for stationary signals. Their starting point is the Cramér-Loève spectral representation for a complex harmonizable random process, to understand polarization ellipse we are considering the simplest case which is monochromatic and deterministic. Its real and imaginary parts are then given by:

$$\begin{aligned} E_x(t) &= E_{0x}\cos(\omega t + \varphi_x) \\ E_y(t) &= E_{0y}\cos(\omega t + \varphi_y) \end{aligned} \tag{1}$$

the components and give rise to a resultant vector in the transverse x-y plane. The resultant vector describes a locus of points whose form (equation) is now determined. In order to derive the equation described, Eq. (1) are written as:

$$\begin{aligned} \frac{E_x(t)}{E_{0x}} &= \cos(\omega t)\cos(\phi_x) - \sin(\omega t)\sin(\phi_x) \\ \frac{E_y(t)}{E_{0y}} &= \cos(\omega t)\cos(\phi_y) - \sin(\omega t)\sin(\phi_y) \end{aligned} \tag{2}$$

By straightforward algebra the following relation can then be found:

$$\varphi = \varphi_y - \varphi_x$$

Eq. (4) is recognized as the equation of an ellipse and shows that at any instant of time the locus of points described by an ellipse, in particular, is called the polarization ellipse.

As shown in Fig. 1, the ellipse has three major parameters, major axis, minor axis and a common parameterization uses the orientation angle, ψ, the angle between the major axis of the ellipse and the x-axis as shown in Eq. (5) [18].

$$\begin{aligned} \frac{E_x(t)}{E_{0x}}\sin(\varphi_y) - \frac{E_y(t)}{E_{0y}}\sin(\varphi_x) &= \cos(\omega t)\sin(\varphi_y - \varphi_x) \\ \frac{E_x(t)}{E_{0x}}\cos(\varphi_y) - \frac{E_y(t)}{E_{0y}}\cos(\varphi_x) &= \sin(\omega t)\sin(\varphi_y - \varphi_x) \end{aligned} \tag{3}$$

Square Eq. 3 and add the two equations then yield:

$$\frac{E_x^2(t)}{E_{0x}^2} + \frac{E_y^2(t)}{E_{0y}^2} - 2\frac{E_x(t)E_y(t)}{E_{0x}E_{0y}}\cos(\varphi) = \sin^2(\varphi) \tag{4}$$

$$\psi = \tan^{-1}\left(\frac{2E_x(t)E_y(t)}{E_{0x}^2 - E_{0y}^2}\cos(\varphi)\right) \tag{5}$$

And the ellipticity (ε), the minor to major axis ratio (also known as the axial ratio) as shown in Eq. (6):

$$\varepsilon = \frac{A_{ma}}{A_{mi}} \tag{6}$$

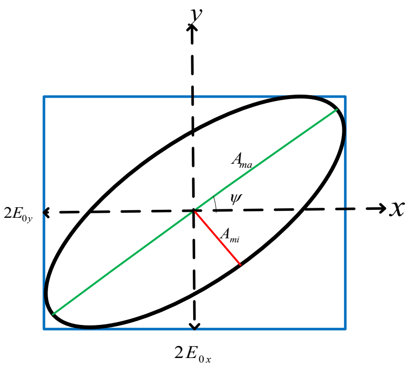

Fig. 1 The polarization ellipse generate from two phasors.

By using Euler formula for Eq. (1) and substitute in Eq. (4), the ellipse can be represented as sum of positive and negative angular frequency phasors [19]:

$$E(t) = E^{+}e^{jwt} + E^{-}e^{-jwt} \tag{7}$$

Where,

$$E^{+} = \left|E^{+}\right|e^{j\varphi^{+}},\ E^{-} = \left|E^{-}\right|e^{j\psi^{-}}$$

$$A_{ma} = \left\|E^{+}\right| + \left|E^{-}\right\|,\ A_{ma} = \left\|E^{+}\right| - \left|E^{-}\right\|,\ \psi = \frac{1}{2}\left(\psi^{+} + \psi^{-}\right)$$

2.2 Degenerate States of the Polarization Ellipse

Case 1: The two orthogonal components are in phase. In this case the ratio of the strengths of the two components is constant, so the direction is constant this special case is called linear polarization and the ellipticity (ε) will equal zero:

Case 2: Two orthogonal components have exactly the same amplitude and are exactly ninety degrees out of phase. In this case one component is zero when the other component is at maximum or minimum amplitude. There are two possible phase relationships that satisfy this requirement: the x component can be ninety degrees ahead of the y component or it can be ninety degrees behind the y component. So this special case is called circular polarization and the ellipticity (ε) will equal one, this case we will use it to represent the healthy condition (no fault).

Case 3: The two components are not in phase and either do not have the same amplitude. This kind of polarization is called elliptical polarization because the electric vector traces out an ellipse in the plane (the polarization ellipse) and the ellipticity (ε) will be greater than 0 and less than 1, this case we will use it to represent the faulty condition. The different types of faults can be distinguished by using the ellipse parameters (major axis, minor axis, orientation angle (ψ) and ellipticity (ε)) [20].

3. Fault Detection and Classification Based on Polarization Ellipse

3.1 Features Estimation of Fault Signal

We will demonstrate for general case then will define the parameters depend on fault type, for simple power systems of two buses as shown in Fig. 2. The three phase voltage signal is described by the Eq. (8). To satisfy ellipse polarization requirement must get two orthogonal phasers, so as to get this condition we can use Clarke transformation described by the Eq. (8). Traditionally, power systems have been analyzed using symmetrical components, Clarke transformation, or any other modal transformation. These polyphase transformations decouple symmetric and cyclic polyphase systems. In balanced power systems or in systems without a neutral return, the zero sequence components are zero. Positive and negative sequences have similar behavior, especially in symmetric poly phase systems [21].

$$\begin{aligned} Va(t) &= V_{af}\cos(\omega t - \varphi_a) \\ Vb(t) &= V_{bf}\cos(\omega t - \varphi_b) \\ Vc(t) &= V_{cf}\cos(\omega t - \varphi_c) \end{aligned} \tag{8}$$

$$\begin{pmatrix} x_\alpha(t) \\ x_\beta(t) \\ x_0(t) \end{pmatrix} = \frac{2}{3}\begin{pmatrix} 1 & -\frac{1}{2} & -\frac{1}{2} \\ 0 & \frac{\sqrt{3}}{2} & -\frac{\sqrt{3}}{2} \\ \frac{1}{2} & \frac{1}{2} & \frac{1}{2} \end{pmatrix}\begin{pmatrix} v_a(t) \\ v_b(t) \\ v_c(t) \end{pmatrix}$$

$$x(t) = x_\alpha(t) + jx_\beta(t) = \frac{2}{3}\begin{bmatrix} 1 & e^{j\frac{2\pi}{3}} & e^{j\frac{4\pi}{3}} \end{bmatrix}\begin{bmatrix} v_a(t) \\ v_b(t) \\ v_c(t) \end{bmatrix} \tag{9}$$

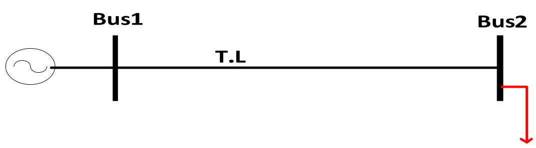

Fig. 2 Simple power distribution system.

By using Euler formula for Eq. (8) and substitute in Eq. (9) the result will be shown in Appendix 1:

$$Va(t) = V_{af}\cos(\omega t) = \frac{V_{af}}{2}\left(e^{j(\omega t-\varphi_a)} + e^{-j(\omega t-\varphi_a)}\right)$$

$$Vb(t) = V_{bf}\cos(\omega t - \frac{2\pi}{3}) = \frac{V_{bf}}{2}\left(e^{j(\omega t-\varphi_b)} + e^{-j(\omega t-\varphi_b)}\right)$$

$$Vc(t) = V_{cf}\cos(\omega t - \frac{4\pi}{3}) = \frac{V_{cf}}{2}\left(e^{j(\omega t-\varphi_c)} + e^{-j(\omega t-\varphi_c)}\right)$$

For healthy condition (ideal system):

$$V_{af} = V_{bf} = V_{cf} = V \Rightarrow$$

$$\bar{x} = \frac{2}{3}\left[\left(\frac{3V}{2}\right)e^{j(\omega t)} + \frac{V}{3}\left(1 - \frac{1}{2} + j\frac{\sqrt{3}}{2} - \frac{1}{2} - j\frac{\sqrt{3}}{2}\right)e^{-j(\omega t)}\right] = Ve^{j(\omega t)}$$

The trajectory plane will circle with radius equal of rated voltage of the system, but for fault condition we will exam that trajectory parameter according to type of fault but before starting there some important points must be clarified to be more realistic.

3.2 Single Phase to Ground Fault

Three different ground faults (AG, BG and CG) can occur in a power system, which are the most common fault type, starting to determine the ellipse parameters we must understand the system paviour during the fault:

• a decrease of voltage (undervoltage) in the faulted phase;

• high or low unfaulted voltages, depend on an X0/X1 equivalent behind the fault. If the ratio X0/X1 is greater than 1, higher voltage will occur on the unfaulted phases. As an example, for a ratio of 3, the overvoltage will reach about 126% of normal values. If the ratio X0/X1 is less than 1, undervoltage will be experienced on the unfaulted phases. If ration *X0/X1* equals 1, the unfaulted-phase voltages will stay undisturbed [22];

• unfaulted phases are not identical, there are some differences between them depending on phase sequence. As an example of AG fault the effect in phase b is greater than that in phase c in abc sequence;

• for grounding system or low impedance fault the voltage value between faulted and unfaulted phases is high and voltage value between unfaulted phases is also high. For ungrounding system or high impedance fault voltage value between faulted and unfaulted phases is low and voltage value between unfaulted phases is low. Now we will set the above condition in Eq. (11) to define the ellipse parameters. Also, we set there is no phase shift change during the fault $\phi_a = 0$, $\varphi_b = 2\pi/3$ and $\varphi_c = 4\pi/3$.

(1) phase A to ground (AG):

$$V_{af} = V_f,\ V_{bf} = \delta_s V,\ V_{cf} = V \Rightarrow$$

Where,

$$\frac{V_f}{V} \le \delta_s < 1$$

The orientation angle (ψ) value during AG Fault within $\frac{\pi}{3} < \psi \le \frac{\pi}{2}$ are shown in Fig. 3 and major axis A_{ma}, minor axis A_{mi} at δ_s will equal $A_{ma} = V,\ A_{mi} = \frac{2V_f + V}{3}$.

(2) phase B to ground (BG):

$$V_{bf} = V_f,\ V_{cf} = \delta_s V,\ V_{af} = V \Rightarrow$$

Where,

$$\frac{V_f}{V} \le \delta_s < 1$$

The orientation angle (ψ) value during BG fault within:

$$0 < \psi \le \frac{\pi}{6}$$

are shown in Fig. 4 and major axis , minor axis at δ_s will equal:

$$A_{ma} = V,\ A_{mi} = \frac{2V_f + V}{3}$$

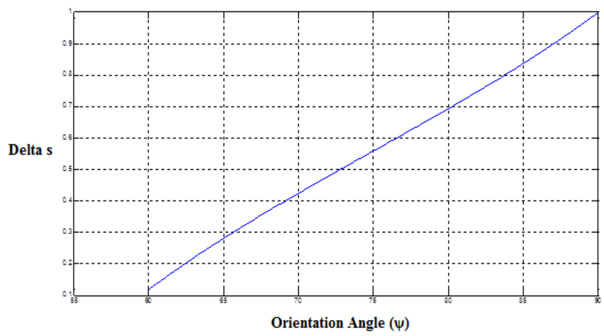

Fig. 3 The orientation angle (ψ) value during AG fault.

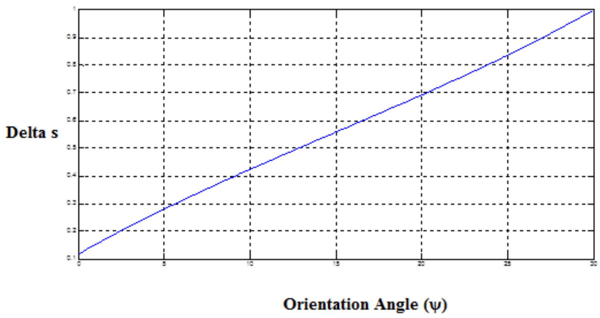

Fig. 4 The orientation angle (ψ) value during BG fault.

(3) phase C to ground (CG):

$$V_{cf} = V_f, V_{af} = \delta_s V, V_{bf} = V \Rightarrow$$

where,

$$\frac{V_f}{V} \leq \delta_s < 1$$

The orientation angle (ψ) value during CG Fault within $\frac{2\pi}{3} < \psi \leq \frac{5\pi}{3}$ are shown in Fig. 5 and major axis A_{ma}, minor axis A_{mi} at δ_s = 1 will equal $A_{ma} = V$, $A_{mi} = \frac{2V_f + V}{3}$.

In Fig. 6, the large diameter circle represents the health (no fault condition) with diameter equal the rated voltage), and the small diameter circle represents the fault condition with upper limit orientation angles (ψ) are $\pi/2$, $\pi/6$, and $5\pi/3$ for single phase fault on phase a, b and c respectively also the major axis is equal to rated voltage.

3.3 Double Phase to Ground Fault and Phase to Phase

- A decrease of voltage (undervoltage) in the faulted phases
- About an equal voltage drops in the faulted phases depending on phases sequence. As an example for ABG fault the voltage drop in phase b less than voltage drop in phase an in abc sequence.
- The voltage in the non-faulted phase remains unchanged or increase [22].
- For grounding system or low impedance fault, the voltage value between faulted phases is low and voltage value between faulted and unfaulted phases is also high. For ungrounding system or high impedance fault voltage value between faulted phases is high and voltage value between faulted and unfaulted phases is low.

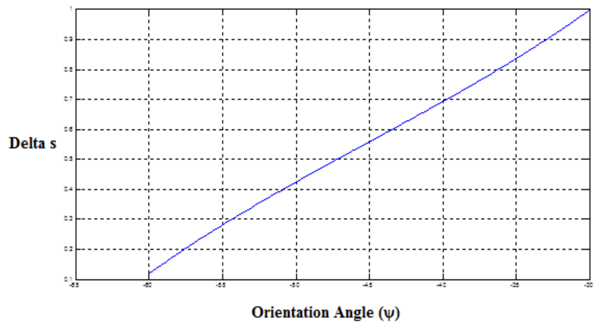

Fig. 5 The orientation angle (ψ) value during CG fault.

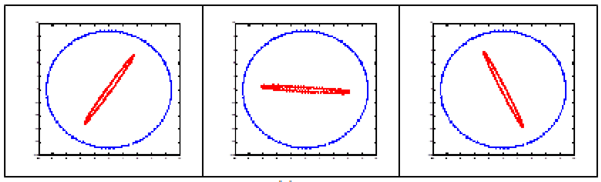

Fig. 6 Polarization ellipse for single phase to ground faults on phase a, b and c comparing with circulation ellipse (no fault condition).

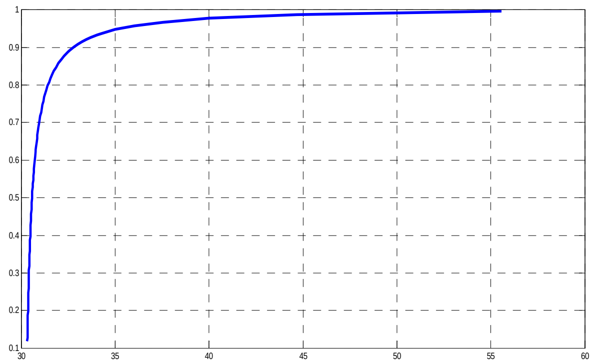

Fig. 7 The orientation angle (ψ) value during CG fault.

(1) phase A and B to ground (ABG) and (AB): $V_{af} = V_f, V_{bf} = \delta_d V_f, V_{cf} = V \Rightarrow$ The orientation angle (ψ) value during ABG Fault within $\frac{\pi}{6} < \psi \leq \frac{\pi}{3}$ as shown in Fig. 7 and major axis , minor axis at $\delta_s = 1$ will equal $A_{ma} = \frac{V_f + 2V}{3}$, $A_{mi} = V_f$.

(2) phase B and C to ground (BCG) and (BC) $V_{bf} = V_f, V_{cf} = \delta_d V_f, V_{af} = V \Rightarrow$ The orientation angle (ψ) value during BCG Fault within $\frac{5\pi}{3} < \psi \leq \pi$ as shown in Fig. 8 and major axis A_{ma}, minor axis A_{mi}

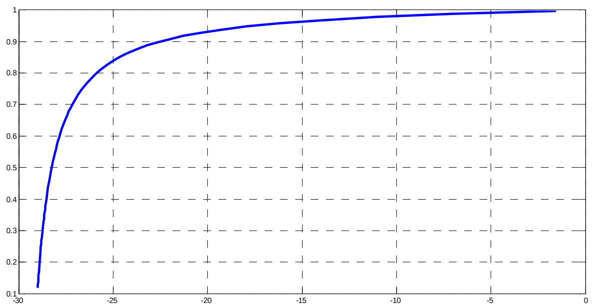

Fig. 8 The orientation angle (ψ) value during CG fault.

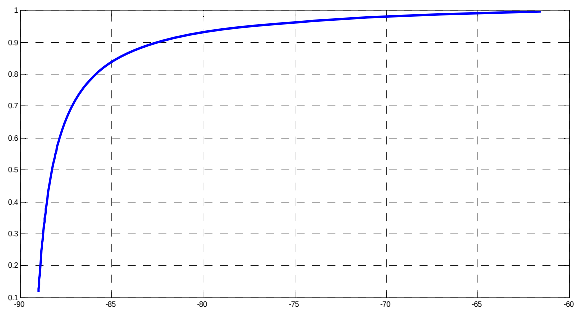

Fig. 9 The orientation angle (ψ) value during CG fault.

at δ_s = 1 will equal $A_{ma} = \frac{V_f + 2V}{3}$, $A_{mi} = V_f$.

(3) phase A and C to ground (ACG) and (AC)

$V_{cf} = V_f, V_{af} = \delta_d V_f, V_{bf} = V \Rightarrow$ The orientation angle (ψ) value during ACG Fault within $\frac{\pi}{2} < \psi \le \frac{3\pi}{2}$ are shown in Fig. 9 and major axis A_{ma}, minor axis A_{mi} at δ_s =1 will equal $A_{ma} = \frac{V_f + 2V}{3}$, $A_{mi} = V_f$.

In Fig. 10, the large diameter circle represents the health (no fault condition) with diameter equal to the rated voltage, and the small diameter circle represents the fault condition with upper limit orientation angles (ψ) are $\pi/3$, π, and $2\pi/3$ for double phase to ground fault abg, bcg and acg, respectively. Also the major axis value is less than rated voltage of the system.

In Fig. 11, the large diameter circle represents the health (no fault condition) with diameter equal to the rated voltage, and the small diameter circle represents the fault condition with upper limit orientation angles (ψ) are $\pi/3$, π and $2\pi/3$ for double phase fault ab, bc and ac respectively. These values are the same orientation angle value for double phase to ground fault and the major axis value is greater than or equals rated voltage, because the non faulted phase does not change but in grounded fault the non faulted phase will changed.

Symmetrical fault:

$$V_{af} = V_{cf} = V_{bf} = V_f \Rightarrow$$
$$A_{ma} = V_f,\ A_{mi} = V_f$$

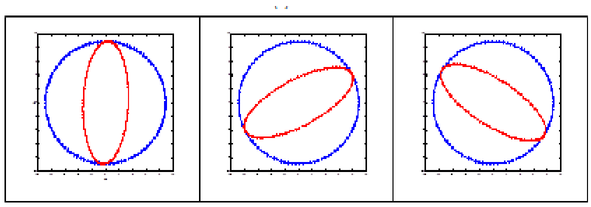

Fig. 10 Polarization ellipse for double phase to ground faults on phase ABG, BCG and ACG comparing with circulation ellipse (no fault condition).

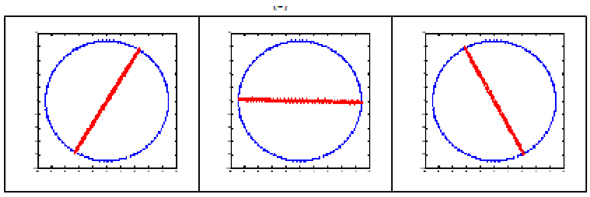

Fig. 11 Polarization ellipse for phase to phase faults on phase AB, BC and AC comparing with circulation ellipse (no fault condition).

In Fig. 12, the blue circle represents the health (no fault condition) with diameter equal to the rated voltage, and the red circle represents the fault condition for symmetrical fault with diameter equal to the voltage fault.

Table 1 shows that the nine types of asymmetric fault can be distinguished by orientation angle easily but for double phase to ground and double phase can be distinguished by using the major axis. Also the angle will changed based on fault resistance. Upper limit will angle will start at very low fault impedance and will reach the lower limit for varying high fault impedance of the end limit with max. Besides, for many buses system orientation angles will be maximum at faulted bus because the min voltage will be at faulted bus and the value of orientation angles will decreased the source.

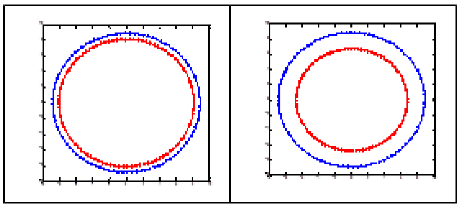

Fig. 12 Polarization ellipse for symmetrical fault comparing with circulation ellipse (no fault condition).

Table 1 Fault feature based on polarization ellipse.

Fault type	ψ	A_{ma}	A_{mi}
AG	$\frac{\pi}{3}<\psi\leq\frac{\pi}{2}$	V	$\frac{2V_f+V}{3}$
BG	$0<\psi\leq\frac{\pi}{6}$	V	$\frac{2V_f+V}{3}$
CG	$\frac{2\pi}{3}<\psi\leq\frac{5\pi}{3}$	V	$\frac{2V_f+V}{3}$
ABG	$\frac{\pi}{6}<\psi\leq\frac{\pi}{3}$	$\frac{V_f+2V}{3}$	V_f
ACG	$\frac{\pi}{2}<\psi\leq\frac{3\pi}{2}$	$\frac{V_f+2V}{3}$	V_f
BCG	$\frac{5\pi}{3}<\psi\leq\pi$	$\frac{V_f+2V}{3}$	V_f
AB	$\frac{\pi}{6}<\psi\leq\frac{\pi}{3}$	V	V_f
AC	$\frac{\pi}{2}<\psi\leq\frac{3\pi}{2}$	V	V_f
BC	$\frac{5\pi}{3}<\psi\leq\pi$	V	V_f
ABC	-	V_f	V_f

4. Conclusions

This paper presented a new mathematical method to detect and classify fault type in power distribution systems. The detection and classification process depends on unique signatures according to voltage fault signal. The above models are then used to design fault detection systems that are proven to be able to detect and reconstruct faults in near real time. Both symmetrical and unsymmetrical faults of various types and combinations are obtained.

References

[1] M. Kezunovic, C.C. Liu, J. McDonald, L.E. Smith, Automated fault analysis, IEEE Power Engineering Society 2 (2000) 819-824.

[2] M. Kezunovic, I. Rikalo, Detect and classify faults using neural nets, IEEE Computer Applications in Power 9 (4) (1996) 42-47.

[3] A. Jain, A. Thoke, R. Patel, Fault classification of double circuit transmission line using artificial neural network, International Journal of Electrical and Electronics Engineering 1 (4) (2008) 230-235.

[4] A. Jain, A. Thoke, Classification of single line to ground faults on double circuit transmission line using ANN, International Journal of Computer and Electrical Engineering 1 (2) (2009) 79-89.

[5] M. Sanaye-Pasand, H. Khorashadi-Zadeh, Transmission line fault detection & phase selection using ANN, in: International Conference on Power Systems Transients, New Orleans, USA, Sept. 28-Oct. 2, 2003.

[6] K.S. Swarup, N. Kamaraj, R. Rajeswari, Fault diagnosis of parallel transmission lines using wavelet based ANFIS, International Journal of Electrical and Power Engineering 1 (4) (2007) 410-415.

[7] V. Malathi, N. Marimuthu, Multi-class support vector machine approach for fault classification in power transmission line, in: IEEE International Conference on Sustainable Energy Technologies ICSET 2008, Singapore, Nov. 24-27, 2008.

[8] Z.X. He, X.Q. Chen, L. Fan, Wavelet entropy measure definition and its application for transmission line fault detection and identification, in: International Conference on Power System Technology, Chong Qing, China, Oct. 22-26, 2006.

[9] S. El Safty, A. El-Zonkoly, Applying wavelet entropy principle in fault classification, International Journal of Electrical Power & Energy Systems 31 (10) (2009) 604-607.

[10] J. Upendar, C.P. Gupta, G.K. Singh, Discrete wavelet transform and genetic algorithm based fault classification of transmission systems, in: National Power Systems Conference (NPSC-2008), Bombay, India, Dec. 16-18, 2008.

[11] D. Biswarup, V. Reddy, Fuzzy-logic-based fault classification scheme for digital distance protection, IEEE Transactions on Power Delivery 20 (1) (2005) 609-616.

[12] K. Razi, M Hagh, G. Ahrabian, High accurate fault classification of power transmission lines using fuzzy logic, in: International Power Engineering Conference IPEC, Singapore, Dec. 3-6, 2007.

[13] S. Vaslilc, M. kezunovic, Fuzzy ART neural network algorithm for classifying the power system faults, IEEE Transactions on Power Delivery 20 (2) (2005) 1306-1314.

[14] S. Samantaray, P. Dash, G. Panda, Transmission line fault detection using time-frequency analysis, in: IEEE Indicon 2005 Conference, India, Dec. 11-13, 2005.

[15] E. Styvaktakis, M. Bollen, I. Gu, Automatic classification of power system events using rms voltage measurements, in: IEEE Power Engineering Society Summer Meeting, Chicago, USA, July 25-25, 2002..
[16] H. Saadat, Power System Analysis, McGraw-Hill Education (India) Pvt Limited, New York, USA, 2002.
[17] P.J. Schreier, Polarization ellipse analysis of nonstationary random signals, IEEE Transactions on Signal Processing 56 (9) (2008) 4330-4339.
[18] Y. Yang, R. Tao, Y. Wang, A new SINR equation based on the polarization ellipse parameters, IEEE Transactions on Antennas And Propagation 53 (4) (2005) 1571-1577.
[19] E. Collett, Polarized light in Fiber optics, The Polawave Groub, Lincroft, NJ, 2003, pp. 46-54.
[20] J.V. Olson, R. Domke, Instrument to measure the polarization state of waves, Review of Scientific Instruments 56 (2) (1985) 278-282.
[21] Y. Xia, D.P. Mandic, Widely linear adaptive frequency estimation of unbalanced three-phase power systems, IEEE Transactions on Instrumentation and Measurement 61 (1) (2012) 74-83.
[22] M.A. Ibrahim, Disturbance Analysis for Power Systems, John Wiley & Sons, Inc, Hoboken, New Jersey, 2012.

Appendix 1

$$E^{+} = \left|E^{+}\right| e^{j\phi^{+}},\ E^{-} = \left|E^{-}\right| e^{j\psi^{-}}$$

$$E^{+} = \left(V_{af} e^{-j\varphi_a} + V_{bf} e^{-j\left(\varphi_b - \frac{2\pi}{3}\right)} + V_{cf} e^{-j\left(\varphi_c - \frac{4\pi}{3}\right)} \right)$$

$$\Rightarrow \left|E^{+}\right| = \frac{1}{3}\sqrt{\left(V_{af}\cos(\varphi_a) + V_{bf}\cos\left(\varphi_b - \frac{2\pi}{3}\right) + V_{cf}\cos\left(\varphi_c - \frac{4\pi}{3}\right)\right)^2 + \left(V_{af}\sin(\varphi_a) + V_{bf}\sin\left(\varphi_b - \frac{2\pi}{3}\right) + V_{cf}\sin\left(\varphi_c - \frac{4\pi}{3}\right)\right)^2}$$

$$\angle\psi^{+} = \tan^{-1}\left(\frac{-\left(V_{af}\sin(\varphi_a) + V_{bf}\sin\left(\varphi_b - \frac{2\pi}{3}\right) + V_{cf}\sin\left(\varphi_c - \frac{4\pi}{3}\right)\right)}{V_{af}\cos(\varphi_a) + V_{bf}\cos\left(\varphi_b - \frac{2\pi}{3}\right) + V_{cf}\cos\left(\varphi_c - \frac{4\pi}{3}\right)} \right)$$

$$\left|E^{-}\right| = \frac{1}{3}\sqrt{\left(V_{af}\cos(\varphi_a) + V_{bf}\cos\left(\varphi_b + \frac{2\pi}{3}\right) + V_{cf}\cos\left(\varphi_c + \frac{4\pi}{3}\right)\right)^2 + \left(V_{af}\sin(\varphi_a) + V_{bf}\sin\left(\varphi_b + \frac{2\pi}{3}\right) + V_{cf}\sin\left(\varphi_c + \frac{4\pi}{3}\right)\right)^2}$$

$$\angle\psi^{-} = \tan^{-1}\left(\frac{V_{af}\sin(\varphi_a) + V_{bf}\sin\left(\varphi_b + \frac{2\pi}{3}\right) + V_{cf}\sin\left(\varphi_c + \frac{4\pi}{3}\right)}{V_{af}\cos(\varphi_a) + V_{bf}\cos\left(\varphi_b + \frac{2\pi}{3}\right) + V_{cf}\cos\left(\varphi_c + \frac{4\pi}{3}\right)} \right)$$

Journal of Energy and Power Engineering 8 (2014) 568-572

Demonstration of Magnetic Energy Harvesting from Electrical Appliances

Kunihisa Tashiro, Hiroyuki Wakiwaka and Syoichiro Shimada

Spin Device Technology Center, Shinshu University, Nagano 380-8533, Japan

Received: October 18, 2013 / Accepted: December 03, 2013 / Published: March 31, 2014.

Abstract: The purpose of this study is to use magnetic field of 50/60 Hz up to 0.2 mT for energy source. This paper focuses on magnetic energy harvesting from electrical appliances which can be also used for power consumption monitoring. The magnetic energy harvesting device consists of an energy harvesting module, Cockcroft-Walton circuit and storage capacitor. First of all, typical magnetic fields around several electrical appliances are investigated. In order to harvest 10 mJ energy, the shape of magnetic flux concentration flange in energy harvesting module and number of steps in Cockcroft-Walton circuit are considered. From experimental results, magnetic energy harvesting of 17 mJ from a refrigerator is successfully demonstrated.

Key words: Magnetic energy harvesting, electrical appliances, environmental magnetic field, Cockcroft-Walton circuit, magnetic flange.

1. Introduction

There are many sensors existing in living environment developed in our information society. In the 21st century, electric power consumption of sensors in digital device has been decreasing. Nowadays, sensor's electric power consumption is in the order of mW or μW. Therefore, energy harvesting is a key technology for constructing a wireless sensor network without batteries, using environmental energy as a power source [1].

In previous report [2], the magnetic energy harvesting from the environmental magnetic fields at power line frequency was proposed. The purpose of this study is to use magnetic field of 50/60 Hz up to 0.2 mT for energy source. One of the targets is the magnetic field generates around electrical appliances, electrical wires, etc.. Furthermore, the continuous magnetic field includes variety of energy sources, no dependence on the weather and the environmental condition.

The new energy source is used to energize a wireless sensor network. The wireless sensor network is used to gather information on environmental condition by the Japanese ministry of Internal Affairs and Communications. The wireless sensor network is not only used for information gathering to prevent disaster, but also for control of physical distribution in the study group on existing sensor network technology. If the magnetic field generates energy source able to be harvested around the wireless sensor, a new sensor network could be developed without using new power sources. The new sensor network is able to function as long as the existing sensor network is functioning. Therefore, the aim of this paper is to harvest 10 mJ from the environmental magnetic field to drive sensor.

In previous report [3], 100 mW of energy harvesting from a uniform magnetic field of 90 μT at 60 Hz has been successfully demonstrated. This was done by using a Brooks coil which has an outer diameter of 28 cm. Table 1 shows the power consumption of mobile devices [4, 5]. These devices

Corresponding author: Kunihisa Tashiro, associate professor, research fields: magnetic engineering which includes magnetic sensor, magnetic shielding, biomagnetic measurement, non-destructive evaluation and energy harvesting etc.. E-mail: tashiro@shinshu-u.ac.jp.

Table 1 Power consumption in mobile devices [4, 5].

Device	Energy (mJ/s)
Quartz watch	0.005
Wireless sensor node	0.100
Heart rate meter	0.833
Respiratory rate meter	0.833

can be energized by using this energy harvesting system if about 1 mW could be harvested. Based on them [2], it is found that such energy required is possible to harvest under uniform magnetic field condition. The next stage is to harvest energy from environmental magnetic field.

The aim of this paper is magnetic energy harvesting of 10 mJ from electrical appliances. First of all, typical magnetic fields around several electrical appliances were investigated. The magnetic energy harvesting devices consists of an energy-harvesting module, CW (Cockcroft-Walton) circuit and storage capacitor. Because the induced voltage of the coil in the energy harvesting module is low, the shape of magnetic flux concentration flange [6] was considered. Compared with commercial boost-up DC-DC converter [7], CW circuit has an advantage in power loss [7]. According to previous reports, suitable numbers of steps in CW were also investigated. Consequently, magnetic energy harvesting of 17 mJ from a refrigerator has been successfully demonstrated.

2. Magnetic Energy Harvesting Device

2.1 Configuration of Magnetic Harvesting Device

Fig. 1 shows the block diagram of the magnetic energy harvesting device. It consists of a magnetic energy harvesting module, a CW circuit and a storage capacitor. The charged state of the storage capacitor depends on the constant time of the circuit. In this paper, the small capacity capacitor of 10 mF with a low time constant was used.

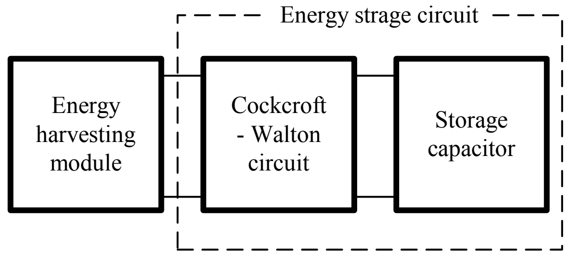

Fig. 1 Block diagram of magnetic energy harvesting device.

2.2 Magnetic Harvesting Module

Magnetic energy harvesting is power generation from induced voltage when the environmental magnetic field crosses a cross section of a coil.

Fig. 2 shows the magnetic energy harvesting module and Table 2 shows the specifications of the Brooks coil. In this paper, a 20 mm outer diameter was used. The module has a magnetic core and a magnetic flange. In Ref. [6], the induced voltage of a coil which had cores of either with PC permalloy or pure iron was compared. As a result, the induced voltages were higher in cores of PC permalloy than pure iron. Therefore, the magnetic material was used in the PC permalloy. The outer diameter of the magnetic core is 10 mm and the length is 100 mm. The outer diameter of the magnetic flange is 60 mm and its thickness is 0.5 mm. The design procedure of the magnetic flange will be described in next chapter.

Based on the Faraday's law of induction and Thevenin's theorem, the amplitude of the voltage source V_{in} (V) can be expressed by:

$$V_{\mathrm{in}} = 2\pi^2 f n a^2 \mu_0 \mu_{\mathrm{eff}} H \text{ (V)} \quad (1)$$

where, f (Hz) is the frequency of the magnetic field, n (turn) is the number of coil windings, a (m) is the mean radius of the coil, μ_0 is the mean permeability of vacuum, μ_{eff} is the mean effective permeability of PC permalloy, and $\mu_0 \times \mu_{\mathrm{eff}} \times H$ (T) is the mean flux density crossing with the mean cross section of the coil. This means that induced voltage depends on the magnetic flux of the core and the flange. Moreover, the higher induced voltage obtained the higher electrical energy stored.

2.3 Cockcroft-Walton Circuit

Fig. 3 shows the building block of CW circuit. The building block of the CW circuit consists of two diodes and two capacitors, and can provide twice value

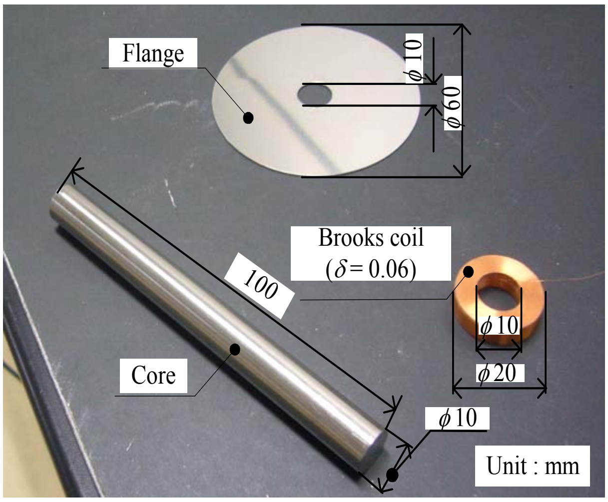

Fig. 2 Magnetic energy harvesting module.

Table 2 Specifications of the Brooks coil.

Property	Value
Outer diameter of flange, c_t (mm)	60
Thickness of flange, c_s (mm)	0.5
Wire diameter, δ (mm)	0.06
Mean radius, a (mm)	7.5
Outer diameter of coil, a_t (mm)	20
Number of turns, n (turn)	4,280
Inductance of coil, L (H)	2.21
Resistance of coil, R (Ω)	933

of DC output voltage. In an ideal CW circuit, the number of building block, or numbers of steps, can make the multiple the value of the DC output voltage.

In this paper, the CW circuit component was chosen based on the analysis result of a circuit simulator (LTSpice, Linear Technology Inc.). In previous report [8], the CW circuit was constructed from Schottky diodes (1N5818, ST Microelectronics corp.), and 47 µF capacitors. It was confirmed that the capacitors of 47 µF produced low ripple voltage and fast step time, and this Schottky diodes has a capability to be driven in low-voltage. Because an increasing number of steps produced a decrease in output DC current, suitable numbers of steps should be decided. From these simulation results, the maximum number of steps was defined to 10.

The charged energy, P (J) in the storage capacitorcan be expressed as:

$$P = 0.5\ CV_{out}^2\ \text{(J)} \tag{2}$$

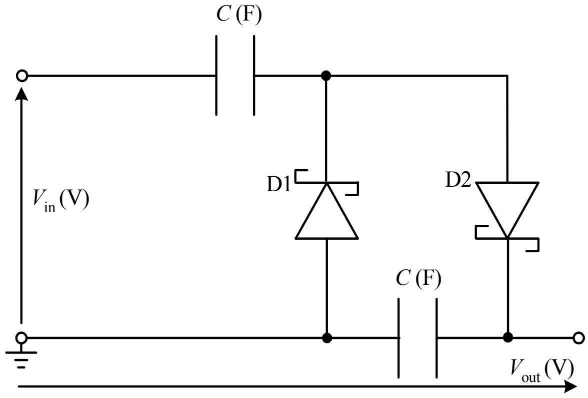

Fig. 3 Cockcroft-Walton circuit (*s* = 2).

where, C (F) is the mean capacitance of the storage capacitor and V_{out} (V) is the mean voltage at both ends of the storage capacitor. In this paper, the capacitance of the storage capacitor was 10 mF.

3. Magnetic flange

3.1 Measurement of Environmental Fields

Since electrical appliances are a target for magnetic energy harvesting, it is necessary to know the amplitude of the energy surrounding them. The environmental magnetic field around the electrical appliances was measured by using a magnetic sensor (HIOKI, 3470). The distance between electrical appliances and the magnetic field hitester was 10 mm. Table 3 shows the summary of the typical value of measured magnetic flux density. Because maximum magnetic flux density was measured from the refrigerator, it was targeted to harvest magnetic field.

Fig. 4 shows an example of measured magnetic flux density around the refrigerator as a function of measuring time. Although the refrigerator was constantly powered, and 139 µT of magnetic flux density is generated, however, it was unfortunately not consistent. Based on the observation of refrigerator inner components, it was found that the cooling fan was the main source of this magnetic field. When the cooling fan stopped, the magnetic field was much lower as compared with the cooling fan running. The time interval between the working and stopping time was about 14 min.

Table 3 Summary of typical value of measured magnetic flux density around electrical appliances.

Electrical appliance	Magnetic flux density B, (μT)
Refrigerator	139.1
Electric fan	51.0
Desktop PC	25.8
Toaster	6.71
Pot	1.88
Light (Inverter 32 W)	0.769

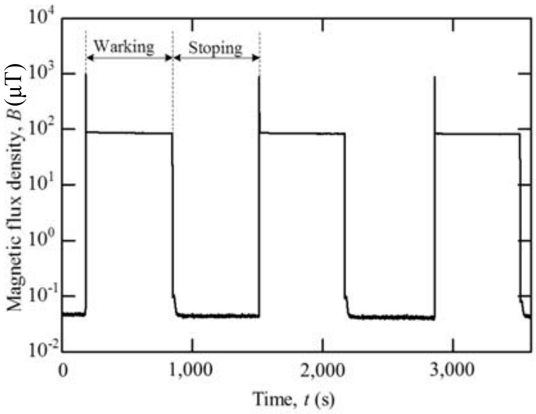

Fig. 4 An example of measured magnetic flux density around the refrigerator as a function of measuring time.

3.2 Design of Magnetic Flange

In order to design the magnetic flange, a suitable area was investigated, where both amplitude and phase of measured magnetic flux density was relatively the same. Although there were several options, a suitable area was defined. It was square area of 60 mm length, and average magnetic flux density was 73.2 μT. From this preliminary investigation, the size of the magnetic flange made of PC permalloy was prepared.

4. Experimental Results

Fig. 5 shows the experimental setup for magnetic energy harvesting. The energy harvesting device was set to have a magnetic flange. The DC output voltage V_{out} (V) was measured at both ends of the capacitor with a true RMS multimeter (Digital tester 187, Fluke.) and the harvested energy was then calculated. The harvest time was 14 min and the number of steps was varied to 2, 4, 6, 8 and 10. After that, the experiment was redone without the magnetic flange.

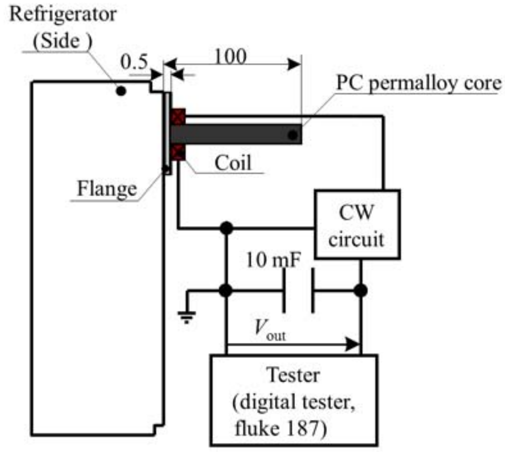

Fig. 5 Experimental setup for magnetic energy harvesting. The harvest time was 14 min and the number of steps was varied to 2, 4, 6, 8 and 10. After that, the experiment was redone without the magnetic flange.

Fig. 6 shows the harvested energy from a refrigerator as a function of measuring time as a parameter of numbers of steps. The initial harvested energy was high when the number of steps is small. However, the final harvested energy was limited due to the low output voltage. If the number of steps was two, the final harvested energy was a few mJ. In contrast, the final harvested energy was 17 mJ when the number of steps was six. Compared with other numbers of steps, this value was maximum.

Fig. 7 shows the final harvested energy from a refrigerator as function of numbers of steps. It was found that the use of the magnetic flange made the harvested energy high. When the number of steps was six, the harvested energy with a flange was 4.6 times larger than that without flange. From the experiments, the benefit of magnetic flange was successfully demonstrated.

5. Conclusions

This paper presented a demonstration of magnetic energy harvesting of 10 mJ from electrical appliances. The magnetic energy harvesting device consists of an energy harvesting module, CW circuit and storage capacitor. First of all, typical values of magnetic flux density around electrical appliances were investigated. Because usable magnetic field was limited, magnetic

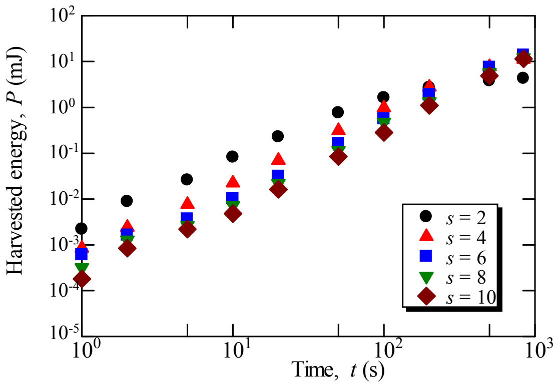

(a) With flange

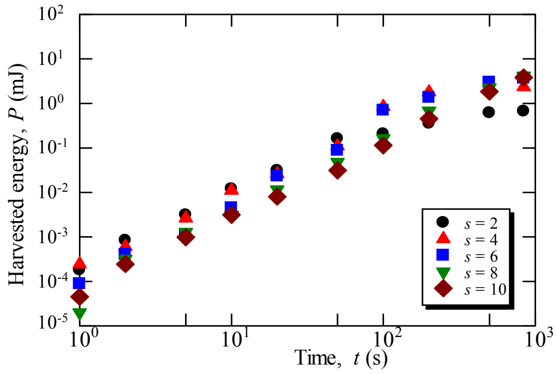

(b) Without flange

Fig. 6 Harvested energy from a refrigerator as a function of measuring time, as a parameter of number of steps in CW circuit from magnetic field around a refrigerator.

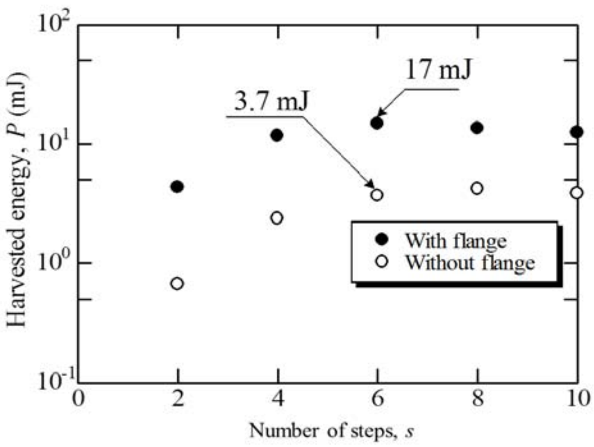

Fig. 7 Final harvested energy from a refrigerator as a function of numbers of steps. Measuring time was 14 min.

flange for the energy harvesting module was designed. It was possible to harvest larger than 10 mJ when the number of steps in CW circuit was four. The design procedure of magnetic flange could be also useful for magnetic energy harvesting from other electrical appliances. In an ideal CW circuit, the number of steps can make the multiple the value of the DC output voltage different. However, losses in capacitors and diodes should be taken into account. From experimental results, suitable numbers of steps were confirmed.

The harvested energy of 10 mJ could activate a wireless sensor node, and send "one-shot" signal. Because the harvested energy is related to the activity of electrical appliances, it could be also used for power consumption monitoring.

Acknowledgments

This work was supported in part by JSPS KAKENHI, Scientific Research (c), Grant Number 25502001, 2013-2015.

References

[1] R.J.M. Vuller, R. van Schaijk, I. Doms, C. Van Hoof, R. Merten, Micropower energy harvesting, Solid-State Electronics 53 (2009) 684-693.

[2] K. Tashiro, H. Wakiwaka, S. Inoue, Y. Uchiyama, Energy harvesting of magnetic power-line noise, IEEE Transactions on Magnetics 47 (2011) 4441-4444.

[3] K. Tashiro, H. Wakiwaka, Y. Uchiyama, Theoretical design of energy harvesting module or wireless power transmission receiver using magnetic field of 0.2 mT at 60 Hz, Journal of Energy and Power Engineering 7 (2013) 740-745.

[4] R.J.M. Vuller, R. Schaijk, I. Doms, C. Van Hoof, R. Merten, Micropower energy harvesting, Solid-State Electronics 53 (2009) 684-694.

[5] J.G. Rocha, L.M. Goncalves, P.F. Rocha, M.P. Silva, S. Lanceros-Mendez, Energy Harvesting From Piezoelectric Materials Fully Integrated in Footwear, IEEE Transactions on Magnetics 57 (2010) 813-819.

[6] G. Hattori, K. Tashiro, H. Wakiwaka, Consideration of magnetic flux concentration coil for magnetic energy harvesting, in: EPJ Web of Conferences, Parma, Italy, Sept. 9-14, 2013.

[7] K. Tashiro, H. Wakiwaka, Y. Uchiyama, Loss measurement in power conditioning module for power-line magnetic noise energy harvesting device, Journal of the Japan Society of Applied Electromagnetics and Mechanics 20 (2) (2012) 440-445.

[8] K. Tashiro, H. Wakiwaka, Y. Uchiyama, Consideration of energy strage circuits for magnetic energy harvesting, Journal of the Japan Society of Applied Electromagnetics and Mechanics 21 (2) (2013) 308-313.

Journal of Energy and Power Engineering 8 (2014) 573-577

The Industrial Biomass Combustor Design for Producing Heat in Dried Tuna Fish Production of Halla Food Factory

Sarayooth Vaivudh and Una Tontrakulchanchai

School of Renwable Energy Technology, Naresuan University, Phitsanulok 65000, Thailand

Received: September 05, 2013 / Accepted: November 11, 2013 / Published: March 31, 2014.

Abstract: The industrial biomass combustor of Halla food factory in Thailand was designed for drying tuna fish product. The purpose of this paper needed to present the design of a factory combustor for producing heat in the drying process by thermal energy from biomass fuel combustion to reduce the investment cost. A drying chamber was made from four concrete walls in the rectangular volume of 4.7 × 4.7 × 2.5 m^3 for drying tuna fishes that sliced to small pieces of around 2,680 kg fresh tuna. The hot air tube in the combustor was used for driving hot air to dry fishes in the drying chamber. Heat from acacia wood burning in the combustor with the consumption rate of 50.1 kg/h was transferred by the hot air. The design result was calculated for thermal energy and the efficiency of around 200 kW, and 32%, respectively in the case of 0.62 m^3/s hot air flow rate that circulation between the combustor and the drying chamber. The experimental result shows that the moister content of 78.9%wb was decreased to around 13.8%wb in 5 days without petroleum fuel. The drying temperature was controlled at 70 °C continuously for reducing hard containing, and the closed loop tube design for the less of BaP (benzo (a) pyrene) from combustion smoking of the drying industrial process.

Key words: Biomass combustor, producing heat, dried tuna fish.

1. Introduction

Environmental clean technology of industrial production process is responsible for making the most important contributor to climate change by the fossil fuels burning.

Many industries face a crisis of fuels depletion resulting in high capital investment to the industrial process that requires more energy because the fuel price continues to increase. Some typical forms of energy used in the industrial processes are electricity and heat as elementary energy as use in some food factory such as Halla food (Thailand) as shown in Fig. 1, a factory of smoked dry tuna fish in Thailand. This factory is one company in the group of the company that works on transforming tuna raw materials into smoked dry tuna products, and finally exports to Korea for trading.

Tuna industry is the forefront of the Thailand export qualities that are important to Thai economy. In 2009, Thailand exported 534,491 tons of tuna products, with an export value worth USD $1,676.9 million which represents about 43.2% of the world's tuna market. However, the industrial process still uses more expensive fuel for drying tuna. For minimizing this problem, the tuna industry sets up a method for reducing fuel demand while seeking to substitute other forms of renewable energy. A renewable energy fuel for burning is biomass from acacia timber as firewood in a kiln and produces heat to dry chamber for substitute for electricity or other petroleum fuels. Drying process is an important process in the tuna factory production that requires heat for producing hot air in the temperature range of around 50-90 °C in the drying tuna chamber. Thermal drying of tuna is characterized by a high energy

Corresponding author: Sarayooth Vaivudh, lecturer, research fields: renewable energy and thermal energy system. E-mail: sarayooth_v@hotmail.com.

Fig. 1 Halla food (Thailand) Co., Ltd., Rayong, Thailand.

consumption of the industry. Drying of tuna from wet material food to dry and smoked in the drying chamber requires standards of food production. The process of the industry includes washing, boiling and cutting tuna, and then feeding the tuna in a hot dry chamber requires of no contamination by insects, dust and moisture that result in poor quality products. Thermal energy used in drying process from biomass combustion requires the cleaning performance from dirty smoke and some toxic contamination on the food product.

2. Drying Process and Moisture Content

The process of tuna drying started from cutting and sliced to small pieces, removed the product waste and then boiled the fresh tuna raw material in a boiler before drying in the chamber with heat and smoke from the acacia firewood fuel burning in a combustor for transferring heat by the hot air into the drying chamber.

In the industrial drying process, the most energy consumption was drying the tuna that consumed around 90% of the whole heat whereas the surplus heat was 10% of boiled tuna before drying. The thermal energy consumption in the drying process was calculated from the heat of the water evaporating from the mass loss of tuna related to the Eq. (1) from wet basis drying [1].

$$M = \frac{m_w - m_d}{m_d} \qquad (1)$$

where, M is the moisture content, wb; m_w is the sample product mass, kg; m_d is the drying mass of the sample product, kg.

For determining the tuna mass loss, the moisture content and the mass relation was derived in Eq. (2) as follow [2]:

$$W_f = W_i \frac{1-M_i}{1-M_f} \qquad (2)$$

where, W_f is the final tuna mass, kg; W_i is the initial tuna mass, kg; M_f is the final moisture, wb; M_i is the initial moisture, wb.

From the data of Halla food industry product, tuna was dried in the drying chamber from the starting mass of 2,680 kg and the moisture content of 78.9%wb (3.74 db) to the final mass when finished with the mass of 656 kg and the moisture content of 13.1%wb (0.15 db). The drying curve of moisture ratio in the dry basis (db) was shown in Fig. 2 for describing the drying performance of the product. Finally the energy calculated in this drying data was 4626.4 MJ [3].

In particular of a drying tuna process sample from Halla food factory was informed as the total drying time of 5 days. In the first day the moisture content of fresh tuna was decreased by warm air in 5 h at the drying temperature of 90 °C, and left in room temperature to reach the equilibrium point alternately. Then the same performance was repeated in the second day, but the temperature was reduced to 80 °C. Similarly, the drying process was continued with the same process of lower drying temperature at 70, 60 and 50 °C in the 3rd, 4th, and 5th day, respectively. Drying time in these three days was reduced to 4 h and still left in room temperature alternately until the product reached the standard moisture content of around 13%wb (0.15 db) that corresponded with the water activity (a_w) of 0.6.

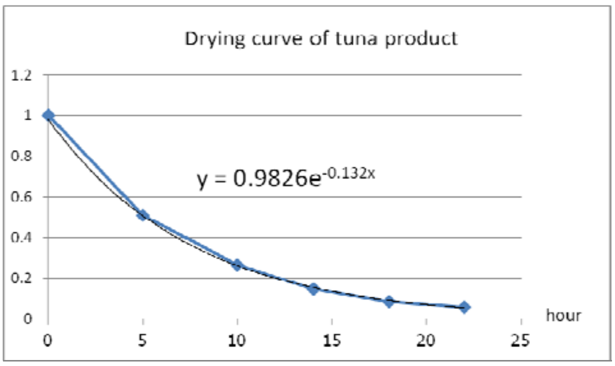

Fig. 2 Drying curve of tuna product in 22 h for 5 days.

In Fig. 2, the drying rate of tuna product is determined in exponential fitting curve according with the mathematical model of Henderson and Pebis [4] when a is 0.982 where the model is following (3):

$$MR = a\exp(-kt^n) \tag{3}$$

where, MR is the moisture ratio (simplified to M/M_0); M_0 is the initial moisture content; M is the moisture content in dry basis, db.

$$k = 0.132 \text{ and } n = 1$$

3. A Combustor Design for Drying Energy

Thermal energy requirement for the drying process was calculated by using heat transfer principle [5] from the combustion of acacia wood fuel burning to produce heat and transfer by the hot air into the drying chamber. The result of total heat calculation from each day summation was around 4,648.7 MJ. These data was related to the fuel mass by using a calculation of heating value as shown in Fig. 3 for comparing the maximum energy on the first day and decreasing every day with the fuel mass of 250 kg to 2.17 kg, respectively.

In Fig. 3, thermal energy requirement is from the combustion of acacia wood which reached the heating value of 15.8 MJ/kg. The combustion air volume was determined for achieving the complete combustion and the combustor size. The volume of air depended on the fuel mass by the principle of complete combustion with sufficient oxygen. A case of the fuel of 250 kg/day for drying fresh tuna from 2,680 kg to 1,022 kg of the first day consumed the combustion air of 4.54 m^3/h. Drying

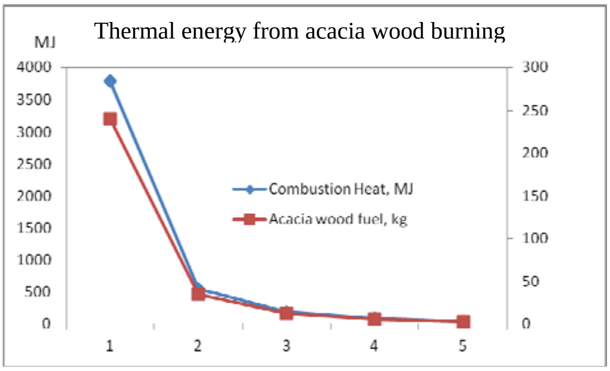

Fig. 3 Thermal energy from fuel burning in drying energy process requirement.

in the first day of tuna was done for 5 h per day by the combustion heat of 790 MJ/h from the firewood of 50 kg/h. The air inlet to the drying chamber was calculated for the volume of 62 m^3/s and was transferred heat to dry the product in the first day and decrease in next 5 days by the tube in a heat exchanger that is located in the combustor.

The combustor structure was fabricated by firebricks and covered with concrete in the volume of 3 m^3 (1 × 2 × 1.5 m^3) for the maximum wood fuel of around 250 kg and the air requirement to meet a complete combustion. A tube of diameter of 15 cm was used to connect the combustor and the drying chamber for driving the hot air by a blower that is located in the tube. A heat exchanger was placed in the combustor for transferring heat from the hot combustion air to the air inside the tube. The combustor power was varied with the fuel mass from 250 kg to 100 kg that produced heat of 219.4 kW to 109.7 kW which was determined by (4):

$$\dot{Q} = \dot{m}_f \, LHV \tag{4}$$

where, $\dot{Q}$ is the power of combustion, kW; W_i is the mass rate, kg/s; M_f is the final moisture, wb; LHV is the fuel lower heating value, MJ/kg.

The energy of combustor was transferred by the hot air to dry the product in the drying chamber. The hot air from the heat exchanger flowed to dry the product with the rate of 0.6 m^3/s to 0.1 m^3/s varied by the product as follow by Eq. (5):

$$\dot{Q} = \dot{m}_a \left(h_f - h_i\right) \tag{5}$$

where, $\dot{m}_a$ is the hot air flow rate for drying tuna kg/s; h_f is the enthalpy of hot air, kJ/kg; h_i is the enthalpy of ambient air, kJ/kg;

The combustor and connection tubes were installed by the design that mounted the tube to the heat exchanger for transferring heat by the air inside the tube. The hot air flowed from the heat exchanger to the drying chamber and circulated in closed loop back to the heat exchanger again for keeping clean drying air as shown in Fig. 4.

The drying energy depended on the tuna mass that it was controlled by the wood fuel mass and the blower of

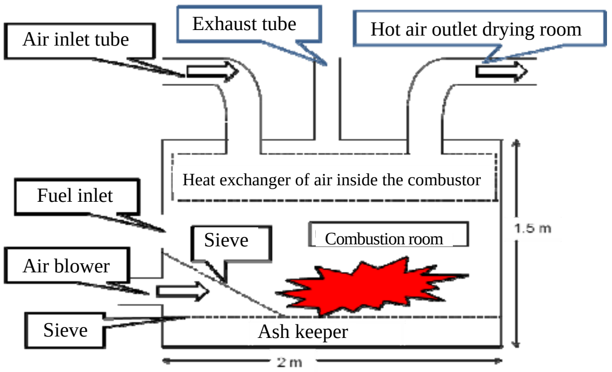

Fig. 4 The wood combustor and connection tube for drying product.

the hot air. Drying temperature in the drying chamber was controlled by the exhaust tube for removing the humid air from the drying chamber to reduce the drying air relative humidity.

4. Experimental Setup

The data of combustion air flow rate was measured in the volume of 280 m^3/h when the maximum fuel of 250 kg per day with the consumption rate of 50 kg/h. An excess air was 1.23 and the whole air (280.4 m^3/h-140.2 m^3/h) was driven by the blower at the front of the combustor into the combustor. The drying chamber in each batch started to dry the various tuna fresh raw material from 1,000 kg to over 2,000 kg. The experiment was set up to operate the combustor for producing heat to dry 6 batches of tuna over 2,000 kg and dry for 7 days to meet the requirement final product with the high power performance of the combustor. The results of tuna drying performance were shown in Table 1.

The smoked dry tuna product was left in the temperature of below 70 °C to prevent high BaP from being that toxic for consumers. The combustor of firewood released this chemical from the wood burning in high temperature, therefore the food product would be smoked after drying to avoid toxication from high temperature burning. The combustor not only produced heat but also smokes to meet favorite smell for consumers. From Table 1 the wood combustor reached to the efficiency of average 32% for high amount of thermal energy because of more tuna product. In the other case of lower product, the efficiency result would be changed to about 0.22 since the heat loss increased by the vacancy in the drying chamber expansion comparing with the first experiment. In addition, the more heat loss from the drying process increased by the removed humid hot air from the drying chamber by the exhaust tube.

5. Conclusions

The biomass wood combustor was designed for drying tuna product in Halla food factory. Tuna fish was the raw material of the process that started from the moisture content of around 78.9% wb (3.74 db) in the mass of 2,680 kg to 656 kg at the moisture content of 13.1% wb (0.15 db). The energy was taken from the combustion in the wood combustor around 150 kW at maximum power by the fuel consumption rate of 50 kg/h or 250 kg/d. Heat from the combustor was transferred by hot air inside the tube that was connected between the heat exchanger in the combustor and the drying chamber in the close loop circulation. In experiment of drying 6 batches in the factory product with an average of 2337.8 kg to 572.25 kg at the moisture content from 78.9%wb (3.74 db) to

Table 1 Experimental results of drying tuna by the wood combustor energy.

Number	Starting product (kg)	Final Product (kg)	Drying energy (MJ)	Combustor power (kW)	Efficiency (ratio)
1	2,378	582.08	4092.9	131.7	0.35
2	2,472	605.10	4254.7	146.3	0.32
3	2,210	540.96	3803.7	131.7	0.32
4	2,419	592.12	4163.5	146.3	0.32
5	2,434	595.80	4189.3	146.3	0.31
6	2,114	517.46	3638.3	131.7	0.31
Average	2,337.8	572.25	4023.8	139.0	0.32

13.8%wb (0.16 db), the combustor produced heat on an average of 139 kW at the average efficiency of 0.32. In the case of product below 2,000 kg the combustor efficiency reduced to around 0.22 from the higher loss.

Acknowledgments

The research was supported by the Halla food factory to study and collect data. The author would like to thank for the accommodation of the factory.

References

[1] T. Gebreegziabher, A. Olajire Oyedun, C.W. Hui, Optimum biomass drying for combustion—A modeling approach, Energy 53 (2013) 67-73

[2] V. Sarayooth, S. Sukruedee, Biomass bamboo knot furnace for replacement to heavy oil in Joss paper mill, in: 3rd Int. Conf. on Addressing Climate Change for Sustainable Development through Up-Scaling Renewable energy Technologies, Kathmandu, Nepal, Oct. 12-14, 2011.

[3] J. Waewsak, S. Chindaruksa, C. Punlek, A mathematical modeling study of hot air drying for some agricultural products, Thammasat Int. J. Sc.Tech. 11 (1) (2006) 14-20.

[4] S. Duangporn, N. Pumsa-ard, L. Wiset, Drying equations of Thai Hom Mali paddy by using hot air, carbon dioxide and nitrogen gasses as drying media, Food and Bioproducts Processing 90 (2) (2012) 187-198.

[5] J.H. Lienhard IV, J.H. Lienhard V, A Heat Transfer Textbook, 3rd ed., Phlogiston Press, Cambridge, Massachusetts, 2003, p. 766.

Journal of Energy and Power Engineering 8 (2014) 578-584

Research on Airborne Terrain Matching System

Yachong Zhang and Yazhou Yue

Science and Technology on Aircraft Control Laboratory, Flight Automatic Control Research Institute, Xi'an 710065, China

Received: October 01, 2013 / Accepted: November 26, 2013 / Published: March 31, 2014.

Abstract: In view of the airborne application characteristics such as flexible flight, large error of altimeter, large initial error of inertial navigation system, etc., a new terrain matching system architecture which is suitable for airborne application is presented. The key techniques in terrain matching system realizing process including system workflow, terrain matching algorithm and selection criterion of matching region are expatiated. The experimental results prove the rationality and feasibility of the proposed solution.

Key words: Terrain aided navigation, acquisition probability, applicability, performance evaluation.

1. Introduction

TAN (terrain aided navigation) system is an important development direction of modern aviation navigation technology. It has high-autonomy, high-precision and good anti-jamming ability, which attracts widespread concern and attaches great importance to the international navigation community.

In the early 1950s, the developed countries began to research TAN principle. During the 1970s, United States, Britain and other countries developed various types of TAN systems and performed a wide range of flight experiments. These TAN systems are available in the 1990s [1, 2]. Now the most widely used TAN system is TERPROM (terrain profile matching) system developed by BAE (British Aerospace Corporation). It has been widely used in transport aircraft, bomb, helicopter and other aircrafts and made tremendous economic and military interests [3, 4].

The domestic relevant research institutes also carried out basic theory and applied technology research to TAN system [5, 6]. There have been some breakthroughs and a wide utilization in practical engineering has been found. However, there is a large gap from international advanced level in research capacity and related technology maturity.

2. Terrain Matching System

2.1 Terrain-Aided Navigation System Principle

Uneven and different distributions of surface features on the earth surface form the typical characteristics of different regions. These features generally do not change with time and climate and are difficult to camouflage. TAN system's basic theory is to use these features to determine the location of the aircraft. In principle, TAN system simulates human's process of localization-memory, observation and judgment; in essence, it aligns the same region's observational data of different sensors in space, and determines the relative displacement between the two sets of data, thus determining the deviation between the position indication of the aircraft navigation equipment and the actual geographical location.

In accordance with the working principle, TAN can be divided into terrain height data matching system (terrain matching system) and scene matching system which is shown in Fig. 1.

Terrain matching refers to the aircraft utilizing onboard barometric altimeter and radio altimeter to measure the topographic profile below the aircraft, calculating with the pre-stored baseline terrain in

Corresponding author: Yachong Zhang, researcher, research fields: terrain matching and integrated navigation. E-mail: whhzyc802@163.com.

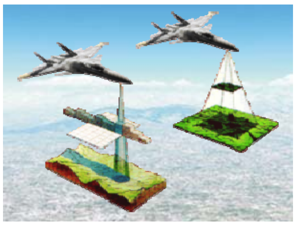

Fig. 1 Terrain-aided navigation system schematic.

accordance with certain correlation criterion to obtain accurate aircraft position, and then completing correction to INS (inertial navigation system). The schematic diagram is shown in Fig. 2 [7]. Different from other integrated navigation systems, terrain matching system can only play the role of auxiliary correction to the main navigation system. Leaving the main navigation system, terrain matching system could not provide any navigation information.

The combination of barometric altimeter and radio altimeter onboard is able to independently measure the terrain elevation with little interference by the outside world; the undulating topography of the earth's surface is independent of time and artificial landscape change does not occur frequently, so the preparation of digital elevation map has a long-term application value. Therefore, terrain matching system is an independent, anti-jamming and all-weather positioning system.

Besides, terrain matching system is mainly a software system. Compared to other integrated navigation systems, terrain matching system does not require more hardwares, but it can improve the navigation accuracy by nearly one order of magnitude.

2.2 Airborne Terrain Matching System Structure

The basic working conditions of terrain matching system onboard is that INS guides the aircraft to the matching region and describes the direction of terrain profile through the position and velocity, controls and measures the sample points and completes the matching location. A block diagram of terrain matching system is shown in Fig. 3.

In general literature terrain matching is considered as one-dimensional elevation matching. In fact, terrain

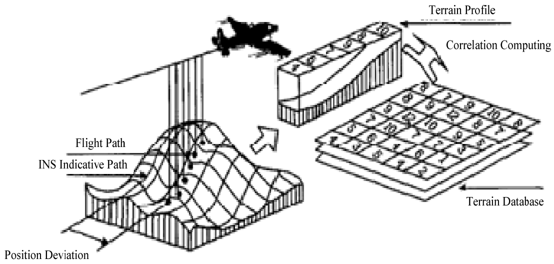

Fig. 2 Terrain matching system schematic.

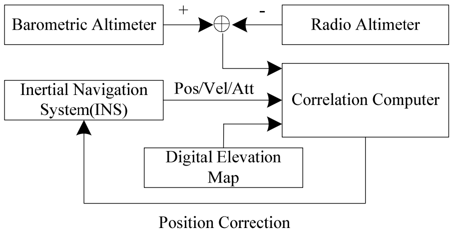

Fig. 3 Terrain matching system.

matching system completes horizontal direction constraint through the horizontal error of INS, that is, it determines searching area according to the horizontal error of INS. At the same time, it completes vertical direction constraint by using altimeters' measurements of topography profile perpendicular. And it ultimately achieves the purpose of high-precision positioning.

In view of the airborne application characteristics such as flexible flight, large error of altimeter and large initial error of INS, this paper's emphasis is placed on the error characteristics of INS and altimeter, the error of digital elevation map preparation, terrain correlation length and the matching sequence length in the process of the program implementation. Besides, this paper integrates the above factors with the system solution and forms airborne terrain matching system structure to ensure the rationality, the feasibility and the acquisition probability of the matching process.

2.3 System Workflow

In order to improve the aircraft's ability to perform and complete the custome-built task, this paper divides the mission which adopting terrain system into two stages: mission preparation and mission execution.

The proposed workflow of terrain matching system is shown in Fig. 4. In order to improve the aircraft's ability to perform and complete the custom-built task, this paper divides the mission which adopts terrain matching system into two stages: mission preparation and mission execution.

The main work of the mission preparation phase is to collect and analyze the intelligence in the mission area, and plan and optimize route through threat information, then get the reference flight path of the global optimum. Then a reasonable matching region is determined by the topographical features.

After takeoff, terrain matching system comes into a waiting state. When Airborne INS output position is located in the matching region, terrain matching system will transfer the matching reference data of the digital elevation from the data memory to the memory of terrain matching system, and start sampling terrain elevation data, synchronously acquire the data of INS position, velocity, barometric altimeter, radio altimeter and clock. When the sampling number of terrain profile achieves the number required, terrain matching system starts searching position. After the completion of matching location, terrain matching system outputs positioning results and positioning time. When the aircraft flies out of matching region, terrain matching system will send signal so that the terrain matching is completed and re-enters the waiting state. When the aircraft reaches the next matching region, terrain matching system repeats the above process.

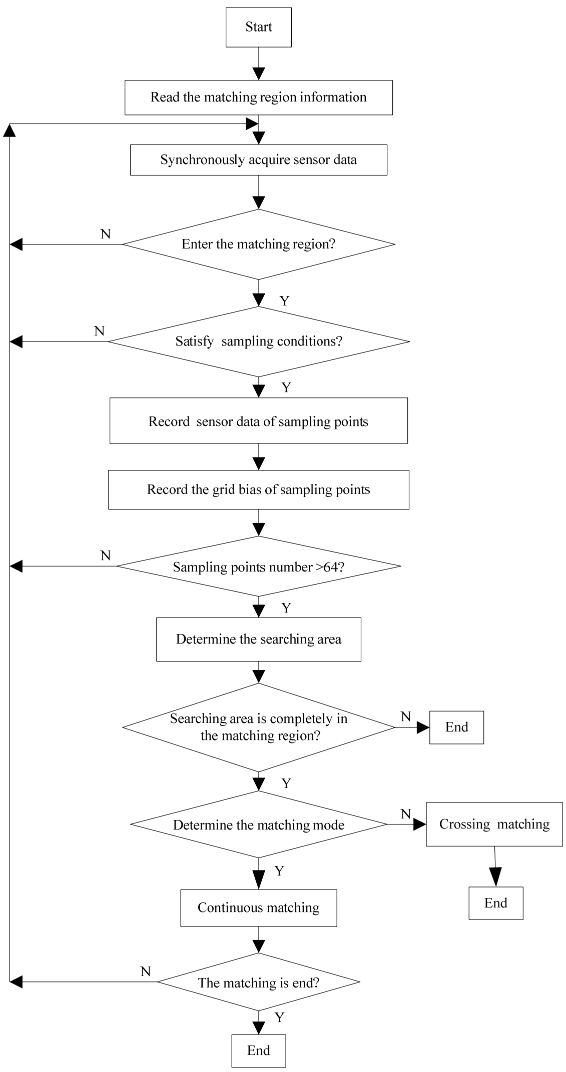

Fig. 4 Terrain matching system workflow.

3. Key Technologies of Terrain Matching System

The basic principle of terrain matching system is very simple, however, because there is a certain degree of noise in both the measured terrain profile data and benchmark terrain data, matching process isn't a simple process, especially to achieve the level of practical engineering applications. According to relevant documents, E-system Company spent more than ten years of experimentation and analysis mastering this technology. At present, domestic and foreign reference material are largely concentrated on terrain matching algorithm or selection criterion of matching region. There are significant limitations:

(1) The accuracy of individual terrain matching algorithm is very high, but the value for practical engineering applications is poor due to the error of height measurement error and the INS error propagation characteristics;

(2) The positioning accuracy of terrain matching and acquisition probability not only relate to matching algorithm, but also to selection criterion of matching region and performance of airborne equipment. General research only analyses the impact of the

terrain statistical characteristics on terrain matching performance, while ignoring the influence of initial error, the INS accuracy, barometric altimeter, radio altimeter measurement accuracy as well as the matching sequence length and other factors, thereby reducing the engineering feasibility [5].

In terms of terrain matching the credibility of correct positioning is more important than system accuracy. Therefore, early in the design of terrain matching system we need to carefully consider the actual working conditions of the aircraft so as to ensure the rationality and feasibility of the system solution.

3.1 Matching Algorithm

Terrain matching is essentially a kind of software function. Therefore, its implementation methods need to be arranged carefully.

At present, common terrain matching algorithm includes the TERCOM (terrain contour matching) and the SITAN (sandia inertial terrain aided navigation). TERCOM is based on the principle of correlation analysis, while SITAN is based on extended kalman filter theory.

It can be seen from the literature: “Tomahawk” cruise missiles adopting TERCOM algorithm, which has high maturity and good effect. In TERCOM algorithm the purpose of correlation processing is to find a path on the stored digital elevation map which is paralleling to the path of INS instructions and closest to terrain profile measurement value sequences of altimeters. TERCOM algorithm is the basis and key of the entire terrain matching system.

This paper presents a terrain matching algorithm suitable for engineering applications: According to the planning of predetermined accuracy and error characteristics of INS, the error characteristics of the barometric altimeter and the radio altimeter, the preparation error of digital elevation map and reasonable matching regions, it completes terrain contour matching through the interaction of terrain matching system and onboard control system. This paper adopts the MSD algorithm and COR algorithm fusion voting mechanism to ensure the correct match of the first matching point; it adopts the majority vote decision-making mechanism as the technical measures to improve acquisition probability; it uses the modified MSD algorithm and the modified COR algorithm to improve the matching accuracy and acquisition probability; forecasts location through positioning results and INS outputs, and then uses the weighted average of the location prediction and the latest matching results as the positioning output.

Algorithm fusion voting mechanism is based on the following considerations: MSD algorithm is a distance decision-making in the statistical decision method, while COR algorithm belongs to the shape decision-making, in the case of no measurement error, these two algorithms would locate in the same location. If INS has a grid error when TAN system acquiring a terrain profile data, two algorithms located in the same location is relaxed for one grid.

Majority vote of decision-making mechanism is mainly based on the design ideas of the joint probability, and restricts the rationality of matching results through two independent consecutive matching positioning [8].

Using the modified MSD algorithm and the modified COR algorithm eliminates the systematic bias in the measurement of the barometric altimeter and the radio altimeter [8, 9].

The modified COR algorithm is given below:

$$J_{COR} = \frac{1}{L}\sum_{i=1}^{L}[T_A(i) - \overline{T}_A]\cdot[T_S(x+i\tau_x, y+i\tau_y) - \overline{T}_S]$$

The modified MSD algorithm is given below:

$$J_{MSD} = \frac{1}{L}\sum_{i=1}^{L}\left|[T_A(i) - \overline{T}_A] - [T_S(x+i\tau_x, y+i\tau_y) - \overline{T}_S]\right|^2$$

In the formulae, L is the number of calculated data points, and has some connection with correlation processing of the terrain contour length. $T_A(i)$ is NO. i terrain height value; $i = 1, 2\cdots\cdots L$, $T_S(x+i\tau_x, y+i\tau_y)$ is NO. i terrain height value of the digital elevation map;

x, y are the coordinates of the center of selected matching grid; τ_x, τ_y are the distances between two adjacent sampling of the aircraft flying in the two coordinate axis. $\bar{T}_A$ is the mean of the L calculated terrain height values, $\bar{T}_S$ is the mean of the L elevation values of the digital elevation map.

The calculation of the optimal path maximizes J_{COR} and minimizes J_{MAD} and J_{MSD}.

3.2 Selection Technology of Matching Region

In terms of terrain matching system, there is always a limit which can broadly divide the terrain into the regions system working in the areas affected by noise restrictions. Therefore, there is an urgent problem how to evaluate and plan the matching region to ensure the acquisition probability.

The effect of terrain matching system is closely and inseparably related to the selection of matching region. It can be said that the suitable matching region will directly affect the positioning accuracy and the acquisition probability. Therefore, proper planning and strict identification to the matching region are necessary.

When studying the selection criteria of matching region, we need to consider a variety of problems contained in the aircraft mission planning such as working conditions and terrain parameters which contain the undulating topography standard deviation, terrain roughness, terrain correlation length surrounding the expected route, as well as the matching algorithm, the measurement error of height sensor, the preparation error of digital elevation map and INS error characteristics [3]. Considering all these factors a reasonable matching region is then determined.

3.3 Modeling Technology of Altimeter Error

The barometric altimeter could provide height of above mean sea level and the radio altimeter could provide heights relative to ground. The terrain elevation below the aircraft could be acquired through a combination of the radio altimeter and barometric altimeter. Because barometric altimeter and radio altimeter are the measurement equipment of terrain matching system, the measurement accuracy directly determines the performance of terrain matching system. The test and error modeling of these altimeters are critical techniques in studying the terrain adaption capacity of altimeters and improving the performance of TAN system.

In the general study, the system noise is determined by prior knowledge. In order to test the validity of these indicators, the actual noise based on flight test data should be calculated.

3.4 Inertial Navigation System Technology

INS is the final amendments object of the terrain matching system, and it is also an important part of the terrain matching system as well as normal working premise. In practical application we should ensure that the aircraft could enter the scheduled matching region, and do not deviate from the matching region before the completion of positioning. The accuracy of INS determines the size of the searching area and the size of the searching area determines the acquisition probability. Thus, mastering the performance and analyzing the error sources of INS are also critical techniques of the terrain matching system.

3.5 Error Distribution Technology

Corresponding to the requirements of acquisition probability and matching accuracy which are combined with the basic principle of terrain matching system, we can initially fix the signal noise ratio of the terrain matching system. Further, according to the current technical level of the related equipments, with the help of the requirements of SNR, we can allocate the various errors in the system, such as digital elevation map preparation error, the requirements of INS accuracy, the requirements of height sensor accuracy, the requirements of matching computer performance and so on.

4. Verification Test

In terms of the technical characteristics of terrain matching system, we developed a prototype of terrain matching system, completing the design and development of terrain matching system software, as well as the load/delete of digital elevation map, the download of matching data, the programs curing of terrain matching system, and other accessibility software development, fulfilled the mathematical simulation, the semi-physical simulation system and the ground experimental setup.

In order to verify the technical feasibility of the proposed system solution, we verified the system's functionality and performance with the help of the actual digital elevation map. Four matching regions are chosen initially, and each matching region is 40 km × 20 km. A chose matching region is shown in Fig. 5.

Table 1 is the statistical mean and standard deviation of elevation in the map area, and the acquisition probability (when matching error is larger than one grid mismatch will happen, the grid is 100 m × 100 m). In view of the statistical results, the technical solution is reasonable and feasible. The program simulates INS ground speed error, heading error, position (longitude and latitude) error entering the matching region, radio altimeter measurement error, barometric altimeter measurement error and so on. Then we acquire the statistical properties of the terrain matching system.

In Fig. 6, the red line indicates the measurement value sequences of the terrain profile while black lines represent the sequences of the searching terrain profile. The abscissa axis is the number of sampling points and the vertical axis is the terrain elevation.

In the system algorithm, we center on the location indicated by INS at the moment of sampling points, use 6σ range of the estimated INS error as the searching area, completing correlation matching of every possible path in the searching area. In order to study the interaction of INS, altimeters and matching computer working at the same time, some introduced

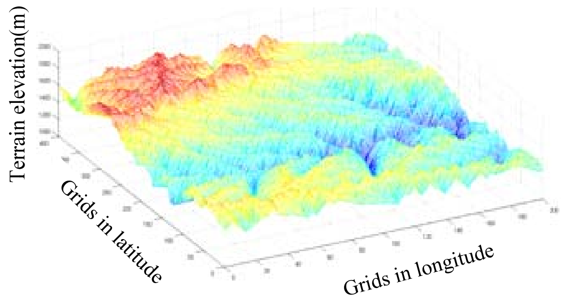

Fig. 5 Terrain elevation map.

Table 1 Verification results.

Case	Mean of elevation (m)	Standard deviation of elevation (m)	Acquisition probability
1	1,419	126	100%
2	1,485	113	92%
3	1,357	128	94%
4	1,484	135	94%

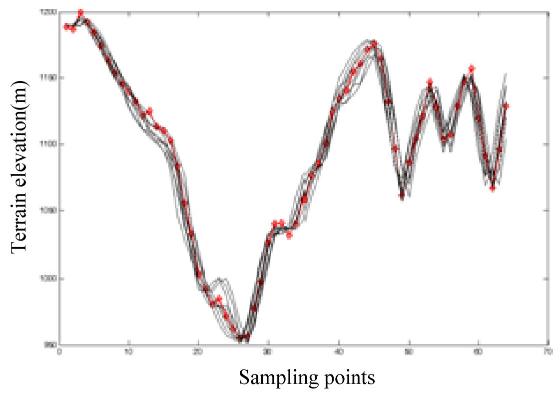

Fig. 6 Searching terrain profile diagram.

error factors. We made further efforts to develop matching computer and verify the physical interface and protocol validation of terrain contour matching system through the actual INS, altimeters, digital elevation map and other equipments. The ground testing and logic verification of the entire system were done. The experimental results prove the rationality and feasibility of the proposed solution.

5. Conclusions

Terrain matching system as an ideal correction system has the characteristics of high-autonomy, anti-jamming and high-precision, having been successfully applied in cruise missiles and tactical aircraft acquires a great deal of value and economic

benefits. Looking at the existing research progress, it is recommended as soon as possible to study airborne terrain matching system application technology, especially in improving the system engineering reliability and environmental adaptability to accommodate the needs of modern navigation.

Acknowledgments

This work was supported by the National Key Basic Research and Development (973) Program of China (Grant No. 2010CB731806) and Aeronautical Science Foundation of China (Grant No. 20100818018).

References

[1] L.X. De, Terrain-Aided Navigation System Technology, Publishing House of Electronics Industry, Beijing, China, 1994.

[2] N. Priestley, Terrain referenced navigation, in: IEEE Position Location and Navigation Symposium, Las Vegas, Mar. 20-23, 1990.

[3] M. Cowie, N. Wilkinson, R. Powlesland, Latest development of the TERPROM digital terrain system (DTS), in: Proceedings of the IEEE Position, Location and Navigation Symposium, Monterey, Mar. 6-8, 2008.

[4] W. Nick, B. Tom, P. Andy, G. Martin, Latest developments of the TERPROM digital terrain system 2009, in: Joint Navigation Conference, Orlando, June 1-4, 2009.

[5] L. Zhao, Robust inertial terrain aided navigation algorithm, Acta Phys. Sin. 61 (10) (2012) 104301-1-7X.

[6] Y.B. Pei, Z. Chen, BITAN Ⅱ: An updated terrain aided navigation algorithm, in: Proceedings of the IEEE Industrial Electronics, Control, and Instrumentation, Taibei, Aug. 9, 1996.

[7] X. Yuan, J.X. Yu, Z. Chen, Navigation System, Aviation Industry Press, Beijing, China, 1993.

[8] L. Zhao, An algorithm for terrain-aided inertial navigation based on nonlinear optimal filtering, Science China Physics, Mechanics & Astronomy 54 (6) (2011) 1083-1088.

[9] K. Wu, L. Zhao, Terrain contour matching navigation algorithm applicable for aviation, Piezoelectric and Acoustooptics 32 (5) (2010) 754-757.

Journal of Energy and Power Engineering 8 (2014) 585-588

Surface Tension Profiles under Various Microwave Radiation Modes

Yusuke Asakuma[1], Yushin Kanazawa[1], Harisinh Parmar[2], Vishnu. Pareek[2], Chi M. Phan[2] and G. Evans[3]

1. Mechanical and System Engineering, University of Hyogo, Hyogo 671-2280, Japan

2. Chemical Engineering, Curtin University, Perth, WA 6845, Australia

3. Chemical Engineering, University of Newcastle, Chemical Engineering, Callaghan, NSW 2308, Australia

Received: September 13, 2013 / Accepted: November 11, 2013 / Published: March 31, 2014.

Abstract: Surface tension of fluids is crucial for multiphase systems and is often controlled during industrial processes by introducing surfactants. In this study, effect of various microwave radiation modes on surface tension of water was investigated as an alternative physical method to manipulate the surface tension without using chemicals. It is found that surface tension decreased quickly while temperature increased during microwave. Once the radiation was turned off, the temperature returned rapidly as expected. However, surface tension did not recover so much. The minimum surface tension after microwave radiation depended on the power. Moreover, a second radiation can have additional reduction on surface tension.

Key words: Microwave, surface tension, water memory.

1. Introduction

Application of microwave irradiation for chemical processes, such as emulsification and polymerization, has been reported [1, 2]. Surfactant free emulsion can be produced with the help of microwave irradiation. Surface tension is an important property for the industrial process such as foaming/defoaming, wetting/dewetting and flotation. Similarly, the interfacial tension plays a crucial role in separation and mixing process of two immiscible liquids, which are important unit operations in chemical engineering. In practice, surface and interfacial tensions are often altered by introducing surfactants. Surface tension of water depends on hydrogen bonding of the water molecule. The decreasing surface tension with temperature increasing has been measured and reported in Refs. [3, 4]. Temperature effects on hydrogen bonding were discussed by Shin-Pon Ju and co-workers [5]. On the other hand, specific property for surface tension of water droplet under magnetic field was found in previous research [6].

In our previous research, specific property for surface tension of water droplet under microwave radiation was found [7]. For example, lower surface tension after the radiation was measured and maintained for a long time. The formation of nano-bubble might be the reason behind the surface tension reduction. However, the exact mechanism is not clear. This study investigates the influence of microwave radiation modes on surface tension of water.

2. Procedure

Fig. 1 is the schematic diagram of the microwave reactor (designed and built by Shikoku Instrumentation Co., Inc.) from side view and 3D view, respectively. Pendant method was employed for the measurement of surface tension of water. Since metal is not microwave friendly, Teflon pipe with the dimension of 1 mm inside

Corresponding author: Yusuke Asakuma, associate professor, research fields: heat, mass transfer and microwave. E-mail: asakuma@eng.u-hyogo.ac.jp.

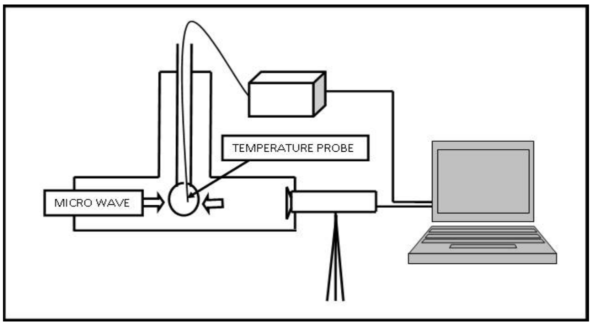

(a) Side view

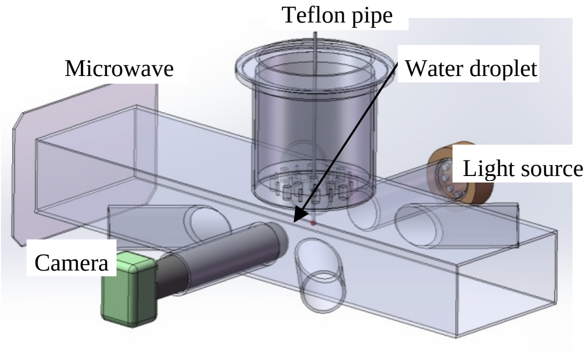

(b) 3D view

Fig. 1 Experimental apparatus.

inside and 2 mm outside diameter (and 1.4 cm long) was chosen for the experiments. Droplet was produced via injection syringe with exactly 25 micro liter of distilled water. Temperature was measured with the help of temperature measurement equipment, designed by Anritsu meter Co., LTD (device model: FL-2000 Optical fiber: FS100-M), which was inserted from the top of the reactor to check the temperature inside the droplet during microwave irradiation.

Water droplet was suspended from the top of the microwave reactor. Light source was used from one end of the microwave reactor and high speed camera (Sigma Koki Co., LTD Model SK-TC202USB-AT) was employed from the other end to capture the shape of the droplet. Analysis of experiments is as follows:

(1) initially capturing of the image before microwave irradiation to measure initial surface tension of the water droplet.

(2) capturing of the images during and after microwave irradiation for all experiments.

Two kinds of experiment were conducted as shown in Table 1.

Table 1 Experimental conditions for surface tension.

No.	1st radiation (W)	2nd radiation (W)	Radiation time (s)
1	600	150	120
2	450	150	120

ADSA (axisymmetric drop shape analysis) in Fig. 2 was employed to measure initial surface tension of the droplet and droplet images captured during and after microwave irradiation. ImageJ software [8] was used to edit droplet images to make it compatible for ADSA software prior to analyzing droplet image under ADSA software [9, 10].

3. Results and Discussions

Fig. 3 shows surface tension of water droplet for different radiation power as a function of time and temperature. Solid symbols and unfilled symbols show values during radiation and after radiation, respectively. First, surface tension profiles of first radiation (600 W and 450 W) are considered. During the microwave radiation, the temperature increased as expected. The surface tension decreased significantly as well. Once the microwave is turned off (at 120 s), the temperature dropped quickly to the room temperature, whereas the surface tension recovered slowly. However, surface tension did not recover to the original value. Instead, the surface tension becomes almost constant, which depends on the radiation power. During the radiation, temperature is expectedly varied greatly between the surface, which is equilibrium with room temperature, and the droplet center, which is almost boiling temperature. Accordingly, during the radiation, surface tension is larger than reference values [3, 4]. On the other hand, after the radiation, the values are below the references. The data after microwave radiation clearly demonstrated the non-thermal behavior of surface tension.

Secondly, surface tension of water droplet for second radiation (150 W) was included after the first radiation. Second solid symbols mean surface tension during second radiation. Surface tension becomes lower than the constant values of first radiation after

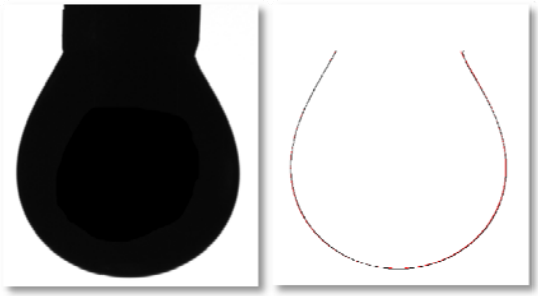

(a) Drop profile (b) Smoothed edges

Fig. 2 ADSA method for final surface tension measurement.

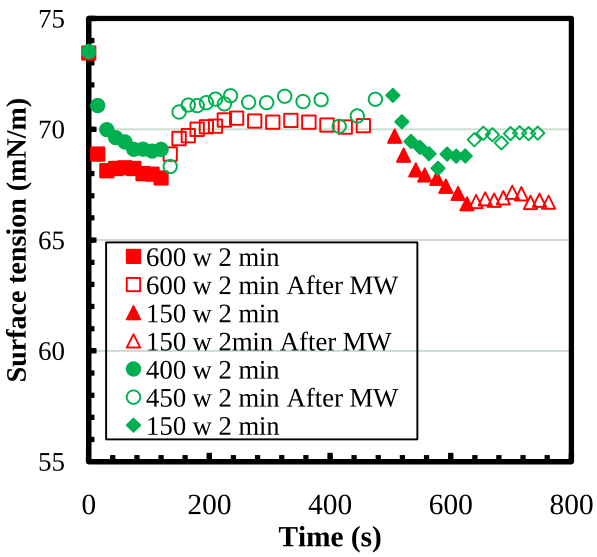

(a) Time

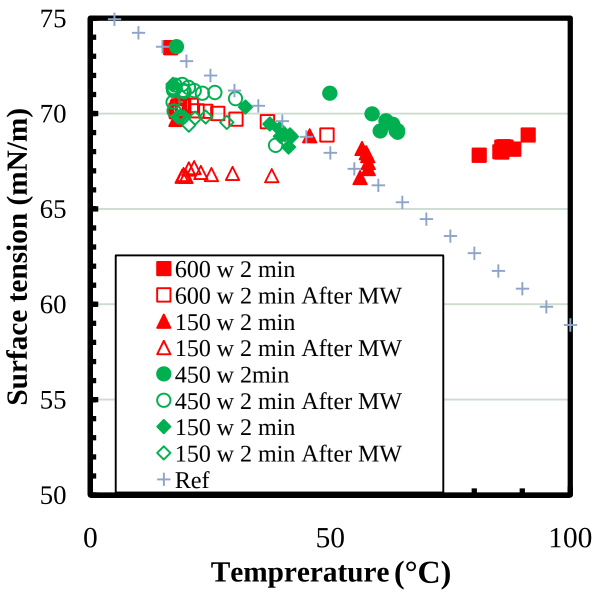

(b) Temperature

Fig. 3 Surface tension of water droplet for multiple radiations as a function of time and temperature (solid symbols: during radiation, unfilled symbols: after radiation).

the second microwave is radiated. The reduction ratio is about 4 mN/m. It is similar with that of single radiation of 150 W [7]. It means that water molecule structure has not reached equilibrium and microwave effect of the second radiation can reduce further. The second radiation was more effective than single radiation (as the recovery degree of surface tension after second radiation is smaller).

The data clearly indicated a non-thermal effect of microwave on water surface tension. The lasting impact of MW can be explained by current knowledge of magnetic-induced effect on water surface tension [6]. Independent studies have shown that water retains some "memory" after exposing to magnetic field. Since the electromagnetic component of the microwave is also varying, it is expected that the net impact is similar.

Recently, studies on surface water have shown that the outmost layer of the water molecules has 25% less than hydrogen bonding [11, 12], whereas hydrogen bonding at the interfacial layer plays a deterministic role in surface tension [13]. Consequently, a rapid change can be expected in surface tension if the outmost water molecules are changed. It is also noteworthy that microwave can only penetrate 1.4 cm deep into water and entire droplets in this study were influenced by microwave. Accordingly, the behavior can be explained by the formation of nano-bubbles inside the water droplet due to homogeneous heating [14-16]. Nano-bubble is normally produced by high shear flow and ultrasonic because network of water molecule is organized at a molecular level. It can be created by microwave in a similar manner because of water molecule rotation. Water molecule is arranged by strong absorption of microwave because droplet size is smaller than penetration depth. These nano-bubbles are negatively charged and might reduce surface tension. It is kind of "impurity effect" which generally reduces the surface tension. Since nano-bubble is more stable, the surface tension remains the lower value for longer time after the radiation. Moreover, nano-bubble is

produced additionally through the second radiation, surface tension becomes lower than constant values after the first radiation. On the other hand, extinction of thermal effect because of temperature drop after the radiation might be the reason why surface tension recovers a little after a second radiation.

4. Conclusions

The surface tension and temperature of water droplet were measured directly under various microwave irradiation modes. It was found by thermal effect that surface tension decreased quickly during microwave. However, surface tension recovery was much slower than temperature after radiation is off. For the highest power, the surface tension remains lower values for more than five min. It is conclusive that the surface tension reduction is not due to thermal heating. Moreover, a second radiation is more effective for the surface tension reduction. The results showed that water was changed structurally at molecular level during the microwave, and retained some “memory” after microwave, which might be caused by nano-bubble. These direct and indirect effects by microwave will play important roles for the application in multiple-phase processes.

References

[1] J. Bao, M. Zhang, Poly (methyl methacrylate) nanoparticles prepared through microwave emulsion polymerization, Appl. Polym. Sci. 93 (2004) 2815-2820.

[2] R. Hoogenboom, U.S. Schubert, Microwave-assisted polymer synthesis: Recent developments in a rapidly expanding field of research, Macromol. Rapid Commun. 28 (2007) 368-386.

[3] G.J.J. Gittens, Variation of surface tension of water with temperature, Colloid Interface Sci. 30 (1969) 406-412.

[4] N.B. Vargaftik, B.N. Volkov, L.D. Voljak, International tables of the surface tension of water, J. Phys. Chem. Ref. Data 12 (3) (1983) 817-820.

[5] S.P. Ju, S.H. Yang, M.L. Liao, Study of molecular behavior in a water nanocluster: size and temperature effect, The Journal of Physical Chemistry B 110 (2006) 9286-9290.

[6] R. Cai, H.W. Yang, J.S. He, W.P. Z, The effects of magnetic fields on water molecular hydrogen bonds, J. Mol. Struct. 938 (2009) 15-19.

[7] H. Parmar, M. Asada, Y. Kanazawa, Y. Asakuma, C.M.P han, V. Pareek, et al., Microwave-induced memory of water, Nature Communication, Langmuir, 2014, submitted 2013-04649t.

[8] M.D. Abràmoff, S.J. Ram, P.J. MagalhÃes, Image processing with image, J. Biophotonics International 11 (2004) 36-42.

[9] M. Hoorfar, A.W. Neumann, ADSA (axisymmetric drop shape analysis) for the determination of surface tension and contact angle, The Journal of Adhesion 80 (2004) 727-743.

[10] Y.Y. Zuo, M. Ding, A. Bateni, M. Hoorfar, A.W. Neumann, Improvement of interfacial tension measurement using a captive bubble in conjunction with axisymmetric drop shape analysis (ADSA), Colloids Surf. 250 (3) (2004) 233-246.

[11] Q. Du, E. Freysz, Y.R. Shen, Surface vibrational spectroscopic studies of hydrogen-bonding and hydrophobicity, Science 264 (1994) 826-828.

[12] Y.B. Fan, X. Chen, L.J. Yang, P.S. Cremer, Y.Q. Gao, On the structure of water at the aqueous/air interface, J. Phys. Chem. B 113 (2009) 11672-11679.

[13] C. Phan, T. Le, C. Nguyen, S. Yusa, Modeling adsorption of cationic surfactants at air/water interface without using the gibbs equation, Langmuir 29 (2013) 4743-4749.

[14] R.P. Berkelaar, J.R.T. Seddon, D. Lohse, Temperature dependence of surface nanobubbles, J. Chem. Phys. Chem. 13 (2012) 2213-2217.

[15] S. Yang, H.J.W. Zandvliet, E. Kooij, D. Lohse, Characterization of nanobubbles on hydrophobic surfaces in water, Langmuir 23 (2007) 7072-7077.

[16] J.R.T. Seddon, J.H. Weijs, D. Lohse, Diffusive shielding stabilizes bulk nanobubble clusters, ChemPhysChem 13 (2012) 2179-2187.

DAVID PUBLISHING

Journal of Energy and Power Engineering
Volume 8, Number 3, March 2014

David Publishing Company
240 Nagle Avenue #15C, New York, NY 10034, USA
Tel: 1-323-984-7526, 323-410-1082; Fax: 1-323-984-7374, 323-908-0457
http://www.davidpublishing.com, www.davidpublishing.org
energy@davidpublishing.com, energy@davidpublishing.org, energy-power@hotmail.com

ISSN 1934-8975
03